

This item was submitted to [Loughborough's Research Repository](#) by the author.  
Items in Figshare are protected by copyright, with all rights reserved, unless otherwise indicated.

## The use of low-temperature thermal expansion for the detection of paramagnetic ions in dielectrics

PLEASE CITE THE PUBLISHED VERSION

PUBLISHER

© Ian Jesse Brown

PUBLISHER STATEMENT

This work is made available according to the conditions of the Creative Commons Attribution-NonCommercial-NoDerivatives 4.0 International (CC BY-NC-ND 4.0) licence. Full details of this licence are available at: <https://creativecommons.org/licenses/by-nc-nd/4.0/>

LICENCE

CC BY-NC-ND 4.0

REPOSITORY RECORD

Brown, Ian J.. 2019. "The Use of Low-temperature Thermal Expansion for the Detection of Paramagnetic Ions in Dielectrics". figshare. <https://hdl.handle.net/2134/32812>.

BLL ID NO. - D 44656/83

LOUGHBOROUGH  
UNIVERSITY OF TECHNOLOGY  
LIBRARY

AUTHOR/FILING TITLE

BROWN, I J

ACCESSION/COPY NO.

127211/02

VOL. NO.

CLASS MARK

~~127211~~  
11 MAR 1993

LOAN COPY

012 7211 02



THE USE OF LOW TEMPERATURE  
THERMAL EXPANSION FOR THE DETECTION  
OF PARAMAGNETIC IONS IN DIELECTRICS.

by

IAN JESSE BROWN

A DOCTORAL THESIS

Submitted in partial fulfillment of the  
requirements for the award of DOCTOR  
OF PHILOSOPHY of the Loughborough  
University of Technology.

OCTOBER 1982

© by Ian Jesse Brown 1982.

|  |           |
|--|-----------|
| Loughborough University<br>of Technology Library |           |
| Shelf  | Sec 32    |
| Class  |           |
| Acc.<br>No.                                      | 127211/02 |

## CONTENTS

|   | <u>Page</u> |
|---|-------------|
| ABSTRACT  | 4           |
| <u>CHAPTER 1</u> <u>An Introduction</u>   | 5           |
| 1.1    The use of thermodynamic properties<br>for the detection of paramagnetic ions<br>in dielectric crystals. | 6           |
| 1.2    The use of thermal expansion for the<br>detection of paramagnetic ions in dielec-<br>trics.              | 9           |
| 1.3    Scope of the thesis.   | 10          |
| <u>CHAPTER 2</u> <u>A Simple Theoretical Treatment of Thermal<br/>                    Expansion</u>             | 14          |
| 2.1    Introduction.  | 15          |
| 2.2    General thermodynamic theory of thermal<br>expansion.  | 15          |
| 2.2.1    Introduction.  | 15          |
| 2.2.2    Isotropic solids.  | 17          |
| 2.2.3    Anisotropic solids.  | 19          |
| 2.2.4    Symmetry considerations.   | 22          |
| 2.2.5    Paramagnetic ions.   | 24          |
| 2.3    The calculation of $\chi_s$ in various crystal<br>environments.  | 25          |
| 2.3.1    Static crystal field model.  | 25          |
| 2.3.2    Jahn-Teller model.   | 28          |
| 2.3.3    Triplet orbital states.  | 28          |
| 2.3.4    Tunnelling splitting model.  | 29          |
| <u>CHAPTER 3</u> <u>The Experimental Determination of Thermal<br/>                    Expansion</u>             | 31          |
| 3.1    Introduction   | 32          |
| 3.2    Review of Dilatometers   | 32          |

|   | Page |
|---|------|
| 3.2.1 X-ray diffraction.  | 32   |
| 3.2.2 Optical interferometers.  | 33   |
| 3.2.3 Optical amplifiers.   | 33   |
| 3.2.4 Electrical inductance.  | 33   |
| 3.2.5 Electrical capacitance.   | 34   |
| 3.3 The three terminal capacitance dilatometer  | 34   |
| 3.4 Capacitance and linearity of Kelvin Guard -<br>ring capacitance transducers.  | 37   |
| 3.5 Constructional details of the capacitance<br>cells used.  | 40   |
| 3.6 Techniques of sample mounting.  | 59   |
| 3.7 The transformer ratio bridge and detector<br>circuitry.   | 60   |
| <u>CHAPTER 4</u> <u>Cryogenic Equipment for the Experimental<br/>Determination of Thermal Expansion at<br/>Low Temperatures</u> | 64   |
| 4.1 Introduction and design parameters.   | 65   |
| 4.2 Cryostat design and performance.  | 67   |
| 4.3 Experimental technique.   | 81   |
| 4.4 Data processing.  | 83   |
| <u>CHAPTER 5</u> <u>The Thermal Expansion of Doped Aluminium<br/>Oxide</u>  | 85   |
| 5.1 Introduction and preliminary experiments.   | 86   |
| 5.2 Thermal expansion corrections due to<br>expansion of dilatometer electrodes and<br>sample supports.                         | 88   |
| 5.3 Thermal expansion of $\text{Al}_2\text{O}_3:\text{Cr}$ (Ruby).  | 89   |
| 5.4 Thermal expansion of $\text{Al}_2\text{O}_3:\text{Mn}$ .  | 96   |
| 5.5 Thermal expansion of $\text{Al}_2\text{O}_3:\text{V}$ .   | 99   |
| 5.6 Summary.  | 100  |
| <u>ACKNOWLEDGEMENTS</u>   | 129  |
| <u>REFERENCES</u>   | 130  |
| <u>APPENDIX 1</u> <u>Fortran Package for Processing Thermal Expansion<br/>Data.</u>   | 133  |

ABSTRACT

The object of the thesis is to demonstrate the existence of Schottky type anomalies in the low temperature thermal expansion of dielectric crystals produced by the presence of a small concentration of strongly coupled paramagnetic impurity ions.

Cryogenic equipment, utilising a three terminal capacitance dilatometer, for the semi-automatic measurement of thermal expansion at low temperatures using a dynamic measurement technique has been designed, constructed and commissioned. The results of application of this apparatus to determine the contribution to the thermal expansion at low temperatures of aluminium oxide ( $\text{Al}_2\text{O}_3$ ) due to small concentrations of strongly coupled paramagnetic ions ( $\text{Cr}^{2+} (3d^4, 5D)$ ,  $\text{Mn}^{3+} (3d^4, 5D)$ ,  $\text{V}^{3+} (3d^2, 3F)$ ) is presented. Peaked anomalies in the thermal expansion of  $\text{Al}_2\text{O}_3$  doped with these ions have been observed which are not present for undoped samples. The effects observed are in contrast with those predicted using a static crystal field model but may be interpreted in terms of a dynamic Jahn-Teller model.

CHAPTER 1

| <u>An Introduction</u>   | Page |
|--|------|
| 1.1 The use of thermodynamic properties for the detection of paramagnetic ions in dielectric crystals. | 6    |
| 1.2 The use of thermal expansion for the detection of paramagnetic ions in dielectrics.                | 9    |
| 1.3 Scope of the thesis.   | 10   |



### 1.1 The Use of Thermodynamic Properties for the Detection of Paramagnetic Ions in Dielectric Crystals

It is a principle of basic thermodynamics that we can define the thermodynamic properties of a system in terms of various thermodynamic potentials. These potentials will be additive functions of state in that it is possible to express them in terms of components of each of the various degrees of freedom of the state. For instance, if we consider a system with  $n$  degrees of freedom, we may express the internal energy ' $U$ ' of the system in terms of  $2n$  primary variables.

$$dU = Tds + \sum_{i=1}^{n-1} X_i dx_i \quad (1.1)$$

Where  $T$  and  $S$  are the temperature and entropy of the system, and the  $X_i$  and  $dx_i$  are the pairs of conjugate primary variables for the various contributing subsystems (the products  $X_i dx_i$  having dimensions of energy).

The various thermodynamic variables may be expressed in terms of differentials of these thermodynamic potentials. For instance, the specific heat at constant volume,  $C_v$ , may be expressed in terms of the Helmholtz free energy,  $F$ , of the system by the 2nd differential

$$C_v = -T \left( \frac{d^2 F}{dT^2} \right)_v \quad (1.2)$$

We would hence expect the specific heat at constant volume to be a sum of components due to the  $n$  different contributing subsystems.

$$C_v = \sum_{M=1}^n C_{vM} \quad (1.3)$$

In particular we should expect a contribution to these thermodynamic potentials due to the presence of paramagnetic entities in the crystal lattice. These will have a discrete energy level structure and the physical properties of such will be dominated by transitions between these levels, either as a thermally excited average or by individual transitions induced by thermal excitation or by electromagnetic or 'acoustic' radiation.

In particular we will have a contribution to specific heat at constant volume due to thermal excitation of a series of energy levels  $E_0, E_1, \dots, E_n$ , with degeneracies  $f_0, f_1, \dots, f_n$  which is given by ((Griffith 1961) eqn 2-16)

$$C_{vs} = \frac{(\langle E^2 \rangle - \langle E \rangle^2)}{RT^2} \quad (1.4)$$

Where the triangular brackets,  $\langle \rangle$ , denote thermal averages of the form:

$$\langle x_i \rangle = \frac{\sum_{i=1}^n f_i x_i \exp(-E_i/RT)}{\sum_{i=1}^n f_i \exp(-E_i/RT)} \quad (1.5)$$

and where  $k$  is the Boltzmann constant ( $k = 1.381 \times 10^{-23} \text{ JK}^{-1}$ ). The quantity  $C_{vs}$  is the well known Schottky specific heat with the characteristic peaked profile as shown in figure (1.1).

We should hence expect to observe a peaked anomaly in the specific heat of a crystal containing a concentration of paramagnetic ions provided that:-

- 1/ The concentration of the ion is such that the magnitude of the Schottky peak is comparable with the sum of other contributions to the specific heat.
- 2/ The concentration of the ion is such that the magnitude of the Schottky peak is within the sensitivity of the measurement technique.

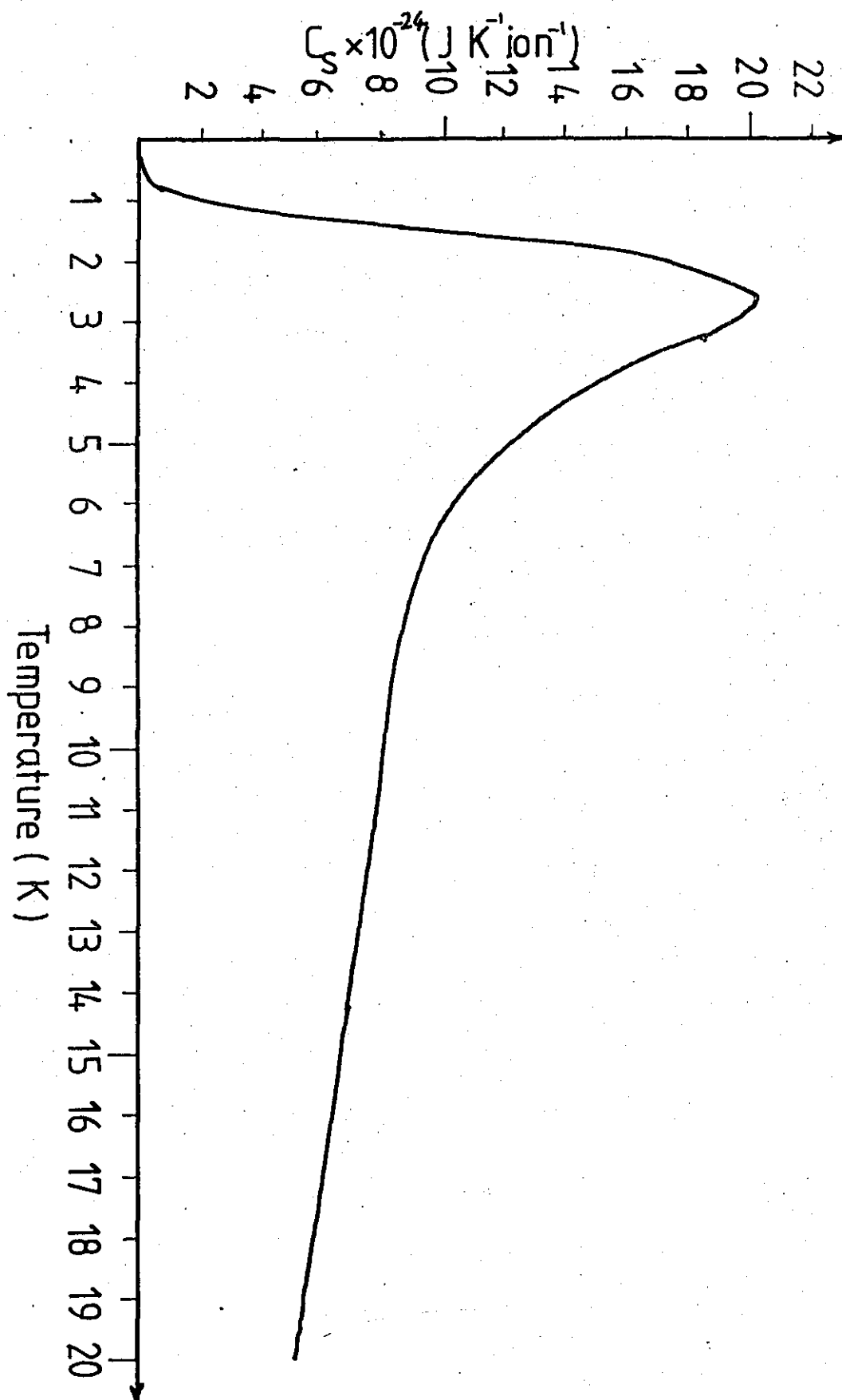


FIG. 1.1 Theoretical Schottky Contribution to the Specific Heat of  $\text{Al}_2\text{O}_3$  due to the Presence of  $\text{Cr}^{2+}$  Impurity Ions.

In general there may also be contributions to other thermal properties resulting from a concentration of paramagnetic ions such as thermal conductivity (eg Callaway (1959)) and thermal expansion (to be discussed later)

## 1.2 The Use of Thermal Expansion for the Detection of Paramagnetic Ions in Dielectrics

The standard Gruneisen theory for thermal expansion (eg Collins & White (1964)) may be generalised to include the effect of two level impurity ions, with level splitting  $E_s$ . The volume expansion coefficient  $\beta$  is then given by:

$$\frac{\beta}{\chi_T} = \frac{\gamma_L C_L + \gamma_S C_S}{V} \quad (1.6)$$

Where  $C_L$  and  $C_S$  are the heat capacities at constant volume  $V$  of the lattice and ions respectively,  $\chi_T$  is the isothermal compressibility, and  $\gamma_L$  and  $\gamma_S$  are the lattice and "Magnetic" Gruneisen parameters. Expressions for  $\gamma_L$  and  $\gamma_S$  will be studied in more detail later but the magnetic (or Schottky) Gruneisen parameter is broadly defined as the volume dependence of the energy splitting  $E_s$ :-

$$\gamma_S = - \left( \frac{\partial \ln E_s}{\partial \ln V} \right) \quad (1.7)$$

There will be an observable effect in the crystal thermal expansion when  $\gamma_L C_L \sim \gamma_S C_S$ . When this condition is satisfied, we should expect to observe a peaked anomaly in thermal expansion at a temperature similar to the Schottky peak in specific heat. We will again show later that this theory may be readily generalised to multi-level system by defining Gruneisen parameters for each of the  $n$  individual levels, that is:-

$$\beta = \frac{\chi_T \gamma_L C_L}{V} + \beta_S$$

Where  $\beta_S$  is the Schottky thermal expansion expressed by:-

$$\beta_S = \frac{\chi_T}{VKT^2} \left( \langle \gamma_i E_i^2 \rangle - \langle \gamma_i E_i \rangle \langle E_i \rangle \right)$$

Where the triangular brackets denote thermal averages as before. We should hence expect the anomaly in thermal expansion to occur at the same temperature to that in specific heat only when the levels have equal Gruneisen parameters.

As we have previously described, specific heat measurements provide information on the energy level splittings of the paramagnetic ions and also ionic concentrations but are experimentally difficult measurements to perform. Thermal expansion measurements provide additional information in the Gruneisen coefficient  $\gamma_s$ . This when determined would point in a more direct fashion to the existence of a strong Jahn-Teller effect.

The value of  $\gamma_s$  predicted by a static crystal field model, assuming a tetrahedral environment where the crystal field splitting  $\Delta \propto a^{-5}$  ('a' is the atomic spacing), is  $\gamma_s = -\frac{5}{3}$ . The value of the parameter in the presence of a dynamic Jahn-Teller effect is more complex, but in general large ( $\sim 50$ ) positive values are to be expected in the presence of a tunnelling splitting or strong dynamic Jahn-Teller effect (see Chapter II) (Sheard (1971)).

Some experimental observations of volume dependence associated with discrete energy levels have been reported in TmSb (Ott and Luthi (1976)), solid argon (Tilford and Swenson (1969)), alkali halides (Case et al (1974)) and upon natural crystals of ZnS containing Fe impurities (Sheard et al (1977)). The experimental results obtained in the ZnS measurements suggested a magnetic Gruneisen parameter of  $\gamma_s = -\frac{5}{3}$  which is consistent with the predictions of a static crystal model (although the presence of a weak Jahn-Teller effect was not precluded).

### 1.3

#### Scope of the Thesis

A great deal of experimental and theoretical work, over several years, has been performed on the properties of various paramagnetic ions in several host lattices (see Bates (1978) for an extensive bibliography); Of particular interest are ions which, using static field theory, have E type orbitals in an octahedral environment, such as  $\text{Cr}^{2+}$  ( $3d^4, ^5D$ ) in  $\text{MgO}$ , when it is thought that the orbit-lattice interaction is so strong that a simple description using static crystal theory is inadequate. In this situation, the electronic states couple to the vibrations of the neighbouring atoms

producing a dynamic Jahn-Teller system (Sturge (1957)) which has been calculated in some detail for the case of  $\text{Cr}^{2+}$  in  $\text{MgO}$  (Fletcher and Stevens (1969)).

Experimentally, the quantitative measurement, or even the detection of small quantities of impurity ions is extremely difficult. The energy level splittings of such ions are typically in the range  $\sim 10 \text{ cm}^{-1}$  and are difficult to measure by resonance techniques using electromagnetic or acoustic radiation. However, the presence of very small amounts of magnetic ions, strongly coupled to the lattice, can have quite large effects on the physical properties of materials. One example is the ruby system ( $\text{Al}_2\text{O}_3:\text{Cr}$ ) which has received a great deal of attention. Davies et al (1965) showed that the laser efficiency of a ruby was increased three fold by  $\gamma$ -irradiation and later work (Brown et al (1973)) showed that  $\gamma$ -irradiation caused the formation of  $\text{Cr}^{2+}$  (again strongly-coupled to the  $\text{Al}_2\text{O}_3$  lattice). The properties of  $\text{Cr}^{2+}$  were investigated qualitatively with some success using thermal conductivity techniques and it was shown that very small concentrations of  $\text{Cr}^{2+}$  (estimated to be  $\sim 0.1 \text{ ppm}$ ) acted as an effective energy short-circuit taking energy from the active  $\text{Cr}^{3+}$  ions and transferring it to the lattice.

The purpose of this thesis is to demonstrate the presence of peaked, Schottky type, anomalies in thermal expansion at low temperatures due to small quantities of various paramagnetic ions in Aluminium Oxide and hence demonstrate the possibility of using thermal expansion at low temperatures as a technique for the detection and study of such ions.

Semi-automated cryogenic equipment was constructed and developed for the measurement of thermal expansion at low temperatures. This equipment incorporated a sensitive, three terminal, capacitance dilatometer and a ratio arm transformer capacitance bridge for the precise measurement of thermal expansion utilising a dynamic measurement technique.

This apparatus was used in an extensive series of experiments to measure the thermal expansion of  $\text{Al}_2\text{O}_3$ , both as pure crystals, and doped with small concentrations of Chromium, Vanadium and Manganese impurities.

Aluminium oxide ( $\text{Al}_2\text{O}_3$ ) was chosen as the dielectric for two important reasons.

- 1/ Large crystals of aluminium oxide, both pure and containing various species of paramagnetic impurities were readily available.
- 2/ The Debye temperature of  $\text{Al}_2\text{O}_3$  is high (1023) so that lattice contributions to thermal expansion at low temperatures will be very small and not dominate any magnetic contributions.

Particular effort was expended in study of the ruby ( $\text{Al}_2\text{O}_3:\text{Cr}$ ) system. This was of considerable interest <sup>because</sup> :-

- 1/ As chromium is a substitutional impurity for aluminium in the  $\text{Al}_2\text{O}_3$  lattice the valence state of a majority of the chromium ions present will be +3. The concentration of  $\text{Cr}^{2+}$  (a very strongly coupled ion) may then be varied by  $\gamma$ -irradiation and U-V treatment. The anomaly in thermal expansion, if due to  $\text{Cr}^{2+}$ , should hence be turned on and off by such treatments.
- 2/ Although Cr substitutes for Al which experiences essentially a trigonally distorted cubic field, there is evidence (Brown (1971), Bates and Wardlaw (1980)) that  $\text{Cr}^{2+}$  produces an almost pure cubic field environment for itself.
- 3/ The static cubic field model does not explain the behaviour of  $\text{Cr}^{2+}$  in  $\text{Al}_2\text{O}_3$  (Challis and de Goer (1970)) and consequently the dynamic Jahn-Teller model has been developed (Bates and Wardlaw (1980)) in some detail for this system.
- 4/ The theoretical work of Sheard suggests that the magnetic Gruneisen parameter for ions experiencing a strong (tunnelling splitting) Jahn-Teller effect should be markedly different (large and positive) to that expected from a static crystal model ( $\gamma_s = -\frac{5}{3}$ ). Thermal expansion measurements should hence help to reinforce evidence for a tunnelling splitting effect.

The experimental work on the samples have shown positive anomalies in the low temperature thermal expansion of  $\text{Al}_2\text{O}_3:\text{Mn}^{3+}$  and  $\text{Al}_2\text{O}_3:\text{Cr}^{2+}$  with  $\gamma_s \sim 100$ , consistent with a tunnelling splitting model. It has also been demonstrated that the anomalous effect attributed to the presence of  $\text{Cr}^{2+}$  in the ruby sample could be 'turned on and off' by  $\gamma$ -irradiation and UV treatment respectively.

Negative anomalies in the thermal expansion of  $\text{Al}_2\text{O}_3:\text{V}$  at temperatures

consistent with the presence of  $V^{3+}$  ions in the sample have been observed with a Gruneisen parameter of  $\gamma_s \sim -6$ .

No anomalies were observed in the thermal expansion of pure  $Al_2O_3$  in the temperature range measured (2-25 K) .



CHAPTER 2

Page

A Simple Theoretical Treatment of Thermal Expansion.

|       |  |    |
|-------|--|----|
| 2.1   | Introduction.  | 15 |
| 2.2   | General Thermodynamic Theory of Thermal Expansion.           | 15 |
| 2.2.1 | Introduction.  | 15 |
| 2.2.2 | Isotropic Solids.  | 17 |
| 2.2.3 | Anisotropic Solids.  | 19 |
| 2.2.4 | Symmetry Considerations.                                     | 22 |
| 2.2.5 | Paramagnetic Ions.   | 24 |
| 2.3   | The Calculation of $\chi_s$ in Various Crystal Environments. | 25 |
| 2.3.1 | Static Crystal Field Model.                                  | 25 |
| 2.3.2 | Jahn-Teller Model.   | 28 |
| 2.3.3 | Triplet Orbital States.                                      | 28 |
| 2.3.4 | Tunnelling Splitting Model.                                  | 29 |

## 2.1 INTRODUCTION

In this chapter an attempt will be made to provide a simplified overview of the theoretical description of the thermal expansion of crystals, and contributions to the thermal expansion due to small concentrations of paramagnetic impurity ions in the crystal lattice. A detailed discussion of theoretical modelling techniques which have been used to describe the crystal lattice is unnecessary and is discussed extensively in several review articles (eg Barron et al (1980)). Similarly a detailed discussion of the role of the Jahn-Teller effect applied to paramagnetic ions is not given as this also is discussed extensively in the literature and several excellent review articles exist (eg Bates (1978)). The discussion here will be limited to a description of the 'standard' Gruneisen theory of thermal expansion and how this may be extended to include contributions from small concentrations of paramagnetic ions and the physical parameters describing the ions which determine the magnitude of these contributions to thermal expansion.

## 2.2 GENERAL THERMODYNAMIC THEORY OF THERMAL EXPANSION

### 2.2.1 Introduction

Thermal expansion, which we understand as being any dimensional change with change in temperature, may be characterised by a volumetric expansion coefficient,  $\beta$ . This coefficient of volumetric expansion may be defined algebraically to be:-

$$\beta = \left( \frac{\partial \ln V}{\partial T} \right)_P \quad (2.1a)$$

Where  $V$  is the sample volume and  $T$  is the temperature. Using simple thermodynamic relations it is easily demonstrated that the expansion coefficient may also be expressed by:-

$$\beta = \frac{1}{\alpha_T} \left( \frac{\partial P}{\partial T} \right)_V \quad (2.1b)$$

Where  $P$  is the pressure and  $\alpha_T$  is the isothermal compressibility :-

$$\alpha_T = - \left( \frac{\partial \ln V}{\partial P} \right)_T$$

We can also describe volumetric expansion, for cubic and isotropic solids, in terms of the linear expansion coefficient  $\alpha$  by:-

$$\beta = 3\alpha = 3 \left( \frac{\partial \ln \ell}{\partial T} \right)_P \quad (2.1c)$$

Where  $\ell$  is the sample length.

But, in general, for anisotropic solids, the expansion must be expressed in terms of the macroscopic strain parameters,  $\eta_i$ , by the expansion tensor:-

$$\alpha_i = \left( \frac{\partial \eta_i}{\partial T} \right)_P \quad (2.2)$$

Where  $\eta_i = \frac{\Delta \epsilon_i}{\epsilon_i}$

The subscripts,  $i$ , describe principal directions in the Voigt notation.

The dimensional changes are such as to minimise the Helmholtz free energy of the lattice. This, being an additive function of state, has contributions not only from the lattice but from itinerant electrons, electric dipoles, magnetic ions, nuclear spins and other properties. Thus we should expect the thermal expansion also to have contributions from these various properties.

The microscopic theory of thermal expansion derives from the work of Mie (1903) and Gruneisen (1912). Many theoretical and experimental studies are now defined in terms of a parameter,  $\gamma$ , known as the Gruneisen parameter and defined algebraically as:-

$$\gamma = \frac{\beta V}{\chi_T C_V} = \frac{\beta V}{\chi_S C_P} \quad (2.3)$$

Where  $\chi_T$  and  $\chi_S$  are isothermal and adiabatic compressibilities and  $C_V$ ,  $C_P$  are heat capacities at constant volume and pressure. Gruneisen, using a quantum Einstein model characterised by a single vibrational frequency  $\nu$  derived from inter-atomic forces, found that this parameter  $\gamma$  was indeed identified by:-

$$\gamma \equiv - \frac{\partial (\ln \nu)}{\partial (\ln V)} \quad (2.4)$$

This expresses the essential role of anharmonicity of the crystal lattice potential. For a purely harmonic lattice potential the

parameter  $(\partial \ln \gamma / \partial \ln V)$  is zero. As little is known concerning the specific values of these anharmonic contributions in a particular crystal lattice, the thermal expansion is normally studied within the confines of a quasi-harmonic approximation. In this technique the anharmonic terms in the lattice potential energy are neglected and the interaction constants of the harmonic model considered to be volume dependent (eg Leibfried and Ludwig (1961), Barron and Klein (1962)).

### 2.2.2 Isotropic Solids

The volumetric expansion coefficient,  $\beta$ , may be related to the Helmholtz free energy,  $F(V, T)$ , via standard thermodynamic transformations.

$$\beta = - \left( \frac{\partial \ln V}{\partial P} \right)_T \left( \frac{\partial P}{\partial T} \right) = \chi_T \left( \frac{\partial F}{\partial T} \right) \quad (2.5)$$

$$= - \chi_T \left( \frac{\partial^2 F}{\partial V \partial T} \right) = \chi_T \left( \frac{\partial S}{\partial V} \right)_T \quad (2.6)$$

Where  $S$  is the entropy and  $\chi_T$  is the isothermal compressibility. The isothermal bulk modulus,  $B_T$ , may be defined algebraically as:-

$$B_T = - \left( \frac{\partial P}{\partial \ln V} \right)_T = V \left( \frac{\partial^2 F}{\partial V^2} \right)_T \quad (2.7)$$

Therefore it is simply shown that

$$\beta B_T = \frac{\partial^2 F}{\partial V \partial T} \quad (2.8)$$

Similarly the specific heat at constant volume may be defined in terms of the free energy as:-

$$C_V = - T \left( \frac{\partial^2 F}{\partial T^2} \right)_V \quad (2.9)$$

The Helmholtz free energy being an additive function of state, subject to the limitations of the adiabatic principle, may be expressed as a sum of terms due to the different 'components' of the system. The separation being valid providing that the energy states of any one of the components can be calculated to good accuracy by assuming the

energy states of the other components to be in some 'frozen' averaged configuration, that is, to have sufficiently different relaxation times for the component systems. Independent additive contributions can thus also be obtained for the derivatives of the free energy  $F$ , such as entropy, heat capacity and bulk modulus. This is not so for thermal expansion which is a ratio of derivatives. Since the bulk modulus, which at low temperatures is normally dominated by the static lattice energy, varies little with temperature we may, however, conclude that the thermal expansion may be assumed to be a sum of contributions from the  $n$  component systems.

$$\beta = \sum_{m=1}^n \beta_m \quad (2.10)$$

So we observe from eqn (2.6) that the magnitude of the components,  $\beta_m$ , is dependent on the sensitivity of the free energy contributions,  $F_m$ , to changes in strain.

$$\beta = \sum_{m=1}^n \beta_m = \chi_T \sum_{m=1}^n \left( \frac{\partial S_m}{\partial V} \right)_T \quad (2.11)$$

Gruneisen constants may also be defined for the various components of the thermal expansion but it will be useful to firstly define the Gruneisen constant,  $\chi$ , in terms of more fundamental thermodynamic quantities. The dimensionless Gruneisen function may be conveniently defined by considering the differential change in entropy resulting from changes  $dV$  and  $dT$  in volume and temperature.

$$dS = \left( \frac{\partial S}{\partial T} \right)_V dT + \left( \frac{\partial S}{\partial V} \right)_T dV \quad (2.12)$$

$$= C_V d \ln T + \beta B_T V d \ln V \quad (2.13)$$

And hence at constant entropy we define the Gruneisen constant:

$$\chi(T_S V) \equiv \frac{\beta B_T V}{C_V} = - \left( \frac{\partial \ln T}{\partial \ln V} \right)_S \quad (2.14)$$

Other expressions for  $\chi$  may be obtained by thermodynamic transformation:

$$\chi(T_S V) = \frac{\beta V}{\chi_T C_V} = \frac{\beta V}{\chi_S C_P} \quad (2.15)$$

$$\gamma(T, V) = \frac{V(\partial P / \partial T)_V}{C_V} = \frac{(\partial(PV) / \partial U)_V}{C_V} \quad (2.16)$$

Where  $U$  is the internal energy

$$\gamma(T, V) = \frac{(\partial S / \partial \ln V)_T}{C_V} = V \left( \frac{\partial^2 F}{\partial V \partial T} \right) / T \left( \frac{\partial^2 F}{\partial T^2} \right)_V \quad (2.17)$$

The Gruneisen constants for the different contributing components may be expressed from eqn (2.17) by considering the entropy as a sum of the separate contributions  $S_m$ .

$$S = \sum_{m=1}^n S_m$$

$$\text{Hence } C_V = \sum_{m=1}^n (\partial S_m / \partial \ln T)_V = \sum C_m \quad (2.18)$$

So that we have:-

$$\gamma_m = \left( \partial S_m / \partial \ln V \right)_T / C_m \quad (2.19)$$

The measured  $\gamma$  defined by eqn (2.15) is then a weighted average of the  $\gamma_m$  of the various components.

$$\gamma = \sum_{m=1}^n \gamma_m C_m / \sum_{m=1}^n C_m \quad (2.20)$$

### 2.2.3 Anisotropic Solids

For most materials the treatment considered above is insufficient and must be generalised to include a change in shape, as well as a change in volume, with temperature. The thermal expansion of the material must be described in terms of an expansion tensor  $\underline{\alpha}$ , which may be defined by:-

$$\underline{\alpha}_{\alpha\beta} = \underline{\alpha}_{\beta\alpha} = \left( \partial \eta_{\alpha\beta} / \partial T \right)_t \quad (2.21)$$

Where the  $\alpha_{\alpha\beta}$  are anisotropic expansion coefficients at constant stress,  $\eta_{\alpha\beta}$  is a Lagrangian finite strain coordinate describing the deformation of the body from some 'reference' configuration, and  $t_{\alpha\beta}$  is the conjugate stress to  $\eta_{\alpha\beta}$  ie

$$t_{\alpha\beta} = t_{\beta\alpha} = V^{-1} \left( \frac{\partial F}{\partial \eta_{\alpha\beta}} \right)_{T, \eta'} \quad (2.22)$$

Here the subscript  $\eta'$  denotes that all other strain coordinates are kept constant,  $V$  is the volume of the reference configuration which we define to be the instantaneous volume of the solid at zero stress. To use to advantage the independence of only six of the elements of a symmetric strain tensor we adopt Voigt's notation for the six strain coordinates.

$$\eta_1 = \eta_{11}, \text{ etc}; \eta_4 = 2\eta_{23} = 2\eta_{32}, \text{ etc} \quad (2.23)$$

Similarly we can define the coordinates of thermal expansion using an exactly similar notation.

$$\alpha_1 = \alpha_{11}, \text{ etc}, \alpha_4 = 2\alpha_{23} = 2\alpha_{32}, \text{ etc} \quad (2.24)$$

And also the conjugate stress tensor to  $\eta_\lambda$ .

$$t_1 = t_{11}, \text{ etc}; t_4 = t_{23} = t_{32} \text{ etc} \quad (2.25)$$

Having defined this abbreviated notation, equations (2.21) and (2.22) may be simply expressed as;

$$\alpha_\lambda = (\partial \eta_\lambda / \partial T)_t \quad (2.26)$$

$$t_\lambda = V^{-1} \left( \partial F / \partial \eta_\lambda \right)_{T, \eta'} \quad (2.27)$$

Where  $\lambda = 1 \text{ to } 6$

As a preliminary to deriving the usual thermodynamic relationships we must first generalise the bulk modulus and compressibility before, to give the elastic stiffness and compliances:

$$\left. \begin{aligned} \sigma_{\lambda\mu}^T &= \left( \frac{\partial t_\lambda}{\partial \eta_\mu} \right) \eta'_\mu, T \\ \delta_{\lambda\mu}^T &= \left( \frac{\partial \eta_\lambda}{\partial t_\mu} \right) t'_\mu, T \end{aligned} \right\} \quad (2.28)$$

$$\sum_i \sigma_{\lambda\nu}^T \sigma_{\nu\mu}^T = \delta_{\lambda\mu} \quad (2.29)$$

With similar definitions for the adiabatic elastic constants  $(\sigma_{\lambda\mu}^S \sigma_{\lambda\mu}^S)$ . Here  $\delta_{\lambda\mu}$  is the Kronecker delta function, equation (2.29) replacing the simple reciprocal relationship between the bulk modulus and the compressibility.

Thermodynamic relations may now be established, as before, by manipulation of partial derivatives but must be generalised to allow for there being more than two independent variables and these are stated below (Barron et al (1980)).

Equations (2.5) and (2.6) become for an anisotropic material.

$$\begin{aligned} \alpha_\lambda &= \sum_\mu \sigma_{\lambda\mu}^T \left( \frac{\partial S}{\partial \eta_\mu} \right) \eta'_{\lambda T} / V \\ &= \sum_\mu \sigma_{\lambda\mu}^T \left( \frac{\partial t_\mu}{\partial T} \right) \eta'_{\lambda T} \end{aligned} \quad (2.30)$$

Gruneisen functions are generalised from equation (2.17).

$$\gamma = \left( \frac{\partial S}{\partial \eta_\lambda} \right) \eta'_{\lambda T} / C_\eta \quad (2.31)$$

Where  $C_\eta$  is the heat capacity at constant strain. Other expressions for  $\gamma$  may also be derived.

$$\begin{aligned} \gamma_\lambda &= - \left( \frac{\partial \ln T}{\partial \eta_{T\lambda}} \right) \eta'_{\lambda S} \\ &= -V \left( \frac{\partial t_\lambda}{\partial U} \right) \eta'_{\lambda S} \end{aligned} \quad (2.32)$$

Thus defining a Gruneisen tensor also in the Voigt notation.

$$\gamma_{11} = \gamma_1, \text{ etc; } \gamma_{23} = \gamma_{32} = \gamma_4 \text{ etc} \quad (2.33)$$

As with the isotropic case, if contributions to the free energy from various subsystems are considered, we may define Gruneisen tensors for each of the contributing subsystems by considering the entropy of the material to be the sum of that due to the contributing subsystems.

$$\begin{aligned} S &= \sum_m S_m \\ \gamma_{\lambda,m} &= \left( \partial S_m / \partial \eta_\lambda \right) \eta'_{\lambda T} / C_{\eta,m} \end{aligned} \quad (2.34)$$



The measured  $\gamma_\lambda$  are again given by a weighted average of the separate  $\gamma_{\lambda,m}$ .

$$\gamma_\lambda = \sum_m \gamma_{\lambda,m} C_{\eta,m} / \sum_m C_{\eta,m} \quad (2.35)$$

The relationship between the Gruneisen tensor and that of the thermal expansion is defined by generalising equation (2.14).

$$\left. \begin{aligned} \gamma_\lambda(T, \eta) &= V \sum_\mu q_{\lambda\mu}^T \alpha_\mu / C_\eta \\ &= V \sum_\mu q_{\lambda\mu}^S \alpha_\mu / C_p \end{aligned} \right\} \quad (2.36)$$

And also

$$\left. \begin{aligned} \alpha_\lambda &= C_\eta \sum_\mu S_{\lambda\mu}^T \gamma_\mu / V \\ &= C_p \sum_\mu S_{\lambda\mu}^S \gamma_\mu / V \end{aligned} \right\} \quad (2.37)$$

The coefficient of volumetric expansion may then be expressed

$$\left. \begin{aligned} \beta &= \sum_{\lambda=1}^3 \alpha_\lambda = \frac{C_\eta \sum_{\mu=1}^6 \chi_\mu^T \gamma_\mu}{C_p \sum_{\mu=1}^6 \chi_\mu^S \gamma_\mu} \end{aligned} \right\} \quad (2.38)$$

Where  $\chi_\mu^T$  and  $\chi_\mu^S$  are generalised compressibilities, that is

$$\begin{aligned} \chi_\mu^S &= -(\partial \eta_\mu / \partial P)_S = \sum_{\lambda=1}^3 S_{\mu\lambda}^S \\ &= \left( \frac{\partial \ln V}{\partial t_\mu} \right)_{S, t'} \end{aligned} \quad (2.39)$$

#### 2.2.4 Symmetry Considerations

For crystals, such as aluminium oxide, exhibiting axial symmetry properties (group  $C_3$  for  $Al_2O_3$ ) the general anisotropic analysis given above can be simplified (Barron et al (1980)). Here we may define two principal coefficients of expansion, given algebraically by:-

$$\left. \begin{aligned} \alpha_1 &= \alpha_2 = \alpha_\perp = (\partial \ln \alpha / \partial T)_P \\ \alpha_3 &= \alpha_{||} = (\partial \ln c / \partial T)_P \end{aligned} \right\} \quad (2.40)$$

Where  $a$  and  $c$  denote lengths perpendicular and parallel, respectively, to the main crystal axis. The principal Gruneisen functions are:-

$$\begin{aligned}\gamma_{\perp} &= \frac{1}{2} \frac{(\partial S / \partial \ln a)_{c,T}}{C_K} = \frac{\sqrt{\{ (C_{11}^S + C_{12}^S) \alpha_{\perp} + C_{13}^S \alpha_{\parallel} \}}}{C_P} \\ \gamma_{\parallel} &= (\partial S / \partial \ln c)_{a,T} = \frac{\sqrt{\{ 2 C_{13}^S \alpha_{\perp} + C_{33}^S \alpha_{\parallel} \}}}{C_P}\end{aligned}\quad (2.41)$$

Here the factor  $\frac{1}{2}$  arises because 'a' determines two of the crystal dimensions. These equations are rearranged to give the principal coefficients of expansion in terms of the principal Gruneisen functions.

$$\begin{aligned}\alpha_{\perp} &= \frac{\{ (S_{11}^S + S_{12}^S) \gamma_{\perp} + S_{13}^S \gamma_{\parallel} \} C_P}{\sqrt{\quad}} \\ \alpha_{\parallel} &= \frac{\{ 2 S_{13}^S \gamma_{\perp} + S_{33}^S \gamma_{\parallel} \} C_P}{\sqrt{\quad}}\end{aligned}\quad (2.42)$$

The compliances are related to the stiffness  $C_{\lambda\mu}$  by

$$\left. \begin{aligned}S_{11} + S_{12} &= C_{33} / D & S_{33} &= (C_{11} + C_{12}) / D \\ S_{13} &= -C_{13} / D & D &= (C_{11} + C_{12}) C_{33} - 2 C_{13}^2\end{aligned}\right\} \quad (2.43)$$

The volume coefficient of expansion is then given by the trace of the expansion tensor.

$$\beta = 2\alpha_{\perp} + \alpha_{\parallel} = \frac{(2\chi_{\perp}^S \gamma_{\perp} + \chi_{\parallel}^S \gamma_{\parallel}) C_P}{\sqrt{\quad}} \quad (2.44)$$

Where  $\chi_{\perp}^S$  and  $\chi_{\parallel}^S$  are the principal linear adiabatic compressibilities. The Gruneisen parameter,  $\gamma$ , for volume expansion is a linear combination of  $\gamma_{\perp}$  and  $\gamma_{\parallel}$  weighted by the respective linear compressibilities.

$$\gamma = (2\chi_{\perp}^S \gamma_{\perp} + \chi_{\parallel}^S \gamma_{\parallel}) / \chi^S \quad (2.45)$$

For a random direction  $x$  making an angle  $\psi$  with the  $c$ -axis, the resolved value  $\alpha_x$  of the thermal expansion in this direction is then:-

$$\begin{aligned}\alpha_x &= \sum_{\alpha\beta} \alpha_{\alpha\beta} x_{\alpha} x_{\beta} \\ &= \alpha_{\perp} \sin^2 \psi + \alpha_{\parallel} \cos^2 \psi\end{aligned}\quad (2.46)$$

### 2.2.5 Paramagnetic Ions

It has been demonstrated before that the measured Gruneisen parameter  $\gamma$  is a weighted average of the components  $\gamma_m$  due to the  $m$  contributing subsystems. For an isotropic material this was shown to be:-

$$\gamma = \sum_m \gamma_m C_m / \sum_m C_m \quad (2.20)$$

Where  $C_m$  is the contribution to the specific heat of the  $m^{\text{th}}$  subsystem. The separate  $\gamma_m$  have been shown to be expressed by:-

$$\gamma_m = (\partial S_m / \partial \ln V)_T / C_m \quad (2.19)$$

Where  $S_m$  is the contribution to the entropy due to the  $m^{\text{th}}$  contributing subsystem.

In order to calculate the contribution to the thermal expansion of a host lattice due to a paramagnetic impurity ion, we firstly consider the Schottky contribution to the specific heat due to such ions. The Schottky contribution to the specific heat resulting from thermal excitation of a series of energy levels  $E_0, E_1, \dots, E_n$  with degeneracies  $f_0, f_1, \dots, f_n$  is given by (Griffith 1961, eqn 2.16)

$$C_s = \frac{(\langle E_i^2 \rangle - \langle E_i \rangle^2)}{KT^2} \quad (2.47)$$

Where the brackets  $\langle \rangle$  denote thermal averages of the form:-

$$\langle x_i \rangle = \frac{\sum_{i=1}^n f_i x_i \exp(-E_i/KT)}{\sum_{i=1}^n f_i \exp(-E_i/KT)} \quad (2.48)$$

The Schottky contribution to the volumetric expansion coefficient, is similarly expressed (Barron<sup>etal</sup> (1980)) by:

$$\beta_s = \left( \frac{\alpha_T}{VK T^2} \right) \{ \langle E_i^2 \gamma_i \rangle - \langle E_i \rangle \langle E_i \gamma_i \rangle \} \quad (2.49)$$

Where  $\gamma_i$ , the contribution to the Gruneisen parameter due to the  $i^{\text{th}}$  energy level, is given by (Sheard (1969)):-

$$\gamma_i = - (\partial \ln E_i / \partial \ln V)_T \quad (2.50)$$

Expressions 2.47 and 2.49 may hence be combined resulting in an expression for the Gruneisen parameter for the thermally excited energy levels of:

$$\gamma_s = \frac{\beta_s V}{\alpha_T C_s} = \frac{\{\langle E_i^2 \gamma_i \rangle - \langle E_i \rangle \langle E_i \gamma_i \rangle\}}{\{\langle E_i^2 \rangle - \langle E_i \rangle^2\}} \quad (2.51)$$

The above analysis assumes that the contributions to thermal expansion due to the presence of paramagnetic ions are purely isotropic. A rigorous analysis of the phenomena should include allowance for anisotropic contributions from these ions. The Gruneisen parameter defined in equation (2-50) should hence be in general used to give, in tensor form:

$$\gamma_{i,\lambda} = -(\partial \ln E_i / \partial \ln \eta_\lambda) \eta'_{\lambda,T} \quad (2.52)$$

Where  $\gamma_{i,\lambda}$  is expressed in the Voigt notation. The volume Gruneisen parameter for the thermally excited level group must also be generalised to:

$$\gamma_s = \sum_{\lambda=1}^3 \left[ \frac{\{\langle E_i^2 \gamma_{i,\lambda} \rangle - \langle E_i \rangle \langle E_i \gamma_{i,\lambda} \rangle\}}{\{\langle E_i^2 \rangle - \langle E_i \rangle^2\}} \right] \quad (2.53)$$

For axial crystals, such as  $\text{Al}_2\text{O}_3$ , expressions (2.52) and (2.53) may be simplified to produce two independent Gruneisen parameters per level as in expression (2.40):

$$\left. \begin{aligned} \gamma_{\perp,i} = \gamma_1 = \gamma_2 &= -\frac{1}{2}(\partial \ln E_i / \partial \ln \eta_a) \eta'_{a,T} \\ \gamma_{\parallel,i} = \gamma_3 &= -(\partial \ln E_i / \partial \ln \eta_c) \eta'_{c,T} \end{aligned} \right\} \quad (2.54)$$

Where  $\eta_a$  and  $\eta_c$  are macroscopic strain parameters in the crystallographic 'a' and 'c' directions as defined in section 2.2.4. Values for  $\alpha_{\perp}$  and  $\alpha_{\parallel}$  are calculable from expressions (2.42) and the value of  $\alpha$  in any direction is calculable from expression (2.46).

We will now continue to estimate the value of  $\gamma_s$  for paramagnetic ions. We will firstly consider a static crystal field model (in the absence of a Jahn-Teller effect) and then continue to consider the modifications necessary in the presence of a dynamic Jahn-Teller effect.

## 2.3 THE CALCULATION OF $\gamma_s$ IN VARIOUS CRYSTAL ENVIRONMENTS

### 2.3.1 Static Crystal Field Model

If we consider a static crystal field model specific values of  $\gamma_i$ , the Gruneisen parameter corresponding to the  $i^{\text{th}}$  level, may be deduced. If, for example, we consider iron group transition metal ions in a tetrahedral environment (Sheard (1972)).

A schematic diagram of the energy level system for a typical ion ( $\text{Cr}^{2+}$ ,  $3d^4$ ,  $^5D$ ) in a tetrahedral crystal field is given in figure 2.1. A tetrahedral crystal field splits the  $^5D$  free ion term into a lower orbital triplet (transforming as  $T_2$ ) and an upper doublet (transforming as  $E$ ) having an energy separation  $\Delta$  ( $\sim 10^4 \text{ cm}^{-1}$ ). If the orbital angular momentum is not quenched (only for  $T_1$  and  $T_2$  irreducible representations) there are splittings due to spin-orbit coupling in first order perturbation theory of magnitude  $\lambda$  ( $\sim 10^2 \text{ cm}^{-1}$ ). When the lowest level is then more than four-fold degenerate it will be further split in 2nd order perturbation theory giving small splittings ( $\sim \frac{\lambda^2}{\Delta} = D'$ ) of  $\sim 1$  to  $10 \text{ cm}^{-1}$ . On the point charge model (Hutchings (1964)) the crystal field splitting  $\Delta \propto a^{-5}$  where,  $a$ , is the distance between the magnetic ion and its neighbours. Since  $\lambda \propto a^3$ , and  $E_5 \approx D'$ , and since the spin orbit coupling parameter is assumed volume independent (eg Barron *et al* (1980)) we have that:

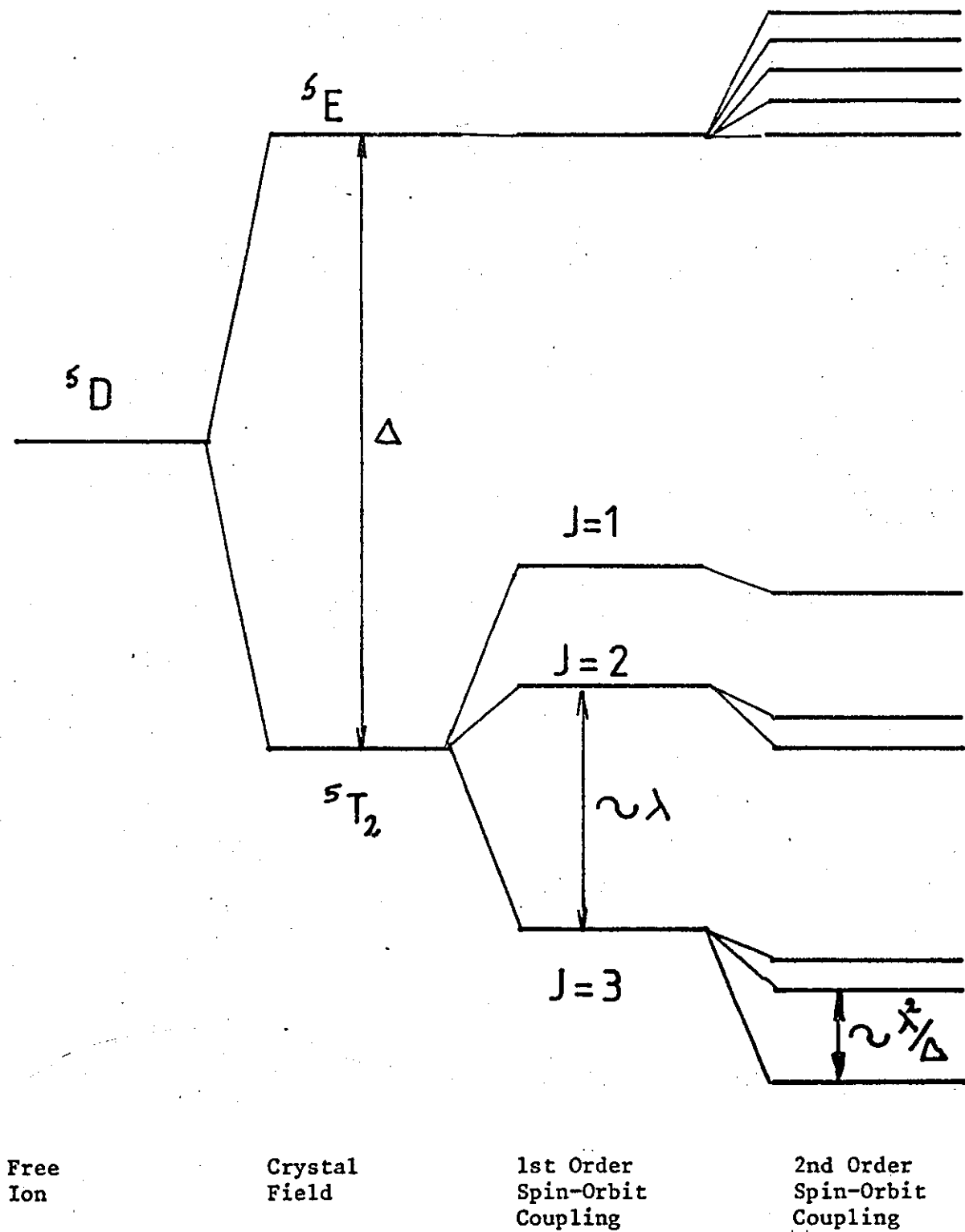
$$\gamma_5 = -\left(\frac{1}{3}\right) \left( \frac{\partial \ln E_5}{\partial \ln a} \right) \sim -5/3 \quad (2.55)$$

For a  $3d^4$  ion in a trigonally distorted octahedral environment (such as  $\text{Al}_2\text{O}_3$ ,  $C_3$  symmetry) the  $^5D$  free ion term is split into a lower doublet and upper triplet (Bates & Dixon (1969)) with a cubic splitting ( $\Delta$ ) of  $\sim 1800 \text{ cm}^{-1}$ . The trigonal distortion splits the upper triplet into a doublet  $E$  and singlet  $A$ , while the lower doublet remains a doublet also transforming as  $E$ .

The orbital angular momentum of the lowest  $E$  level is quenched and there can only be splittings arising from 2nd order spin-orbit perturbation theory resulting in five levels with mutual separations  $\sim \frac{\lambda^2}{\Delta}$ . As before we should expect these levels to exhibit negative Gruneisen parameters of  $\gamma_5 \sim -5/3$ .

In general we may conclude that in the absence of a Jahn-Teller effect, and when the low lying energy level structure arises from spin-orbit coupling in 2nd order, that the low lying splittings should demonstrate a negative Gruneisen parameter  $\gamma_5 \sim -5/3$  (Sheard (1969)); So we should

Fig 2.1      Energy Levels in Cubic  
Crystal Field:  $\text{Cr}^{2+} (3d^4)$  in a  
tetrahedral field



expect, provided the ion concentration is sufficient so that  $C_s \gamma_s \approx C_L \gamma_L$  ( $C_L$  and  $\gamma_L$  are the specific heat and Gruneisen parameters associated with the lattice), that we should observe a negative expansion anomaly in the region of the Schottky specific heat peak.

### 2.3.2 Jahn-Teller Model

In the presence of a Jahn-Teller effect the problem is more complex. Sheard (1972), assuming a cluster model, has discussed the Gruneisen parameters associated with orbital doublet and triplet states in Jahn-Teller ions and his conclusions are summarized below. The calculation of Ham factors in multimode Jahn-Teller systems is complex (Evangelou et al (1980)) and the discussion here will be limited to the cluster model approach of Sheard. Although this approach is not strictly valid (Bates (1978), Bates and Wardlow (1980), Abou Ghantous and Bates (1978)) it is expected to yield information concerning order and polarity of the respective Gruneisen parameters.

### 2.3.3 Triplet Orbital States

The energy level pattern resulting from spin-orbit coupling in the first order is formally the same as in the absence of a Jahn-Teller effect but the magnitude  $\lambda$  of the splitting is multiplied by a reduction factor  $K$  (Ham (1965)). For the lowest states, corresponding to zero point lattice vibrations, the Ham reduction factor is given by:

$$K = \exp(-3E_{JT}/2\hbar\omega) \quad (2.56)$$

Where  $E_{JT}$  is the Jahn-Teller energy and  $\omega$  is an average vibrational frequency for the neighbouring atoms. The Gruneisen parameter associated with the first order splittings ( $E_s \sim K\lambda$ ), assuming  $\lambda$  independent of volume, is given by:

$$\gamma_s = -(\partial \ln K / \partial \ln V) = (3\gamma_L - \frac{2n}{3})(3E_{JT}/2\hbar\omega) \quad (2.57)$$

Where it has been assumed that the orbit lattice coupling parameter (Ham (1971)) is proportional to  $\alpha^{-n}$ . Here  $\gamma_L$  is the lattice Gruneisen parameter. The value of  $\gamma_s$  may be estimated by assuming that  $\gamma_L \sim 1.2$

(Yates et al (1972)) and  $n=4$  (point charge calculation) giving

$$\gamma_s = 0.9 (3E_{JT} / 2\hbar\omega) \quad (2.58)$$

For interstitial  $3d^6$  ions in silicon, using data obtained from EPR spectra a value of  $(3E_{JT} / 2\hbar\omega) \sim 2.5$  has been estimated producing a value for  $\gamma_s$  of  $\gamma_s \sim 2.3$ .

When the Jahn-Teller energy is large the first order spin-orbit splittings  $\sim K\lambda$  are very small. Second order spin-orbit splittings due to coupling to the higher vibronic levels then become important. The general formulae for these, derived by Ham (1965), are complex but simplify in the limit of very strong Jahn-Teller interactions and Sheard (1972) has estimated the Gruneisen parameter for this case to be:-

$$\gamma_s = 2 \left( \gamma_L - \frac{n}{3} \right) \quad (2.59)$$

#### 2.3.4 Tunnelling Splitting Model

For ions with E type orbitals in an octahedral environment (such as  $Cr^{2+}$ ) the orbit-lattice interaction is expected to be very strong (Fletcher and Stevens (1969)). The coupling of the electronic states to the vibrations of the neighbouring atoms, the dynamic Jahn-Teller effect, has been calculated in some detail in this case (Fletcher and Stevens (1969)). The potential energy of the ion and its neighbours may be reduced by a tetragonal distortion in either of three equivalent directions. Owing to the anharmonicity of the lattice, distortions in other directions lower the energy less, so that the equivalent tetragonal distortions are separated by energy barriers. Tunnelling between the three different modes of distortion occurs and the resulting lattice disturbance is dynamic. The lowest eigen states are separated by a tunnelling splitting barrier. Owing to this exponential dependence we may anticipate that the splitting may change rapidly with variations in crystal volume.

Sheard (1971) has estimated the value of  $\gamma_s$  associated with the tunnelling splitting  $\delta$ . An approximate form of  $\delta$  is (Fletcher and Stevens (1969)):

$$\delta \simeq BR_o^3 e^{-W} \text{ where } W = \frac{\pi^2}{3} \left( \frac{BR_o^5 Mo}{\hbar^2} \right)^{\frac{1}{2}} \quad (2.60)$$

Where  $R_o$  is the average displacement of a neighbouring ion of mass  $Mo$



arising from the Jahn-Teller effect and B is the anharmonic force constant, so that  $BR_0^3$  corresponds to the anharmonic potential barrier. Since  $R_0$  occurs to a high power in the exponential its variation with volume is important. The magnitude of  $R_0$  is determined by the balance between the orbit-lattice coupling energy  $\mathcal{E}R_0$  and the lattice elastic energy  $\frac{1}{2}M_0\omega_D^2 R_0^2$ , and is given by  $R_0 = \mathcal{E}/M_0\omega_D^2$ . On the point charge model the dominant term in the coupling constant  $\mathcal{E} \propto \alpha^{-6}$  hence:

$$\frac{\partial \ln R_0}{\partial \ln V} = 2(\gamma_L - 1) \quad (2.61)$$

This shows that  $R_0$  tends to increase as the lattice expands owing to the weakening of elastic restoring forces. The variation of W with volume is dominated by the variation of  $R_0$ :

$$\frac{\partial \ln W}{\partial \ln V} = -\frac{1}{2}\gamma'_L + \frac{5}{2}\frac{\partial \ln R_0}{\partial \ln V} \sim 5 \quad \text{where } \gamma'_L = -\left(\frac{\partial \ln B}{\partial \ln V}\right)_T$$

So we have:

$$\gamma_s = -\left(\frac{\partial \ln \delta}{\partial \ln V}\right) = \gamma'_L - 3\frac{\partial \ln R_0}{\partial \ln V} + \frac{W}{\delta} \frac{\partial \ln W}{\partial \ln V} \approx 5W - 5.2 \quad (2.62)$$

Fletcher and Stevens (1969) chose parameters such that  $W \approx 7$  to fit acoustic resonance data. This gives rise to a value  $\gamma_s \approx 30$ , the large positive value of  $\gamma_s$  arising primarily from the dependence of  $R_0$  on  $\omega_D$  and the uncertainty inherent in  $\gamma'_L$  does not qualitatively alter this.

In addition to the tunnelling splitting the energies of the lowest states depend also on the second order spin orbit parameter  $\lambda^2/\Delta$  and for  $Cr^{2+}$  in MgO there are also splittings due to random lattice strains. However, these latter terms are relatively insensitive to crystal volume changes compared with the tunnelling splitting.

Thus for low-lying E type states in octahedral environments, theory based upon a tunnelling splitting model predicts large positive values of the Gruneisen parameter. This contrasts strongly with the small negative value ( $\gamma_s = -\frac{5}{3}$ ) to be expected in the absence of Jahn-Teller effects.

## CHAPTER 3

Page

### THE EXPERIMENTAL DETERMINATION OF THERMAL EXPANSION

|       |  |    |
|-------|--|----|
| 3.1   | INTRODUCTION.  | 32 |
| 3.2   | REVIEW OF DILATOMETERS .   | 32 |
| 3.2.1 | X-ray diffraction.   | 32 |
| 3.2.2 | Optical Interferometers.   | 33 |
| 3.2.3 | Optical Amplifiers.  | 33 |
| 3.2.4 | Electrical Inductance.   | 33 |
| 3.2.5 | Electrical Capacitance.  | 34 |
| 3.3   | THE THREE TERMINAL CAPACITANCE DILATOMETER.                                | 34 |
| 3.4   | CAPACITANCE AND LINEARITY OF KELVIN GUARD-RING CAPACITANCE<br>TRANSDUCERS. | 37 |
| 3.5   | CONSTRUCTIONAL DETAILS OF THE CAPACITANCE CELLS USED.                      | 40 |
| 3.6   | TECHNIQUES OF SAMPLE MOUNTING.   | 59 |
| 3.7   | THE TRANSFORMER RATIO BRIDGE AND DETECTOR CIRCUITRY.                       | 60 |

### 3.1 INTRODUCTION

Before giving a detailed description of the dilatometer system used, a review of the various dilatometer systems would serve to place the technique in context with other measurements of low temperature thermal expansion. It is firstly necessary though, to outline the resolution required to provide sufficiently sensitive measurement of thermal expansion in the temperature range considered.

The linear expansion coefficient  $\alpha$  is usually measured by determination of the length change,  $\Delta L$  which occurs when the temperature is varied by some finite value  $\Delta T$ . At ambient temperatures  $\alpha \sim 10^{-5} \text{ K}^{-1}$  so that with a  $\Delta T \sim 1 \text{ K}$  a length resolution  $\frac{\Delta L}{L} \sim 10^{-7}$  would be sufficient to determine  $\alpha$  to say 1%. At low temperatures however,  $\alpha$  may be very much smaller and so require a very much more sensitive dilatometric technique to obtain a comparable accuracy. For example, at temperatures  $T \sim \frac{\Theta_D}{40}$  (where  $\Theta_D$  is the Debye temperature), the linear coefficient  $\alpha \sim 10^{-8} \text{ K}^{-1}$ , so that to obtain a 1% accuracy in  $\alpha$  with a 50 mm sample would require a length resolution  $\Delta L \sim 5 \mu\text{m}$  ( $1 \text{ pm} = 10^{-12} \text{ m} = 10^{-2} \text{ \AA}$ ).

A problem then arises in that detection levels of 10 pm or less are very much smaller than the average interatomic spacing and very much smaller than the scale of surface roughness after even the best lapping and polishing techniques. This requires that we interpret the measured changes,  $\Delta L$ , as being the surface average of the microscopic changes,  $\delta \ell$  over the surfaces being measured. A further result of this dilemma is that we could expect some hysteresis in length on thermal cycling when the measurement depends on the mechanical linkage between surfaces of dissimilar materials. This should not be overlooked in assessing some methods of dilatometry which may appear to have a detection limit of a picometer but depend on mechanical linkages between surfaces of dissimilar materials. Dilatometers have been reviewed in some detail by Mezzetti (1964), Yates (1972 pp 52-63) and Barron et al (1980) and are summarised below.

### 3.2 REVIEW OF DILATOMETERS

#### 3.2.1 X-Ray Diffraction

These measure changes in the lattice parameter,  $a$ . These usually have a resolution of  $\frac{\Delta a}{a} \sim 10^{-5}$ , although a resolution of  $\frac{\Delta a}{a} \sim 5 \times 10^{-6}$  has been achieved using oscillating back-reflection techniques (Batchelder and Simmons (1965), Schuele and Smith (1964), Bond (1960)). This

resolution is not sensitive enough for the determination of  $\alpha$  at temperatures  $T < \theta_0/10$ .

### 3.2.2 Optical Interferometers

Various designs have been used, principally the Fizeau interferometer and the Fabry-Perot multiple beam systems. In the Fizeau interferometer the sample is usually in the form of a hollow cylinder (or three rods of equal lengths) placed so as to vary the separation of two etalon plates as the specimens expand or contract. The practical detection limit is normally about  $10^{-2}$  to  $10^{-3}$  fringes or  $\frac{\Delta L}{L} \sim 10^{-7}$  to  $10^{-8}$ . Better precision is obtained ( $\frac{\Delta L}{L} \sim 10^{-9}$ ) in the Fabry-Perot interferometer by using a stabilised laser (cf Jacobs et al (1970)), precision being limited by laser suitability or by deformation produced when the end plates of the cylindrical cell are not matched in expansion coefficient to the cylinder (or sample).

A more sensitive system which, at present, has only been used above room temperature (up to 1200K) is the polarising interferometer (Roberts (1975)). In this device a hollow cylindrical sample is optically contacted to a flat disc of the same material, interference occurs between elements of a split beam reflected from the disc and the shoulders of the other end of the sample. Deviations of  $\pm 10^{-8} \text{ K}^{-1}$  in  $\alpha$  have been found but these arise chiefly from thermometry errors (Roberts (1978)).

### 3.2.3 Optical Amplifiers

These have been reviewed by Jones (1961) and boast a sensitivity of  $10^{-10}$  radians angular displacement or  $< 1$  pm linear displacement. Principles vary between optical grid-amplifiers (eg Andres (1961 and 1964)) and optical levers (eg Shapiro et al (1964) and Pariera et al (1970)) but in general suffer from drift and hysteresis on thermal cycling due to mechanical linkages coupling the sample to either the grid or lever.

### 3.2.4 Electrical Inductance

The principle of operation of these devices are usually variations on the axial expansion of a sample being transmitted to the inner coil of a mutual inductance whose inductance varies linearly with displacement. Devices have been constructed (Carr and Swenson (1964), Sparks and Swenson (1967)) which have a sensitivity of  $\sim 2$  pm, but the more sensitive

34  
inductance devices suffer from "magnetic problems" (White and Collins (1972)).

### 3.2.5 Electrical Capacitance

These devices normally operate by the changing area or separation of a parallel plate capacitor. Two systems have been developed on this theme, firstly the two terminal capacitance and secondly the three terminal capacitance.

The two terminal capacitance transducer uses a LC resonance circuit and utilises the change in resonant frequency to detect the change in capacitance (eg Bijl and Pullen (1955), Dheer and Surange (1958)). A disadvantage of these is that the lead capacitance is included in the measured capacitance and this has limited their sensitivities to  $\frac{\Delta L}{L} \sim 10^{-7}$ . It has been found, however, that by using tunnel diode oscillators, the entire LC circuit can be localised at low temperatures in the cryostat (eg Tolkachev et al (1975)) improving resolution to  $\Delta L \sim 20 \mu\text{m}$ .

By far the most popular system used recently to measure thermal expansion at low temperatures, and the dilatometers used in these measurements, is the three terminal capacitance system. These are based upon a technology developed largely by Thompson (1958) and utilise transformer-ratio bridges for the measurement of capacitance. Among the major advantages of the three-terminal system is that the balance condition is not affected by lead capacitance, and that bridges are now commercially available that, using lock-in amplifier detection, have sensitivities less than  $10^{-7} \text{ pF}$  corresponding to a length sensitivity in the picometer range (eg White and Collins (1972), Kroegar and Swenson (1977)). The three terminal capacitance system, since it is the system used in this study, will now be considered at length.

### 3.3 THE THREE TERMINAL CAPACITANCE DILATOMETER

In figure 3.1 we have a schematic diagram and equivalent circuit for a three terminal capacitor. The shield electrode surrounds both the other two conductors and in practice forms the local earth shield. The direct capacitance,  $C_{HL}$ , is then the only capacitance that is defined, that is, which does not involve the lead capacitances  $C_{Hq}$  and  $C_{Lq}$ . Two three terminal capacitors may now be connected across a transformer ratio bridge, as in figure 3.2, so that the ground capacitances  $C_{Hq}$  and  $C_{Lq}$  only shunt the ratio arms and the detector D. The small capa-

capacitors  $C_{AL}$  and  $C_{BL}$  across the detector only reduce the sensitivity, and shunting the closely coupled ratio arms, which have a very small effective impedance, has a negligible effect on the balance condition.

$$\frac{C_{AHL}}{C_{BHL}} = \frac{V_B}{V_A} \quad (3.1)$$

So that only the direct capacitances  $C_{AHL}$  and  $C_{BHL}$  have any effect on the bridge balance condition. This argument is, of course, very simple and the construction and operation of transformer ratio bridges will be considered in more detail later.

No physical capacitor is, however, ideal (ie free from inductance and dissipation); So also, the equivalent networks that are used to represent a non-ideal capacitor, do so imperfectly. They are, however, satisfactory if some of the constants are understood to be quasi constants (they must vary somewhat with frequency etc). Figure 3.3(a) represents the non-ideal direct capacitance ( $C_{HL}$  of figure 3.1) with five lumped constants, where:

$R$  = Metallic resistance in the leads and plates.

$L$  = Series inductance of the leads and plates.

$C_1$  = Capacitance between the plates.

$C_k$  = Capacitance of the supporting structure.

$G$  = Dielectric losses in the dielectric between the capacitor plates and the dc leakage conductance.

For most purposes  $C_1$  and  $C_k$  are added as  $C$  (NB  $C_k$  is zero if support-structure capacitance is entirely within  $C_{HL}$  and/or  $C_{BL}$  of figure 3.1). The vector diagram figure 3.3(b) shows how the capacitive and inductive current components add to give  $I_T$ , and how the capacitive inductive and resistive voltage components add to give  $V_T$ .  $I_T$  leads  $V_T$  by the phase angle  $\theta$ , between  $0^\circ$  and  $90^\circ$ ,  $\delta$  is the dielectric loss angle.

Figure 3.3(c) is the equivalent circuit based on the two components of the capacitance measured directly by the general ratio GR1515-A and GR1616 bridges used in these measurements. Terminal properties ( $V_T$ ,  $I_T$ ,  $\theta$ ) are identical with figures 3.3(a) and 3.3(b) and vector diagram figure 3.3(d) represents the vector relationships. The algebraic relationships between these components and those of figure 3.3(a) are given below.

$$C_x = \frac{C(1 - \omega^2 LC) - C_1^2 L}{(1 - \omega^2 LC + RG)^2 + (\omega GL + \omega RC)^2} \quad (3.2)$$

$$G_x = \frac{G(1+RG) + \omega^2 RC^2}{(1 - \omega^2 LC + RG)^2 + (\omega GL + \omega RC)^2} \quad (3.3)$$

There is a resonance at a frequency  $f_0$  but at the frequencies used we observe that  $\omega^2 LC \ll 1$  so we may simplify the above relationships to:

$$C_x = \frac{C - G^2 L}{(1 + RG)^2}$$

$$G_x = \frac{G}{(1 + RG)} \quad (3.4)$$

In practice the values of  $G_x$  measured are very small ( $10^{-12}$  mho) and any changes in  $L$  can be minimised by rigidly coupling the leads to structural members of the cryostat.  $R$  is also small ( $< 1.5 \Omega$ ) so we may assume  $C = C_x$ . The assumption that  $f \ll f_0$  is justified in that no significant change in  $C_x$  occurs when the frequency is varied between  $1 \text{ kHz}$  and  $10 \text{ kHz}$ .

We now consider the structure of three-terminal capacitance dilatometers that have been used at low temperatures. Figure 3.4, which is taken from Kroeger and Swenson (1977) and White (1961), represents a few of the electrode sample configurations that have been used. The 'normal' type (White (1961)) compares the expansion of a sample with those of a reference cell whose expansion coefficient is well known (eg copper cf. White (1961), silicon cf. Villar et al (1980)). This is most useful when the samples and reference materials have expansivities which are of similar order. The 'inverted' geometry (Tilford and Swenson (1972), Schouten and Swenson (1974)) is also of the relative expansion type and has been used upon samples with large expansions. In the third configuration, the 'absolute' configuration, the cell is maintained at a constant temperature while the temperature of the sample is raised by electrical heating. In this configuration the sample is isolated from the cell by means of insulating spacers and the specimen expansion measured by means of two capacitance measurements at the top and bottom of the sample. In each case the sensitivity of the device is inversely proportional to the square of the plate separation, and as some contraction of the gap occurs on cooling due to differential expansion, the sensitivity of the device at room temperature is much less than that at low temperatures. In all these configurations the capacitors were of the Kelvin

guard ring type and analytic expressions for the capacitance of such capacitors will now be considered.

### 3.4 CAPACITANCE AND LINEARITY OF KELVIN GUARD-RING CAPACITANCE TRANSDUCERS

A Kelvin guard-ring capacitor consists of an extensive flat electrode separated by some small distance from a smaller circular electrode which is surrounded by a coplanar extensive flat electrode called the guard-ring electrode. Figure 3.5 is a cross section through such a capacitor, the capacitance between electrodes (1) and (2) is, in the notation of Heerens and Vermeulen (1975), given by:

$$C_0 = \frac{\pi \epsilon_0 \epsilon_r}{d_0} \left(R_i + \frac{s}{2}\right)^2 = \frac{\pi \epsilon_r \epsilon_0 R_i^2}{d_0} \quad (3.5)$$

If  $s \ll d_0$  and  $d_0 \ll R_i \ll R_0$ . Here  $C_0$  is the 'ideal' capacitance,  $\epsilon_0$  is the permittivity of free space ( $= 8.8542 \times 10^{-12} \text{ FM}^{-1}$ )  $\epsilon_r$  is the relative permittivity of the dielectric.

A correction to equation 3.5 for the effect of the width of the gap,  $s$ , between electrodes (2) and (3) is given by Moon and Spark (1948) as:

$$C = C_0 \left[ 1 - \frac{s^2}{2\pi R_i d_0} \coth\left(\frac{\pi R_i}{d_0}\right) \right] \quad (3.6)$$

But from figure 3.4 we have seen that the geometry of most practical dilatometers is that of a Kelvin guard ring capacitor with modified edge geometry as in figure (3.6). A correction for the electrodes being of finite dimension is given by a solution of the Laplace equation for this geometry. Heerens and Vermeulen (1975) have given a solution to this problem and this is in their notation:

$$C = C_0 \left( 1 + \frac{4}{R_i'} \sum_{n=1}^{\infty} \frac{(-1)^n I_1(n R_i')}{n I_0(n R_0')} \right) \quad (3.7)$$

$$\text{Where } R_i' = \frac{\pi R_i}{d_0} \quad R_0' = \frac{\pi R_0}{d_0}$$

The  $I_k(x)$  are modified Bessel functions of the first kind of order  $k$ . If we assume that  $R_0 \gg R_i \gg d_0$  this expression may be reduced to:

$$C = C_0 \left[ 1 - \frac{4}{R_i'} \left(\frac{R_0}{R_i}\right)^{1/2} \exp(-\infty') \right] \quad (3.8)$$



Where  $x' = \pi (R_o - R_i) / d_o$

So we have a set of expressions which describe the disturbing influences upon the simple capacitance expression (3.5). Firstly to account for the width of the gap,  $s$  (eqn 3.6), secondly to account for the non-infinite dimension of the coplanar electrodes and finally to account for the guard ring completely enclosing the high potential electrode (1) (eqns 3.7 and 3.8). A combination of the three expressions should then serve to describe the behaviour of our capacitors and this, in the shortened notation is:

$$C = \frac{\pi \epsilon_o \epsilon_r R_i^2}{d_o} \left[ 1 - \frac{s^2}{2\pi R_i d_o} \coth(R_i') \right] \left[ 1 + \frac{4}{R_i} \sum_{n=1}^{\infty} \frac{(-1)^n I_1(n R_i')}{n I_0(n R_o')} \right]$$

Which for most circumstances at small separations may be simplified to:

$$C = \frac{\pi \epsilon_o \epsilon_r R_i^2}{d_o} \left[ 1 - \frac{s^2}{2\pi R_i d_o} \coth(R_i') \right] \left[ 1 + \frac{4}{R_i} \left( \frac{R_o}{R_i} \right)^{1/2} \exp(-x') \right] \quad (3.9)$$

This relationship (3.9), is, however, cumbersome to use and it has been found that, for electrode separations of  $\approx 250 \mu m$ , an expression derived by Maxwell (1904) and quoted by White (1961) is quite suitable.

$$C = \frac{\pi \epsilon_o \epsilon_r R_i^2}{d_o} \left( 1 + \frac{s}{R_i} \left( 1 + \frac{s}{2R_i} \right) \left( 1 + \frac{0.225}{d_o} \right)^{-1} \right) \quad (3.10)$$

Both expressions (3.9) and (3.10) do, however, assume a narrow, deep gap without a dielectric filling it. One finds that a majority of practical dilatometer systems use an epoxy, such as Stycast 2850FT, as a filler to improve mechanical stability. This has the effect of increasing the capacitance of the slit. Brown and Bulleid (1978) have suggested a semi empirical first order correction to equation (3.10) to account for this difference by including the relative permittivity  $\epsilon_s$  of the epoxy filler.

$$C = \frac{\pi R_i^2 \epsilon_o \epsilon_r}{d_o} \left( 1 + \frac{s}{R_i} \left( 1 + \frac{s}{2R_i} \right) \left( 1 + \frac{0.225}{\epsilon_s d_o} \right)^{-1} \right) \quad (3.11)$$

We now proceed to study the effect upon the linearity of these capacitance transducers of surface damage on the electrodes and of having a slight tilt on one electrode relative to the other.

We will first consider the effect of surface damage on the electrode surfaces. Brown and Bulleid (1978) used a Michelson interferometer to investigate the effect upon capacitance transducers of surface damage and tilt. A summary of their surface damage results is given in figure (3.7)

This figure shows the variation of the point to point gradient of reciprocal capacitance  $\left(\frac{d}{d(d_0)}\left(\frac{1}{C}\right)\right)$  with separation ( $d_0$ ) for a Kelvin guard ring capacitor with polished electrodes and with shot-blasted electrodes (the surface roughness on the shot blasted electrodes being estimated at  $\pm 12\mu\text{m}$ ). From this we may conclude that for plate separations,  $d_0 > 100\mu\text{m}$ , the effect of some degree of surface damage is not important.

Khan et al(1980) extended the work of Brown and Bulleid (1978) to include the detailed effect of tilt on the linearity of capacitance transducers. Their results may be summarized in figure 3.8. In this figure there is plotted the point to point gradient of reciprocal capacitance as a function of separation for guard ring capacitors with various degrees of residual tilt. We may observe immediately that residual tilt has a pronounced effect upon the linearity of these transducers when the electrode separation is less than  $150\mu\text{m}$  (considering electrodes  $25\text{mm}$  in diameter) with only  $5'$  of residual tilt producing a 10% error in linearity at  $120\mu\text{m}$  plate separation and 20% error at  $100\mu\text{m}$ .

Also plotted in figure 3.8, for comparison are the gradients predicted using the two "Maxwellian" relations 3.10 and 3.11. It can be seen that both these relations exhibit sufficiently good agreement in the separation range  $150 - 300\mu\text{m}$ , to describe the behaviour of the guard ring capacitors. For the results reported here, equation 3.10 was used to calculate the electrode separation.

So we may conclude that, for the capacitance transducers to be linear and be described by a simple expression such as 3.10, a number of criteria must first be met.

- (i) The sensitivity of the transducer is inversely proportional to the square of the electrode separation so that for high sensitivity the electrode separation must be as small as possible.
- (ii) To minimise the effects of surface damage and tilt the electrode separation (assuming  $9\text{mm}$  electrode radius) should not be smaller than  $200\mu\text{m}$ .
- (iii) The diameter, and hence the area of the inner electrode should be as large as possible to enable sufficient accuracy to be obtained using a bridge method of capacitance measurement.

- (iv) The diameter of the extensive electrode (1 in figures 3.5 and 3.6) should be large so that  $\pi(R_o - R_i)/d_o$  (eqn 3.9) is large.
- (v) The gap,  $s$ , between the inner electrode and guard ring should be small so that a simple expression such as eqn 3.10 adequately describes the behaviour of the capacitance.
- (vi) The minimum gap,  $s$ , between the inner electrode and guard ring is limited. Decreasing this gap would increase the capacitance between the inner 'low' electrode and earth (guard ring) effectively shunting the bridge detector and decreasing sensitivity.

A solution that has been found to be both linear and sufficiently sensitive is as follows:

|                               |                             |
|-------------------------------|-----------------------------|
| Radius of inner electrode     | $\approx$ 9 mm              |
| Radius of extensive electrode | $\approx$ 13 mm             |
| Width of gap, $S$             | $\approx$ 0.05 mm           |
| Separation of electrodes      | $\approx$ 250 - 350 $\mu$ m |

### 3.5 CONSTRUCTION DETAILS OF THE CAPACITANCE CELLS USED

In these measurements two types of capacitance dilatometer were utilised using two different 'reference' materials. These are detailed below.

#### "HCOF Copper Cell", Type 1

This cell utilised high-conductivity oxygen-free (HCOF) copper as a reference material. Two similar cells (hereafter called Mark I and Mark II) were constructed, both of the 'normal' configuration outlined earlier (figure 3.4 (a)). Simplified sections through these are given in figures 3.9 and 3.10.

The Mark I cell (figure 3.9) consists of a precision machined HCOF copper annular cell (4) which has bolted onto it two HCOF copper plates (3 and 5). One of these (3) forms the guard ring of a Kelvin guard-ring capacitor; Set into and coplanar with this guard ring is the low potential capacitance electrode (2), the gap between this electrode and the guard ring being filled by Stycast 2850 FT (with catalyst 24 LV) epoxy resin. All of these copper components being vacuum annealed before final machining then hand lapped and polished to give optically flat surfaces. The sample (9) was supported in a HCOF copper support (5). A similar struc-

1  
ture at its other end forming the high potential capacitance electrode (1). Mechanical contact between the sample support (6) and the base plate of the assembly (5) being made by a thin layer of varnish. This produces a mechanically stable configuration while producing a lower thermal resistance between sample and cell. The cell in total was suspended by brass screws from a brass support plate (7) which also formed part of the electrical shielding for the low potential electrode. Electrical contact to the capacitor plates being via 0.4mm PTFE coated multi-stranded copper wire. The high and low potential leads being separately shielded by flexible copper braid. The temperature of the assembly was measured by a type CR100 'cryocal' germanium resistor. Facilities for temperature control being provided by a 100  $\Omega$  carbon resistor. Several techniques of sample support were studied and these will be outlined later.

Although figure 3.9 describes the samples as being 50mm long, experiments have been performed in the Mark I cell upon samples 50mm, 100mm and 120mm long. The performance of this cell was, in general, satisfactory, but for highest precision it was found that modifications were necessary. The problems that arose in using the Mark I cell fall into three main classes.

- (i) The copper braid, and electrical shielding in general, was found to be insufficient.
- (ii) The varnish layer between sample holder and base plate was found to be unreliable.
- (iii) Vibration arising from the rigid coupling between the copper and brass support plates.

These problems were rectified to a large extent in the Mark II cell. Figure 3.10 describes a section through the Mark II HCOF copper dilatometer. The electrode configuration for the Mark I and II cells is very similar, the major modifications being as follows:

- (i) The electrical noise problem found in the Mark I cell was cured by replacing the flexible braid screening by a solid stainless steel tubular shield. This shield was manufactured from  $\frac{1}{8}$ " nominal diameter stainless steel tubing, the high potential electrode shield passing right through the copper annular cell.

- (ii) A solution to the stress problem, arising from differential expansion of the copper and brass plates, was found by suspending the dilatometer from the brass support plate (4) by a system of spring-loaded screws (6). This technique also improved the vibrational stability to a large extent by acting as a low pass filter attenuating acoustic vibrations but being ineffective against the subsonic frequencies ( $< 10 \text{ Hz}$ ) which comprised the major part of the vibration problem. The subsonic vibration problem was finally solved by rigidly mounting the cryostat upon a heavy concrete block ( $1\frac{1}{2}$  tons), the concrete block itself being mounted on a vibration free area. Seismic vibration caused by local quarrying activities and nearby motorway and rail services were countered by averaging the detector signal over some 30-100s time constant.
- (iii) Instability and unreliability of the varnish contact between sample holder and base plate was simply cured by a rigid screw mounting. This however, led to thermal contact problems and it was found necessary to improve the thermal contact between sample and cell by wrapping several turns of 18swg copper wire around the sample and then fixing this in place with a glass loaded epoxy resin. (Stycast).

In both the Mark I and Mark II cells, corrections are made for the radial expansion of the low potential electrode and axial expansion of the annular cell by using the expansion data for HCOF copper of Kroegar and Swenson (1977). Being expressed as a power series polynomial expansion in temperature, this data is immediately applicable to analysis using a digital computer. A summary of Kroegar and Swenson's results for copper is given in table 3.1.

In all experiments performed with these cells, a large amount of effort was expended in ensuring that the electrodes were as close to parallel as possible. For this purpose a flat metal disc, hand lapped flat and with parallel faces, was used. This was placed on top of the high potential electrode and the capacitance cell assembled, the presence of the disc producing a gap of 0.3mm between the top of the copper annulus and the guard ring plate. Feeler gauges could then be used and assembly screws adjusted to produce a parallel gap between these surfaces. A very small quantity of varnish was then applied to the sample side and the procedure repeated and left to stand for some hours to allow the varnish to set.

TEMPERATURE RANGECOEFFICIENT OF TERMS OF POWER

$$\text{SERIES } \alpha(\tau) = \sum_{n=0}^{\infty} A_n T^n$$

2 &lt; T &lt; 25 K

|          |                            |
|----------|----------------------------|
| $A_0$    | $2.53507 \times 10^{-10}$  |
| $A_3$    | $2.66846 \times 10^{-11}$  |
| $A_5$    | $3.56435 \times 10^{-15}$  |
| $A_7$    | $5.53091 \times 10^{-17}$  |
| $A_9$    | $-8.23846 \times 10^{-20}$ |
| $A_{11}$ | $3.62967 \times 10^{-23}$  |

25 &lt; T &lt; 50 K

|       |                            |
|-------|----------------------------|
| $A_0$ | $-5.40693 \times 10^{-7}$  |
| $A_1$ | $1.17048 \times 10^{-7}$   |
| $A_2$ | $-9.73141 \times 10^{-9}$  |
| $A_3$ | $3.98470 \times 10^{-10}$  |
| $A_4$ | $-5.79623 \times 10^{-12}$ |
| $A_5$ | $2.97274 \times 10^{-14}$  |

50 &lt; T &lt; 100 K

|       |                            |
|-------|----------------------------|
| $A_0$ | $6.95076 \times 10^{-6}$   |
| $A_1$ | $-6.38706 \times 10^{-7}$  |
| $A_2$ | $2.18457 \times 10^{-8}$   |
| $A_3$ | $-2.82703 \times 10^{-10}$ |
| $A_4$ | $1.74267 \times 10^{-12}$  |
| $A_5$ | $-4.25784 \times 10^{-15}$ |

100 &lt; T &lt; 325 K

|       |                            |
|-------|----------------------------|
| $A_0$ | $-1.12857 \times 10^{-5}$  |
| $A_1$ | $4.13254 \times 10^{-7}$   |
| $A_2$ | $-2.80267 \times 10^{-9}$  |
| $A_3$ | $1.03271 \times 10^{-11}$  |
| $A_4$ | $-1.97422 \times 10^{-14}$ |
| $A_5$ | $1.53667 \times 10^{-17}$  |

TABLE 3.1 Thermal expansion of HCOF copper as a power series expansion in temperature (from Kroeger and Swenson (1977))

4

It has been found that good agreement between data for various samples can be achieved using this technique providing sufficient care and patience is taken when the samples are mounted.

### "Al<sub>2</sub>O<sub>3</sub>" Cell, Type 2

This cell was designed primarily for the measurement of doped Al<sub>2</sub>O<sub>3</sub> samples. The cell utilises three cylinders of 'pure' Al<sub>2</sub>O<sub>3</sub> (supplied by Rubis synthetique des Alpes) as a reference material and is shown in figure 3.11.

In this cell the length of the doped Al<sub>2</sub>O<sub>3</sub> sample (6) is compared with that of three "pure" Al<sub>2</sub>O<sub>3</sub> samples (5). The guard ring electrode (4) and base plate (8) are again both manufactured from stress relieved HCOF copper as is the sample support (10). To assist in supporting the pure Al<sub>2</sub>O<sub>3</sub> samples and to improve electrical shielding we have a HCOF copper cylinder (7). This cylinder is precision machined lapped and polished after being stress relieved to give a gap of  $.25 \pm .005$ mm between the end of the cylinder and the end of the pure Al<sub>2</sub>O<sub>3</sub> reference samples. This gap allows the capacitance electrodes to be set accurately parallel. This adjustment is achieved by assembling the cell without pure reference samples and adjusting the sample via the HCOF copper screw (a) so that the high and low capacitance electrodes are in contact. Application of a small quantity of varnish serves to hold the electrodes in this position when the reference samples are replaced. The pure samples themselves are all spark machined  $50.30 \pm .01$ mm long. The guard ring is connected to the copper cylinder via six spring loaded screws (2) which allow an even pressure to be applied to hold the reference samples in position. The dilatometer as a whole is suspended from the brass support plate (3) via three loosely tightened M3 screws which pass through 4mm holes in the brass plate and are tightened onto spring washers (11). Connection between the dilatometer and the cryostat is via a copper post (1) which also serves as an electrical shield for the low potential capacitance lead. The high potential capacitance lead is again shielded by  $\frac{1}{8}$ " stainless steel tube over its entire length. Radial expansion of the low potential capacitance electrode and axial contributions due to the copper supports and high potential capacitance electrode are again corrected using the copper expansion data of Kroeger and Swenson. The cell was calibrated by performing a measurement upon a fourth pure Al<sub>2</sub>O<sub>3</sub> sample, from the same boule as the three reference samples.

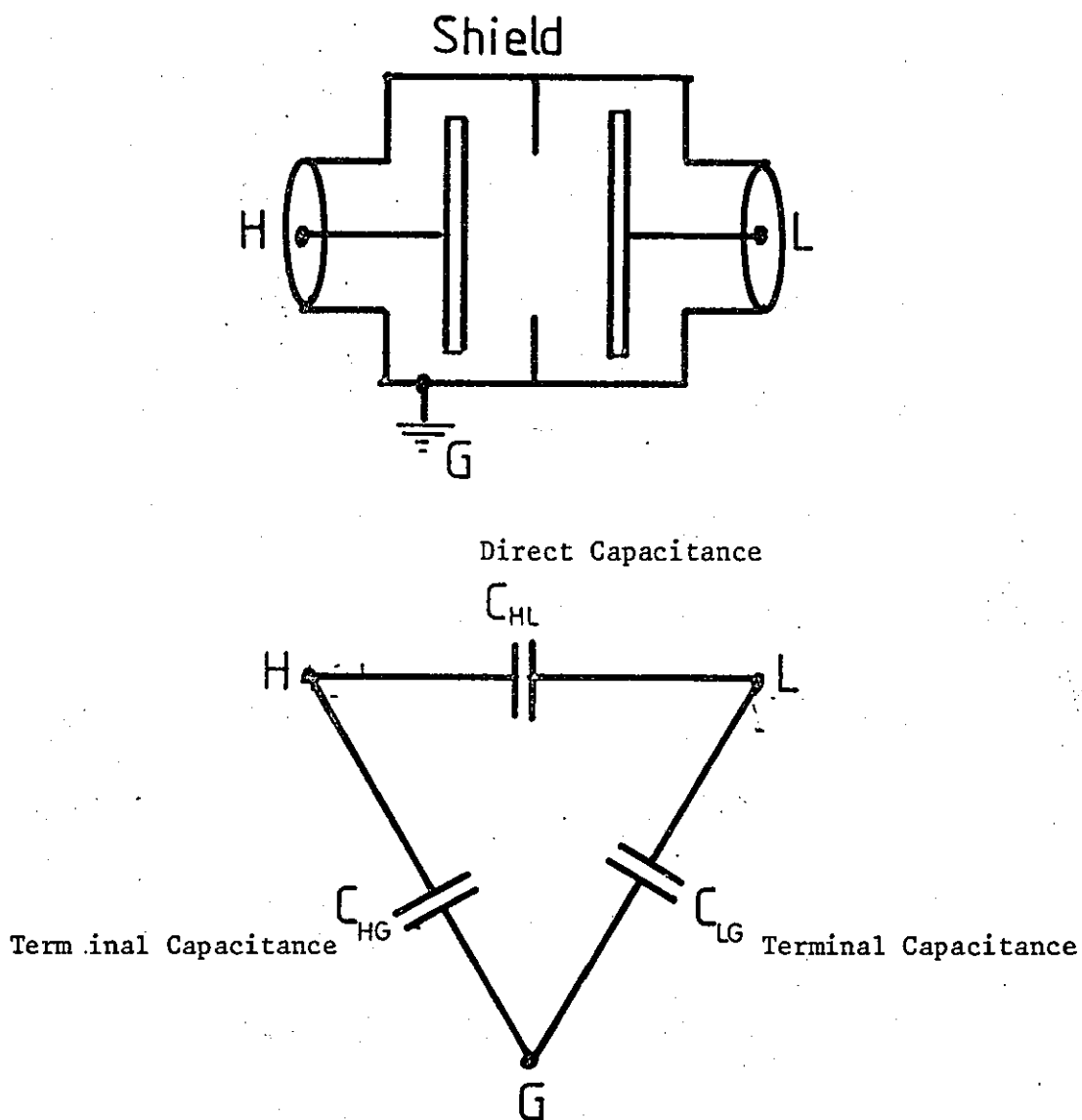


Fig 3.1 Structure and Equivalent Circuit for a 3-terminal Capacitance



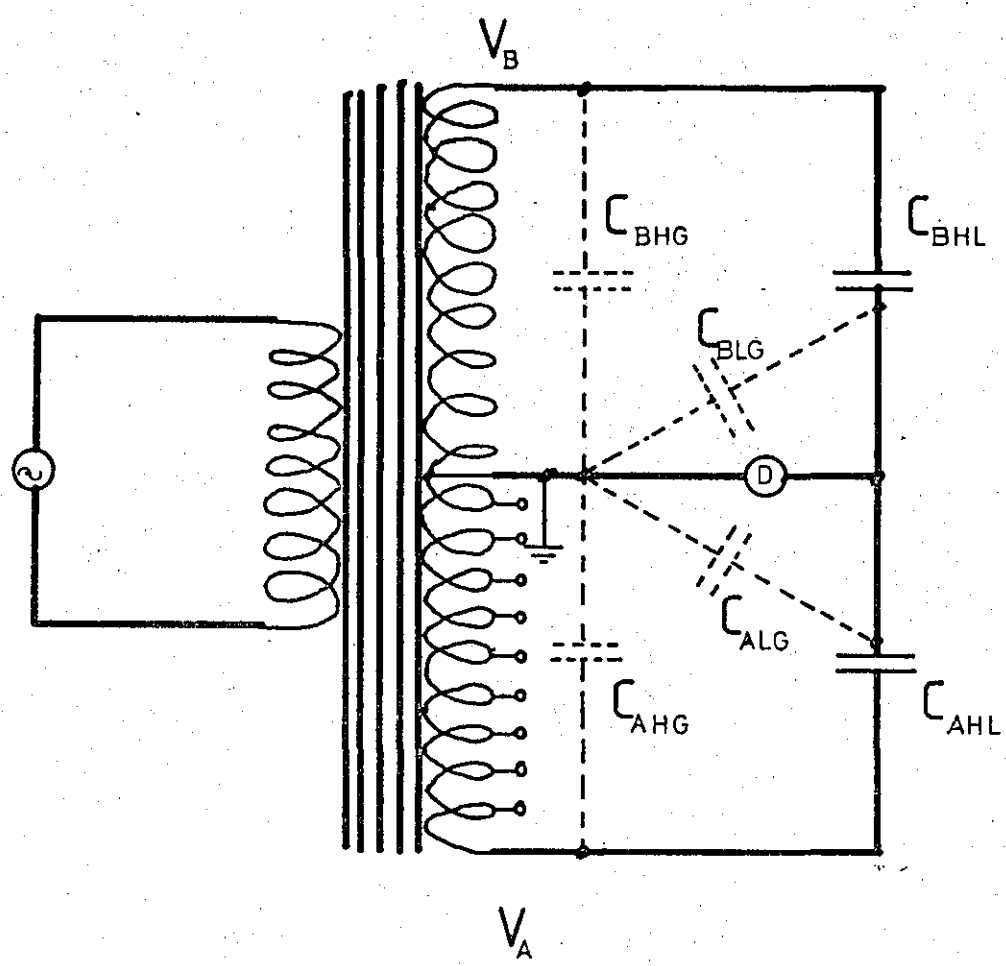
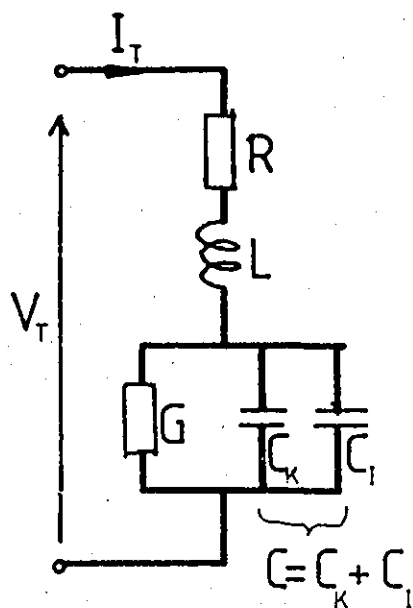
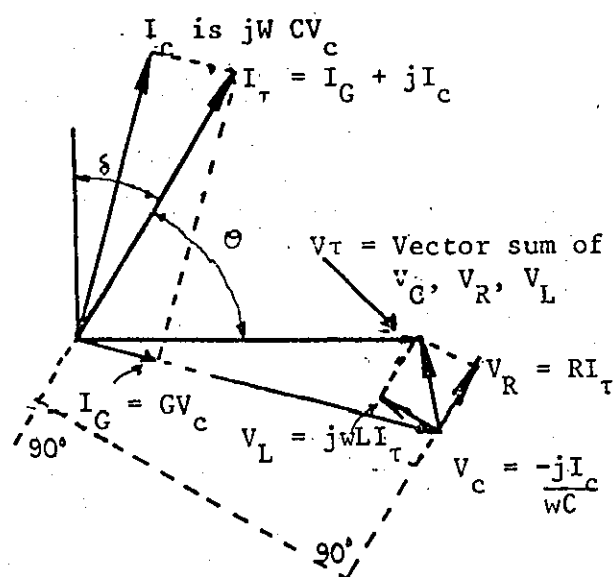


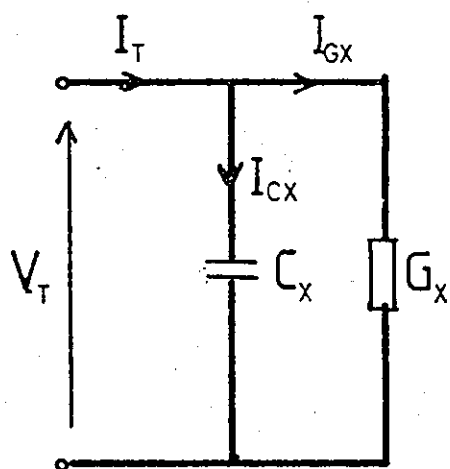
Fig 3.2      Simplified Schematic Diagram  
                of a Transformer Ratio Bridge



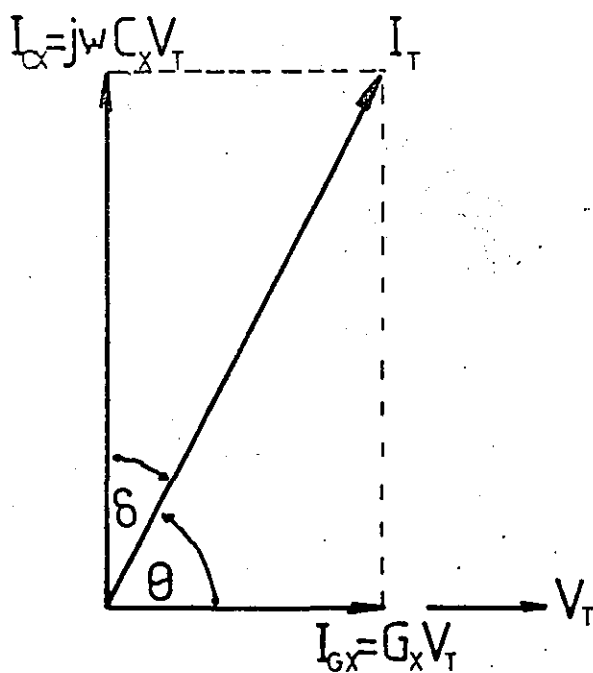
(a)



(a)



(c)



(d)

Fig 3.3 Capacitor Lumped-Parameter Equivalent Circuits and Vector Diagrams

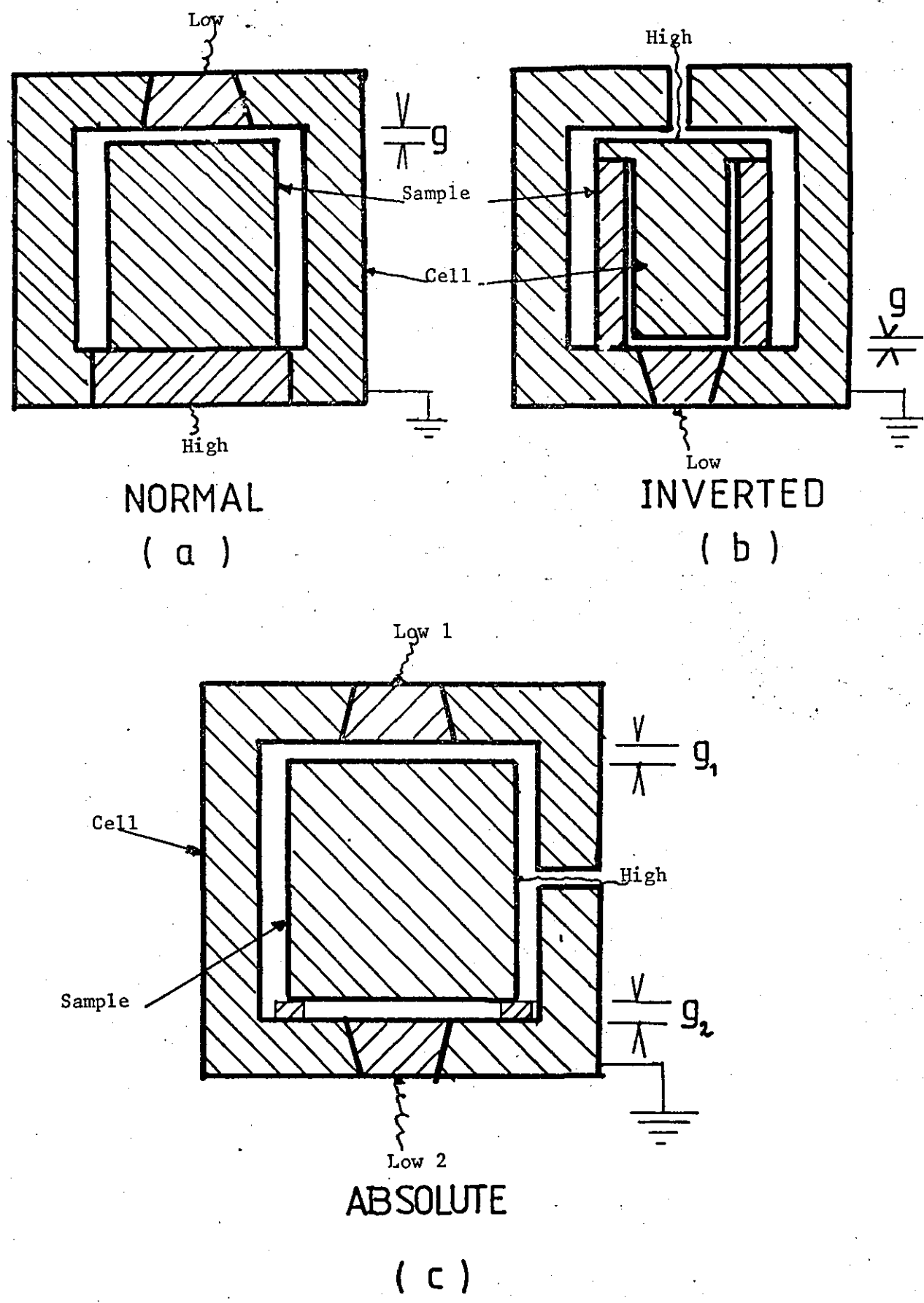


Fig 3.4 Various Configurations for Capacitance Dilatometers

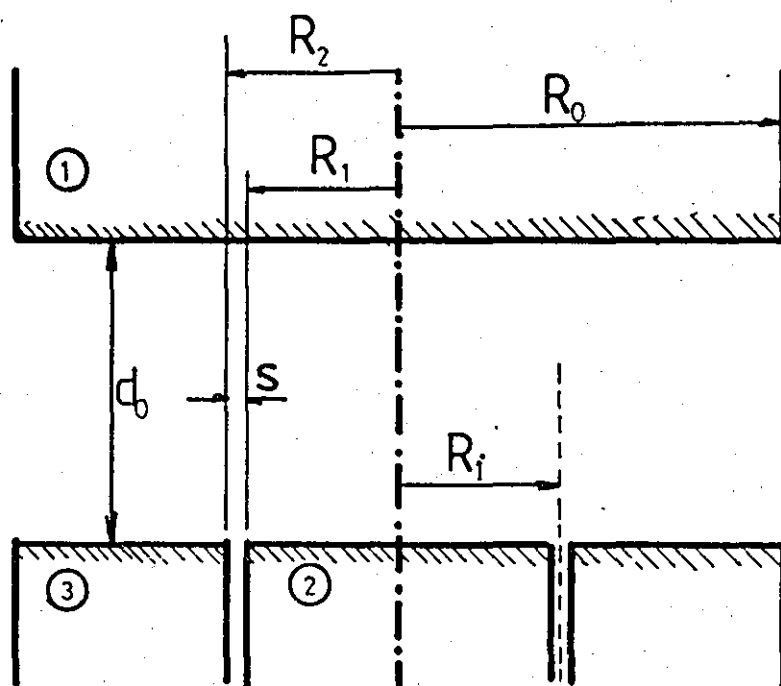


Fig 3.5 Cross-Section of a Kelvin Guard-Ring Capacitor

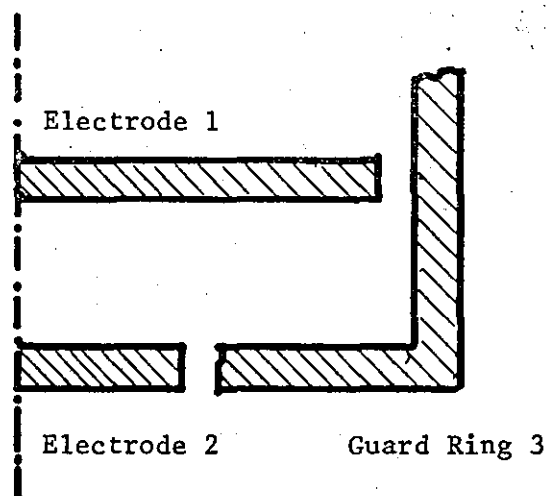


Fig 3.6 Cross-Section of a Guard-Ring Capacitor with Modified Edge Geometry

Fig 3.7

(from Brown and Bulleid 1978)  
Effect of Surface Damage on the  
Linearity of Capacitance Transducers

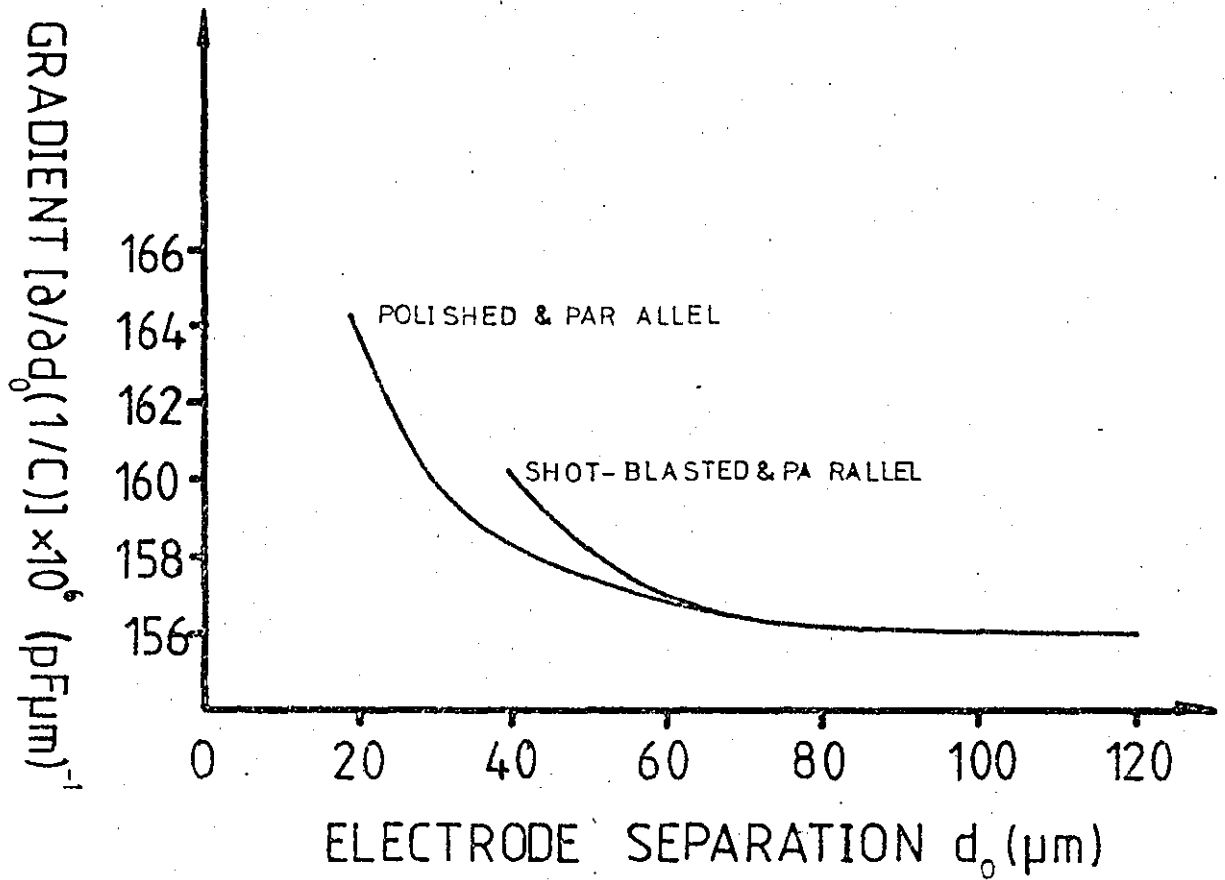
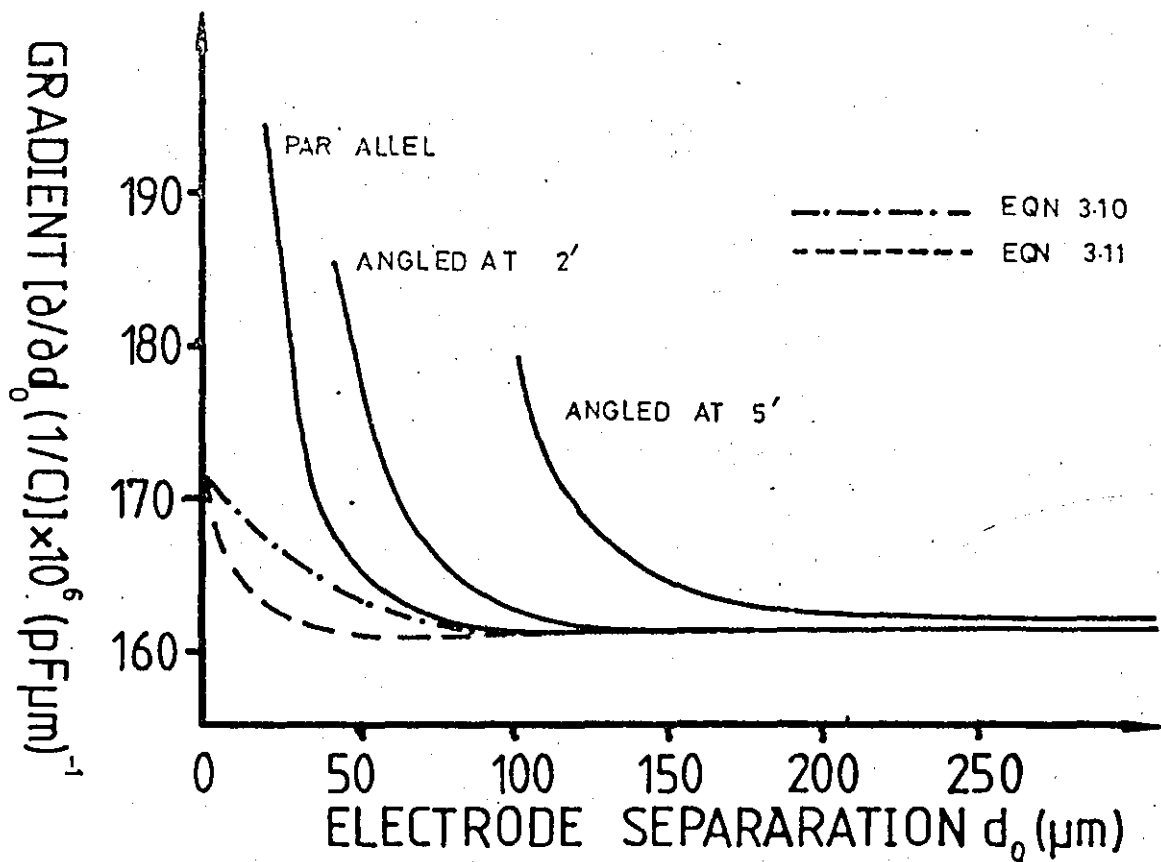


Fig 3.8

Effect of Tilt on Linearity of  
Capacitance Transducers  
(Khan et al 1980)



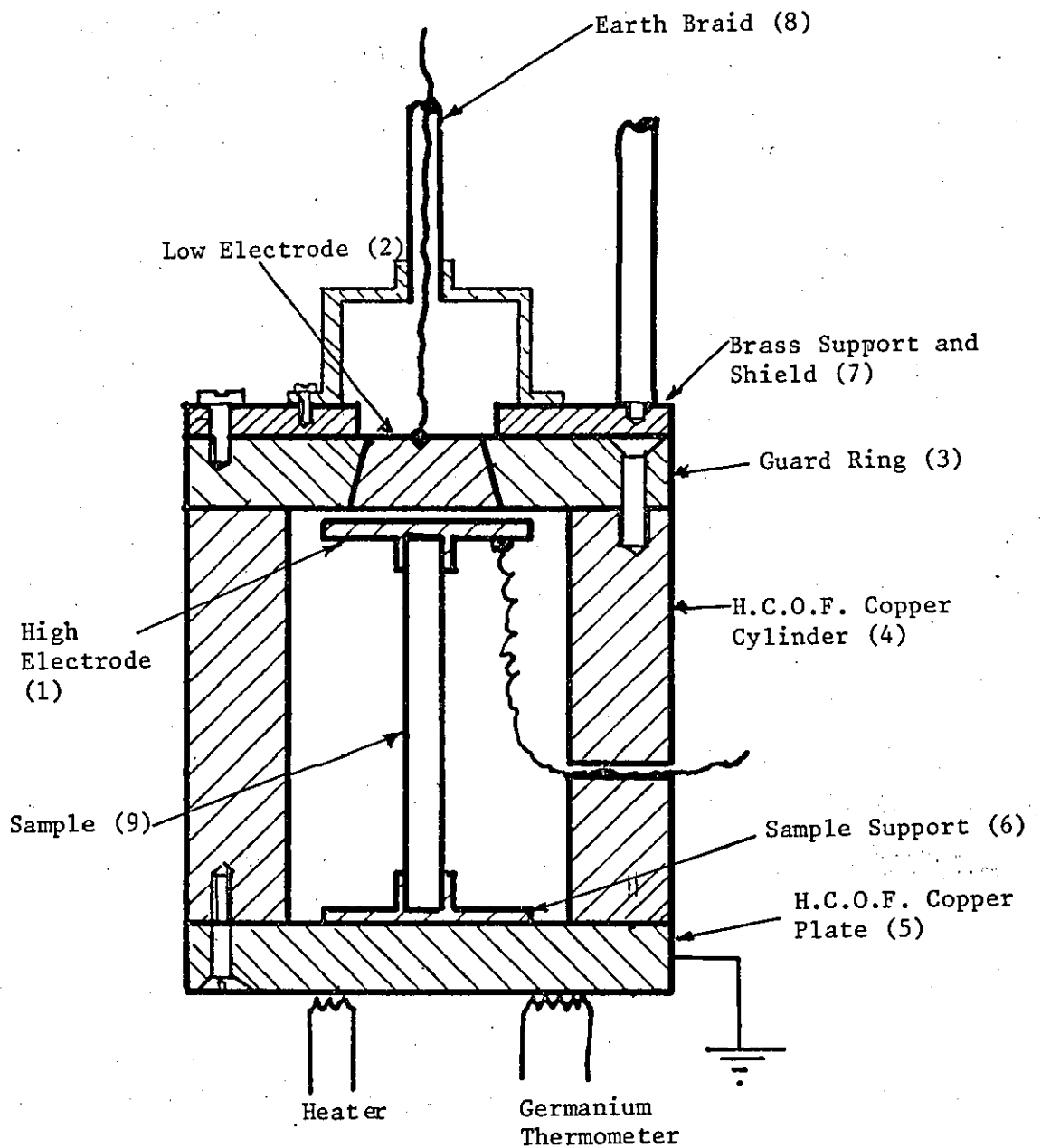


Fig 3.9 MARK I H.C.O.F. Copper Dilatometer Cell

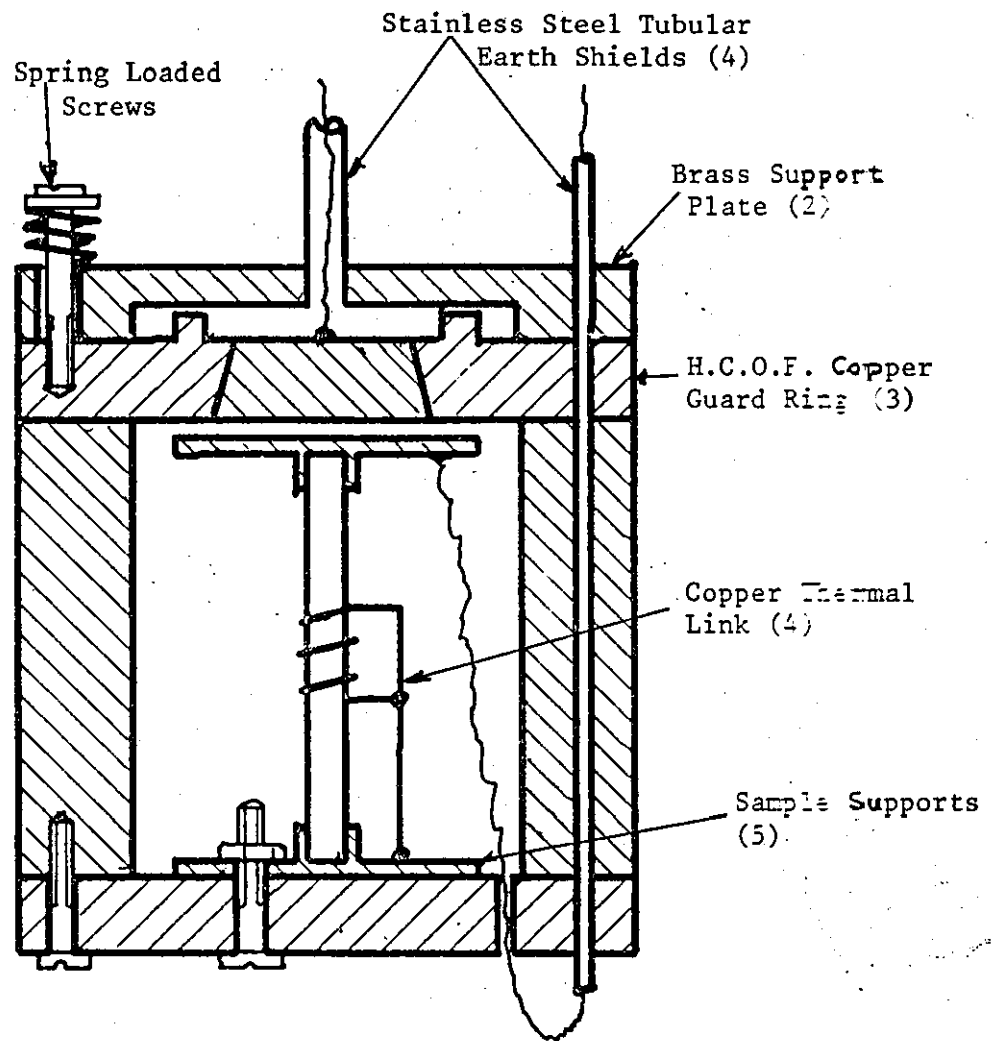


Fig 3.10 MARK II H.C.O.F. Copper Dilatometer Cell

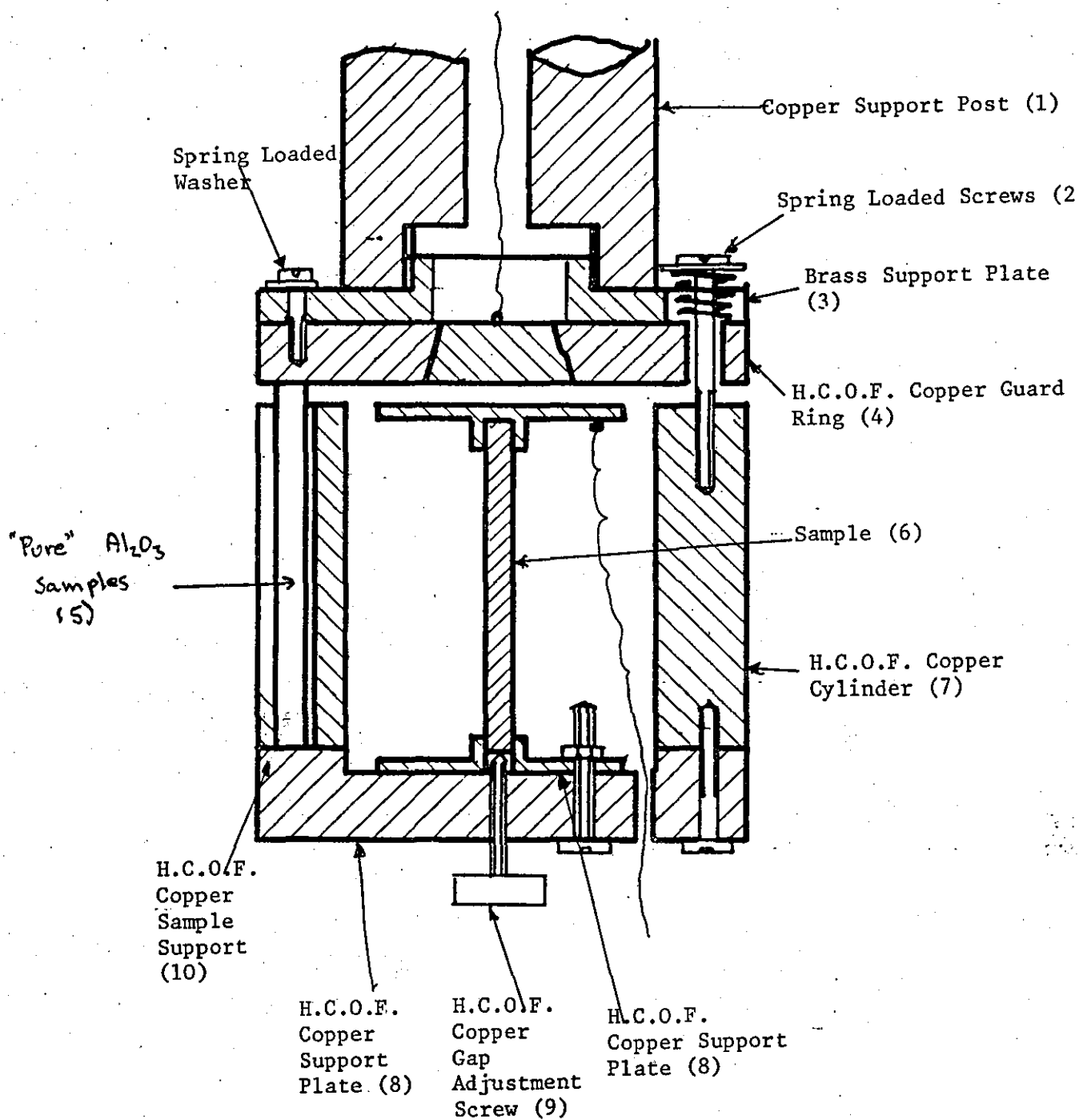
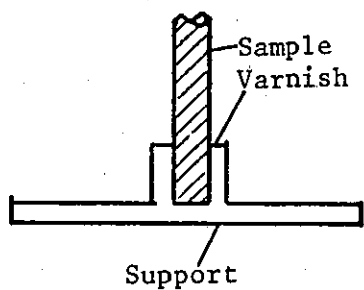
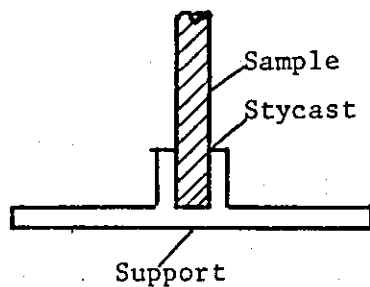


Fig 3.11 'Al<sub>2</sub>O<sub>3</sub>' Cell Dilatometer

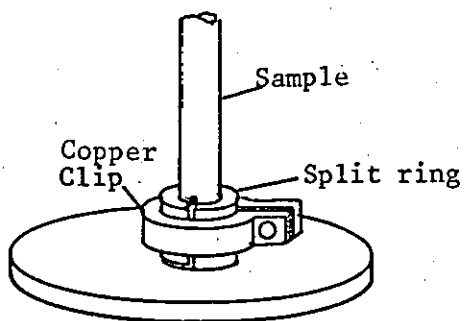




(a)

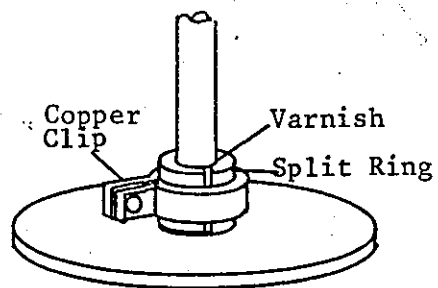


(b)



No Adhesive

(c)



(d)

Fig 3.12 Sample Mounting Techniques

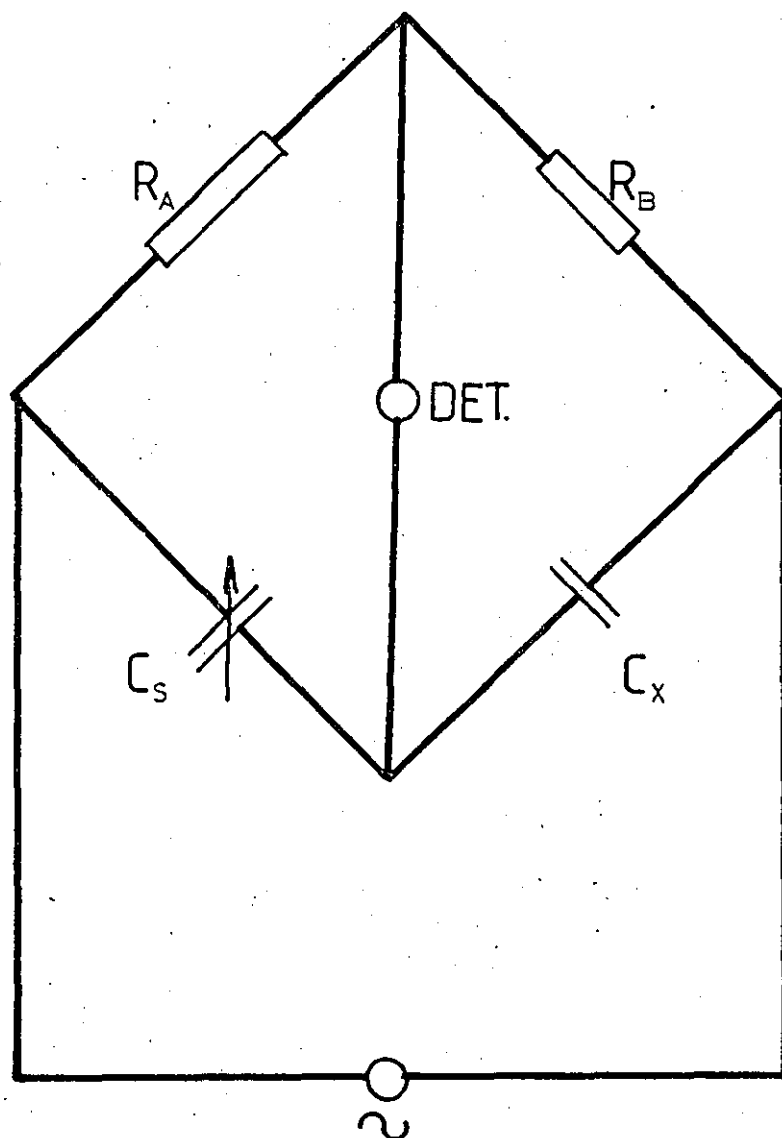


Fig 3.13 Elementary Capacitance  
Measuring Bridge

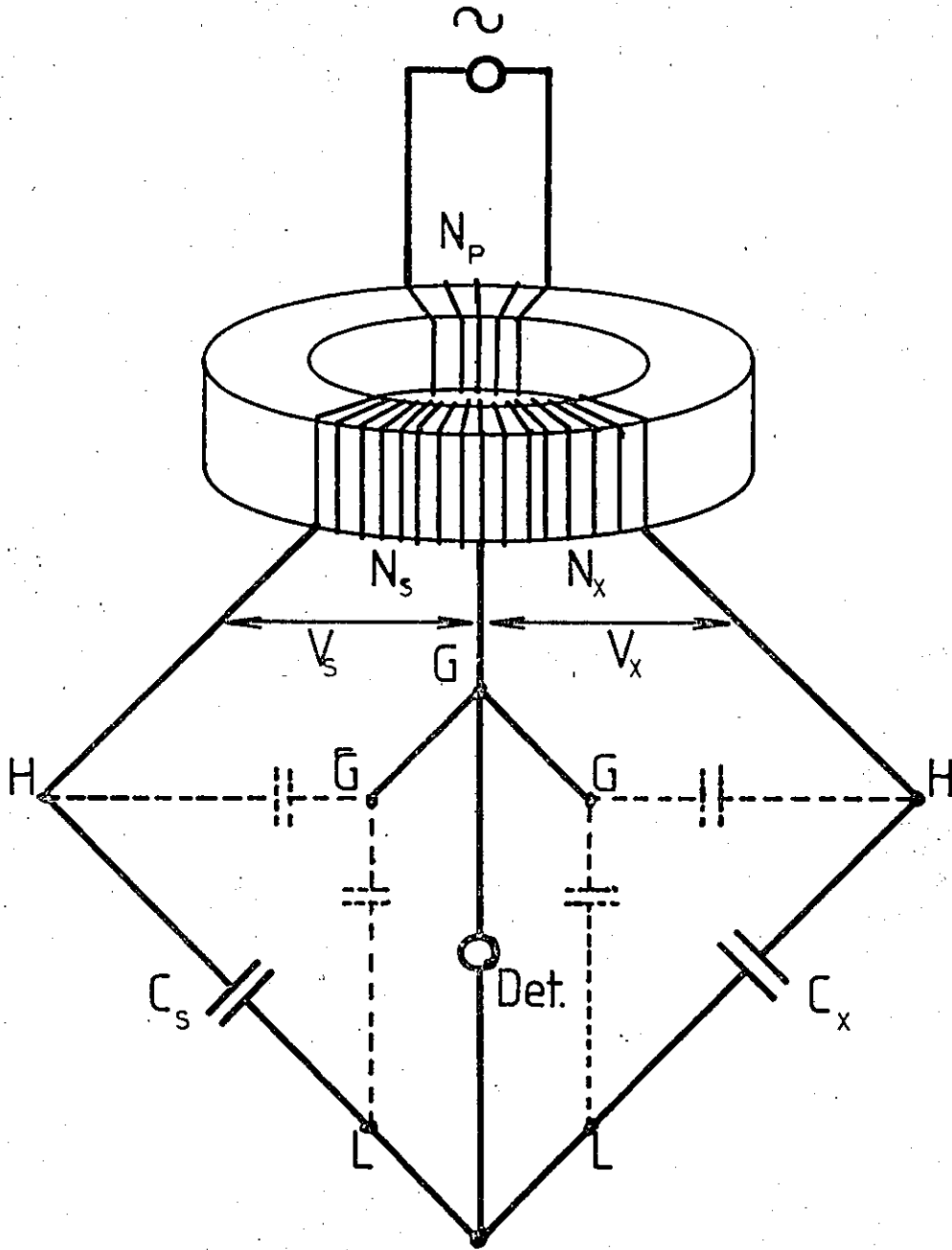


Fig 3.14 Elementary Capacitance Bridge  
with Transformer Ratio Arms

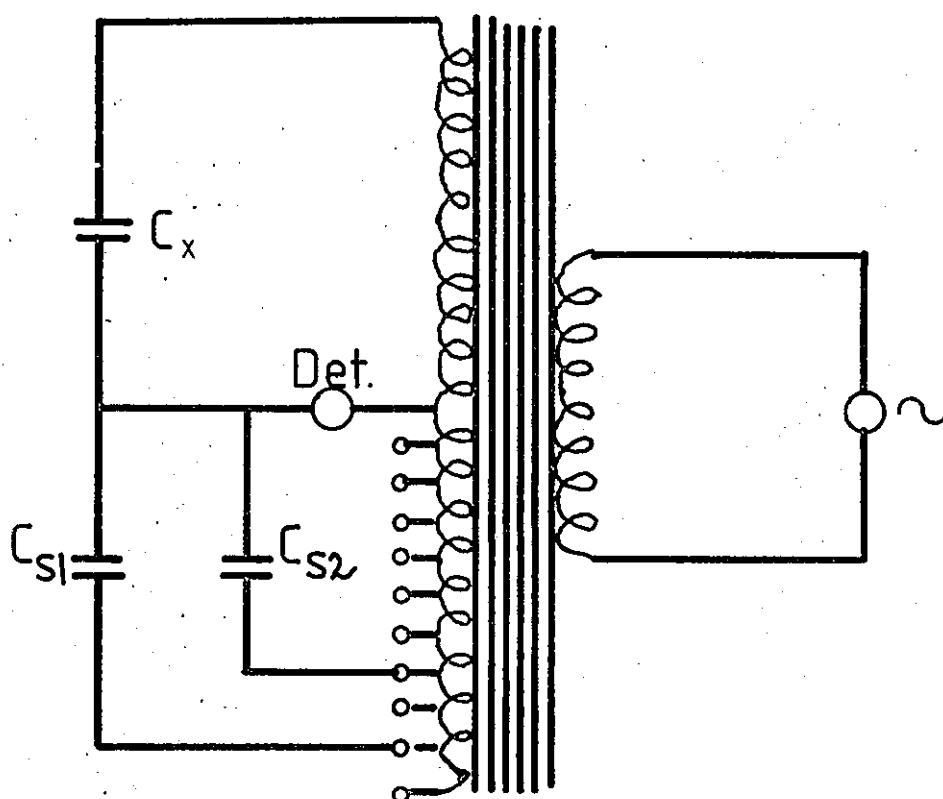
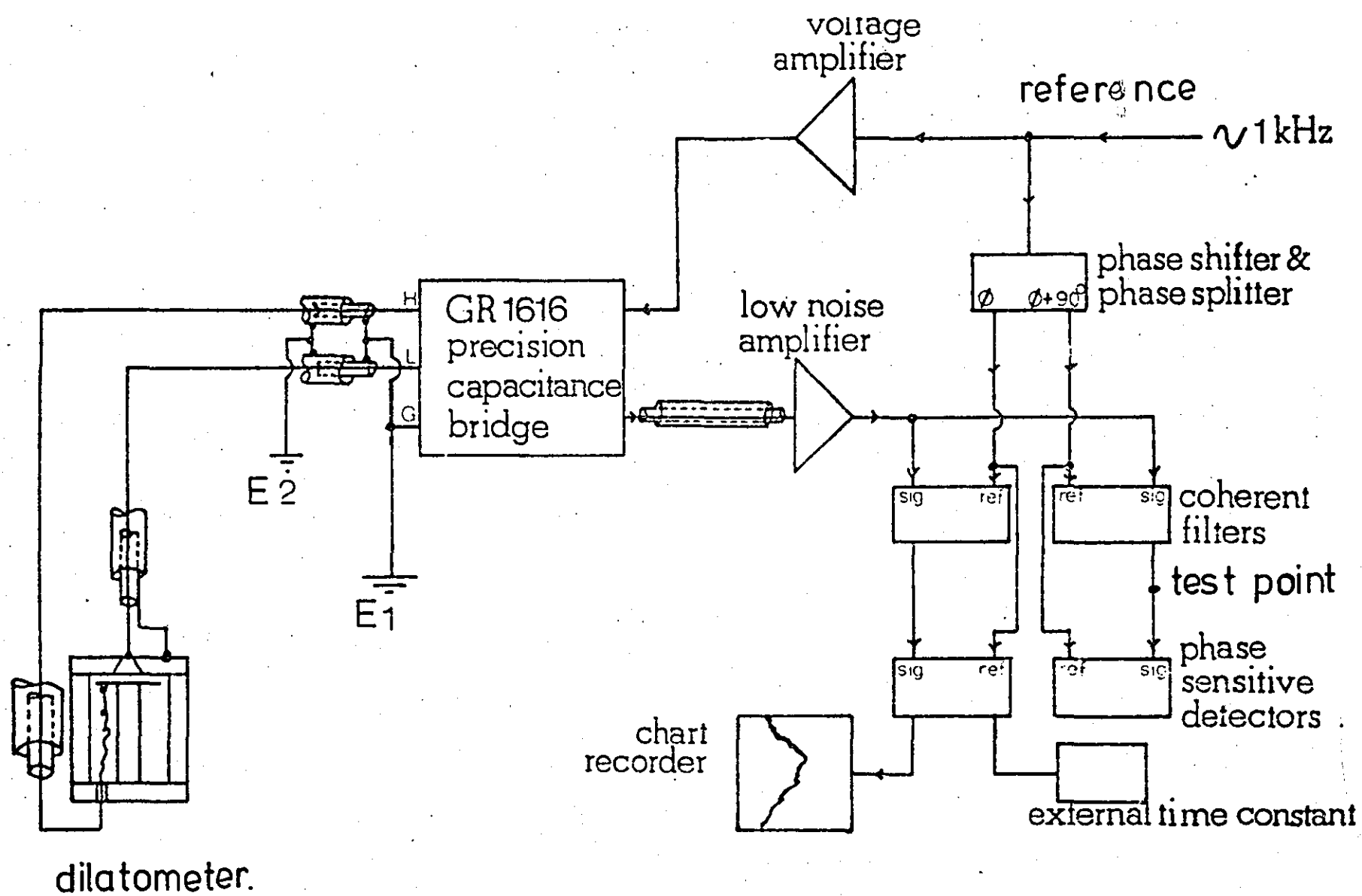


Fig 3.15      Simplified Circuit for  
Type GR16      Capacitance Bridges



Detection Electronics Configuration.

FIG. 3.16

### 3.6 TECHNIQUES OF SAMPLE MOUNTING

In the measurement of low expansivity samples, a critical aspect limiting the reliability of the results obtained, is the technique used for mounting the samples in the dilatometer cell. The sample mounting must be reliable and produce consistently reproducible results. The mounting technique must rigidly support the sample while not contributing any anomalous expansions to the measurements due to any adhesive used to provide mechanical stability and good thermal contact. A diagram of four techniques that have been successfully used in these measurements is given in figure 3.12.

In figures 3.12(a) and 3.12(b) the sample is supported in a thin walled copper cylinder turned on top of a flat plate. To improve thermal link and improve vibrational stability a thin layer of varnish (diagram (a)) or stycast epoxy (diagram (b)) was used. In both cases the hole into which the sample was located, was drilled and reamed to be no more than 0.2 mm larger than the sample itself and the base of the hole was bored flat. The adhesive (varnish or stycast) was applied sparingly around the top of the hole-sample interface, great care being taken to avoid getting any adhesive beneath the sample.

In figures (c) and (d) a somewhat modified system is described. Here the copper cylinder was split axially and the sample clamped using a copper ring clip which has the advantage of making the sample holders detachable (unlike the more dedicated versions described above).

Initially, experiments were attempted without using any form of adhesive between the sample and copper split ring, while this was found to be vibrationally satisfactory, problems arising from the poor thermal contact between sample and copper were found but was improved by using a small quantity of either varnish or silicon vacuum grease. The use of varnish in this case was found to have the further advantage of holding, after suitable adjustment, the capacitance electrodes parallel.

The two techniques (Figure 3.12 (a) and (b)) were found to be extensively laborious in practice. Requiring a new pair of electrode and support to be manufactured for each individual sample measured. The detachable holder (figure 3.12 (d) ) however is now used extensively with the advantage that only a small number of electrodes are required (for samples of various diameters and lengths), and has been found to be both simple, reliable and consistent when used with various doped and pure  $\text{Al}_2\text{O}_3$  samples.

### 3.7 THE TRANSFORMER RATIO BRIDGE AND DETECTOR CIRCUITRY

Measurements of three terminal capacitances, particularly those of high accuracy, are made using some form of the basic ratio bridge shown in figure 3.13. In this bridge an unknown capacitance,  $C_x$ , is compared with a variable standard capacitance,  $C_s$ , by a variable ratio arm,  $R_A/R_B$ . Such bridges, using resistive ratio arms and calibrated variable capacitors, can be used over a wide range of both capacitance and frequency but have a direct reading accuracy which seldom exceeds 0.1%.

When higher resolution is required at audio frequencies, a bridge with inductively coupled or transformer-ratio arms has been found to have many advantages. Among these are that accuracies within a few ppm are not difficult to obtain over a wide range of integral values, that using modern commercially available bridges very small ( $10^{-7}$  pF) changes in capacitance can be detected, and that the transformer ratios are particularly unaffected by age, temperature, and voltage. The low impedance of the transformer ratio arm also make it easy to measure direct impedances and to exclude ground terminal impedances in a three terminal capacitance measurement, without the use of guard circuitry and auxiliary balances (as has been detailed in section 3.3).

A simple capacitance bridge with transformer ratio arms is shown in figure 3.14. On a torroidal core, a primary winding of  $N_p$  turns serves only to excite the core, the number of turns determines the load on the generator but does not influence the bridge network. If the flux is confined to the core, as it is to a high degree in a symmetrically wound torroidal transformer, the ratio of the open circuit voltages induced in the two secondary windings must be exactly equal to the ratio of the number of turns ( $N_s/N_x$ ). This ratio being simply varied by using a series of taps along the two secondaries. But, as previously mentioned, for all practical transformers, the ratio of open circuit voltages is also a function of the flux leakage but this can be made very small. Since changes in the core permeability with time and temperature have only a small effect upon the voltage ratio, this ratio is both highly accurate and highly stable. For the bridge shown in figure 3.4 the balance condition is shown very simply to be:

$$\frac{C_x}{C_s} = \frac{V_s}{V_x} = \frac{N_s}{N_x} \quad (3.12)$$

Two transformer ratio bridges were used in these measurements: firstly a General Radio type GR1615 - A capacitance bridge. This was used in a

feasibility study (Brown (1978)) and in measurements upon  $\text{Al}_2\text{O}_3:\text{Cr}$  (Brown and Brown (1981)); secondly a General Radio type GR1616 Precision Capacitance Bridge acquired to improve stability and accuracy. Both of these bridges differs slightly from that shown in figure 3.14 in that several fixed 'standard' capacitors are used in combination with a single decade divider as shown in figure (3.15). A detailed circuit of the two bridges is unnecessary and are not given here but may be found in the instruction manuals for the respective instruments.

Although the effect of temperature change upon the ratio of open circuit voltages of the two secondaries has been found to be small, we have yet to consider the effect of temperature upon the capacitance standards of the bridge. In the bridges used the standard capacitors are situated in a thermally isolated box with a thermal time constant of six hours. The absolute accuracy of the capacitance measurement is quoted (see instruction manuals) as being less than 10ppm at 1KHz and  $23^\circ\text{C}$  with a temperature coefficient of 3ppm for every  $^\circ\text{C}$  difference in temperature from the  $23^\circ\text{C}$  of calibration. The accuracy of any change in capacitance of  $0.1\text{aF}$  being 20% at  $23^\circ\text{C}$ . So it becomes obvious that the precision of the capacitance measurement is critically dependent upon the ambient temperature at which the bridge is maintained,

and that the bridge should have been at this temperature for some time (24 hours) before a measurement is attempted. In the measurements reported here the bridge and detection electronics were isolated inside a metal cabinet which was maintained at  $23^\circ\text{C}$  by using a temperature controller, the peak temperature variation measured over a 24 hour period being less than  $\pm .25^\circ\text{C}$ .

The sensitivity of the capacitance measurement then reduces to a problem of detecting the low levels of in phase and quadrature signals at the bridge sum point corresponding to the two quantities ( $C_x$  and  $G_x$ ) measured by the bridge and discussed in section 3.3. Figure 3.16 shows a simplified diagram of the detection electronics used and is described in some detail below.

In figure 3.16, the sample cell is connected to the GR166 capacitance bridge via two lengths of doubly shielded cable. It should be noted that the two screens of this cable are connected to two entirely separate earths (labelled E1 and E2) for maximum shielding. The earth connection E2 is via the ordinary 'mains' earth and the earth E1 being connected to a special 'individual' earth constructed purely for this purpose. This earth was constructed from a two metre length of per-



forated copper tubing. This tube was buried, with sand, in a 20cm diameter hole drilled 12ft into bedrock. Good electrical connection to ground was ensured by frequent watering. The ground capacitance between the low terminal (L) and ground (E1), while not affecting the bridge balance condition, does shunt the detector and hence reduces the sensitivity of the measurement. This capacitance should hence be made as small as possible, the total capacitance (including the input capacitance of the detector amplifier) being less than 200pF for maximum sensitivity.

The power supply to the bridge, and the reference voltage to the phase sensitive detectors, was provided by a 20V rms oscillator providing a  $1\text{KH}_2$  sinusoidal signal. This voltage is amplified by a 300W voltage amplifier to provide the 100V supply required by the bridge. The 20V signal also provides a reference signal for a phase shifter/phase splitter. The phase shifter is required to offset any phase shift produced by the amplifiers and bridge transformer circuitry. The phase splitter provides two square wave signals in phase quadrature, one of these being in phase with the reference signal from the phase shifter. The two square wave signals provide reference signals for the two phase sensitive detectors employed.

The 'detector' output of the bridge (corresponding to the sum point voltage on the bridge) passes via doubly shielded cable to a low noise amplifier. This amplifier has a low input capacitance and is impedance matched to the bridge 'detector' output. This amplifier also has a variable gain facility (maximum 100 dB) and provides input to the two phase detection networks. Each of the phase detection networks consists of a filter and a phase sensitive detector. The filter consists of a gated amplifier chopped in phase with the reference signal. Each of these 'coherent filters' behave as narrow band pass (bandwidth 3Hz at 1KHz) phase selective filter with a fixed gain of 40dB. The output of the filter passes to a phase sensitive detector. The output stage of the PSD consists of a DC voltage amplifier low pass filter configuration with a maximum time constant of 10 seconds. In one of the PSD channels, an external capacitance facility has been acquired to extend the maximum time constant of the amplifier to 100 seconds. With the additional gain of the PSD (60dB), the network results in a system producing a high signal to noise ratio (120dB) with a large dynamic range (180dB).

In practice the adjustment of the phase of reference signals is significant to the satisfactory operation of the detection system. A simple practice

3

that has been found to efficiently adjust the detection system is described below.

The phase of the reference signals should be adjusted so as to 'tune' the two phase sensitive detection networks to the resistive and reactive components of the bridge summing voltage. This is conveniently achieved by connecting an oscilloscope to the output of the coherent filter in the detection channel corresponding to the resistive component of the signal. The gain of the low noise amplifier may then be adjusted so as to produce a detectable signal when the bridge is offset from the balanced condition by  $1\text{fF}$ . The phase shifter is then adjusted so as to minimise the amplitude of this signal and the process repeated with iteratively decreasing capacitance offsets. The fine adjustment of the phase shift is achieved by observing the output of the phase sensitive detector of the network corresponding to the reactive component of the signal. The phase shift is adjusted so as to produce equal positive and negative excursions on the PSD output when the bridge capacitance is offset by  $10\text{aF}$ . For ease of recording, the output from this PSD is normally displayed on a chart recorder.

In order to protect the system from "ether" and line born electrical interference it was found necessary to rigorously isolate the detection system from interference sources. With this purpose in mind the detection electronics were situated inside a Faraday cage. Further still it was found that a second cage, constructed from 5mm thick aluminium, was required to isolate the ratio bridge itself from low (audio) frequency interference. To prevent inductive coupling of the bridge components to external sources the bridge was wrapped in mumetal foil and a 3mm thick mumetal shield positioned between the bridge and the remainder of the electronics.

To prevent interference due to supply voltage variation and line born radio frequency interference (RFI) the electronics were decoupled from the 'mains' supply. The 240V, 50Hz supply passes through two stages of RFI filters to a voltage stabiliser which supplies the detection electronics. The individual 50Hz supplies to the units are separately isolated with RFI suppressors.

Another problem encountered was a result of earthloops. To alleviate this problem the bridge and detector were completely isolated, both from each other and from contact with supply earth. Earth loops in the shielded cables of the detection system were prevented by a large coaxial choke incorporated in the bridge circuitry.

4

CHAPTER FOUR

Page

CRYOGENIC EQUIPMENT FOR THE EXPERIMENTAL DETERMINATION OF THERMAL  
EXPANSION AT LOW TEMPERATURES

|     |                                    |    |
|-----|------------------------------------|----|
| 4.1 | INTRODUCTION AND DESIGN PARAMETERS | 65 |
| 4.2 | CRYOSTAT DESIGN AND PERFORMANCE    | 67 |
| 4.3 | EXPERIMENTAL TECHNIQUE             | 81 |
| 4.4 | DATA PROCESSING                    | 83 |

#### 4.1 INTRODUCTION AND DESIGN PARAMETERS

Before continuing a detailed discussion of the cryogenic equipment developed for the measurement of thermal expansion at low temperatures, a summary of the functions it must perform, and some of the design considerations which must be taken into account in its construction is essential.

The measurements undertaken in this study were designed to investigate the presence of Schottky type anomalies in thermal expansion produced by transition metal ions. The energy splittings of these ions, being typically  $1$  to  $10\text{cm}^{-1}$ , suggest that a temperature range of  $1$  to  $20$  K would provide crucial information upon the systems studied.

The measurement technique simplifies to one of measurement of small capacitance changes when the temperature of the dilatometer is varied. The only differences in cryogenic technique from "standard practices" are hence dictated by the need for extensive electrical shielding and mechanical stability of the system.

A final consideration in designing the cryogenic equipment required is determined by the rapid cooling required for some of the samples measured. Many systems measured contained ions in valence states exhibiting relatively rapid population decay (eg  $\text{Cr}^{2+}$  in  $\text{Al}_2\text{O}_3$  produced by  $\gamma$  irradiation of ruby). These samples required rapid cooling to liquid nitrogen temperatures to "freeze" ion valence states in the required populations.

The requirement for a rapid cooling facility suggests the use of a continuous flow  $\text{He}^4$  cryostat as a basis for the system. The use of this was prohibited by the vibrational stability and the temperature range required. A straightforward  $\text{He}^4$  pool cryostat was hence adopted as the basis of the measurement system.

To achieve the required cooling rate an exchange medium facility has been employed with some success. Earlier expansion measurements have been performed using pumped helium bath cryostats with low pressure helium exchange media (eg White (1961)). Recent measurements however have noted some hysteresis in measurement, upon thermal cycling of the dilatometer, when an exchange medium has been employed (Villar et al (1980)). This has been interpreted in terms of an adsorption-desorption process upon the electrode surfaces. Indeed, earlier measurements of the

study reported here have also exhibited some hysteresis upon thermal cycling, when an exchange gas was employed during the final stages of cooling. Stringent cleaning of the dilatometer electrodes prior to cooling has, however, provided significant relief regarding this problem. When this problem has arisen thermally cycling the dilatometer between 4.2 and 12K under vacuum has sufficed as a remedial measure.

To encourage vibrational stability the cryostat and control electronics were mounted on a 'vibration free' area of the laboratory. This consisted of a concrete and 'hard core' pillar with a cross section of 4m x 4m extending through a basement storey beneath the laboratory and down 1m into bedrock. The top of this pillar is flush with the laboratory floor and acoustically isolated from it by a polymer filler. It was further found necessary to mount the cryostat itself rigidly upon a second, reinforced concrete, block isolated from the floor area and with the facility to 'float' this block upon a multitude of heavy duty rubber inner tubes. All vacuum and 'plumbing' connections to the cryostat are via flexible rubber connections.

We will now go on to describe the mechanical details of the cryostat, details of experimental technique, and the processing of experimental data.

## 4.2 CRYOSTAT DESIGN AND PERFORMANCE

A pumped  $\text{He}^4$  cryostat design was adopted and constructed. General views of the system in total is given in plate 4.1 and plate 4.2.

A helium pool cryostat was constructed from a pair of glass dewar flasks. The inner diameters of these were 10cm and 30cm for the helium and nitrogen vessels respectively. To encourage vibrational stability these dewars were mounted in a rigid aluminium frame and this frame bolted on top of a reinforced concrete block. The cryogen capacities of these flasks in assembled form are 3 litres and 20 litres for the liquid helium and liquid nitrogen vessels respectively.

A stainless steel insert of the 'inner pot' design was constructed for immersion in liquid helium within the inner dewar flask. A simplified schematic of the 'cold end' of this is given in figure 4.1. The insert consists of a detachable vacuum chamber (see plate 4.3) suspended from the top of the helium dewar by thin walled stainless steel tubes. Two copper radiation shields are equispaced between the top of the dewar and the top of the vacuum jacket. With the radiation shields in place and with the helium flask at its maximum capacity of 3 litres the cryogen consumption has been estimated to be  $100\text{cm}^3$  liquid helium per hour.

The detachable vacuum jacket surrounds a further cylindrical vessel ('inner pot') suspended from the top of the vacuum jacket via three thin walled stainless steel tubes (see plate 4.4). The dimensions of this cylindrical vessel are diameter 6cm and length 10cm, and when immersed in liquid helium a facility exists by which this 'inner pot' may be filled with liquid helium via a needle valve (see figure 4.1 and plate 4.4). If necessary the liquid helium within this inner pot may then be pumped by a helium sealed pump and its temperature reduced to approximately 1.2K. The temperature of the helium in the inner pot is conveniently determined by measuring its vapour pressure.

To accomplish this a stainless steel tube was provided connected to two manometers containing mercury and oil. The base of this inner pot provides a heat sink, or 'cold finger', to which the experiment may be attached.

Vacuum seal for the detachable jacket is provided by a compressed Indium 'O'-ring. Details of this seal are given in figure 4.2. The indium 'O'-ring is trapped in a tongue and groove arrangement and compressed via 15, M6, screws. This joint has been found successful in

practice provided sufficient care is taken in cleaning joint and indium before assembly.

The dilatometer is suspended from the base of the pumped helium pot and surrounded by a polished copper radiation shield (see plate 4.4 and 4.5). Thermal contact between the copper radiation shield and the inner pot is encouraged by the use of a small quantity of silicone grease on the threaded joint between them. Heat leaks to the experiment space due to thermal conduction down the electrical leads is suppressed by thermally anchoring these leads to the base of the inner pot. Heat leaks due to conduction down the capacitance leads and insulation is suppressed by using PTFE coated copper wire for these connections.

Electrical shielding of the capacitance leads, both from each other and from external influences, is via stainless steel tubular shields. The technique which has been adopted with some success to shield these connections is in the form of two concentric cylindrical stainless steel tubes the outer one of which is 8mm in diameter and the inner one 3.2mm in diameter. The tubes are mounted in a coaxial arrangement with the 'low potential' lead passing down the centre of the inner steel tube and the 'high potential' lead passing between the two tubes as shown in figure 4.3. The inner shield is continued past the pumped helium pot within the vacuum jacket to provide continuous shielding for the low potential electrode, and the low potential lead thermally grounded to a shielded copper post at the centre of the base of the inner pot.

Electrical shielding of the Kelvin guard-ring capacitor is provided via three earthed shields. The first being the walls of the dilatometer itself, the second being the copper '12K' radiation shield connected to the inner pot and the third being the vacuum jacket itself.

To maintain vacuum security, all non-detachable joints that were to be exposed to liquid helium were either silver soldered or argon arc welded. Especially important were those joints which are exposed to superfluid helium. Before any experiments were performed the insert was rigorously tested using a mass spectrometer leak detector and again tested at regular intervals when in use. The vacuum security of the vacuum jacket was tested prior to cooling using the same technique. All room temperature vacuum joints were soft soldered where possible and neoprene rubber "O"-ring seals utilised where a demountable seal was required.

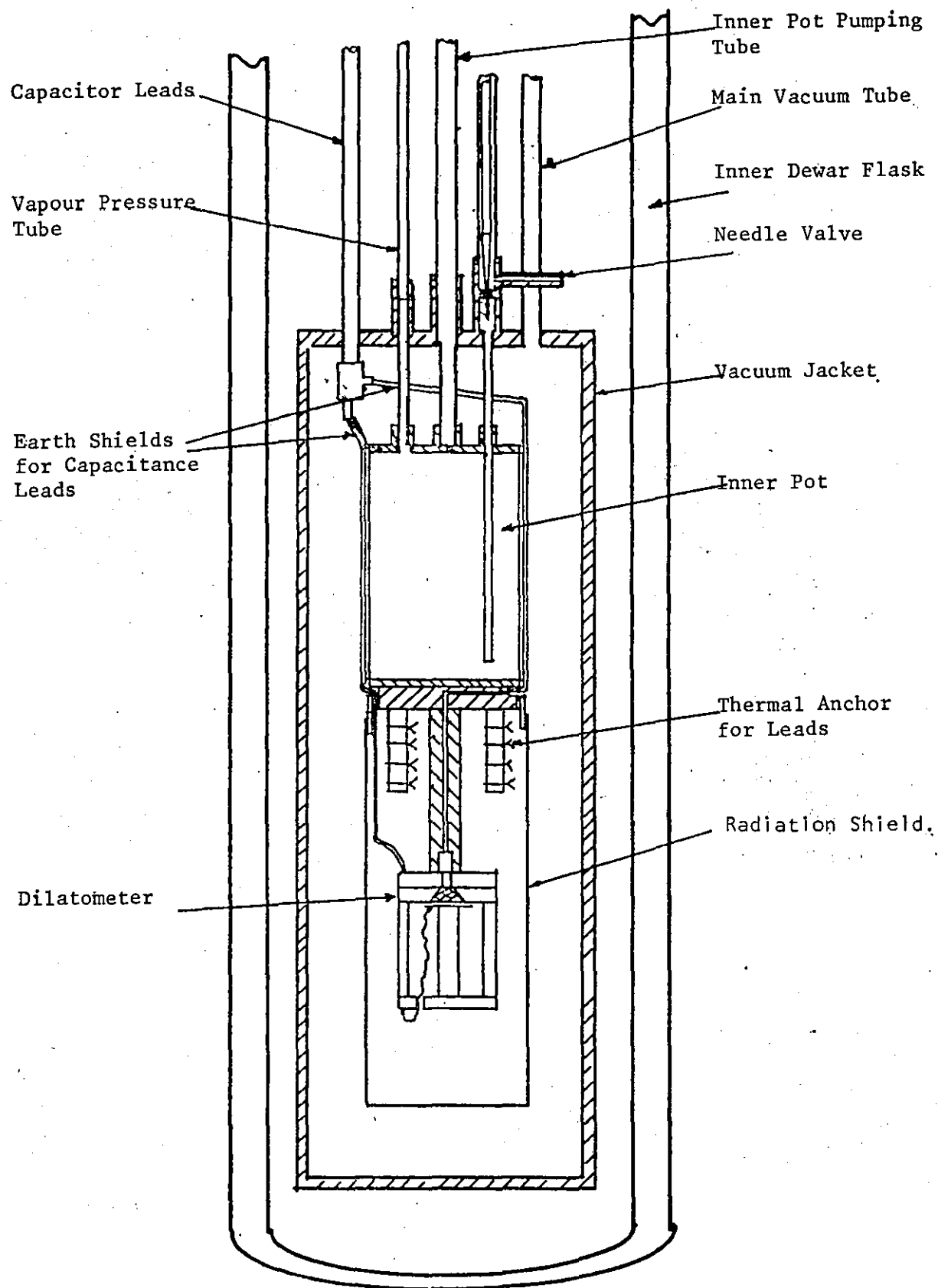


Fig 4.1 Simplified view of Cryostat Insert  
(with detail of Inner Pot)



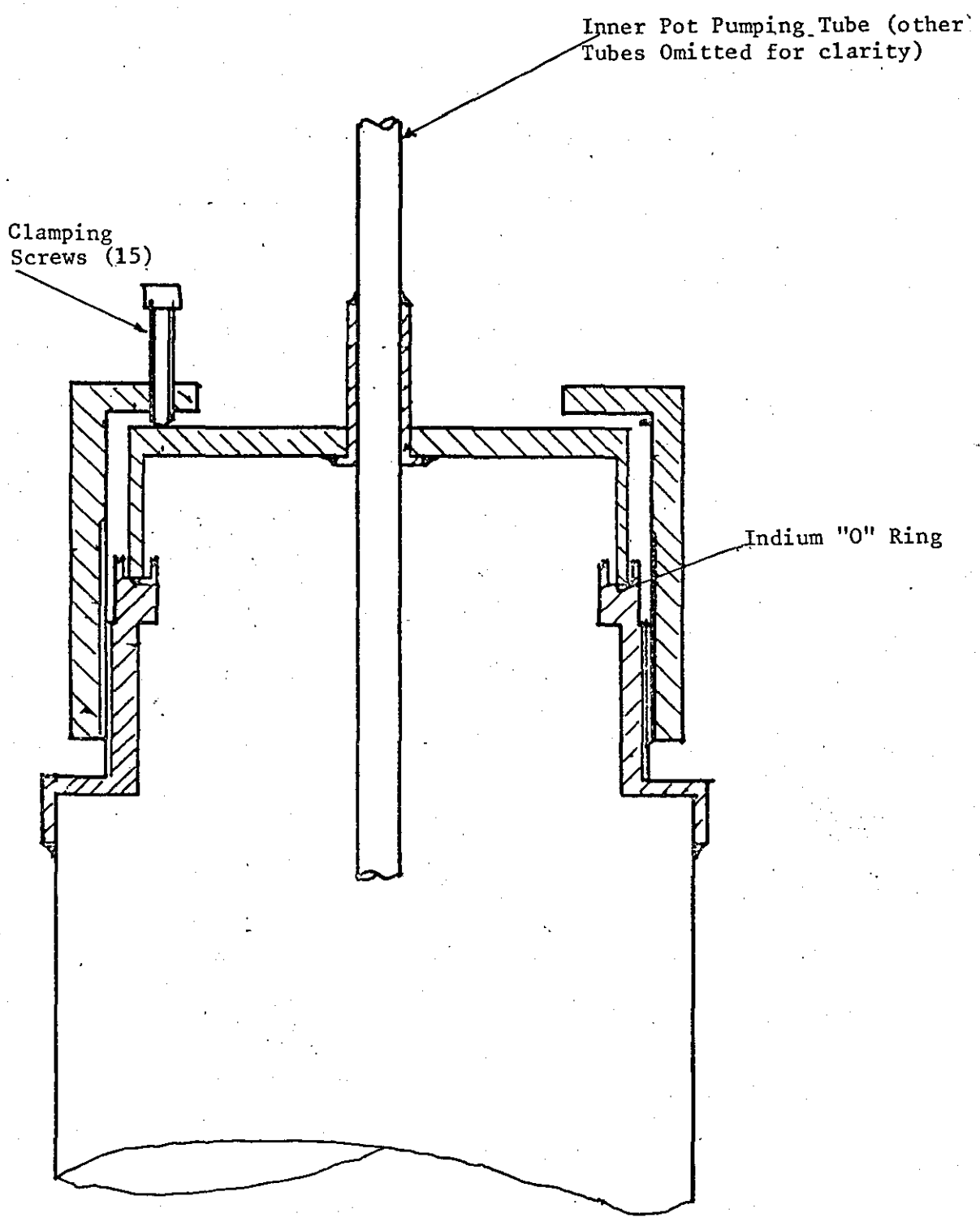


Fig 4.2 Detail of Low Temperature Vacuum Seal

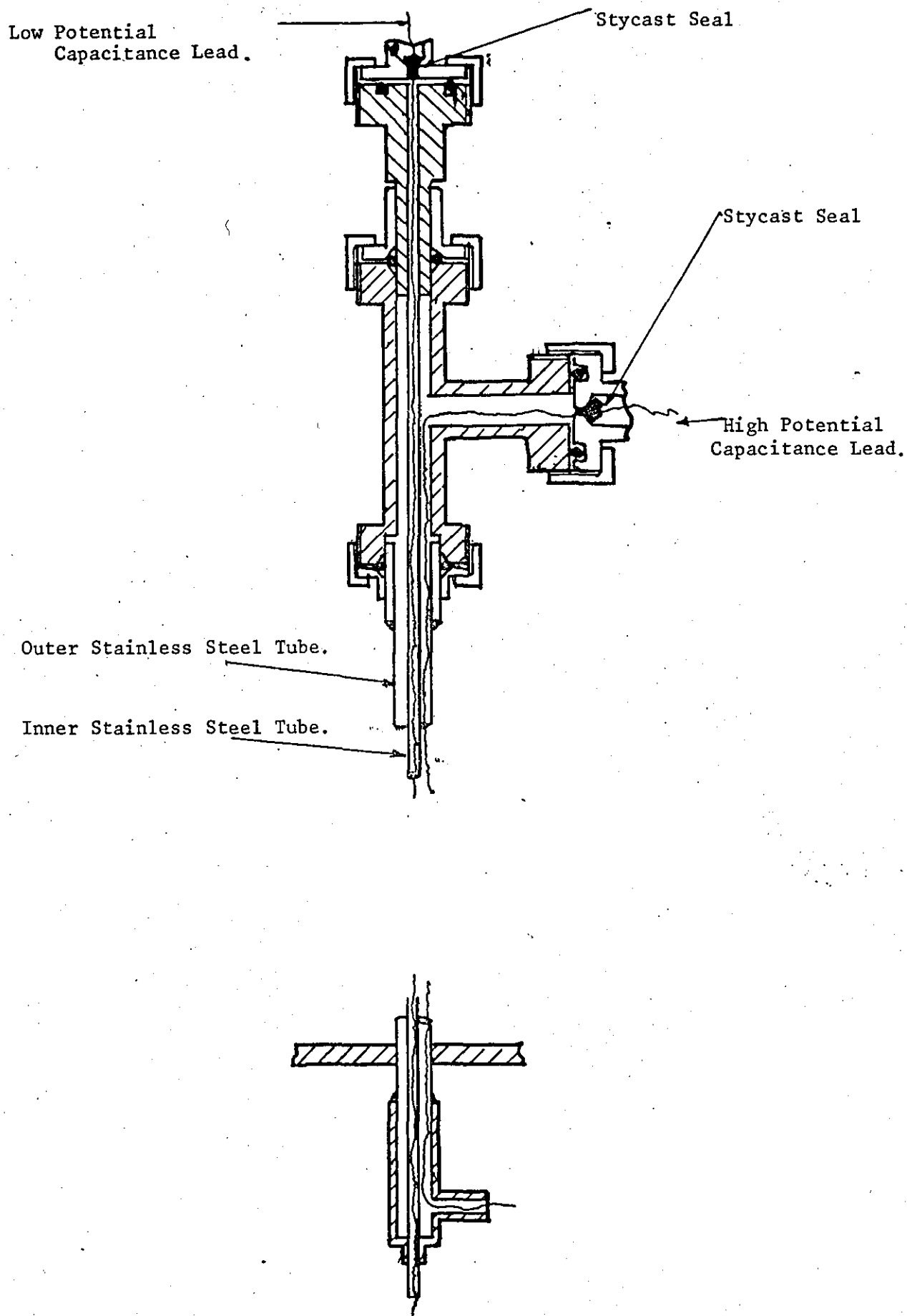


Fig 4.3 Detail of Shielding For Capacitance Leads,

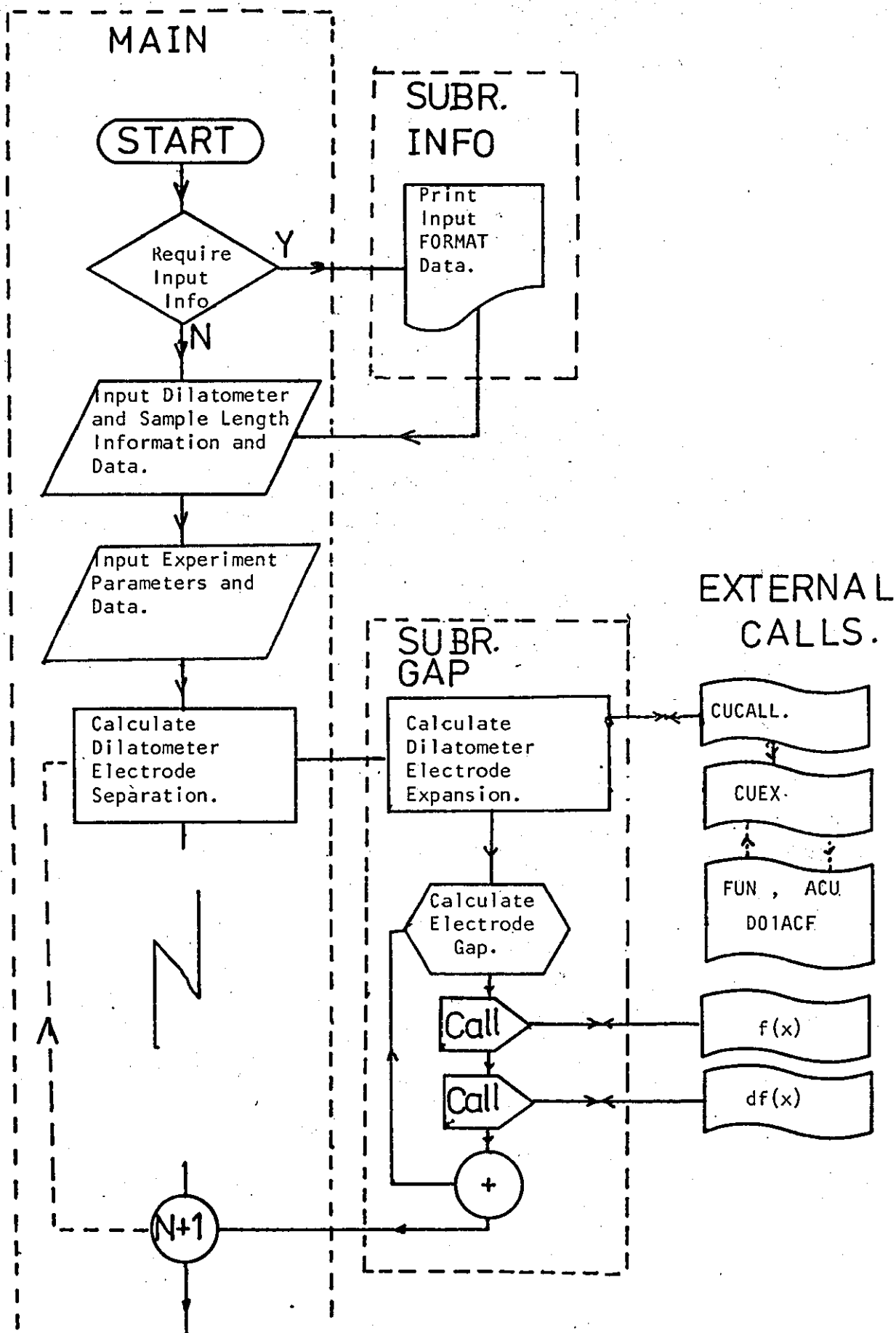


FIG. 4.4(a) Flow Chart For Thermal Expansion Data Evaluation Program.

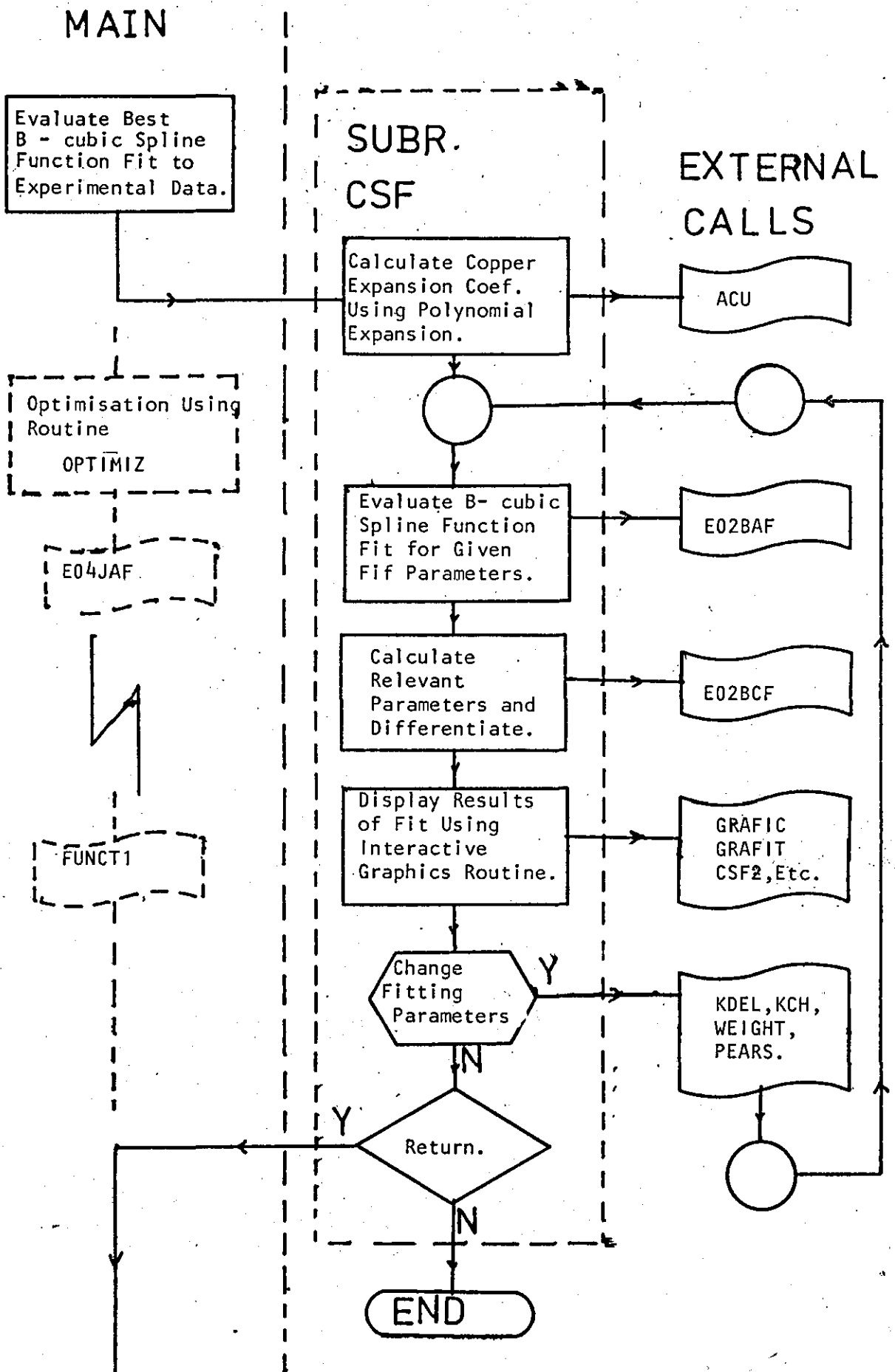


FIG. 4.4(b).

## MAIN

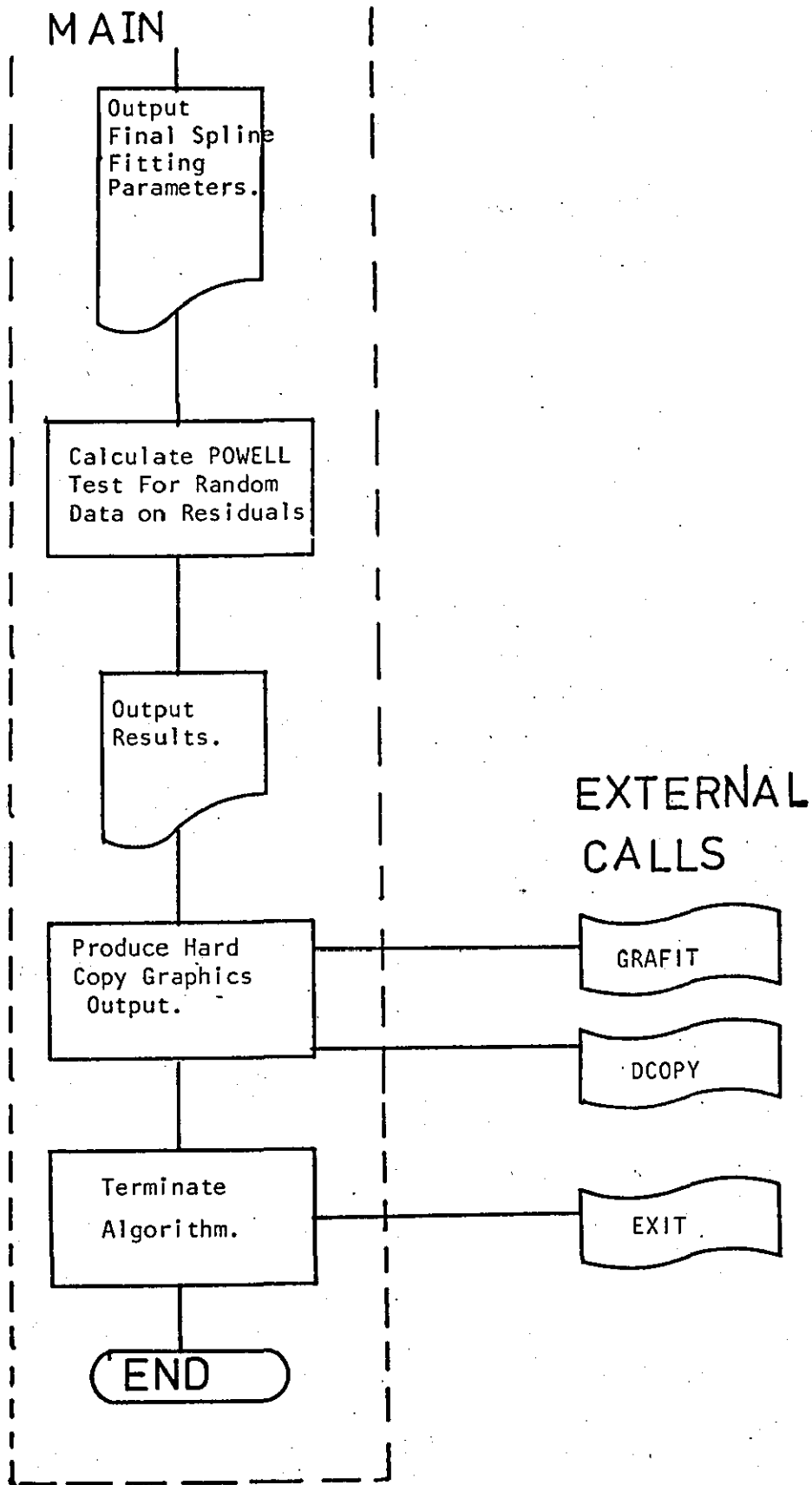


FIG. 4.4(c).

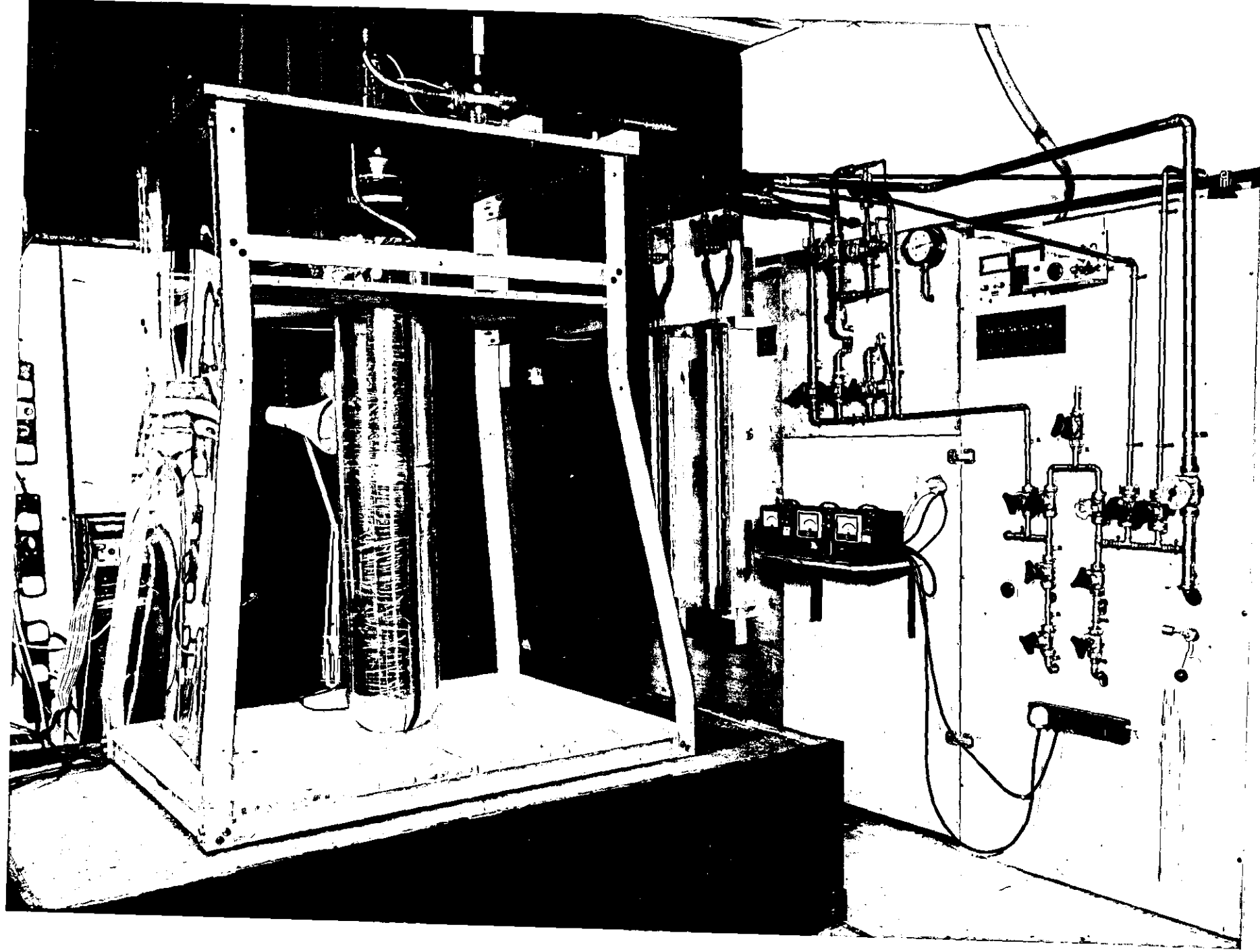


PLATE 4.1 General View of Cryostat.

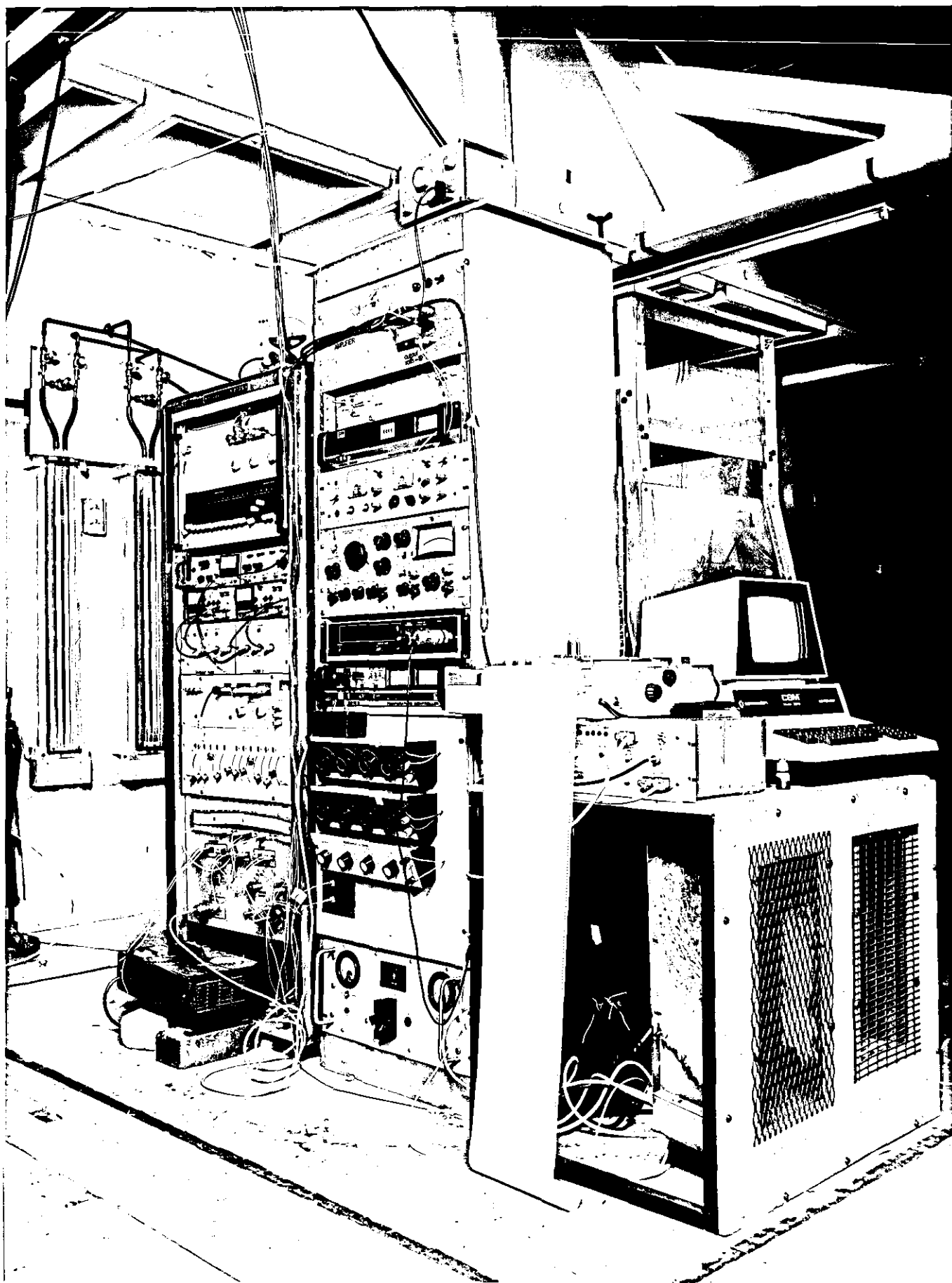


PLATE 4.2

General View of Detection Electronics.

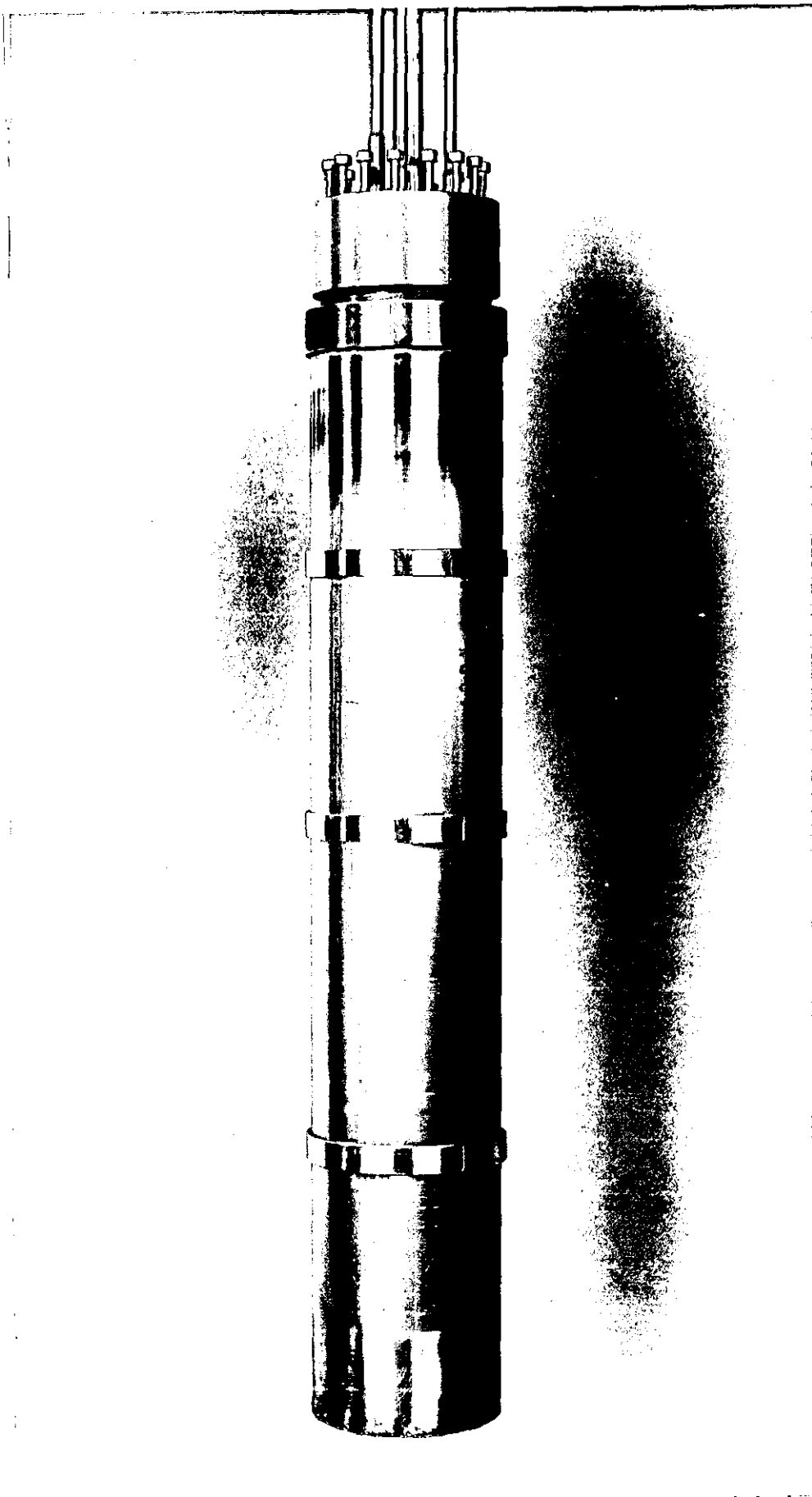


PLATE 4.3

Cryostat Insert Vacuum Chamber.



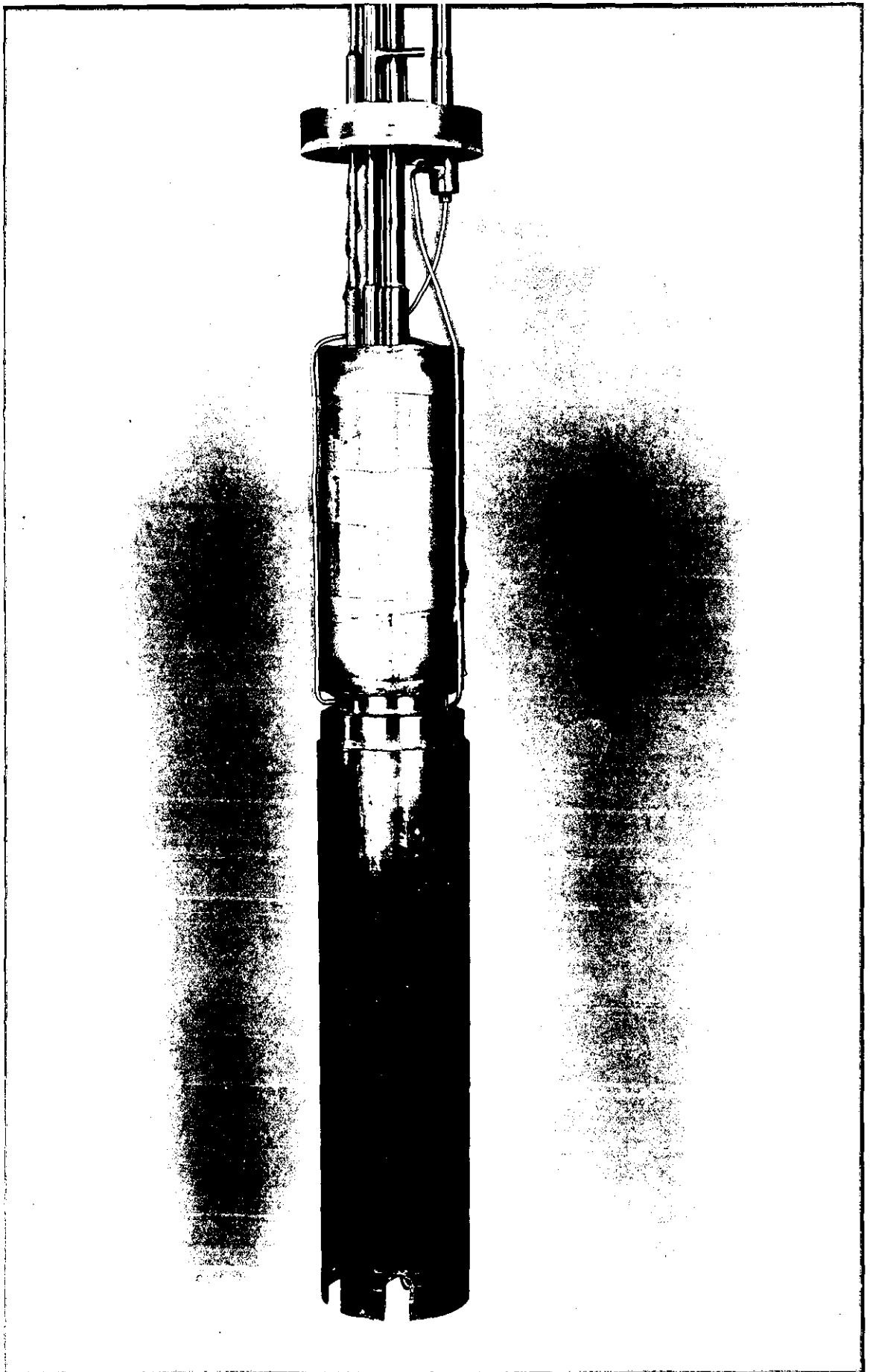


PLATE 4.4 Inner Pot and Radiation Shield Detail.

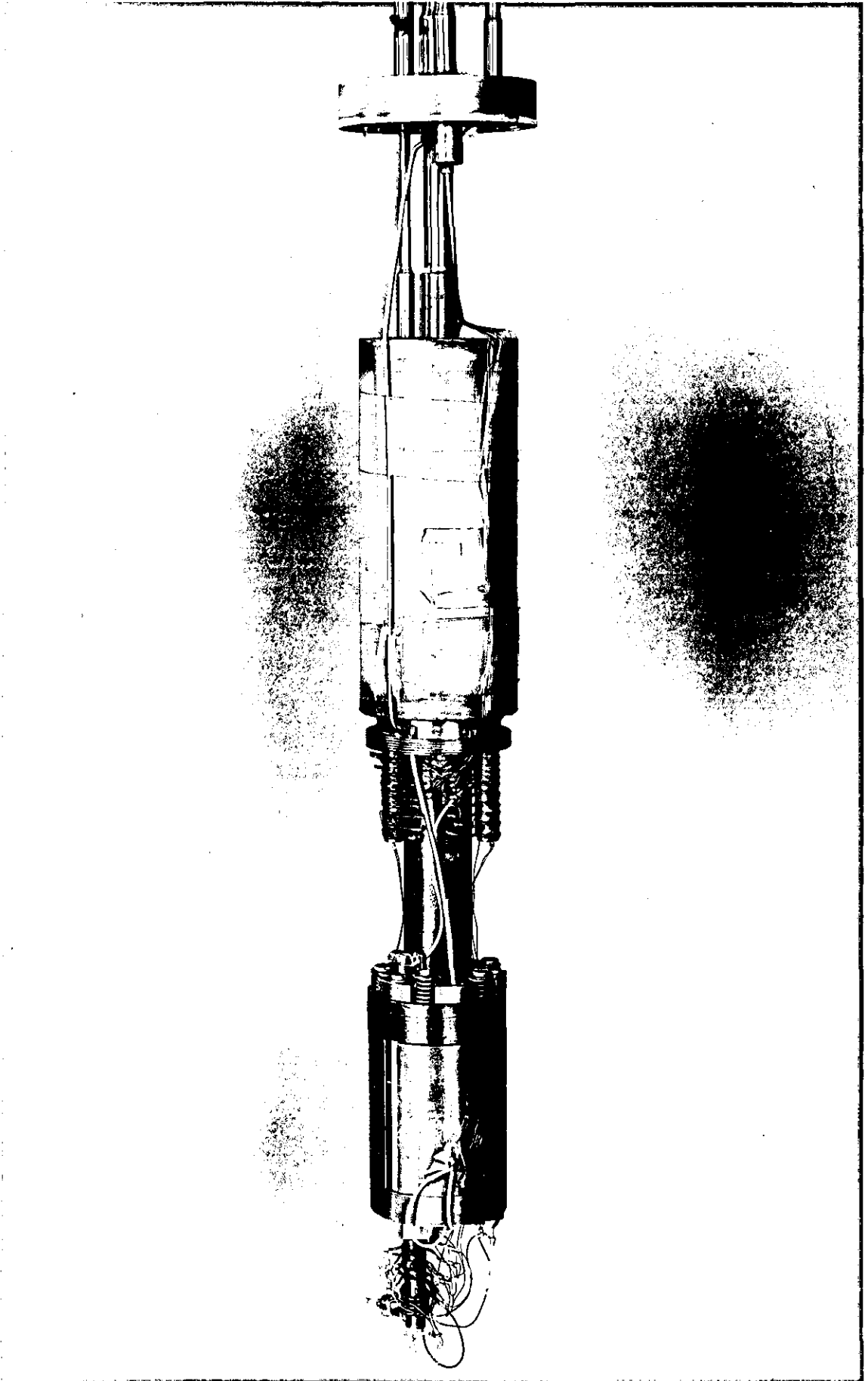


PLATE 4.5 Inner Pot and Dilatometer Detail.

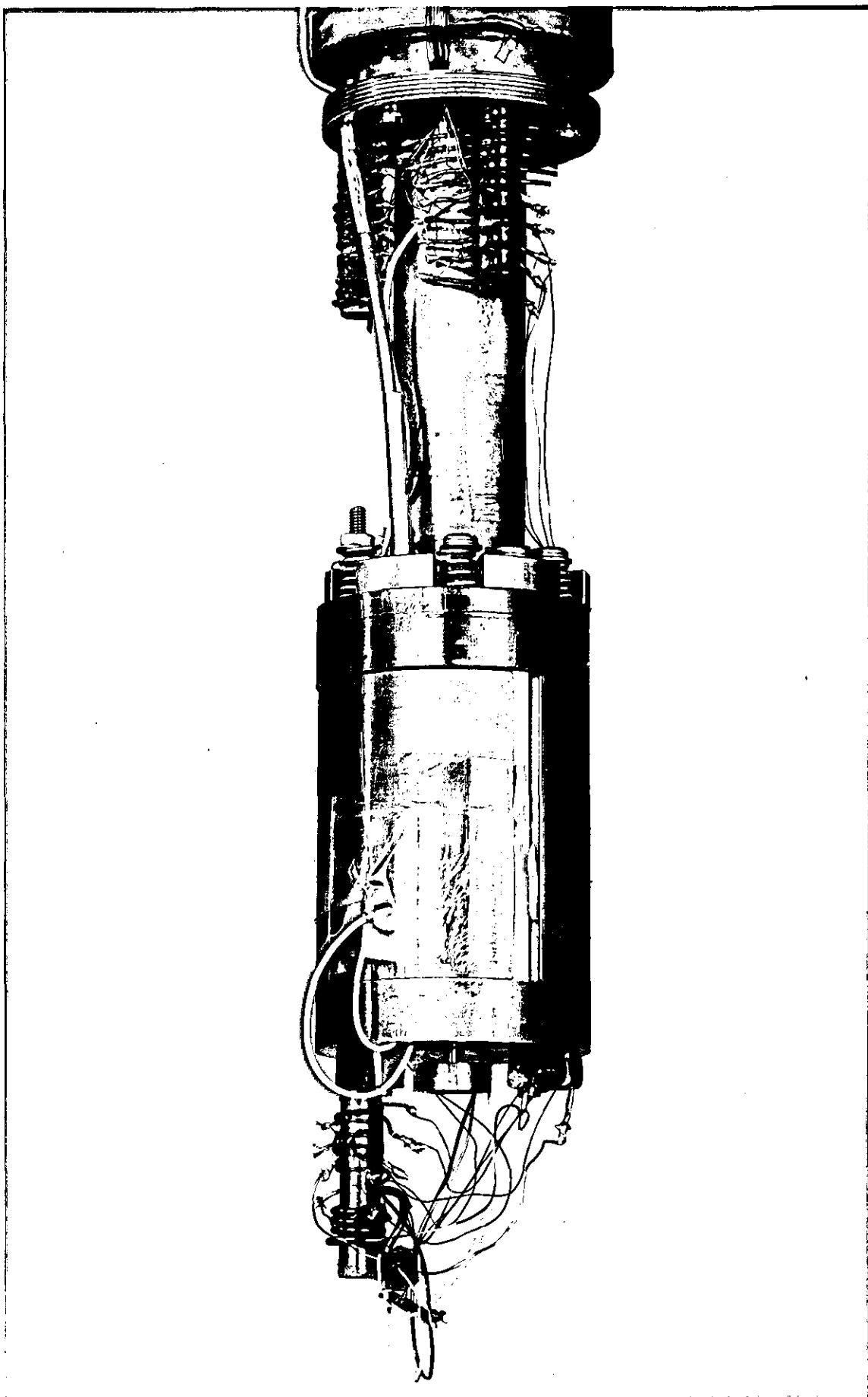


PLATE 4.6      "Al<sub>2</sub>O<sub>3</sub>" Cell Dilatometer Detail.

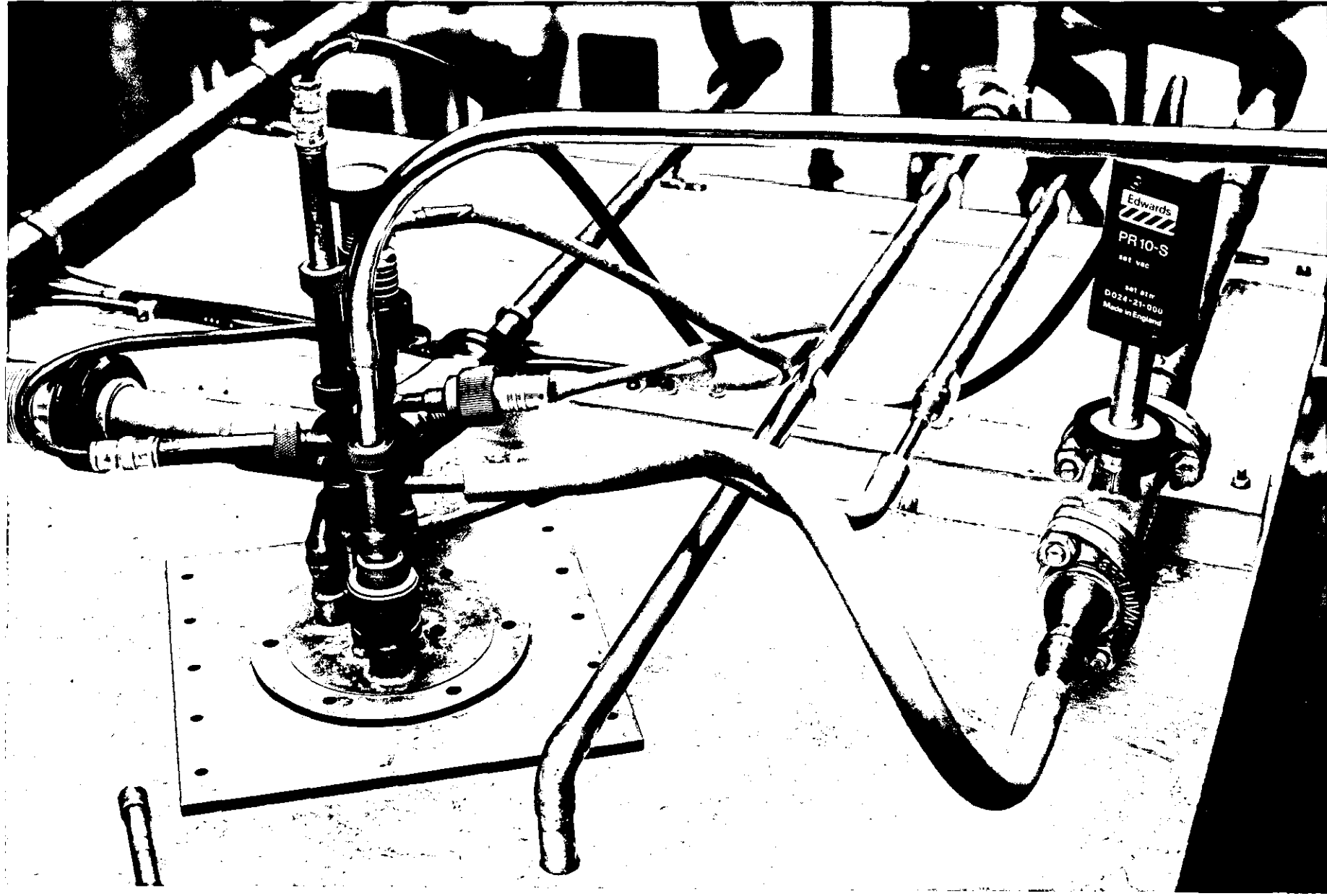


PLATE 4.7 Electrical and Plumbing Connections to Cryostat.

Vacuum and electrical connections to the cryostat are affected at the top of the cryostat (see plate 4.7). Vacuum connection to the insert is via a flexible rubber tube. The pumping line for the pumped helium vessel and the return line for evaporated helium gas are connected to external plumbing by flexible stainless steel bellows attachments. Electrical connection for the capacitance leads is via two BNC connectors in a 'T' arrangement as shown in Plate 4.6. Electrical connection for thermometry and heaters for temperature control is achieved using two, 10 pin connectors. The stainless steel tube housing the enamelled copper wires that provided thermometry connections doubles as the main pumping tube for the vacuum jacket. The other fittings which may be observed in plate 4.7 are a threaded fitting linked to the needle valve controlling liquid helium flow to the inner pot, and a facility for access for a liquid helium syphon.

Sample thermometry utilised calibrated platinum and germanium resistance thermometers. The resistance was determined using a four terminal DC technique using a stabilised current source and a Keighley model 1802 digital nanovoltmeter. The temperature of the pumped helium bath was determined from vapour pressure measurements. When required, a Thor cryogenics model 3010 II temperature controller was utilised with an Allen-Bradley carbon resistor as temperature sensor. The electronics cabinet containing the General Ratio capacitance bridge was temperature controlled using a nickel resistor as temperature sensor.

For rapid cooling of samples an exchange gas (1 Torr of Hydrogen or Helium) was used in the inner of the two glass dewars. Using this technique it was possible to reduce the temperature of the sample from room temperatures to liquid nitrogen temperatures in typically 60 minutes. It is of course possible to cool more rapidly than above but the risk of shattering brittle samples has been found.

#### 4.3 EXPERIMENTAL TECHNIQUE

The techniques used for the measurement of thermal expansion have already been sufficiently described in previous sections (chapter 3). Experimental technique revolves around that used by all authors in the field in that the capacitance of a three terminal dilatometer is determined at discrete temperatures and this information used to calculate specimen expansion. A major object of this study was the refinement of this technique and the application of a microcomputer to automate the measurement process.

The measurements required may be broadly differentiated into two temperature regimes. Firstly for temperatures from 1.2K to 6K requiring the use of an <sup>internal</sup> helium bath and secondly from 4.2K to 20K. A dynamic technique was adopted for the measurements and this is described in more detail below.

The basis of the technique is to perform a data averaging process upon the capacitance of the dilatometer while the temperature of the system is allowed to vary in a controlled manner. In practice this entails the measurement of the temperature of the system at predetermined intervals while the system is allowed to warm, and during the intervals between these measurements the capacitance data averaged. In initial experiments this process was achieved by using a chart recorder to display the capacitance bridge null detector output and the temperature measured and noted at discreet intervals. In later experiments however, a digital voltmeter (Keighley 1802 Nanovoltmeter) was used which had the facility for digital output of the resultant voltage. It was then possible to use a Commodore 'Pet' mini computer to sequentially switch thermometer and capacitance readings to the voltmeter and to record and store the resultant data. The use of a minicomputer enhances the noise performance of the system as it is possible to perform data averaging algorithms over very long time intervals. The period between temperature measurements and periodicity of capacitance measurements were pre-programmed into the system prior to commencing measurements and typical values were:-

|  |                         |
|--|-------------------------|
| Interval between temperature measurements    | = 5 minutes             |
| Typical temperature increase in five minutes | = $0.1^{\circ}\text{K}$ |
| Interval between capacitance measurements    | = 5 seconds             |

For measurements below 4K the inner pot was filled with liquid helium using a needle valve facility. This inner helium bath was then pumped until the bath temperature (as measured using vapour pressure thermometry) had remained constant for some minutes (typically at 1.5K). The bath was then sealed and observations recorded as the system warmed. Thermal isolation of the dilatometer was such that the temperature rise of the system was typically 1K per hour so that thermal equilibrium of the sample and dilatometer may be assumed to be a reasonable approximation. Helium economy was such that the system could be cycled over this temperature range several times.

For measurement above 4K the inner pot was opened and the observations obtained when the cryogen level in the system became limited. This technique allows measurements to be recorded up to typically 18K before the rate of temperature rise detrimentally disrupts measurement precision. Indeed with suitable adjustment of the capacitance bridge and detection electronics it is possible to extend the measurement range up to room temperature with reduced measurement precision.

A great advantage of the automated data acquisition system is that experiments could be conducted over very long periods with minimal operator intervention. Indeed manual intervention was only necessary to effect cryogen transfer and occasional adjustment of bridge balance. Work is still continuing to use the mini computer with an auto-balance facility to further extend measurement precision at higher temperatures. A further advantage of the dynamic experiment technique is the economy of helium consumption that can be achieved; With care a 36 hour experiment may be performed with a maximum helium consumption of 7 litres.

The automated recording facility may be calibrated by measurement of detector output for various known capacitance offsets utilising a standard capacitance. A Lagrangian interpolation procedure may then be used to calculate the capacitance corresponding to any voltage offset. This procedure has been tested by using the capacitance bridge in its "calibration" mode and found accurate to the resolution of the bridge (0.1aF) for small capacitance differences ( $\pm 20\text{aF}$ ).

#### 4.4 DATA PROCESSING

The experiments performed in this study produce data in the form of capacitance of the capacitance dilatometer as a tabulated function of temperature. A significant amount of numerical processing is required to calculate the expansion coefficient from this data and for this purpose a Fortran computer package was developed. The computer package accepts the capacitance-temperature data set and maps this to a second data set consisting of sample length as a function of temperature. This data may then be differentiated numerically to give the expansion coefficient.

A Newton-Raphson technique is used to calculate the separation of the electrodes in the capacitance dilatometer from the measured capacitance using the relation (3.11) derived in Chapter 3 and repeated below:

$$C = \frac{\pi R_1^2 \epsilon_0 \epsilon_r}{d_0} \left( 1 + \frac{S}{R_1} \left( 1 + \frac{S}{2R_1} \right) \left( 1 + \frac{0.22S}{\epsilon_s d_0} \right)^{-1} \right)$$

It should be noted that the variable  $R_1$  is a function of the thermal expansion of the HCOF copper used in the manufacture of the guard ring plate. Its value at any temperature  $T_2$  may be calculated from its measured value at a temperature  $T_1$  by using the relation:

$$R_{1,T_2} = R_{1,T_1} \left( 1 + \int_{T_1}^{T_2} \alpha_{cu} dT \right) \quad (4.1)$$

Where  $\alpha_{cu}$  is the linear thermal expansion coefficient of HCOF copper. In the computer package the power series expansion for  $\alpha_{cu}$  (Kroegar and Swenson (1977)) (Table 3.1) is utilised and is numerically integrated using a Gaussian integration technique. The behaviour of the electrode guard-ring gap,  $s$ , is also expected to be temperature dependent but its effect was corrected by performing calibration experiments.

Numerical differentiation of 'noisy' data is inherently problematic. The technique pursued here was to produce a polynomial, spline function, fit to the data and to differentiate this fit. The functions used, in the software routine, to fit to the data were  $\beta$ -cubic spline functions. The primary reason for the use of these being that library routines were in existence that would calculate not only the polynomial fit, but also the first three derivatives of the fitted polynomial.

A useful advantage of the computer facilities available in Loughborough is that extensive interactive graphics software was available. These have been extensively used in accelerating the process of curve fitting to the data. Some attempt has also been made to optimise the thermal position of the 'knots' used in the fitting routine using a quasi-Newtonian minimisation routine.

A very simplified flow chart describing the computer package is shown in figure (4.4) and a complete listing is available in Appendix I.



CHAPTER FIVETHE THERMAL EXPANSION OF DOPED ALUMINIUM OXIDE

|     |  |    |
|-----|--|----|
| 5.1 | Introduction and Preliminary Experiments   | 86 |
| 5.2 | Thermal Expansion Corrections due to Expansion of Dilatometer Electrodes and Sample Supports | 88 |
| 5.3 | Thermal Expansion of $\text{Al}_2\text{O}_3:\text{Cr}$ (Ruby)                                | 89 |
| 5.4 | Thermal Expansion of $\text{Al}_2\text{O}_3:\text{Mn}$                                       | 96 |
| 5.5 | Thermal Expansion of $\text{Al}_2\text{O}_3:\text{V}$  | 99 |

## 5.1 INTRODUCTION AND PILOT STUDY EXPERIMENTS

An extensive series of experimental observations have been performed to determine the contribution to the low temperature thermal expansion of aluminium oxide crystals due to the presence of small concentrations of strongly coupled paramagnetic ions. The experiments reported involved the measurement of the low temperature thermal expansion of aluminium oxide both as pure crystals and doped with small concentrations of Chromium, Manganese and Vanadium. The samples measured were all of cylindrical geometry and were single crystals, a majority of which had a specimen axis (cylinder axis) at an angle of  $60^\circ$  with the crystallographic c-axis.

A series of pilot experiments were performed, inspired by the theoretical studies of Sheard ((1969), (1971), (1972), and (1977)) to determine the thermal expansion of  $\gamma$  irradiated ruby ( $\text{Al}_2\text{O}_3:\text{Cr}$ ). The reasons for adopting this system are numerous and have largely been discussed earlier. In particular this system was found attractive for the following reasons:

- (i) The concentration of the  $\text{Cr}^{2+}$  ion (thought to be very strongly coupled) in the sample could be conveniently varied by UV and  $\gamma$  irradiation (eg Brown et al (1973), Brown (1971)).
- (ii) The ruby system has been qualitatively studied with some success using other techniques such as thermal conductivity (Brown et al (1973), Brown (1971)).
- (iii) Large monocrystalline samples of ruby were readily available.
- (iv) A dynamic, multi-mode, Jahn-Teller model for this system has been studied in some detail (Bates (1978)).
- (v) The Debye temperature of  $\text{Al}_2\text{O}_3$  is 1023K so that at low temperatures the lattice thermal expansion is small, and should not dominate any paramagnetic contributions.

A three terminal capacitance technique (incorporating a GR 1615A capacitance bridge) was utilised to determine the thermal expansion of three aluminium oxide samples from 3-270K relative to that of a HCOF copper annulus (Brown and Brown (1981)). The three monocrystalline samples were cylindrical in form, one being a "pure"  $\text{Al}_2\text{O}_3$  sample, another being doped with  $\approx 800\text{ppm}$  Chromium (manufacturers quoted value) and the

7

third sample containing  $8100 \pm 200$  ppm Cr (Value obtained by optical measurements (Villedieu, private communications) the manufacturers estimate having been 1.04%). The dimensions of the cylindrical samples were diameters 12, 10 and 5mm and lengths 100, 100 and 50mm for the pure, 800ppm Cr doped and 8100ppm Cr doped samples respectively.

The chromium doped samples were  $\gamma$  irradiated ( $10^7$  rads) using a  $\text{Co}^{60}$  source to produce a saturated population of  $\text{Cr}^{2+}$  ions (Brown (1971)) and then rapidly cooled and measured. The results of this exercise are plotted in figure 5.1 (figure 2 of Brown and Brown (1981)). Clearly, peaked anomalies were observed with a peak at  $\sim 3.9\text{K}$  and the effect was tentatively ascribed to the presence of  $\text{Cr}^{2+}$  (produced from  $\text{Cr}^{3+}$  by  $\gamma$  irradiation). If one takes the published energy levels of  $\text{Cr}^{2+}$  in  $\text{Al}_2\text{O}_3$  (Bates (1978)) and calculates the expected Schottky specific heat anomaly (figure 5.2, peak amplitude  $20 \times 10^{-24} \text{ J K}^{-1} (\text{ion})^{-1}$  at  $2.6\text{K}$ ), and uses the estimated 5% of the total chromium concentration for the number of  $\text{Cr}^{3+}$  ions converted to  $\text{Cr}^{2+}$  ions by  $\gamma$  irradiation (based on low temperature thermal conductivity measurements eg Brown et al (1972)), we obtain an admittedly crude estimation for the "spin" Gruneisen parameter ( $\gamma_s$ ) of  $\sim 180$ . This value contrasts strongly with the value  $\gamma_s = -5/3$  derived from second order spin orbit coupling on a static crystal field model (see section 2.3.1) but may be consistent with a dynamic Jahn-Teller model ( $\gamma_s \sim 30$  for  $\text{MgO}:\text{Cr}^{2+}$  (Sheard (1971)) with tunnelling splitting.

The results plotted in figure 5.1 were obtained using the computer package described in the previous chapter. The position and height of the peak obtained is hence totally dependent upon the actual inflection in the plot of sample length against temperature (figure 5.3). Due to the limited sensitivity of the GR1615A bridge ( $10^{-5}$  pf) and calibration errors discovered after the completion of the experiments, the magnitude of the observed anomaly is subject to large systematic errors and required more detailed analysis using more sensitive apparatus.

The promising result obtained in these measurements however provided the lever required to obtain funds for the purchase of the General Radio 1616 precision capacitance bridge used in the remainder of the experiments performed in this study. This device with its greater intrinsic stability and sensitivity, provides the additional precision required for a more detailed study of the phenomena.

## 5.2 THERMAL EXPANSION CORRECTIONS DUE TO EXPANSION OF DILATOMETER ELECTRODES AND SAMPLE SUPPORTS

As a prelude to the further measurement of doped aluminium oxide samples it was necessary to firstly determine contributions to observed effects which are a result of dilatometer electrode expansion and sample support effects.

To accomplish this, a series of measurements were made using the " $\text{Al}_2\text{O}_3$ " dilatometer described in detail in Chapter 3. This cell utilises three pure aluminium oxide samples (nos. LUT1, LUT2, and LUT3) separating the end plates of the dilatometer (see figure 3.11). The expansion of doped samples could hence be directly compared with that of the three pure samples. These pure samples were manufactured from the same boule and were cylindrical in form with cylinder axes inclined at  $60^\circ$  with the crystallographic c-axis. The dimensions of the samples were lengths 50.3mm and diameter 5mm and they were single crystals.

To determine the expansion effects attributable to dilatometer electrode expansion and sample mountings a fourth pure aluminium oxide sample was utilised (no. LUT4). This sample was identical in all respects to the pure reference samples, being also from the same boule as LUT1, LUT2, and LUT3. All four pure samples were spark machined and precision ground and polished to be of identical lengths ( $\pm 0.004\text{mm}$  tolerance).

Approximate correction of the data due to expansion of the HCOF copper electrodes was accomplished in the computer package using the polynomial expressions from the expansion data of Kroeger and Swenson (1977). The apparent results of measuring the thermal expansion of sample LUT4 relative to samples of LUT1, LUT2 and LUT3 are given in figure 5.4. The graph plotted is of apparent expansion coefficient as a function of temperature (the effect of the known expansion of the HCOF electrodes and supports being previously compensated by the analysis software).

It is immediately obvious that there are no peaked anomalies in this data. The data was further used as compensation values in the results plotted for the doped samples discussed later.

### 5.3 THERMAL EXPANSION OF $\text{Al}_2\text{O}_3\text{:Cr}$ (Ruby)

A detailed study of the thermal expansion of ruby has been performed using the " $\text{Al}_2\text{O}_3$  cell" dilatometer. This study involved the determination of the low temperature thermal expansion from 2K to 20K of the 8100ppm chromium doped aluminium oxide sample following ultra violet and  $\gamma$  irradiation treatments. The expansion of this sample was determined relative to that of the three pure aluminium oxide samples LUT1, LUT2, and LUT3. The dimensions of the samples involved in this study are summarised in table 5.1.

Several experiments were performed and the results of which are reviewed here. Firstly the thermal expansion of the chromium doped sample was determined following ultraviolet irradiation at 365nm. This was performed using a 150W mercury discharge source. The sample was exposed to this treatment for 168 hours with the sample positioned some 3 cm from the UV source. Previous studies (Brown et al (1972)) suggest that this procedure should be sufficient to remove any  $\text{Cr}^{2+}$  ions present in the sample produced from earlier irradiation treatments. The results of several measurements performed over a number of days are summarised in the following figures.

Secondly, the sample was subjected to a  $\gamma$ -irradiation treatment using a  $\text{Co}^{60}$  source for 96 hours at a dose rate in excess of  $10^5 \text{ rad hr}^{-1}$ . The total dosage of  $9.6 \times 10^6$  rads. being sufficient to saturate the population of  $\text{Cr}^{2+}$  ions within the sample (Brown (1972)). The sample was immediately cooled to liquid nitrogen temperatures to prevent excessive decay of the  $\text{Cr}^{2+}$  population (the decay rate being of the order of hours). The sample was again measured at several periods over a period of days, the sample being maintained at a temperature below 25K during the intervals between measurements.

The results of these measurements are reviewed in the following figures. Figure 5.5 contains a representation of the change in capacitance of the three terminal dilatometer with temperature for measurements before and following  $\gamma$ -irradiation treatment. The following figure (5.6) contains the results of the same experiments presented in terms of the thermal expansion of the sample. For clarity, expansion effects due to electrode and mounting expansion (as discussed in section 5.2) have been subtracted. Again a marked peaked feature, with a peak at  $\approx 4\text{K}$ , is observed in the expansion of the  $\gamma$ -irradiated sample which is not present in the UV bleached case, providing more evidence that this

Table 5.1Aluminium Oxide ( $Al_2O_3$ ) Samples Used in the Study

## PURE SAMPLES:

| No        | Length<br>mm    | Diameter<br>mm | Crystal Axis Orientation<br>to Sample Axis |
|-----------|-----------------|----------------|--|
| LUT1      | 50.30 $\pm$ .01 | 5.0 $\pm$ .05  | 60°  |
| LUT2      | 50.30 $\pm$ .01 | 5.0 $\pm$ .05  | 60°  |
| LUT3      | 50.30 $\pm$ .01 | 5.0 $\pm$ .05  | 60°  |
| LUT4      | 50.30 $\pm$ .01 | 5.0 $\pm$ .05  | 60°  |
| "Pure #1" | 100.0           | 12.0           | 60°  |

## DOPED SAMPLES:

| No               | Length<br>mm | Diameter<br>mm | Doping<br>Density<br>ppm | Crystal Axis<br>Orientation<br>Relative to<br>Sample Axis |
|------------------|--------------|----------------|--------------------------|---|
| <u>Chromium</u>  |              |                |                          |   |
| # 1              | 100          | 10             | 800 (*)                  | 60°   |
| # 2              | 48.60        | 5              | 8100 (**)                | 60°   |
| <u>Manganese</u> |              |                |                          |   |
| J1               | 50.0         | 5.0            | 60 (***)                 | 60°   |
| <u>Vanadium</u>  |              |                |                          |   |
| A2               | 50.0         | 5.0            | 1115 (****)              | 60°   |

\* Manufacturers' estimate

\*\* Optical measurements (Villedieu, private communications)

\*\*\* Max possible (De Goer (1969)), thermal conductivity measurement

\*\*\*\* Thermal conductivity measurements (De Goer (1969))

feature is a result of the production of  $\text{Cr}^{2+}$  ions in the sample during  $\gamma$  irradiation.

Before continuing to analyse the results obtained in more detail it would be profitable to discuss the effect of variation of the fitting parameters used in the numerical analysis package. In order to perform the numerical differentiation required to calculate the thermal expansion, a  $\beta$ -cubic spline function least squares fit is performed upon the data (see Appendix 1) and the fitted function differentiated analytically. The resultant expansion coefficient values thus obtained will hence be a function of the exact fit used. To illustrate this point a number of trial function fits of varying success have been reproduced in figures 5.7, 5.8 and 5.9. In the analysis package the spline function fits are evaluated using an interactive graphics routine. This routine compares the experimental data with an optimised user defined  $\beta$ -cubic spline function. The experimental data is reproduced as a change in the separation of the dilatometer electrodes with temperature. The isothermal dotted lines reproduced in figures 5.7, 5.8 and 5.9 represent the position of the "knots" denoting the junction of the various components of the spline fit.

Fit 1 (figure 5.7) represents a "reasonable fit" to the data points produced by using six spline functions to define the fitting function. Fits 2 and 3 (figures 5.8 and 5.9) represent less than ideal fits using seven and five spline functions respectively to define the fit. The expansion coefficient resulting from the differentiation of the fitted functions is reproduced in figure 5.10, here again the expansion effects of the dilatometer and sample supports have been subtracted for clarity. From examination of figure 5.10 we conclude that although the effect of variation of fitting parameters is eminently noticeable the general structure of the evolved expansion coefficient data remains the same.

If we, as in the initial experiments, assume that 5% of the total  $\text{Cr}^{3+}$  concentration in the "bleached" state is converted to  $\text{Cr}^{2+}$  by  $\gamma$  irradiation; And if we use the value of  $3.78 \times 10^{-12} \text{Pa}^{-1}$  for the isothermal compressibility of  $\text{Al}_2\text{O}_3$  (Schauer (1965)); And use the calculated magnitude of the Schottky specific heat plotted in figure 5.2 (calculated from the theoretically derived energy levels of Bates (1978)) of  $2 \times 10^{-23} \text{J ion}^{-1} \text{K}^{-1}$ . If we further make the assumption that the distortion is spherically symmetric

so that the volume expansion coefficient,  $\beta$  is given simply by:

$$\beta = 3\alpha,$$

we may estimate the value for the "spin" Gruneisen parameter ( $\gamma_s$ ) to be  $\gamma_s \approx 50 \pm 15$

It should be noted that the measured peak in expansion coefficient (at  $T \sim 3.9\text{K}$ ) occurs at a different temperature to that predicted from a thermal average of the theoretically derived energy levels (at  $T \sim 2.6\text{K}$ ). This is not surprising however, as expression 2.49 (repeated below) shows us that the phenomena will occur at the same temperature only when the Gruneisen parameters,  $\gamma_i$ , for all the individual energy levels of the system, have the same value and sign.

$$\beta_s = \left( \frac{\gamma_s}{V R T^2} \right) \{ \langle E_i^2 \gamma_i \rangle - \langle E_i \rangle \langle E_i \gamma_i \rangle \}$$

The values of the Gruneisen parameters for  $\text{Cr}^{2+}$  may be estimated from expressions developed in chapter 2.

$$\gamma_i = - \left( \partial \ln E_i / \ln V \right)_T$$

The calculation of the individual Gruneisen parameters for each energy level can be split into two stages (C A Bates, private communications):

- (i) To calculate the energy level variation with varying tunnelling splitting.
- (ii) To calculate how the tunnelling splitting varies with crystal volume.

At present only the first part of this calculation has been completed (Bates, private communication) and tentative results are listed in Table 5.2



Table 5.2

Variation of level energy with tunnelling splitting for  $\text{Cr}^{2+}$  in Aluminium Oxide

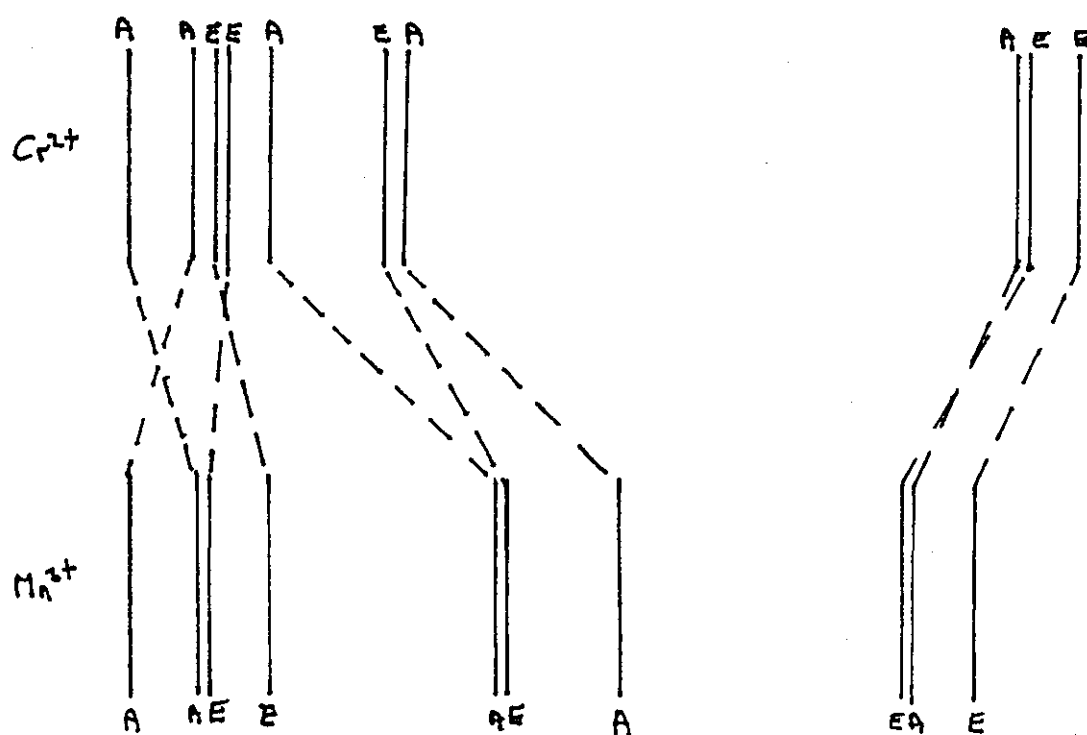
$$f_i = \frac{\Delta E_i}{\Delta (\text{tunnelling splitting})}$$

| Energy ( $\text{cm}^{-1}$ ) | State | $f_i$ |
|-----------------------------|-------|-------|
| 0                           | A(1)  | 1     |
| 4.177                       | A(2)  | -0.31 |
| 5.123                       | E(1)  | 0.39  |
| 6.687                       | E(2)  | 0.13  |
| 9.353                       | A(3)  | -0.14 |
| 17.696                      | E(3)  | -0.06 |
| 18.225                      | A(4)  | -0.07 |
| 29.251                      | E(4)  | +0.39 |
| 29.351                      | A(5)  | +0.39 |
| 32.343                      | E(5)  | +0.32 |

Table 5.3

Theoretically derived energy levels for  $3d^4$  ions ( $\text{Cr}^{2+}$  and  $\text{Mn}^{3+}$ )  
in  $\text{Al}_2\text{O}_3$  (from Bates and Wardlaw (1980))

| SYMMETRY LABEL |              | ENERGY LEVEL ( $\text{cm}^{-1}$ ) |                  |
|----------------|--------------|-----------------------------------|------------------|
| Oh             | $\text{C}_3$ | $\text{Cr}^{2+}$                  | $\text{Mn}^{3+}$ |
| $T_1$          | A            | 0                                 | 4.702            |
| $A_1$          | A            | 4.177                             | 0                |
| $E_1^1$        | $E_{\pm}$    | 5.123                             | 9.511            |
| $T_1$          | $E_{\pm}$    | 6.687                             | 5.312            |
| $T_2$          | A            | 9.353                             | 24.776           |
| $T_2$          | $E_{\pm}$    | 17.696                            | 24.538           |
| $A_2$          | A            | 18.225                            | 32.822           |
| $T_1^u$        | A            | 29.351                            | 50.74            |
| $T_1^u$        | $E_{\pm}$    | 29.251                            | 50.926           |
| $E^u$          | $E_{\pm}$    | 32.342                            | 54.667           |



The result of substituting these values into equation 2.49 is presented in figure 5.11. By comparing this figure with the experimentally determined values in figure 5.6 we observe certain similarities. Both figures exhibit sharply peaked "positive" features with negative "side wings", although there is some difference in temperature of the position of the peak.

In summary, a number of observations of the low temperature thermal expansion of  $\text{Al}_2\text{O}_3:\text{Cr}$  have been performed. Sharp peaked positive features have appeared when the sample crystal had received a saturation dose of  $\gamma$ -irradiation prior to measurement. These features were not present when the sample had undergone an ultra violet irradiation treatment at 365nm. It is suggested that these anomalies are produced by the presence of  $\text{Cr}^{2+}$  ions in the sample produced from the  $\text{Cr}^{3+}$  substitutional ions by  $\gamma$ -irradiation. The measured Gruneisen parameter associated with this strongly coupled ion is not consistent with a static field model of the crystal environment but may be consistent with a strong dynamic Jahn-Teller model with tunnelling splitting. A more complete evaluation of the phenomena is lacking a detailed theoretical calculation of the Gruneisen parameters for the individual energy levels of the  $\text{Al}_2\text{O}_3:\text{Cr}^{2+}$  system which is promised in the future (Sheard, private communication).

#### 5.4 THE THERMAL EXPANSION OF $\text{Al}_2\text{O}_3:\text{Mn}$

In conjunction with the measurements discussed in the previous sections a series of experiments were performed to determine the thermal expansion of aluminium oxide doped with manganese. Being substitutional impurities, the dominant valence state of manganese and chromium in the  $\text{Al}_2\text{O}_3$  lattice is +3. The majority of the manganese atoms are hence expected to be  $\text{Mn}^{3+}$  ions.

The  $\text{Mn}^{3+}$  and  $\text{Cr}^{2+}$  are isoelectronic so it is expected that the  $\text{Mn}^{3+}$  ions will also experience a strong Jahn-Teller effect with tunnelling splitting (eg Bates and Wardlaw (1980)). We would hence expect aluminium oxide crystals doped with manganese to exhibit positive Schottky type anomalies in thermal expansion as have been observed with  $\gamma$  irradiated chromium doped crystals. The essential difference is that the manganese doped crystals are expected to exhibit these anomalies without requiring any prior radiation treatment.

The manganese doped sample used in these experiments was again cylindrical in form with dimension very similar to those of the pure reference samples (see table 5.1). The sample (Ref. No. J1) has been used in many studies of the  $\text{Al}_2\text{O}_3:\text{Mn}$  system using other techniques (for example Zoller et al (1980)) and was loaned from the Service Basses Températures of the Centre D'études Nucleaires in Grenoble.

Low temperature thermal expansion experiments were performed upon this sample using the " $\text{Al}_2\text{O}_3$  cell" dilatometer described in chapter 3 (section 3.5). A series of experimental observations were performed over a period of several days and the results are summarised for many different experiments in the following figures.

The thermal expansion of the manganese doped crystal in the "as received" condition is shown in figure 5.12. In this figure, as before, dilatometer and support effects have been subtracted for clarity. Again positive peaked anomalies with negative "side wings" are observed in thermal expansion with a peak at  $\sim 4\text{K}$ .

It is again beneficial to observe the effect of variation of the fitting parameters used in the numerical analysis package upon the apparent expansion measurements. Figures 5.13, 5.14 and 5.15 represent three trial fits to the same data set using 5, 6 and 6 cubic spline functions respectively to define the fit. The result of differentiation

of these fitted functions are summarised in figure 5.16. Due to the smaller magnitude of the observed effects compared with those obtained with the chromium doped samples, we would expect, and do observe, that there is more uncertainty in ascertaining the actual behaviour of the sample. The three trial fits do, however, exhibit peaks of similar heights and position at 4K.

We may again estimate the value of the Gruneisen parameter for the  $\text{Mn}^{3+}$  ion. Assuming that the total concentration of manganese ions in the sample exist in the  $\text{Mn}^{3+}$  valence state.

Using the value  $1.7 \times 10^{-23} \text{ J ion}^{-1} \text{ K}^{-1}$  for the peak of the Schottky contribution to specific heat (see figure 5.17) calculated from the theoretically derived energy levels of Bates and Wardlaw (1980), we calculate the value  $\gamma_s = 130 \pm 50$  for the Gruneisen parameter of the  $\text{Mn}^{3+}$  ion.

Some effect upon the thermal conductivity of  $\text{Al}_2\text{O}_3:\text{Mn}$  has been reported when samples had received an "Oxidising" heat treatment (eg De Goeer (1969), Zoller et al (1980)). A reduction in the thermal conductivity was reported which has been interpreted in terms of an increase in the  $\text{Mn}^{3+}$  concentration produced by heat treatment in air. In order to investigate the effect upon the low temperature thermal expansion of manganese doped  $\text{Al}_2\text{O}_3$  after an "oxidising" treatment a series of experiments were performed upon sample J1 following heat treatment in air at  $1700^\circ\text{C}$  for 8 hours. The results of these experiments are summarised in figure 5.19. In figure 5.18 the dilatometer capacitance (relative to some convenient base level) is plotted for the manganese doped sample prior to, and following, heat treatment ( $1\text{aF} = 10^{-6} \text{ pF}$ ). The experiments were again performed in the " $\text{Al}_2\text{O}_3$  cell" dilatometer described in section 3.5. Figure 5.19 exhibits the result of analysis of the  $\text{Al}_2\text{O}_3:\text{Mn}$  data before and after "oxidising" treatment to provide the expansion coefficient of the samples relative to that of the "pure" samples (LUT1, LUT2, and LUT3). The effect of variation of numerical fitting parameters is again plotted in figures 5.20 to 5.23.

If we take the peak in the thermal expansion coefficient for the "after treatment" condition and assume that the total manganese population again exists in the  $\text{Mn}^{3+}$  valence state. The apparent

3

Gruneisen parameter for the  $\text{Mn}^{3+}$  ion after heat treatment is reduced to  $\gamma_s = 83 \pm 40$ . Figure 5.19 also suggests that the thermal position of the peak in thermal expansion changes when the sample undergoes this "oxidising treatment". Some significant variation is also observed in the "negative side wings" present in the "as received" condition.

In summary we again observe the presence of positive anomalies in the low temperature thermal expansion of aluminium oxide doped with manganese which are not present in the expansion of the pure crystal. These anomalies are present in the thermal expansion of the crystal both in the "as received" condition, and after receiving an "oxidising treatment". Marked changes have been observed to occur when the sample received this oxidising treatment which may not be simply interpreted in terms of an increase in concentration of the  $\text{Mn}^{3+}$  ions and the mechanism is not understood. There are distinct similarities between the anomalies observed with the  $\text{Al}_2\text{O}_3:\text{Mn}$  in the "as received" condition and the  $\gamma$  irradiated  $\text{Al}_2\text{O}_3:\text{Cr}$  case. Both crystals exhibit positive, sharply peaked anomalies with negative "side wings". An analysis of the effect of variation of tunnelling splitting upon the energy structure is not available but is promised for the future (Bates, private communication).

Again, the large positive values for the "spin" Gruneisen parameter ( $\gamma_s \approx 100$ ) are not consistent with a static crystal field model of the lattice environment. They provide more support for the existence of a strong Jahn-Teller effect with tunnelling splitting for  $3d^4$  ions within a  $C_{3v}$  environment.

## 5.5 THE THERMAL EXPANSION OF $\text{Al}_{2-3}\text{O}_3:\text{V}$

As an example of a non- $3d^4$  type ion which has been observed using low temperature thermal expansion measurement, a series of experiments were performed to attempt to detect the presence of  $\text{V}^{3+}$  ions ( $3d^2$ ) in crystals of aluminium oxide doped with vanadium impurity. The theoretically derived energy level structure for the ground state of  $\text{V}^{3+}$  in  $\text{Al}_2\text{O}_3$  is given in figure 5.24, (Villedieu et al (1977)). If we consider only the thermal average of the lowest two levels ( $3A_2$  and  $3E$ ,  $D = 8.296\text{cm}^{-1}$  (Abou-Ghantous and Bates) and calculate the expected Schottky contribution to specific heat we arrive at figure 5.25. Since we only expect these lowest two levels to contribute significantly to the Schottky specific heat at low temperatures we would expect to observe an anomaly in thermal expansion at  $T \approx 5\text{K}$ .

A series of thermal expansion measurements were made upon an aluminium oxide sample (No.2A, 800ppm total vanadium concentration, see table 3.1) relative to the three "pure" reference samples LUT1, LUT2, and LUT3. The measured expansion coefficient of this sample is shown in figure 5.27. Here again the effects of electrode expansion and mounting effects have been subtracted for clarity.

We see in this figure that a negative thermal expansion anomaly is observed at approximately 3.8K (in contrast with the positive anomaly observed with the manganese and Chromium doped samples). Considering the vanadium ions to be substitutional impurities and assuming that 100% of the vanadium concentration exists in the 3+ valence state. And taking the peak value of the calculated Schottky specific heat ( $10.5 \times 10^{-24} \text{ JK}^{-1} \text{ ion}^{-1}$  at 4.5K) we may estimate the Gruneisen parameter,  $\gamma_s$ , associated with the  $\text{V}^{3+}$  ion to be:

$$\gamma_s = -6 \pm 3$$

If we compare this result with that to be expected considering a static crystal field model ( $\gamma_s = \frac{2}{3}$ ). We see that the observed anomaly would appear to be inconsistent with static crystal field model. Given the limited sensitivity, of the apparatus relative to the small magnitude of the anomaly it is difficult to discriminate positively against the static crystal field model in favour of a weak Jahn-Teller effect.

## 5.6 SUMMARY

A sensitive three terminal capacitance dilatometer for the low temperature measurement of thermal expansion has been designed, constructed, and commissioned. A dynamic measurement technique has been developed to allow semi-automatic measurements to be taken using a digital 'mini' computer for data acquisition. Ergonomic computer software has also been developed to allow rapid assimilation of experimental data into easily recognisable form.

The capacitance dilatometer utilised "pure" aluminium oxide ( $\text{Al}_2\text{O}_3$ ) as a reference material. The apparatus was used to investigate the contribution to the thermal expansion of aluminium oxide at low temperatures produced by small concentrations of paramagnetic impurity ions.

Results have been presented demonstrating the detection of  $\text{Cr}^{2+}$  ( $3d^4$ , 5D),  $\text{Mn}^{3+}$  ( $3d^4$ , 5D) and  $\text{V}^{3+}$  ( $3d^2$ , 3F) in crystals of aluminium oxide doped with chromium, manganese and vanadium impurities respectively. In these cases sharply peaked features are observed in the low temperature thermal expansion of aluminium oxide which are not present for the pure material. In the case of  $\text{Al}_2\text{O}_3:\text{Cr}$  it has proven possible to "turn" the feature on and off when  $\gamma$ -irradiation and ultra-violet treatment at 365nm precede measurement. This suggests that the feature in the thermal expansion of  $\text{Al}_2\text{O}_3:\text{Cr}$  is caused by the  $\text{Cr}^{2+}$  ions produced by  $\gamma$ -irradiation of the substitutional  $\text{Cr}^{3+}$  ions.

When the thermal expansion of  $\text{Al}_2\text{O}_3:\text{Mn}$  and  $\gamma$ -irradiated  $\text{Al}_2\text{O}_3:\text{Cr}$  is measured at low temperatures sharply peaked positive anomalies are observed that are not present in the thermal expansion of the pure crystal. The measured "spin" Gruneisen parameter associated with the  $\text{Cr}^{2+}$  and  $\text{Mn}^{3+}$  ions has been estimated to be  $\gamma_s \approx +100$ . This figure contrasts the value  $\gamma_s = -\frac{5}{3}$  calculated on the basis of a static field model of the crystal environment (assuming a cubic site symmetry for the ion). The value of  $\gamma_s$  has been estimated for  $\text{MgO}:\text{Cr}$  using a crystal model incorporating a strong dynamic Jahn-Teller effect with tunnelling splitting and the result found to be  $\gamma_s \approx +50$ . The approximate 'profile' of the thermal expansion contribution of  $\text{Cr}^{2+}$  has been estimated using a multi-mode model.



The general form of this (sharp positive peak with negative "side wings") compares very favourably with that observed with the  $\gamma$  irradiated  $\text{Al}_2\text{O}_3:\text{Cr}$  and "as received"  $\text{Al}_2\text{O}_3:\text{Mn}$  crystals. The experimental evidence hence appears to provide support for the presence of a strong Jahn-Teller effect with tunnelling splitting for the  $3d^4$  ions in  $\text{Al}_2\text{O}_3$  though a definitive result lacks a detailed theoretical analysis.

A series of measurements has also been performed to determine the effect upon the thermal expansion of the  $\text{Al}_2\text{O}_3:\text{Mn}$  of an "oxidising" heat treatment in air. A reduction in peak height and change in "profile" of the anomaly have been observed. Similar experiments involving the effect upon the low temperature thermal conductivity of such a heat treatment have been interpreted in terms of an increase in population of the  $\text{Mn}^{3+}$  ions in the sample. The thermal expansion effects observed may not be simply interpreted in terms of an increase in  $\text{Mn}^{3+}$  concentration and the mechanism for this is at present unknown.

The low temperature thermal expansion of  $\text{Al}_2\text{O}_3:\text{V}$  has also been measured. In this case a small negative anomaly has been observed which also is not present in the thermal expansion of the pure crystal. If we assume that this effect is produced by the  $\text{V}^{3+}$  ion and further assume that all of the vanadium impurity in the sample exists as the  $\text{V}^{3+}$  ion a value for the spin Gruneisen parameter of  $\gamma_s \sim -6 \pm 3$  is obtained. Unfortunately, given the small magnitude of the anomaly and limited sensitivity of the apparatus it is very difficult to positively distinguish between a static field model and the presence of a weak Jahn-Teller effect.

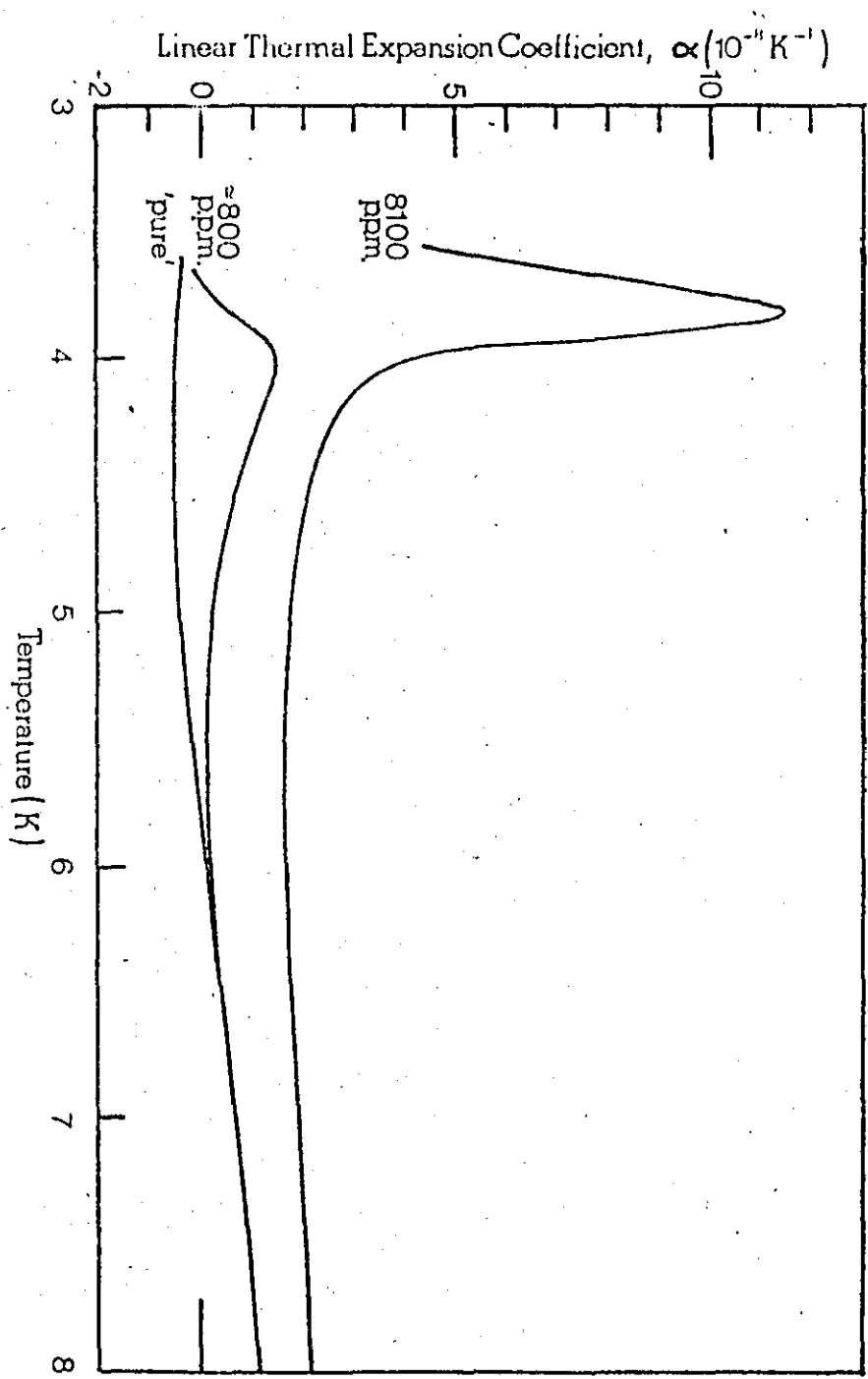


FIG. 5.1 Preliminary Measurement of the Thermal Expansion of  $\gamma$ -Irradiated Ruby( $\text{Al}_2\text{O}_3:\text{Cr}$ ).

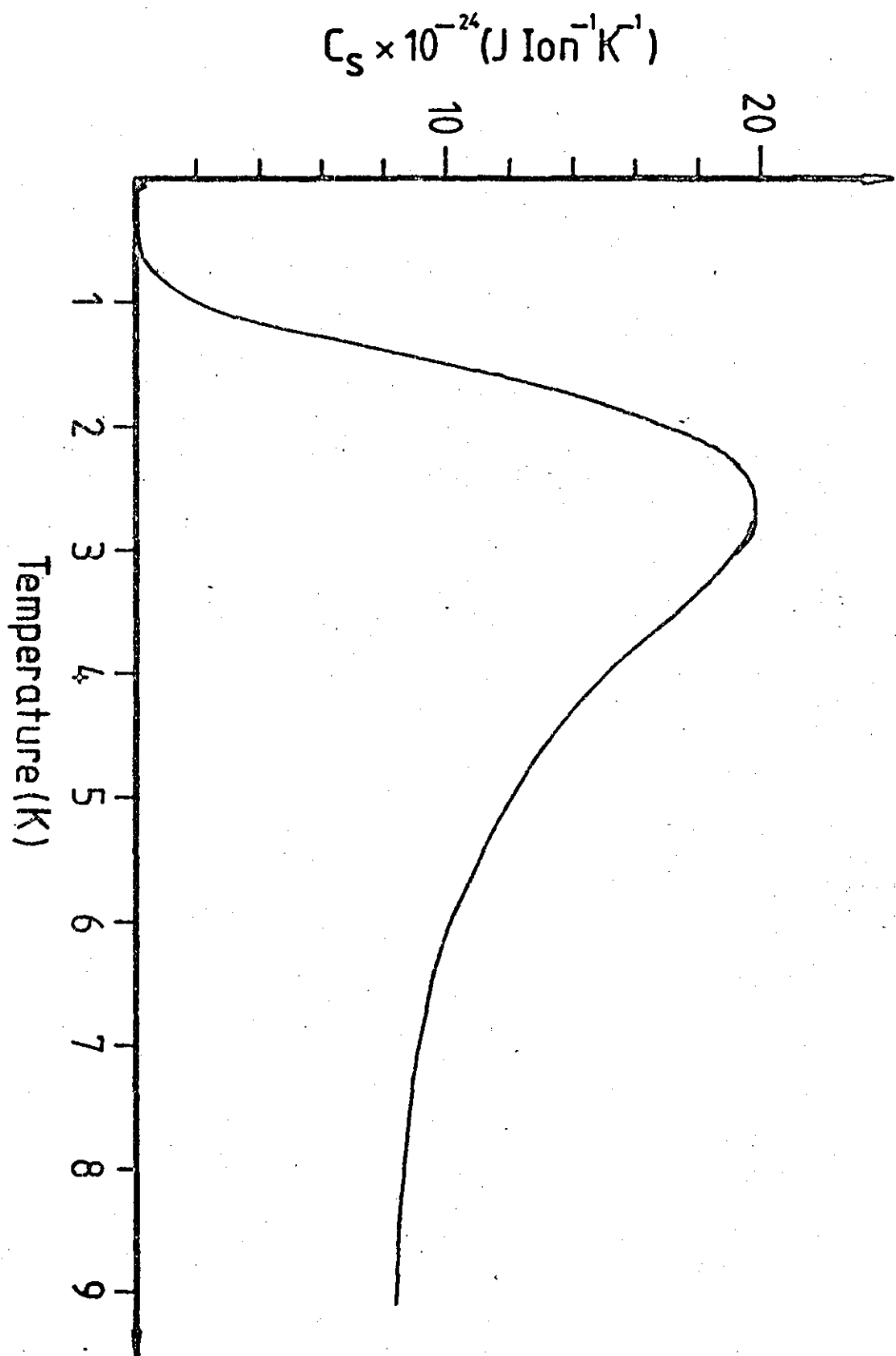


FIG. 5.2 Schottky contribution to the specific heat for  $\text{Cr}^{2+}(3d^4)$  in  $\text{Al}_2\text{O}_3$ .

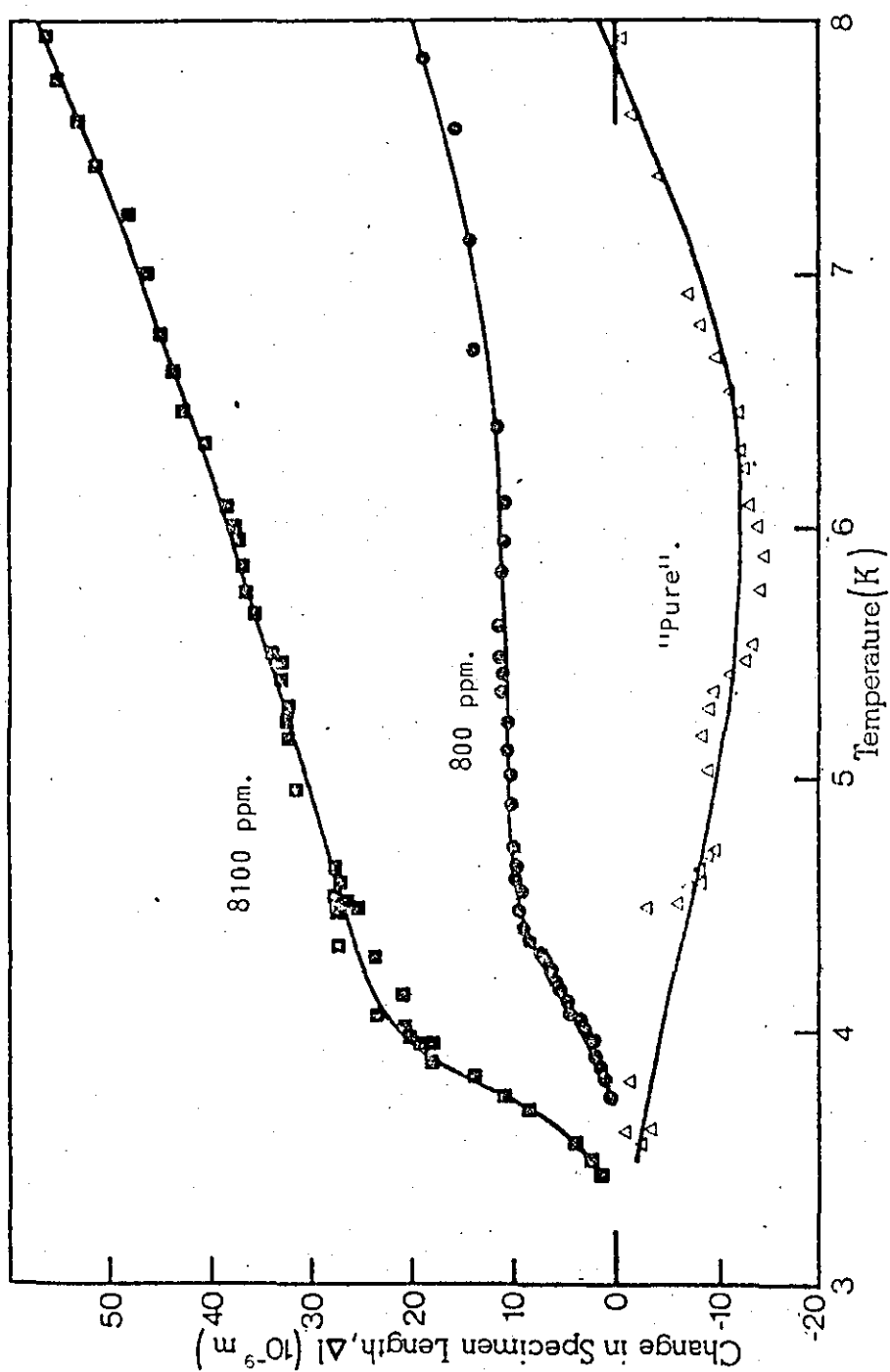


FIG. 5.3 Results of Initial Experiments upon the Thermal Expansion of  $\gamma$ -Irradiated Ruby (specimen length plot).

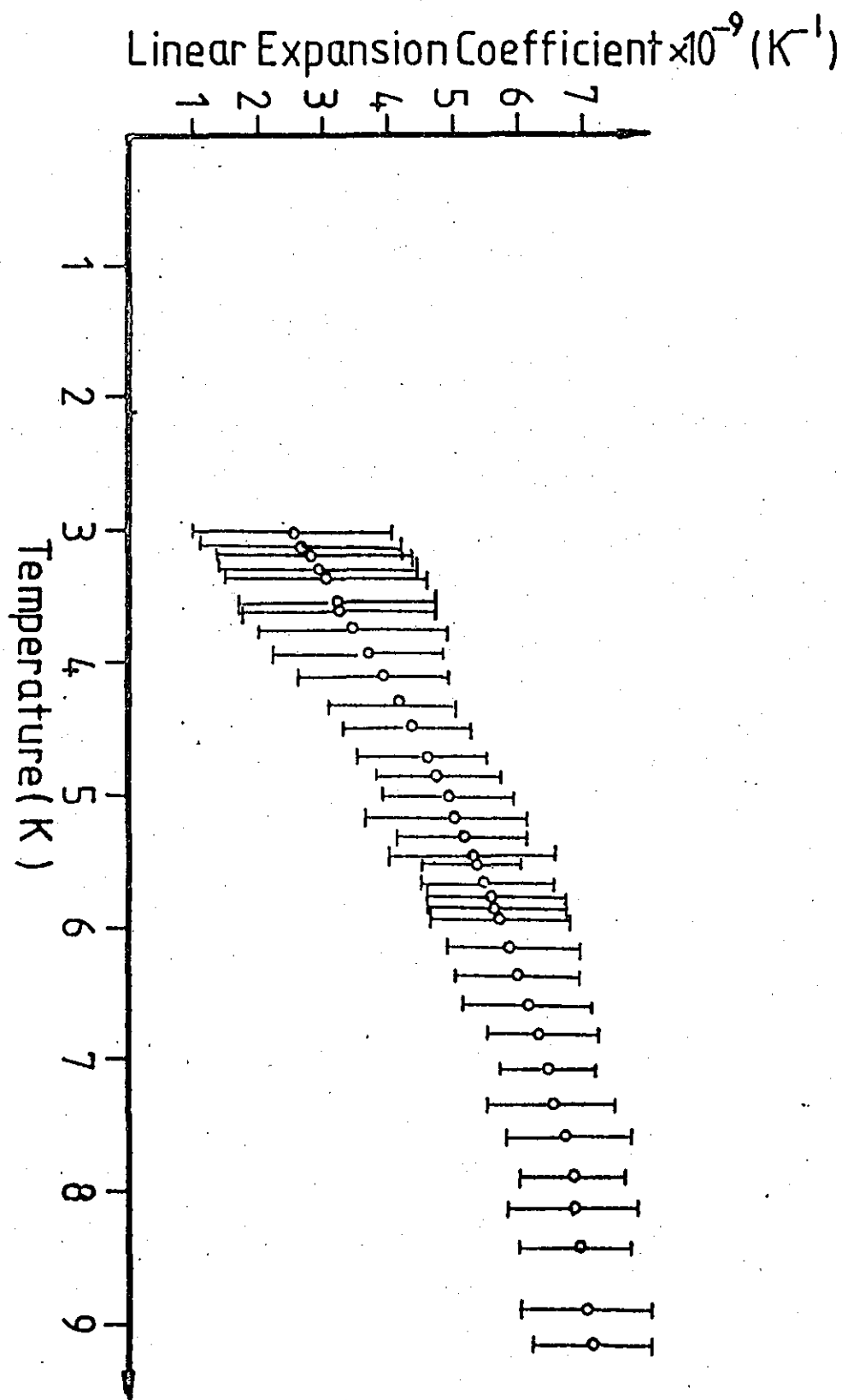


FIG. 5.4

Results of calibration experiment. Apparent Expansion coefficient of Pure  $\text{Al}_2\text{O}_3$  (Sample LUT4), measured relative to pure  $\text{Al}_2\text{O}_3$  (Samples LUT1, LUT2, LUT3) reference material.

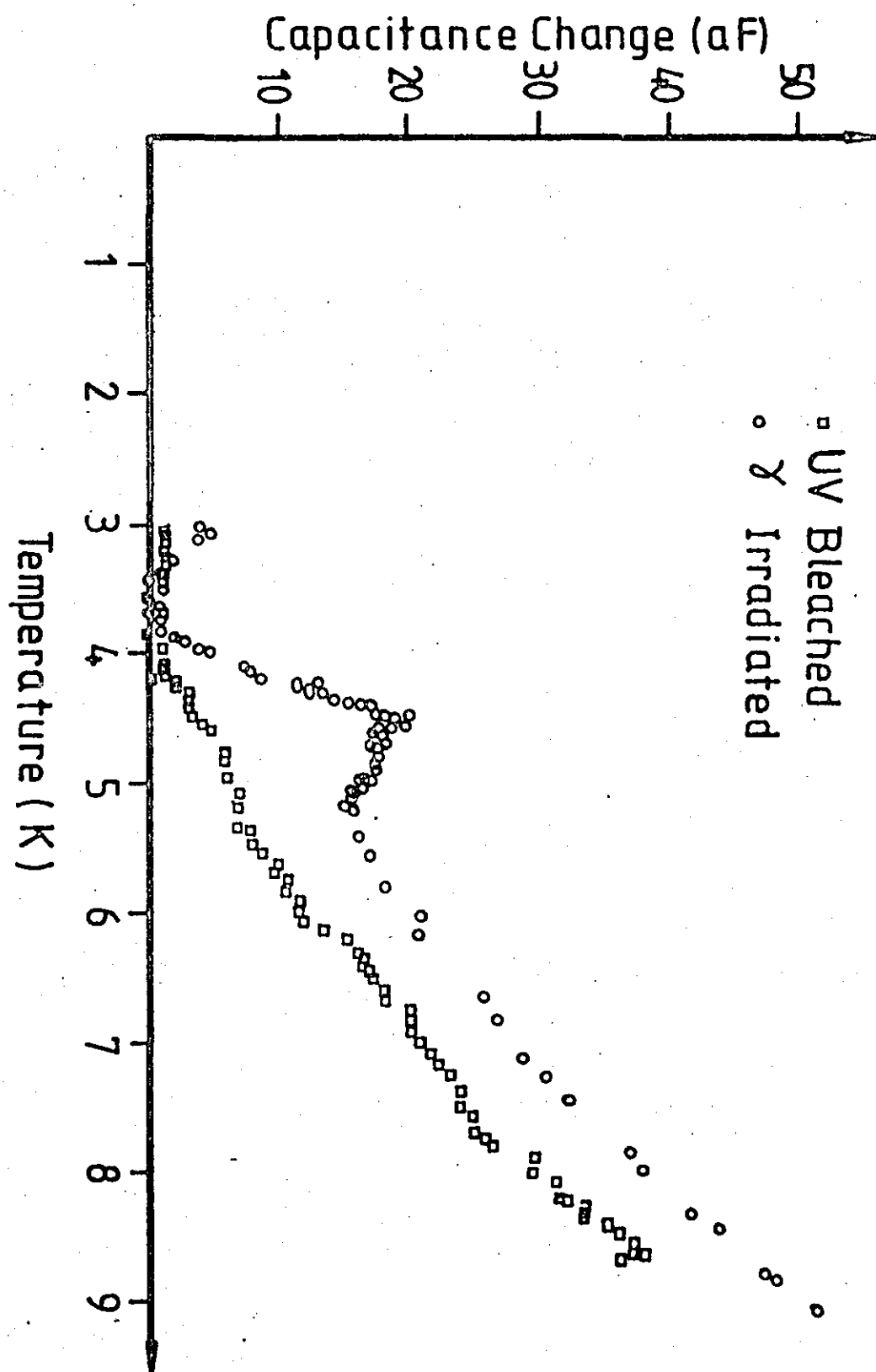


FIG. 5.5

Typical Capacitance change with Temperature of a Dilatometer containing an  $\text{Al}_2\text{O}_3$ : Cr (8100ppm) Sample.

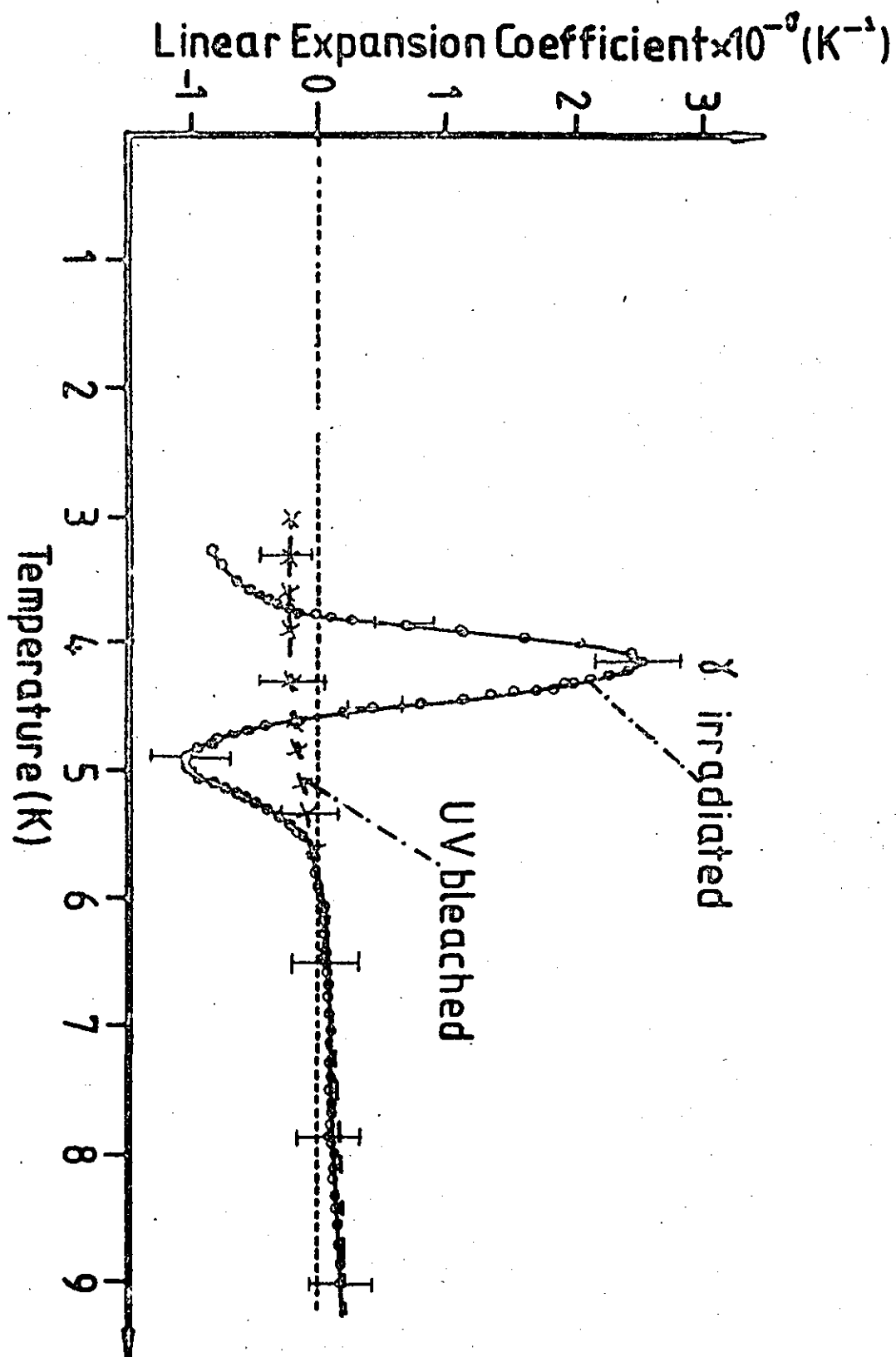


FIG. 5.6 Thermal expansion of  $\text{Al}_2\text{O}_3^{\gamma}(8100 \text{ ppm})$  relative to that of 'pure'  $\text{Al}_2\text{O}_3$ .

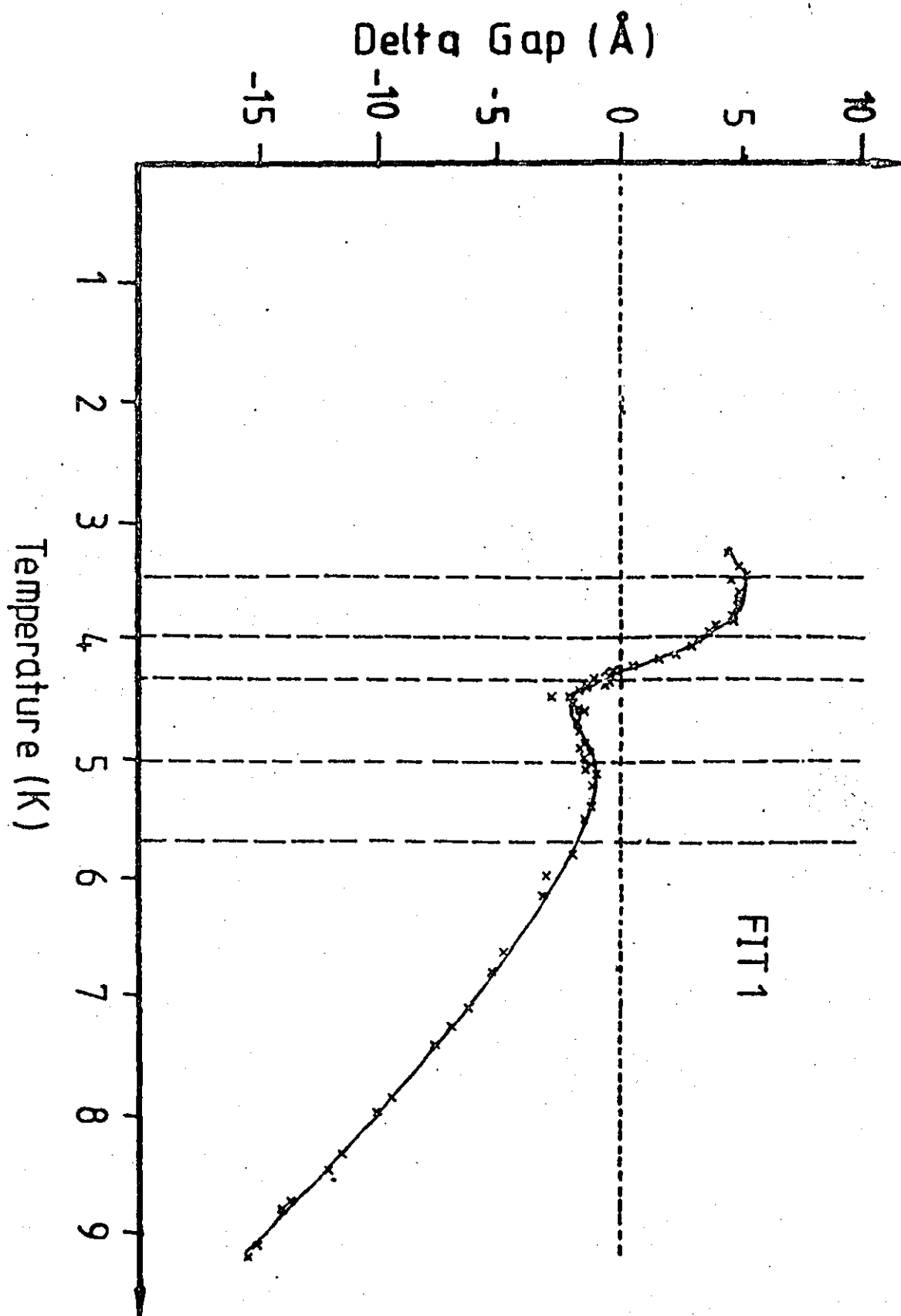


FIG. 5.7 Change of dilatometer electrode separation with temperature for  $\text{Al}_2\text{O}_3\text{:Cr}$  (8100 ppm,  $\gamma$ -irradiated). Effect of variation of spline fitting parameters, 1st Fit.



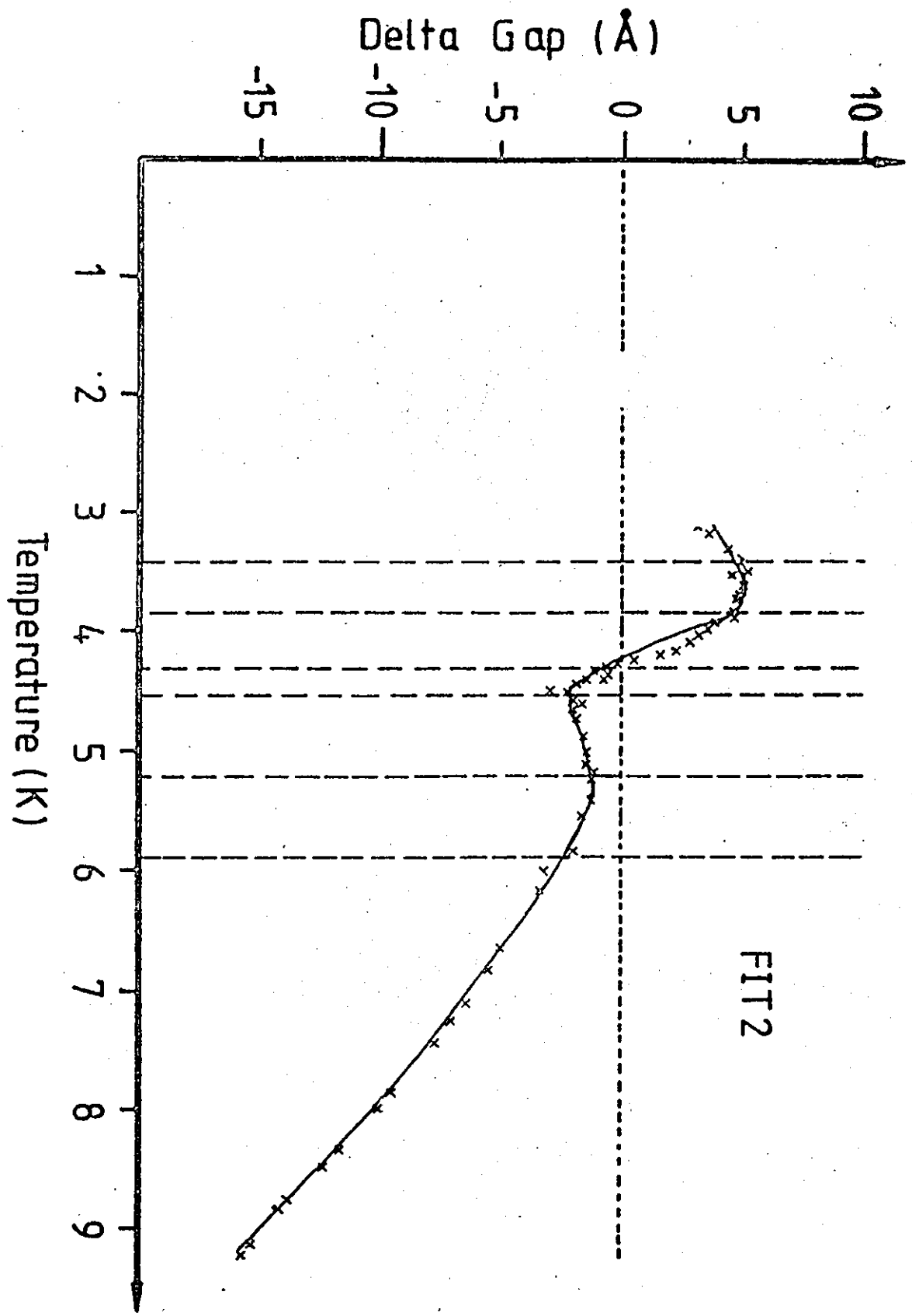


FIG. 5.8 Change of dilatometer electrode separation with temperature for  $\text{Al}_2\text{O}_3:\text{Cr}$  (8100 ppm,  $\gamma$ -irradiated). Effect of variation of spline fitting parameters, 2nd Fit.

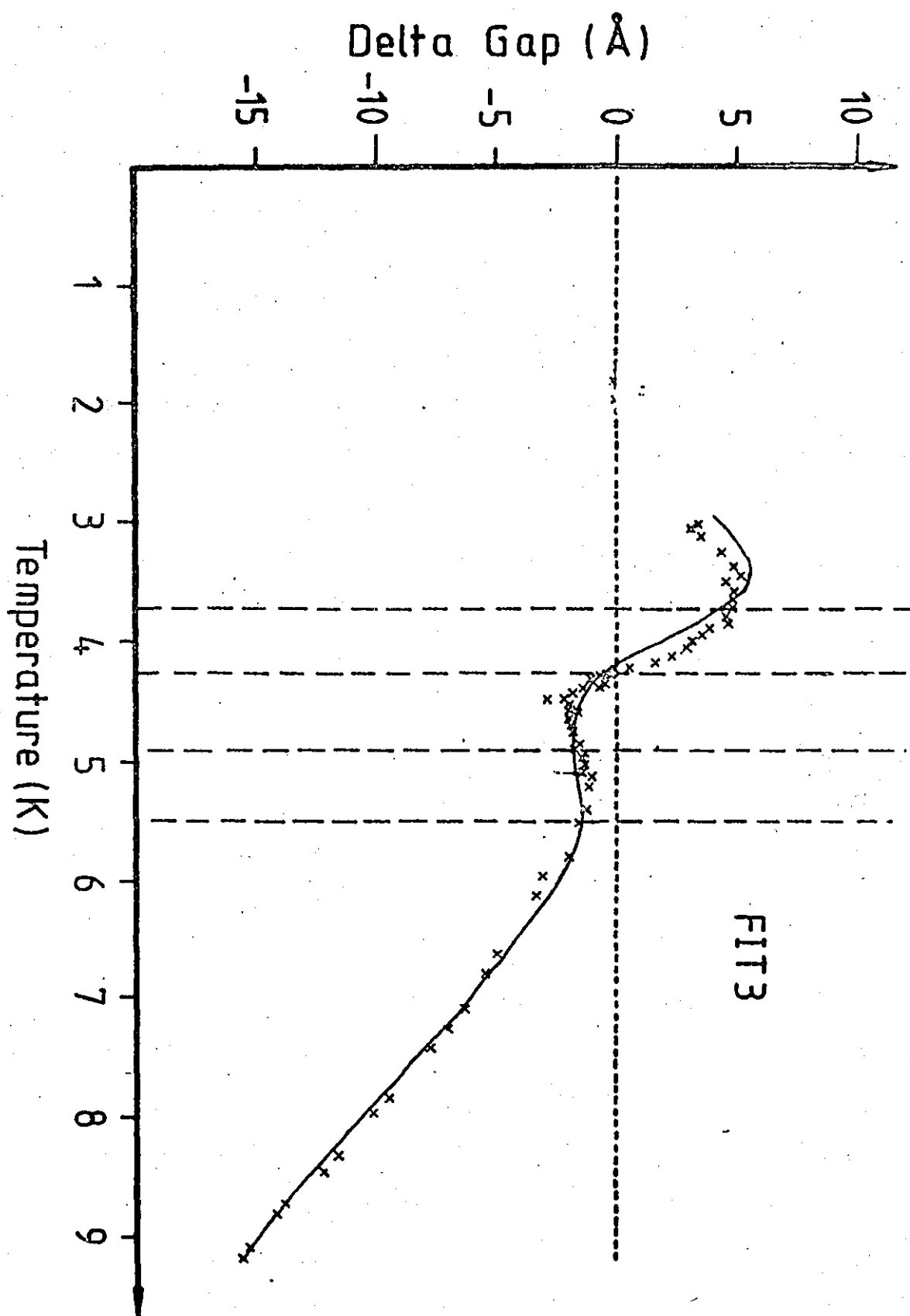


FIG. 5.9

Change of dilatometer electrode separation with temperature for  $\text{Al}_2\text{O}_3:\text{Cr}$  (8100 ppm,  $\gamma$ -irradiated). Effect of variation of spline fitting parameters, 3rd Fit.

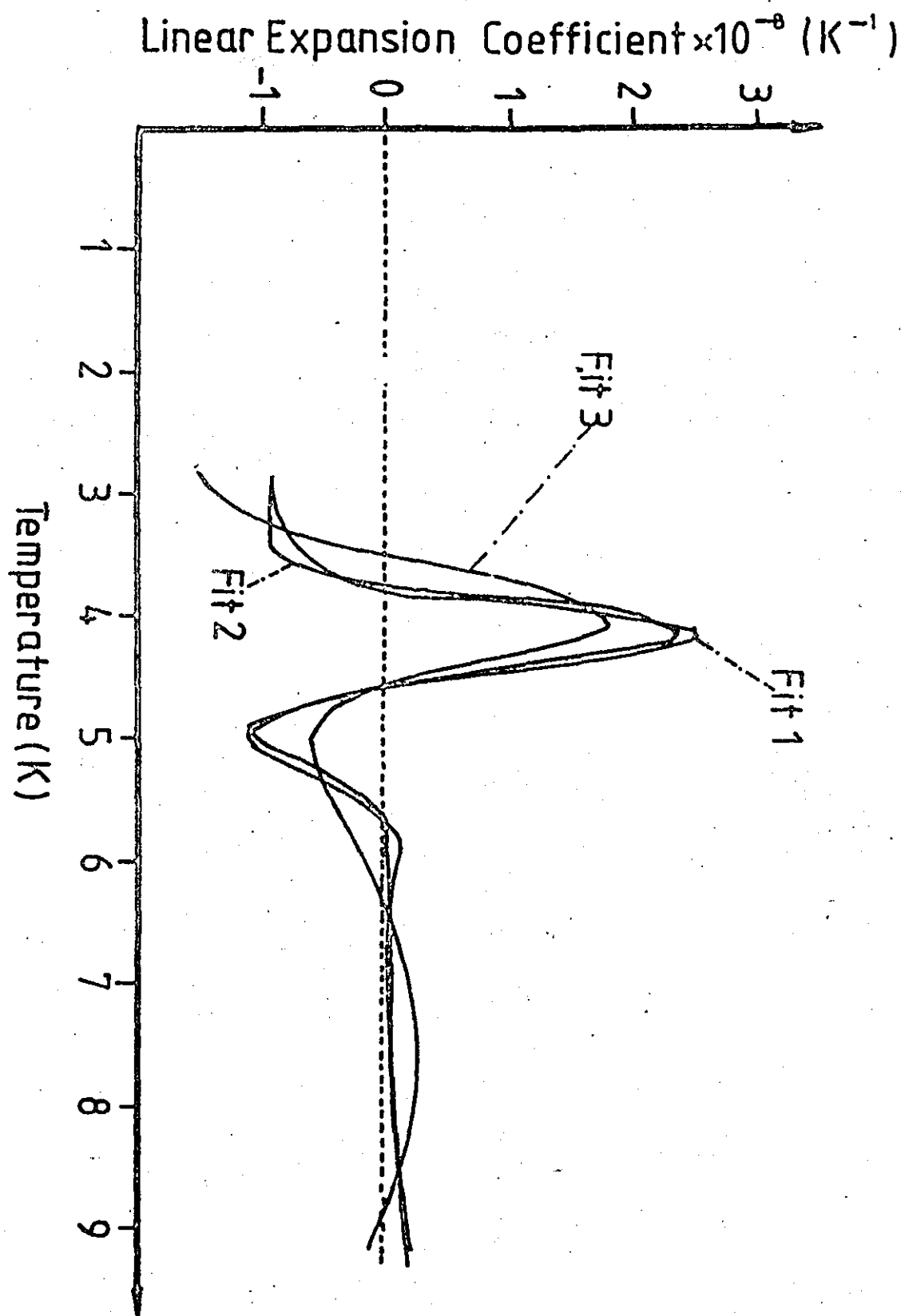


FIG. 5.10

Thermal expansion of  $\gamma$ -irradiated  $\text{Al}_2\text{O}_3\text{:Cr}$  (8100 ppm) relative to that of pure  $\text{Al}_2\text{O}_3$ . Effect of variation of spline fitting parameters for a single data set.

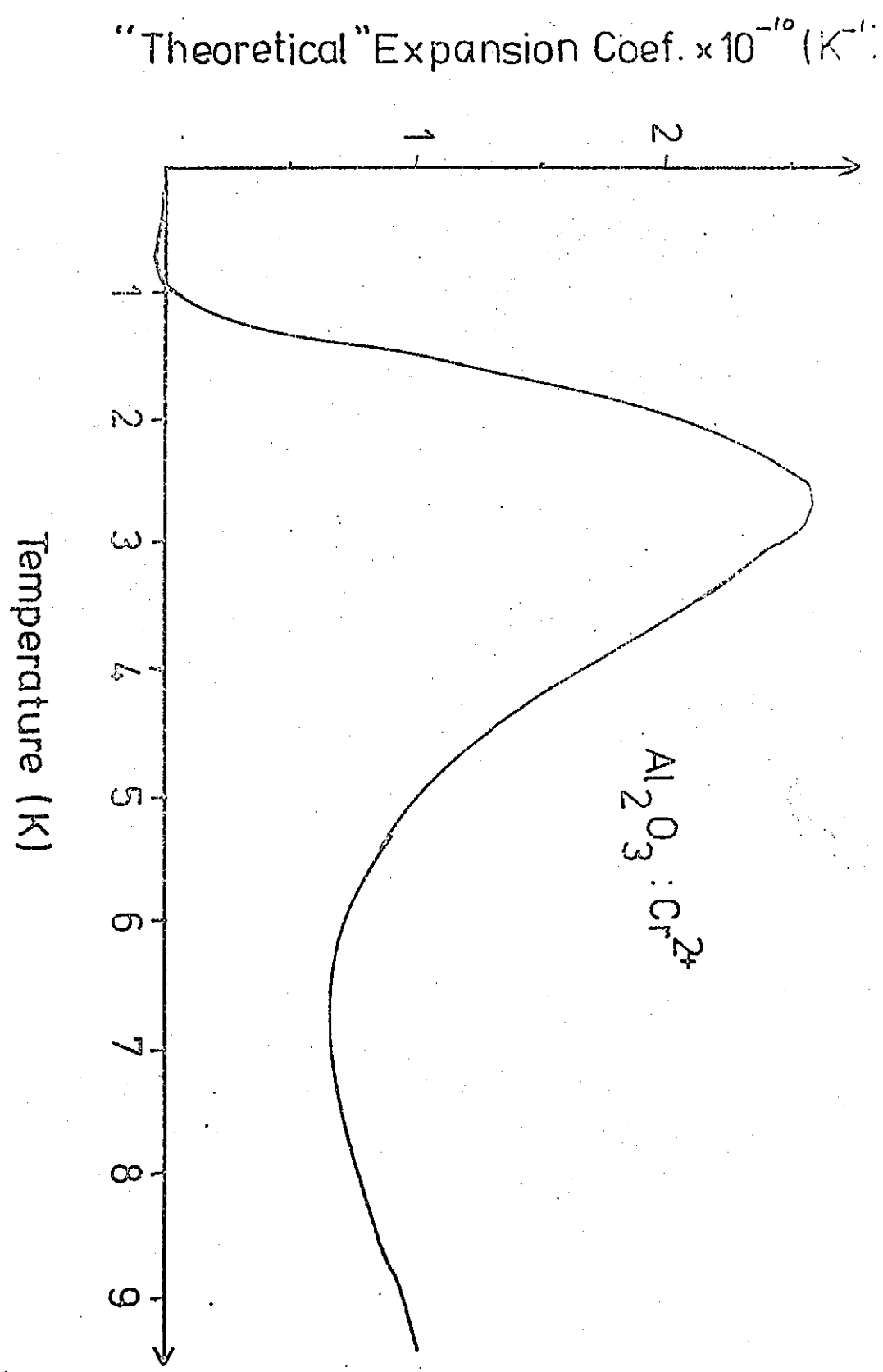


FIG 5.11 "Theoretical" Calculation of the Schottky Thermal Expansion Coefficient for  $Al_2O_3:Cr$  (based on the calculations of Bates(private communications)).

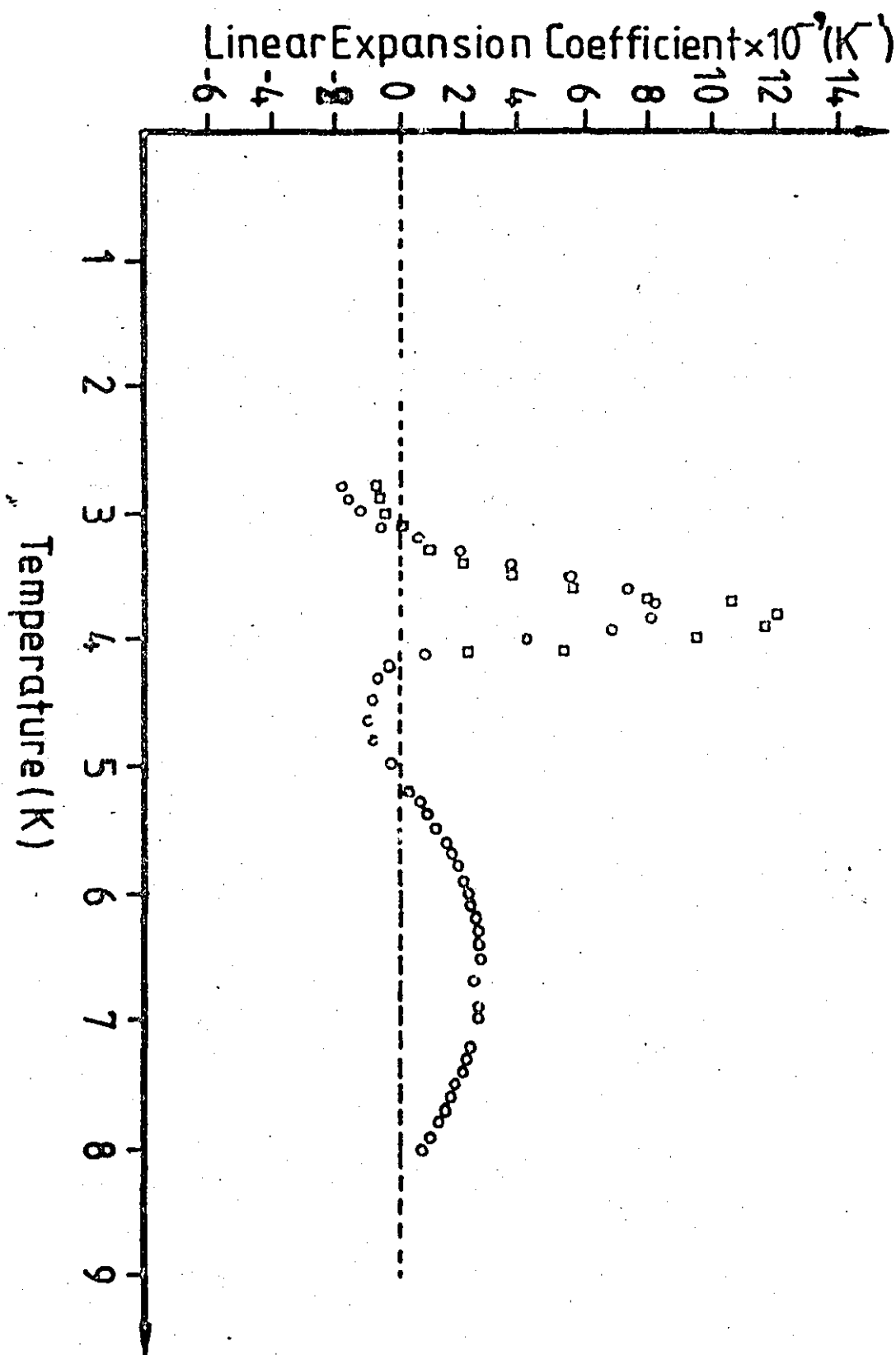


FIG. 5.12 Thermal Expansion of  $Al_2O_3:Mn$  (Sample J1) Relative to that of Pure  $Al_2O_3$ . Two Separate Measurements Upon the Same Sample.

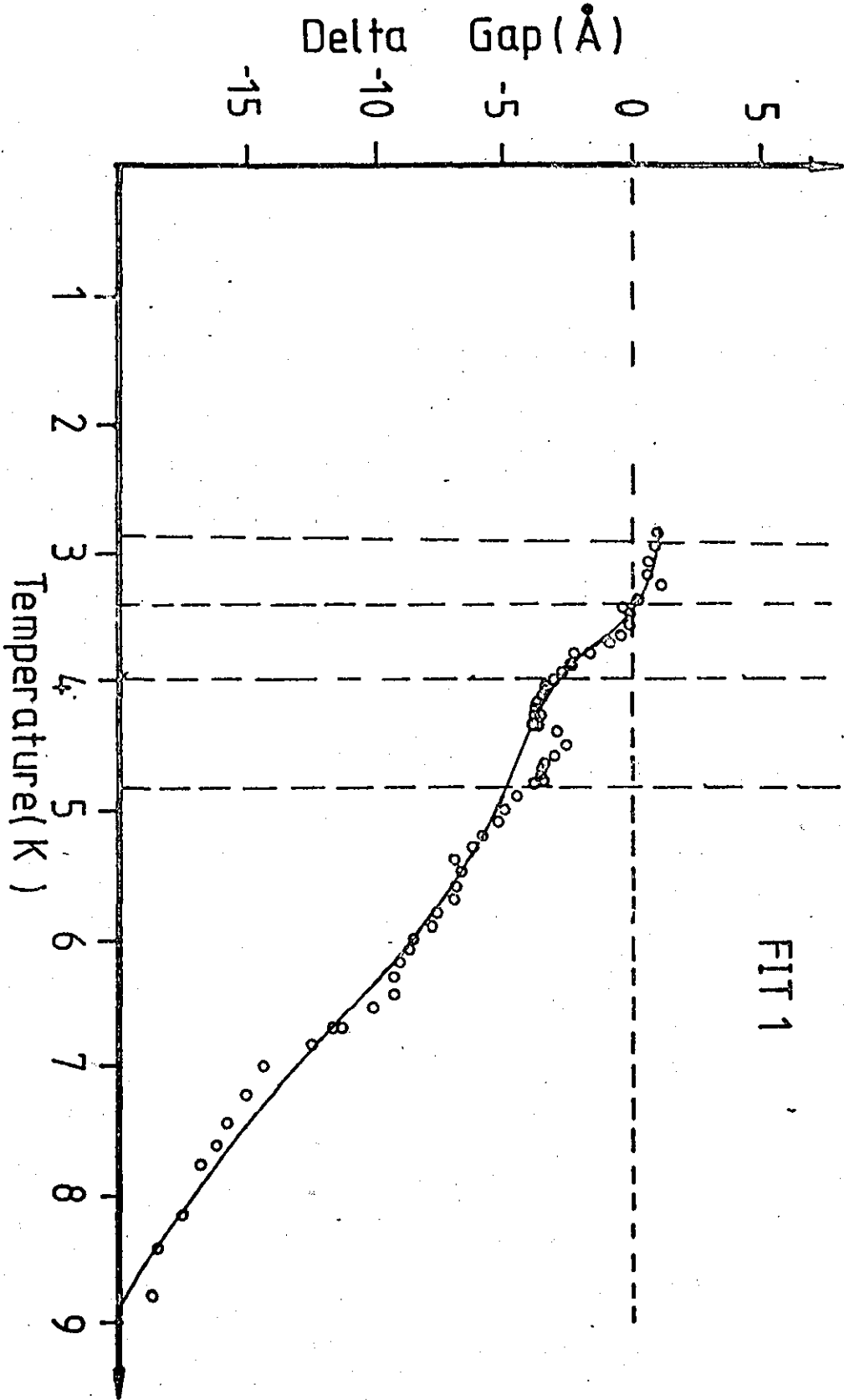


FIG. 5.13

Change of dilatometer electrode separation with temperature for  $\text{Al}_2\text{O}_3$ : Mn (Sample J1). Effect of variation of spline fitting parameters, 1st Fit

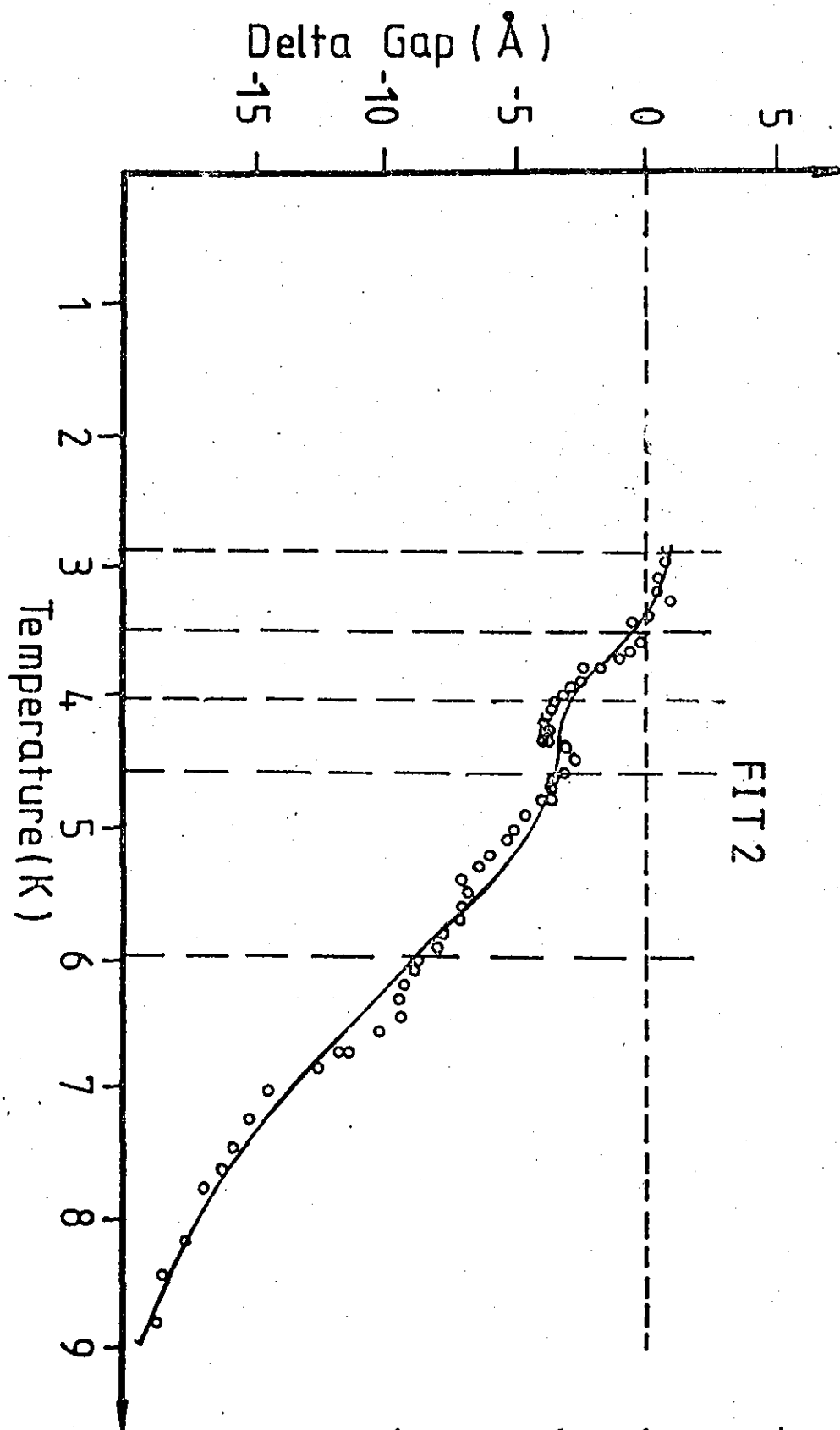


FIG. 5.14

Change of dilatometer electrode separation with temperature for  $\text{Al}_2\text{O}_3:\text{Mn}$  (Sample J1). Effect of variation of spline fitting parameters, 2nd fit

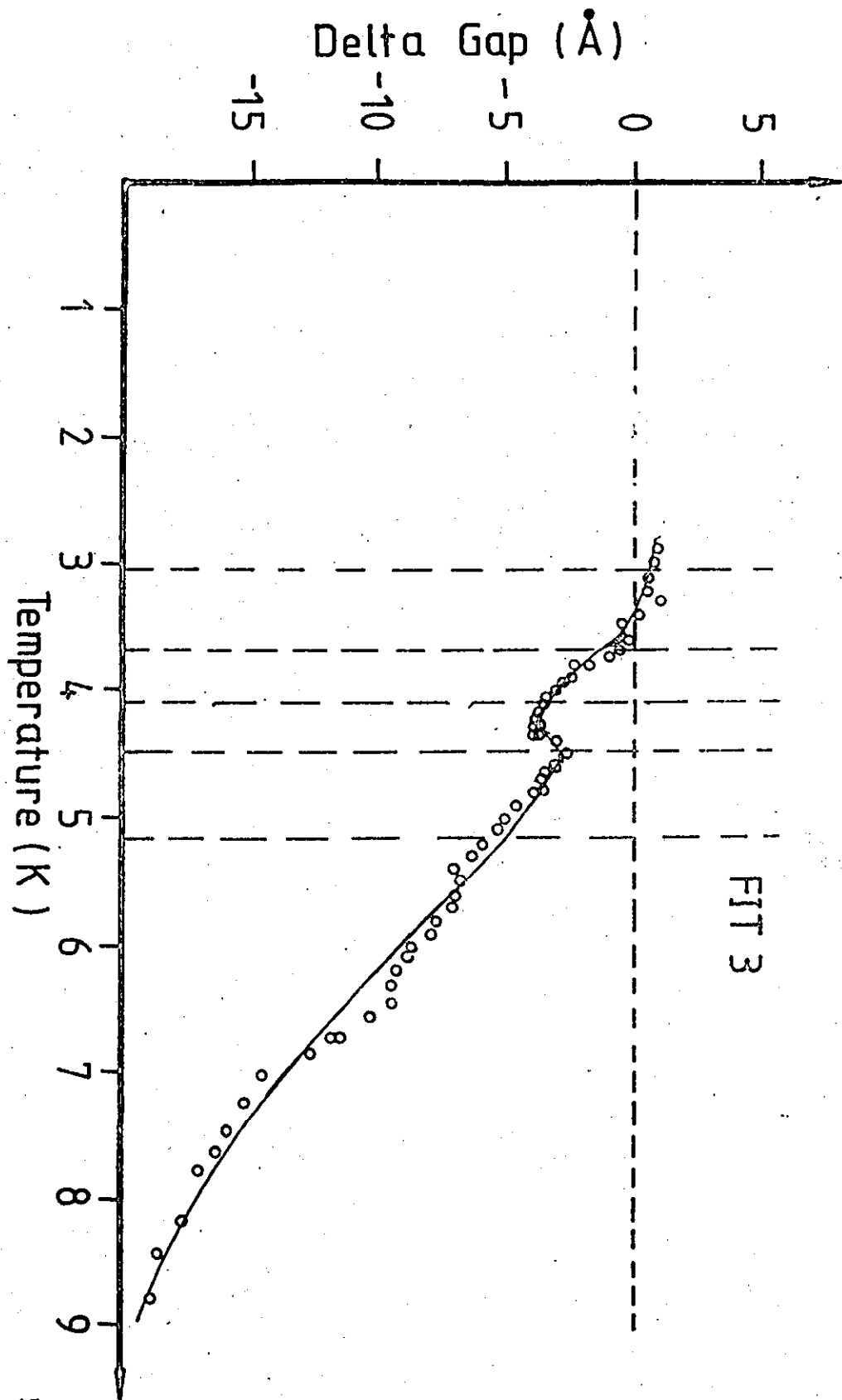


FIG. 5.15

Change of Dilatometer electrode separation with temperature for  $\text{Al}_2\text{O}_3:\text{Mn}$  (Sample J1). Effect of variation of spline fitting Parameters, 3rd Fit



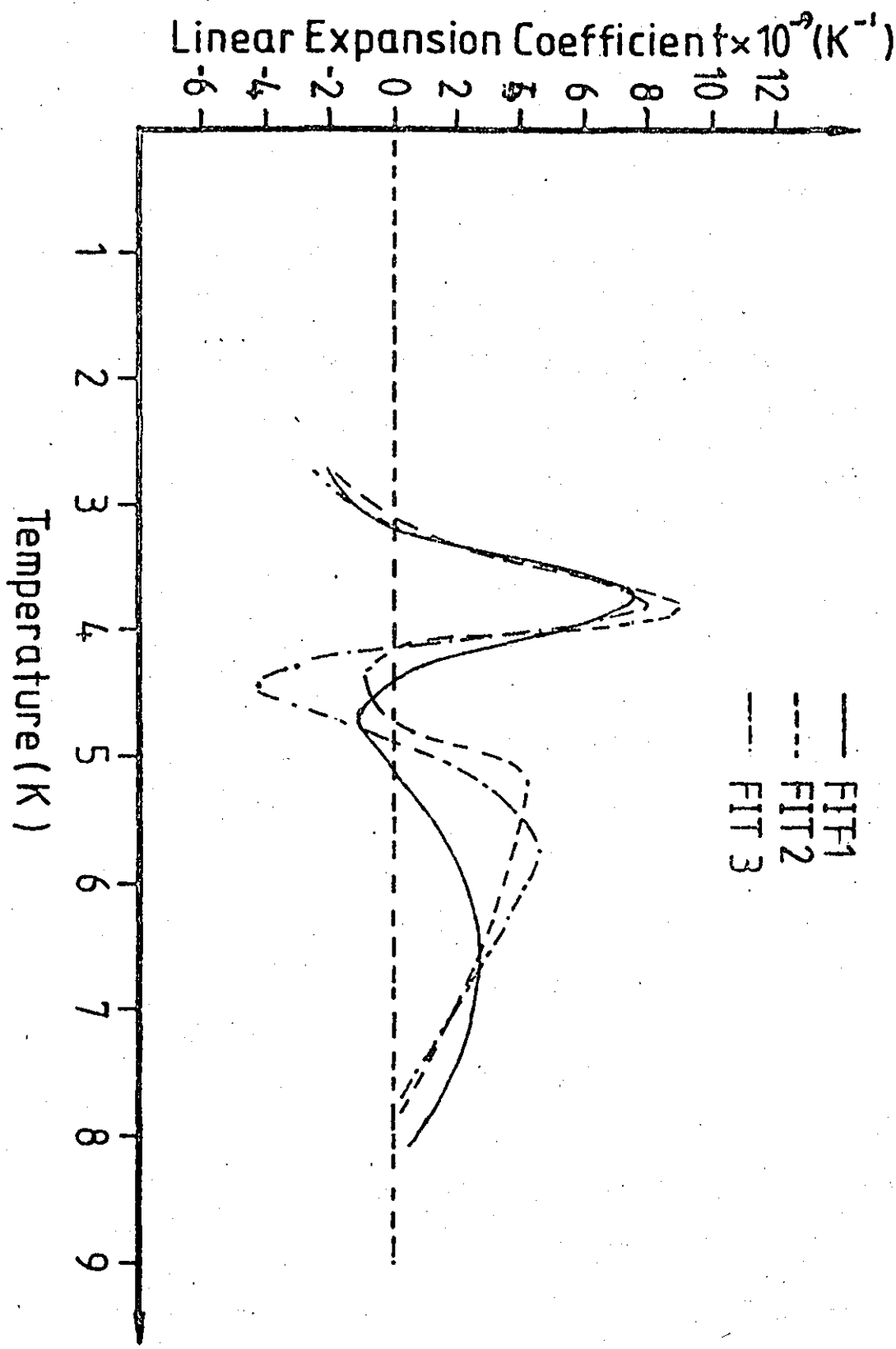


FIG. 5.16

Thermal expansion of  $Al_2O_3:Mn$  (sample J1) relative to that of pure  $Al_2O_3$ . Effect of variation of spline fitting parameters for a single data set.

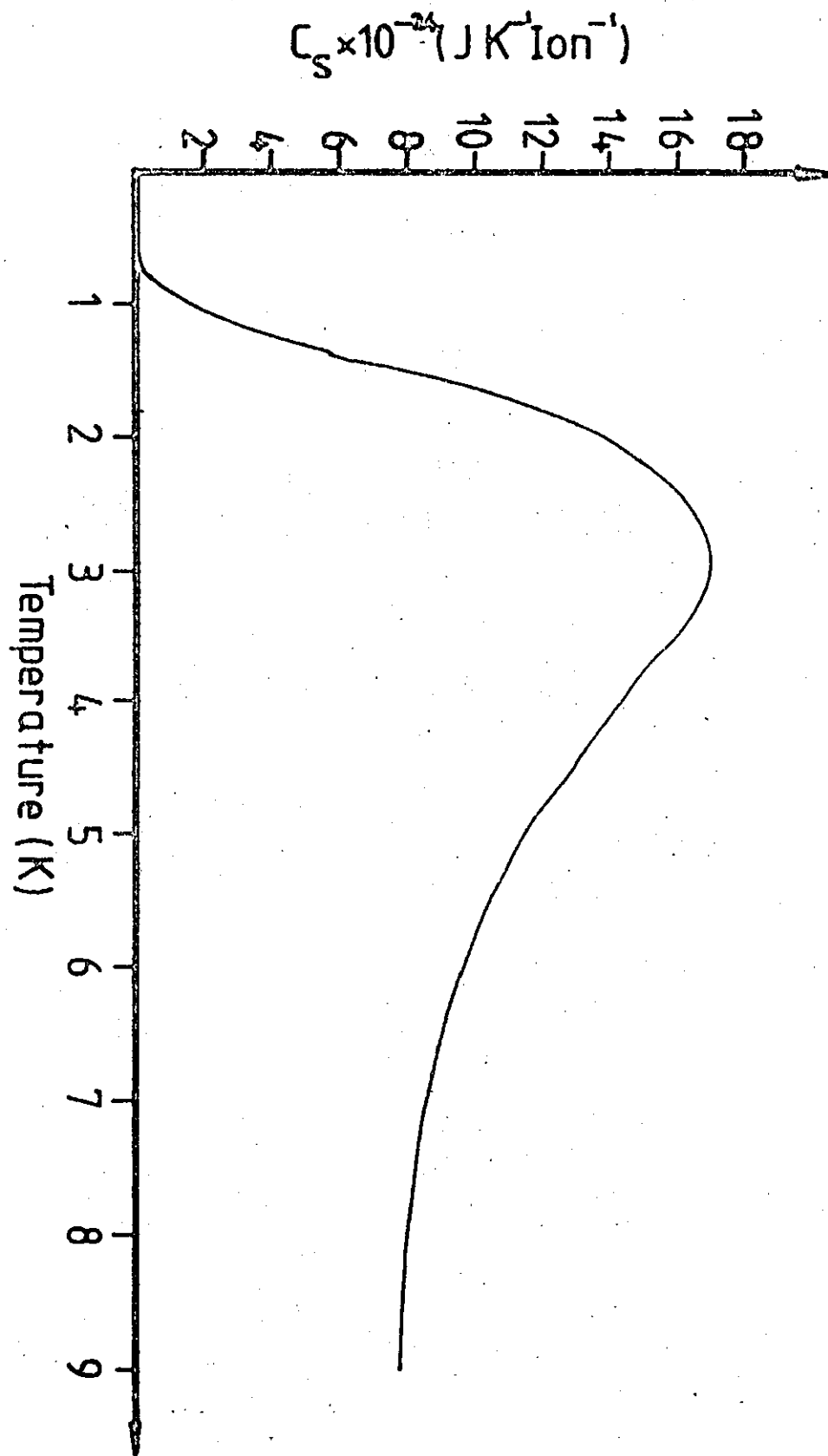


FIG. 5.17 Schottky contribution to the specific heat for  $\text{Mn}^{3+} (3d^4)$  in  $\text{Al}_2\text{O}_3$ .

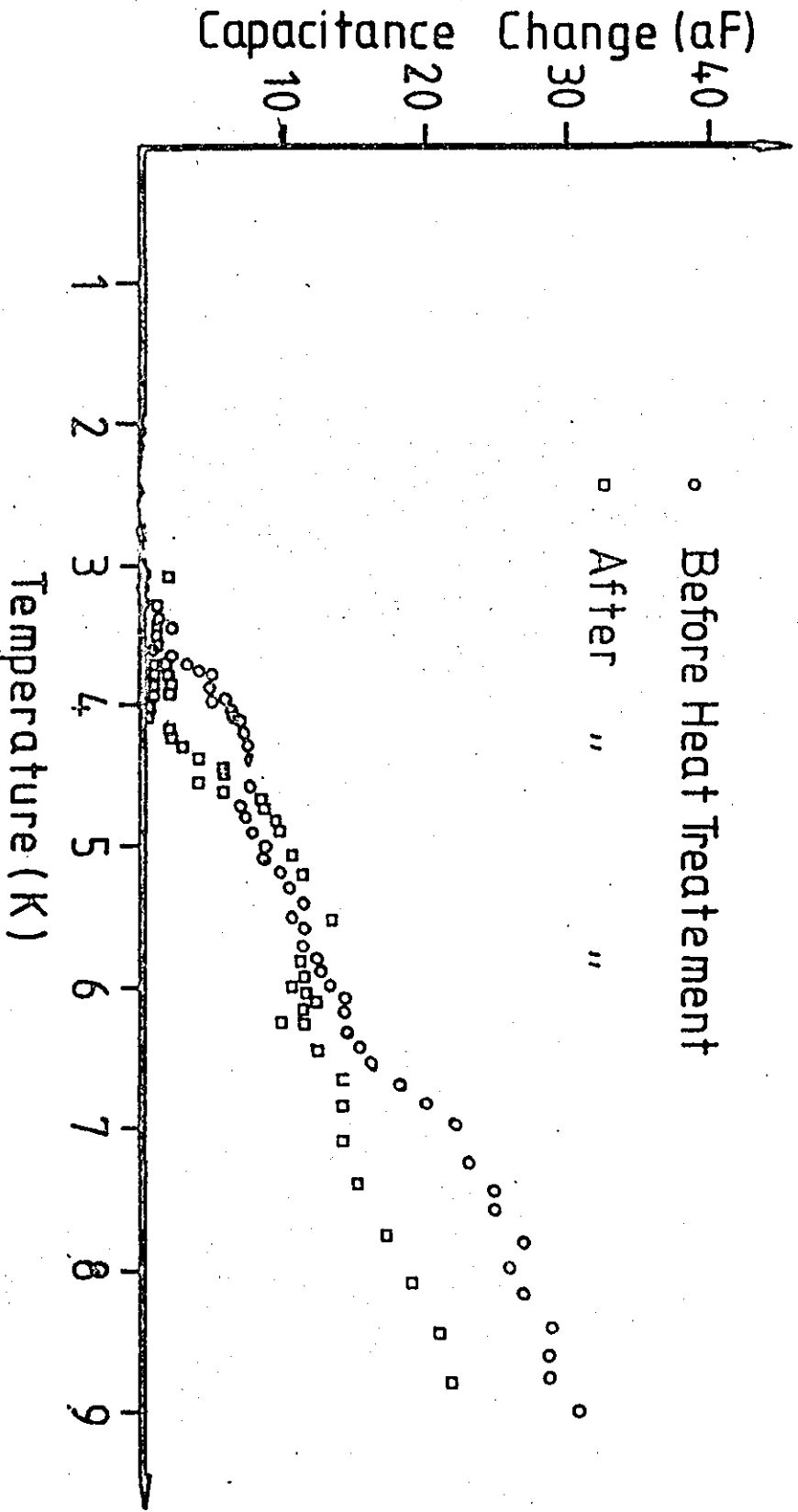


FIG. 5.18

Typical Capacitance change with Temperature of a Dilatometer containing an  $\text{Al}_2\text{O}_3\text{:Mn}$  (J1) Sample.

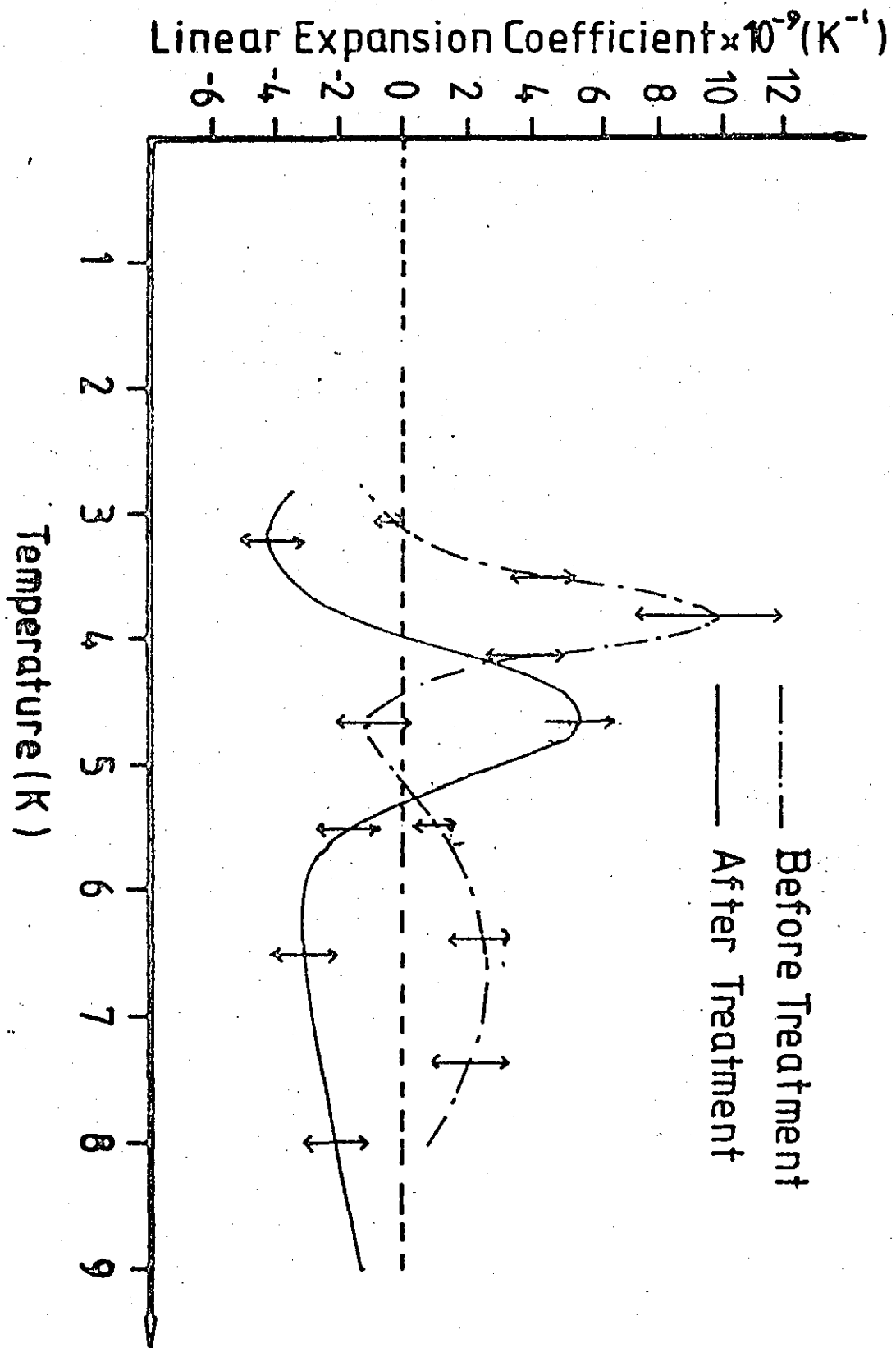


FIG. 5.19

Thermal expansion of  $\text{Al}_2\text{O}_3\text{:Mn}$  (sample J1) relative to that of pure  $\text{Al}_2\text{O}_3$ . Effect of heat treatment.

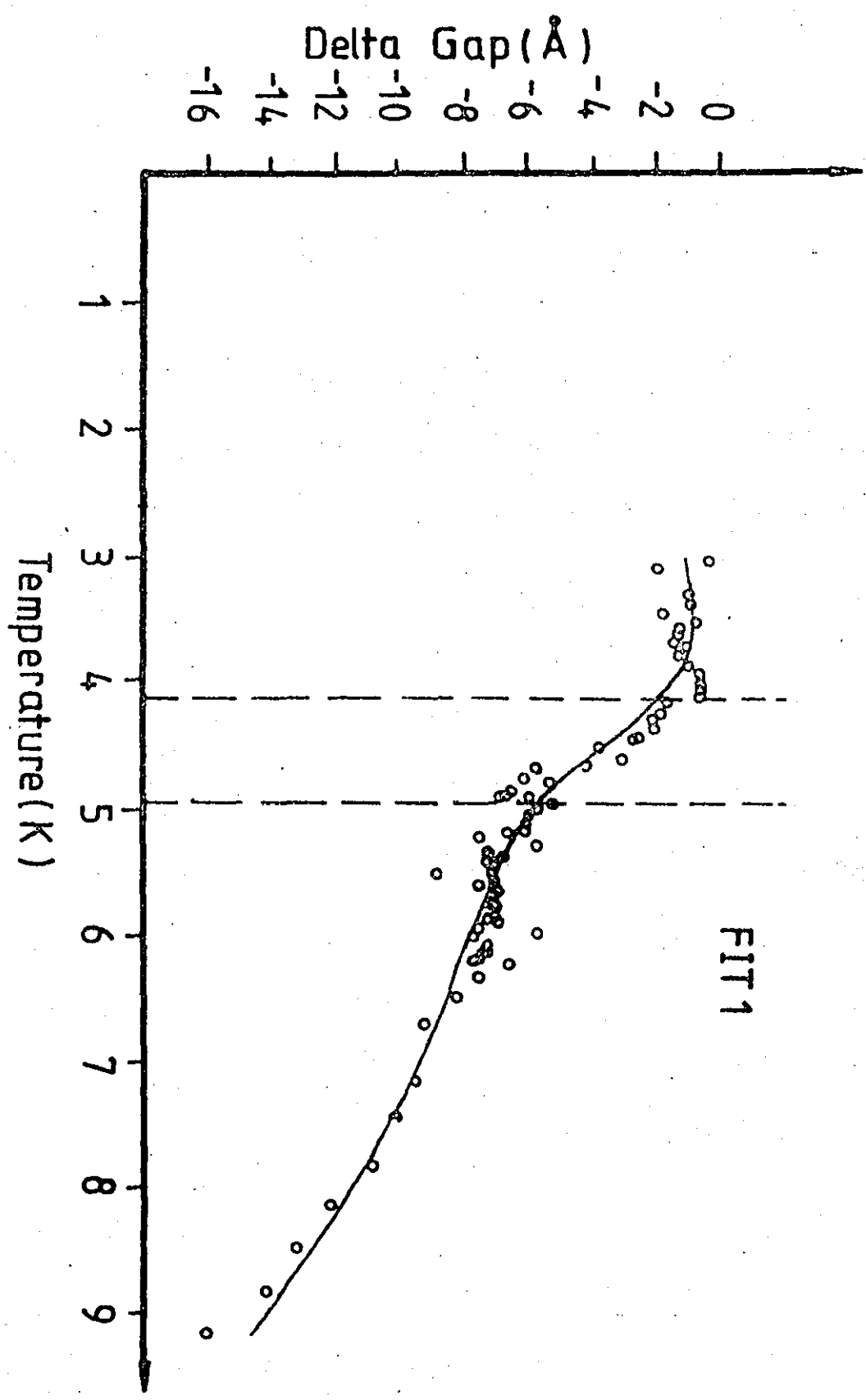


FIG. 5.20 Change of dilatometer electrode separation with temperature for  $\text{Al}_2\text{O}_3\text{:Mn}$  (sample J1, heat treated). Effect of variation of spline fitting parameters, 1st Fit.

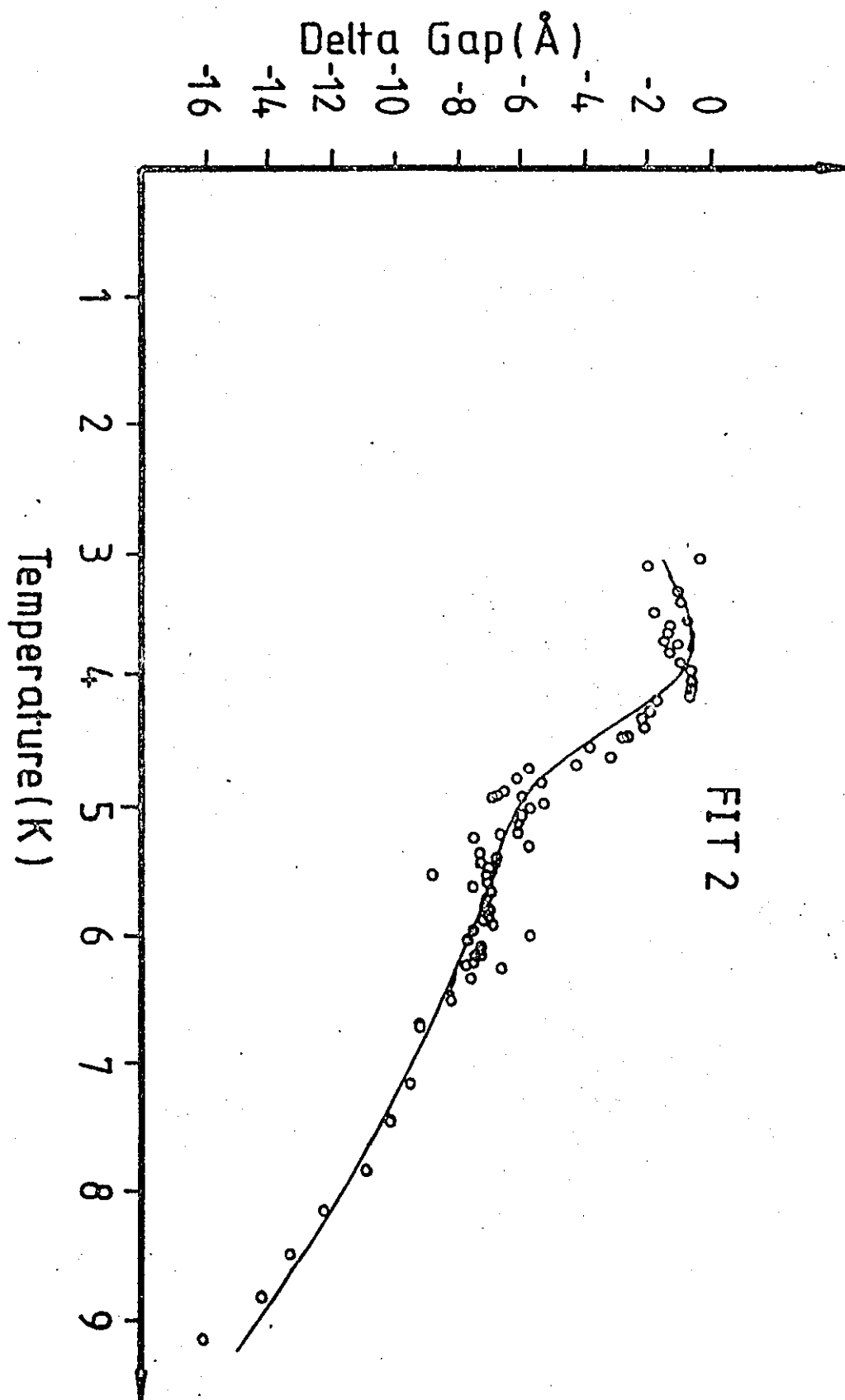


FIG. 5.21

Change of Dilatometer Electrode Separation with Temperature for  $\text{Al}_2\text{O}_3:\text{Mn}$  (Sample J1, Heat treated)  
 Effect of Variation of Spline Fitting Parameters,  
 2nd Fit

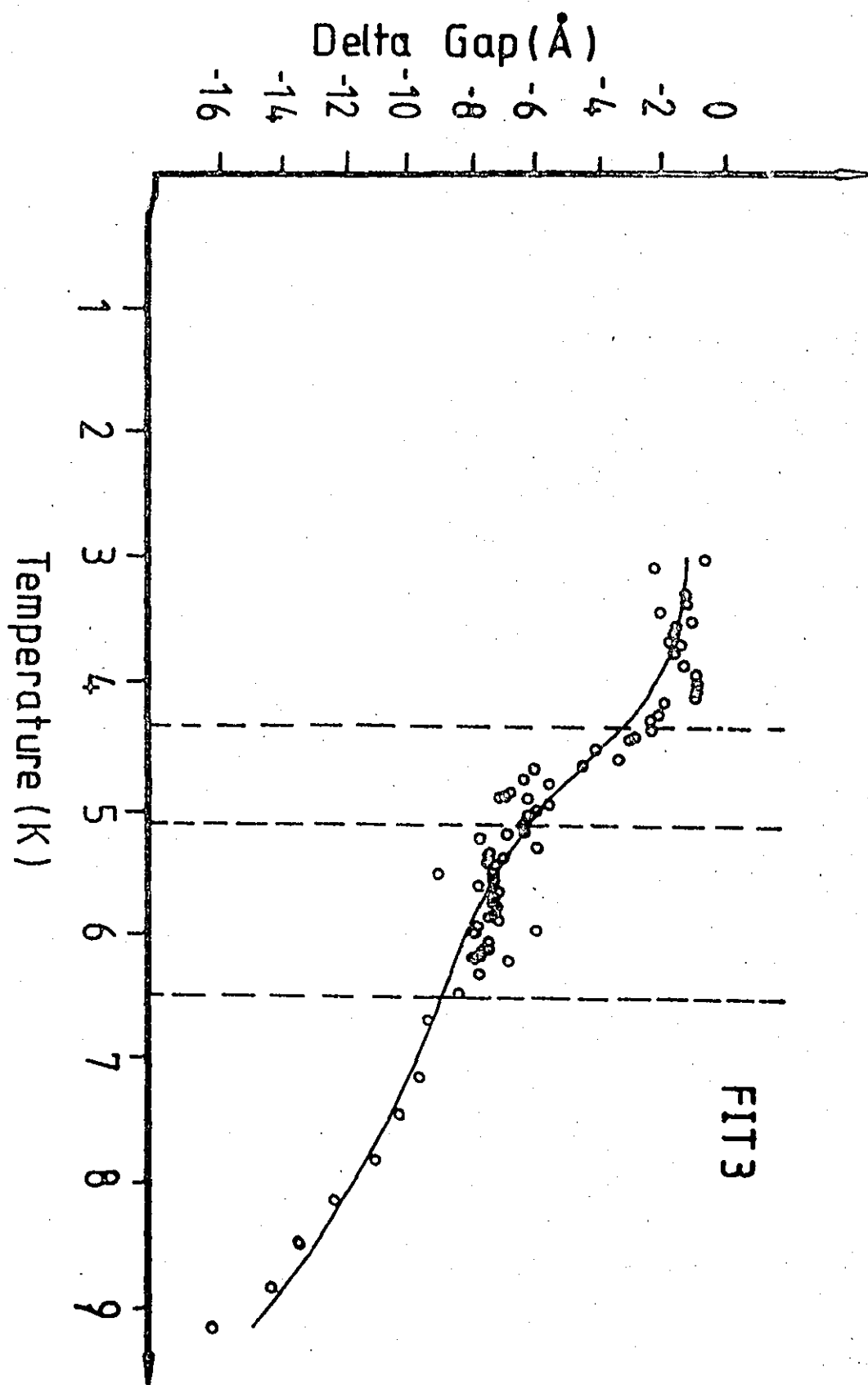


FIG. 5.22

Change of dilatometer electrode separation with temperature for  $\text{Al}_2\text{O}_3\text{:Mn}$  (sample J1, heat treated). Effect of variation of spline fitting parameters, 3rd Fit.

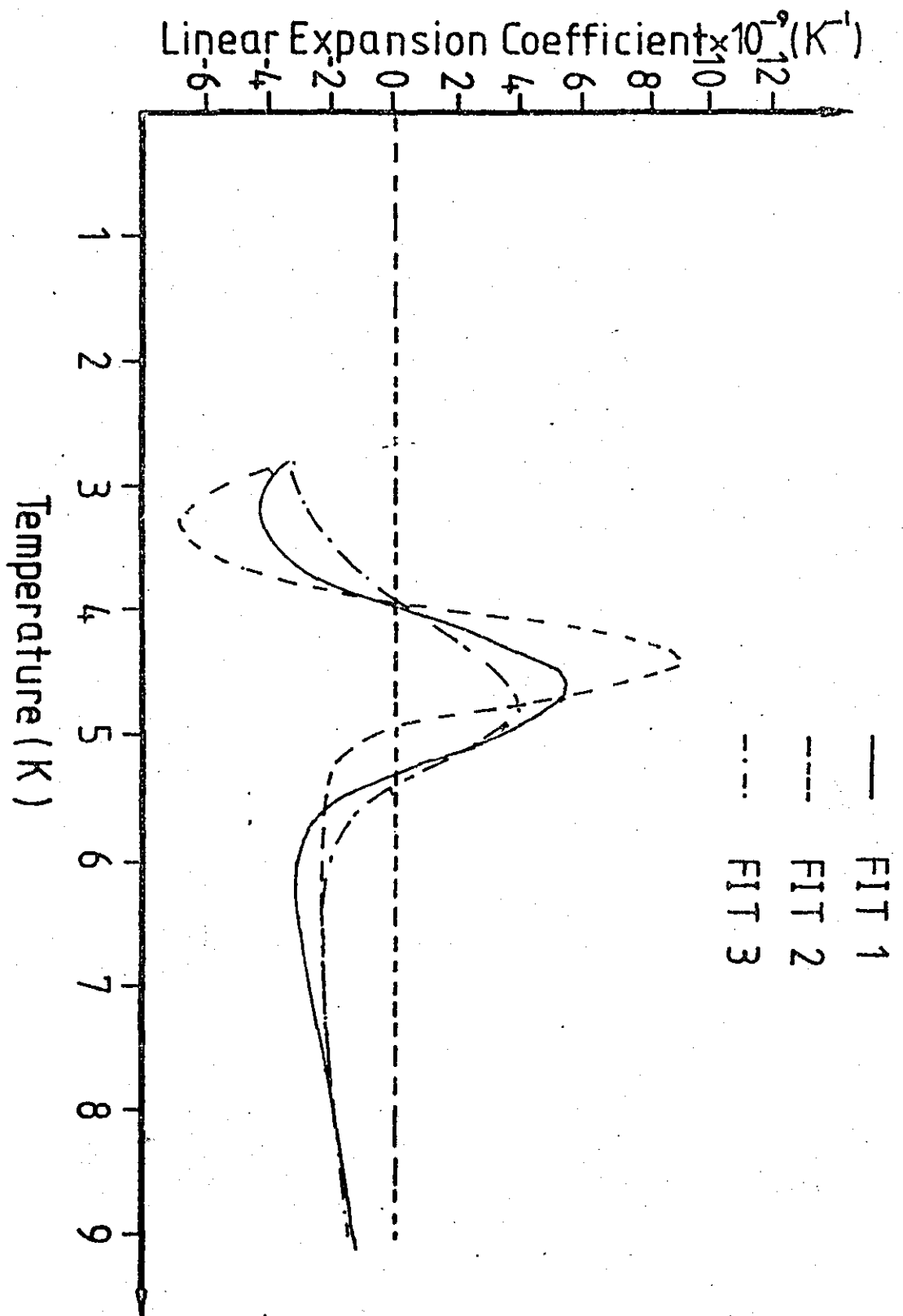


FIG. 5.23 Thermal expansion of heat treated  $Al_2O_3:Mn$  (sample J1) relative to that of pure  $Al_2O_3$ . Effect of variation of spline fitting parameters for a single data set.



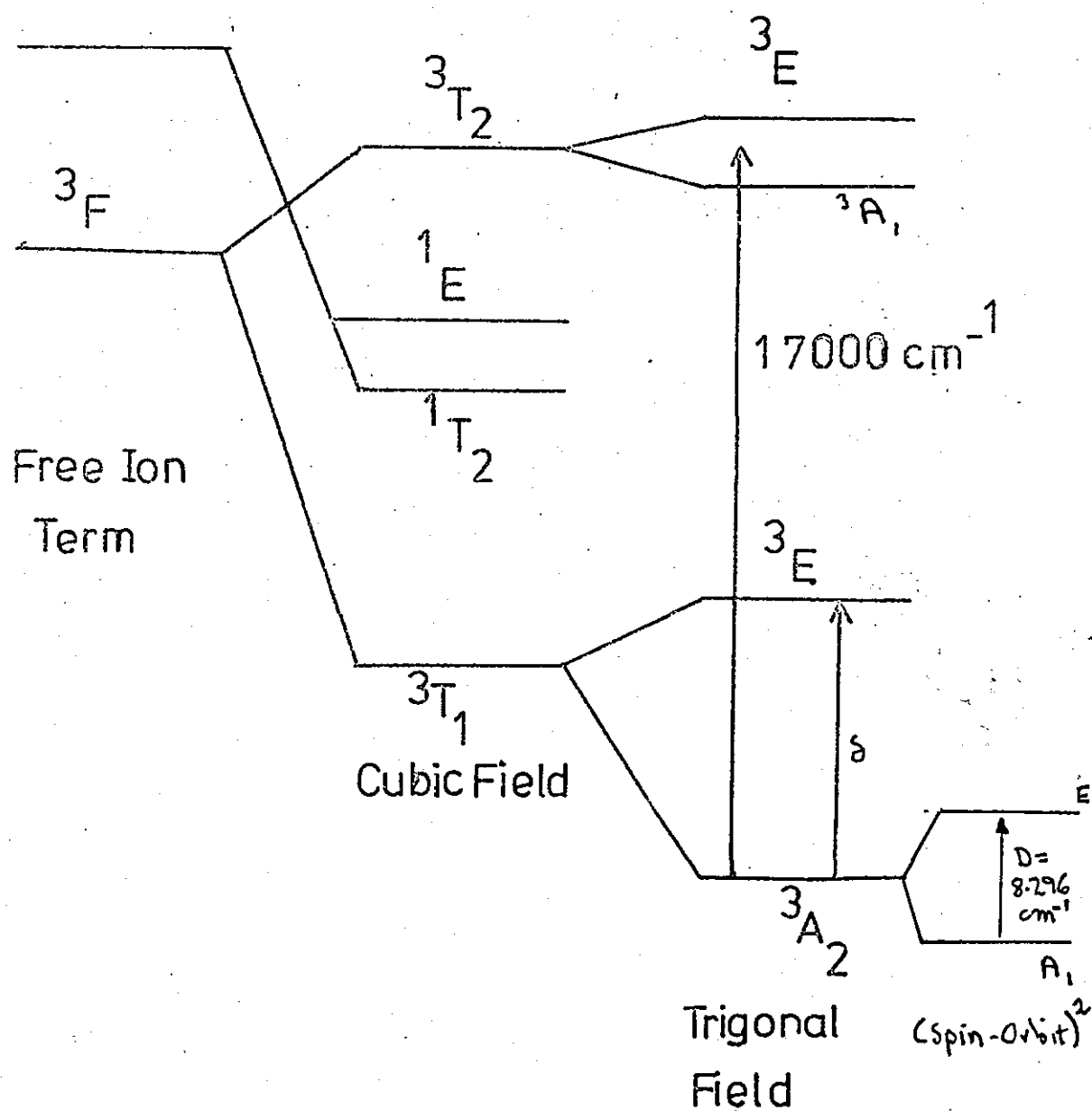


FIG 5.24 Energy Level Diagram for  $V^{3+} (3d^2)$  in  $Al_2O_3$ .

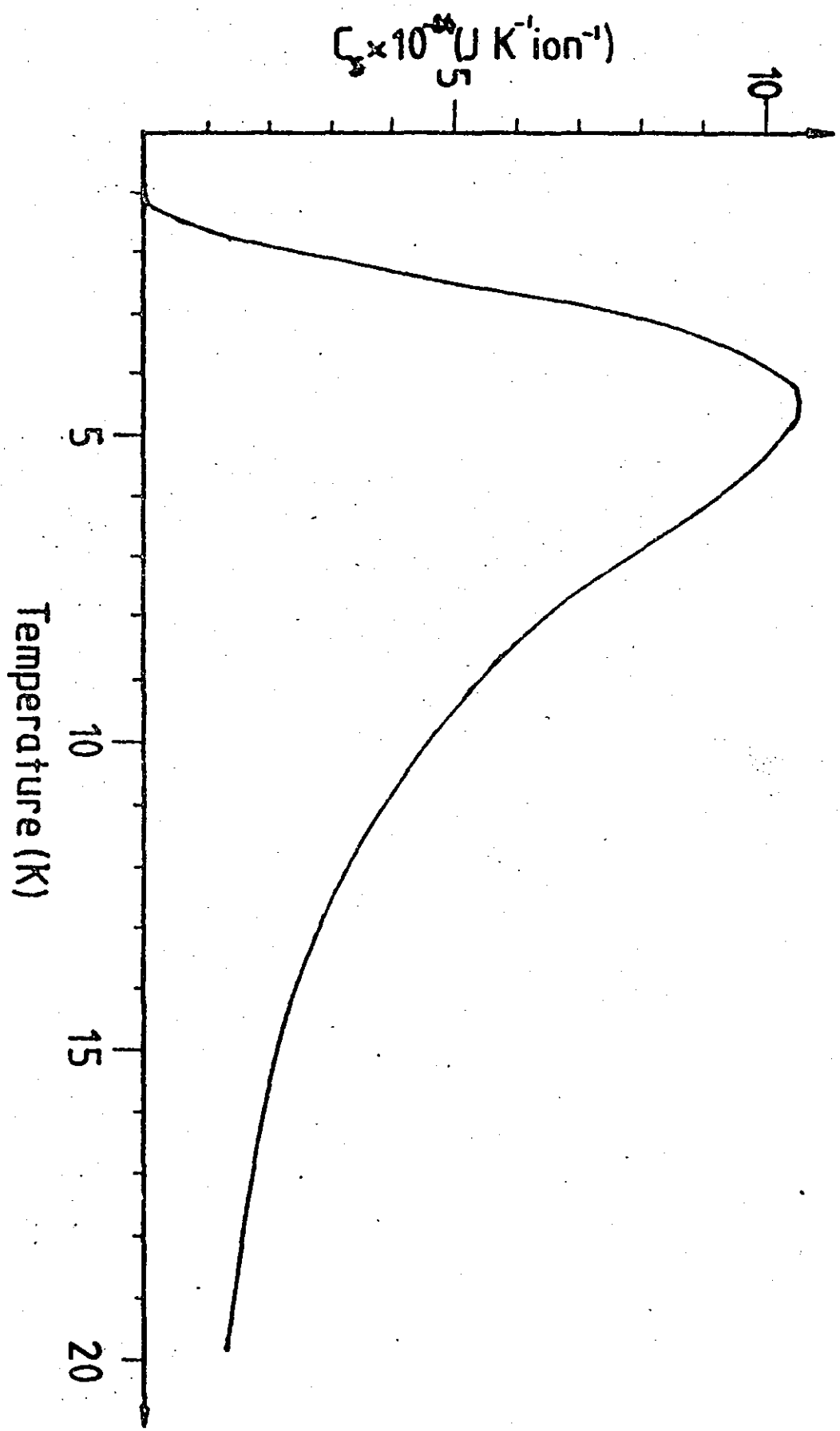


FIG. 5.25 Schottky contribution to the specific heat for  $V^{3+}(3d^2)$  in Al.

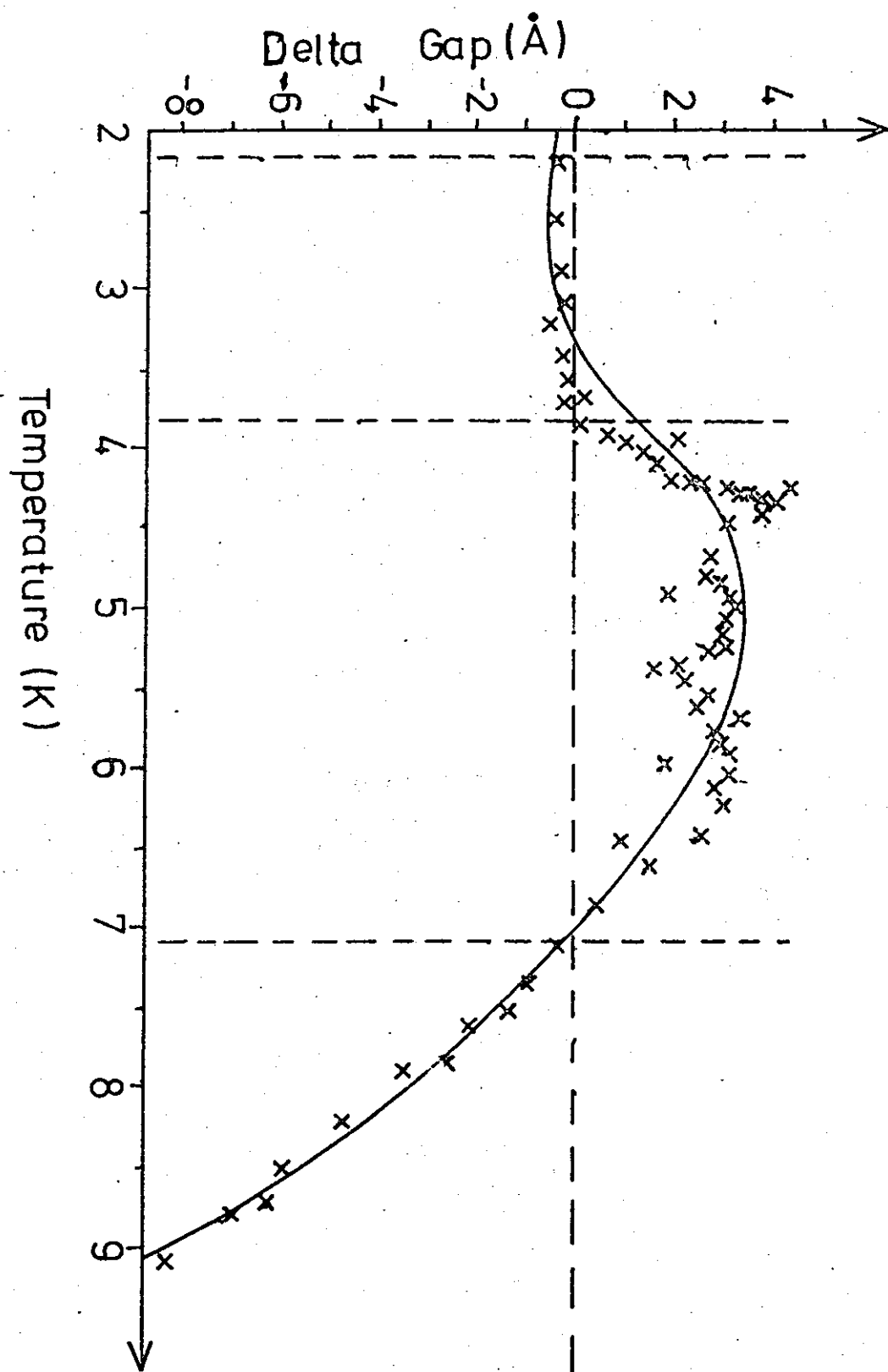


FIG. 5.26 Change of Dilatometer Electrode Separation with Temperature for  $\text{Al}_2\text{O}_3\text{:V}$ (Sample 2A, as received).

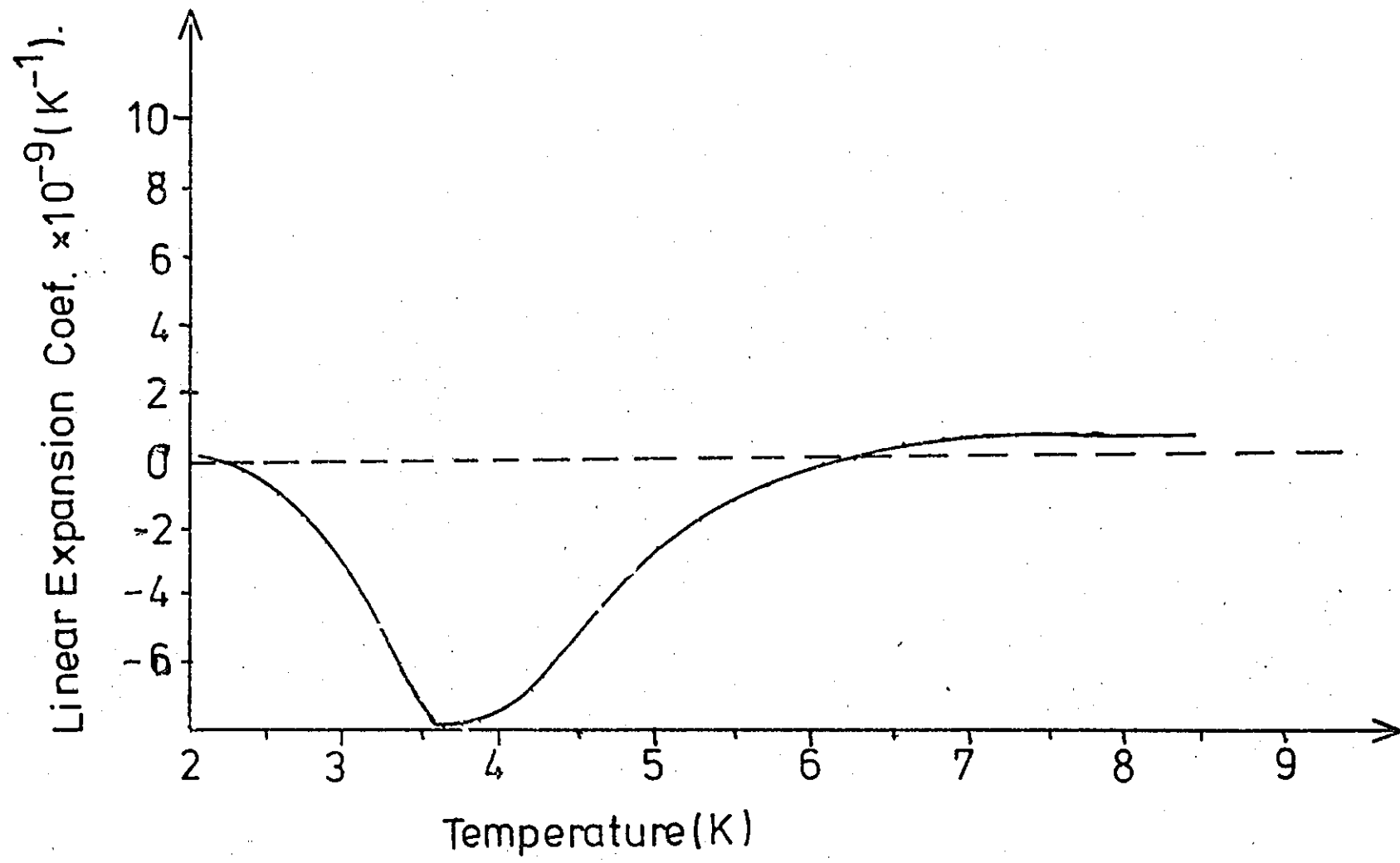


FIG. 5.27 Thermal Expansion of Al<sub>2</sub>O<sub>3</sub>:V (Sample 2A, as received) Relative to that of Pure Al<sub>2</sub>O<sub>3</sub>.

## ACKNOWLEDGEMENTS

The author wishes to acknowledge the assistance and encouragement received from innumerable friends and associates during the tenure of this study.

In particular I wish to record my sincere gratitude to Dr M A Brown and the academic staff and technicians of the Physics department of Loughborough University of Technology. I also wish to thank the Science and Engineering Research Council and the Scientific Affairs Division of NATO for financial support of the research programme, and the staff of the Service Basses Temperatures, Centre D'Etude Nucleaires, Grenoble, and the University of Nottingham Physics Department for assistance and advice over the three years of this study.

## REFERENCES

1. ABOU-GHANTOUS M, BATES C A, 1980, J Physique Lett, 41, L263
2. ANDRES K, 1961, Cryogenics, 2, 93
3. ANDRES K, 1964, Phys Kondens Mat, 2, 294
4. BARRON T H K, KLEIN, M L, 1962, Phys Rev, 127, 1997
5. BARRON T H K, COLLINS J G, WHITE, G K, 1980, Adv in Phys, 29, 4,609
6. BATCHELDER D N, SIMMONS R O, 1965, J Appl Phys, 36, 2864
7. BATES C A, 1978, J Phys C, 11, 3447
8. BATES C A, 1978, Phys Rep, 35, 3, 187
9. BATES C A, DIXON J M, 1969, J Phys C, 2, 2, 2209
10. BATES C A, WARDLAW R S, 1980, J Phys C, 13, 3609
11. BIJL D, PULLAN H, 1955, Physica, 21, 285
12. BOND W L, 1960, Acta Crystallogr, 13, 814
13. BROWN I J, BROWN M A, 1981, Phys Rev Lett, 46, 835
14. BROWN I J, BROWN M A, 1982, to be published
- 14a. BROWN M.A., 1971, Ph.D. Thesis (Nottingham).
15. BROWN M A, De GOER A-M, DE VISMES N, VILLEDIEU M, 1972,  
Conference Internationale sur la Diffusion Des Phonons Dans  
Les Solids, PARIS, 272 (Ed H J Albany, C E N SACLAY, FRANCE)
16. BROWN M A, CHALLIS L J, MOORE W S, YALCIN T, WALDORF D C,  
1973, J Phys C, 10, 4939
- 16a. BROWN M.A., 1978, Private communication.
17. BROWN M A, ROBACH Y, 1978, J Phys C, 10, 4939
18. BROWN M A, BULLEID C, 1978, J Phys C, 11, 429
19. CALLAWAY J, 1959, Phys Rev, 113, 4, 1046
20. CARR R H, SWENSON C A, 1964, Cryogenics, 4, 76
21. CASE C R, SWENSON C A, 1974, Phys Rev B, 9, 4506
22. CHALLIS L J, De GOER A-M, 1970, Progress Report (No 1) on  
NATO Research Grant No 477
23. CHALLIS L J, De GOER A-M, 1970, Phys Lett, 31A, 8, 461
24. CHALLIS L J, De GOER A-M, 1970, Phys Lett, 31A, 8, 463
25. COLLINS J G, WHITE G K, 1964, Chapter IX of "Progress in Low  
Temperature Physics IV" Ed C J Gorter (Amsterdam, North-Holland)

26. DAVIES W R, MENIUS M K, MOSS M K, PHILBRICK C R, 1965, Proc IEEE, 52, 670
27. DHEER P N, SURANGE S L, 1958, Phil Mag, 3, 665
28. EVANGELOU S W, O'BRIEN M C M, PERKINS R S, 1980, J Phys C, 13, 4175
29. FLETCHER J R, MARSHALL F G, RAMPTON V M, ROWELL P M, STEVENS K W H, 1966, PROC ROY SOC, 88, 127
30. FLETCHER J R, STEVENS K W H, 1969, J Phys C, 2, 2, 444
31. FLETCHER J R, GRIMSHAW J M, KNOWLES A P, MOORE W S, 1980, J Phys C, 13, 6391
32. GRIFFITH J R, 1961, "The Theory of Transition Metal Ions", Cambridge University Press, 374
33. GRUNEISEN E, 1912 Ann Phys, 39, 257
34. GRUNEISEN E, 1926, Handb Phys, 10, 1
35. De GOER A-M, 1969, Jour de Phys, 30, 389
36. De GOER A-M, DEVISMES N, 1972, J Phys Chem Solids, 33, 1785
37. HEERENS W C, VERMEULEN F C, 1975, J Appl Phys, 46, 6, 2486
38. HUTCHINGS M T, 1964, Solid St Phys, 16, 227
39. HAM F S, 1965, Phys Rev, 138, 6A, A1727
40. HAM F S, 1968, Phys Rev, 166, 2
41. HAM F S, 1971, Phys Rev B, 4, 11, 3854
42. JACOBS S F, BRADFORD J N, BERTHOLD J W, 1970, Appl Optics, 9, 2477
43. JONES R V, 1961, J Scient Instrum, 38, 37
44. KHAN A R, BROWN I J, BROWN M A, 1980, J Phys E, 13, 1280
45. KROEGER F R, SWENSON C A, 1977, J Appl Phys, 48, 853
46. LEIBFRIED G, LUDWIG W, 1961, Solid St Phys, 12, 276
47. MAXWELL J C, 1873, "A Treatise on Electricity and Magnetism" Article No 201, Oxford: Clarendon
48. MIE G, 1903, Ann Phys, 11, 657
49. MEZZETTI E, 1964, Ricerca Scient I, 4, 473
50. MOON C, SPARKS C M, 1948, J Res Natl Bur Stand (US), A41, 497

51. OTT H R, LUTHI B, 1977, Z Phys B, 28, 141
52. PARIERA F N D D, BARNES C H, GRAHAM G M, 1970, J Appl Phys, 41, 5050
53. ROBERTS R B, 1975, J Phys E, 8, 600
54. ROBERTS R B, 1978, "Thermal Expansion Vol 6", Ed Peggs (New York: Plenum)
55. SCHAUER R, 1965, Can J Phys, 43, 523
56. SCHOUTEN D R, SWENSON C A, 1974, Phys Rev B, 10, 2175
57. SCHUELE D, SMITH C S, 1964, J Phys Chem Solids, 25, 801
58. SHAPIRO J M, TAYLOR D R, GRAHAM G M, 1964, Can J Phys, 42, 835
59. SHEARD F W, 1969, Phys Lett A, 30, 3, 156
60. SHEARD F W, 1971, Journ de Phys, CI, Suppl 2-3, No 32, 939
61. SHEARD F W, 1972, AIP Conf Proc, 3 (New York: AM Inst Phys), 155
62. SHEARD F W, SMITH T F, WHITE G K, BIRCH J A, 1977, J Phys C, 10, 645
63. SPARKS P W, SWENSON C A, 1967, Phys Rev, 163, 779
64. STURGE M D, 1967, Solid State Physics, (New York: Academic Press), 20, 91
65. THOMPSON A M, 1958, I R E Trans Instrum 1-7, 245
66. TILFORD C R, SWENSON C A, 1972, Phys Rev B, 5, 718
67. TOLKACHEV A M, ALEXANDROVSKI I, KUCHNEV V I, Cryogenics, 15, 547
68. VILLAR R, HORTAL M, VIERA S, 1980, Rev Sci Instrum, 51, 1, 27
69. VILLEDIEU M, DEVISMES N, De GOER A-M, 1977, J Phys Chem Solids, 38, 106
70. WHITE G K, 1961, Cryogenics, 1, 151
71. WHITE G K, COLLINS J G, 1972, J Low-Temp Phys, 7, 43
72. YATES B, 1972, "Thermal Expansion" (London:Plenum)
73. ZOLLER W, DIETSCH W, KINDER H, De GOER A-M, SALCE B, 1980, J Phys C, 13, 3591



## APPENDIX I

### FORTRAN PACKAGE FOR PROCESSING THERMAL EXPANSION DATA

The listing that follows is of a fortran package that has been developed to process data produced in thermal expansion experiments. A flow chart and further description may be found in Chapter 4. The comments are self explanatory and further details will not be discussed here.

The programme was developed to be executed by Loughborough Universities "Prime 400" computer, and interactive device, and makes extensive use of the interactive graphics facilities available. Extensive use is made of the "NAGF" and "GINO-F" fortran libraries although several minor faults were found in some of these routines. Where necessary the complete listing of the library routine is given including any modifications that have been found necessary for successful execution of the package.

Although the prime computer is a virtual memory device, it has been found necessary to employ a dummy virtual memory file on disc to cope with the extensive quantities of graphical data generated by the routine.

```

(0001) C*****C
(0002) C C
(0003) C C
(0004) C C
(0005) C THERMAL EXPANSION DATA EVALUATION PROGRAM C
(0006) C C
(0007) C C
(0008) C*****C
(0009) IMPLICIT INTEGER(I,J,L,M,N,R),DOUBLE PRECISION(A-H,K,O-Q,S-
(0010) *,REAL(Z)
(0011) COMMON /A/ NCAP7,K(100),C(100),IFAIL,NCAP,SS,SDASH(4)
(0012) COMMON /B/ A1,A2,A3,NOUT,NIN,A4,A5
(0013) COMMON /C/ X(250),Y(250),W(250),
(0014) *GRAD(250),D(250),SPEXP(250),ARES(250),YCALC(250),
(0015) *WORK1(200),WORK2(4,100),
(0016) *TR1(50),TR2(50),TR3(50),TR4(50),EX(250),SPL1,LSET
(0017) *,SPL2
(0018) COMMON /Z/ ZXRES(500),ZYRES(500),NVVAL,NSYM,
(0019) *ZXSVM(250),ZYSVM(250),NCUR,ZMA,ZMI,NW,NNYY,NDEV
(0020) COMMON /D/M
(0021) COMMON /R/IYTYPE
(0022) DIMENSION N(50),NJ(50)
(0023) EQUIVALENCE (R,IBN,L1),(I,L2)
(0024) EXTERNAL GAP
(0025) DATA NIN/5/,NOUT/6/,NCUR/0/
(0026) C
(0027) C
(0028) C IF INFORMATION IS REQUIRED UPON DATA FORMAT THEN GIVE IT.
(0029) C
(0030) C
(0031) WRITE(1,1532)
(0032) 1532 FORMAT('IF INFORMATION ON DATA PRESENTATION',
(0033) *, ' IS REQUIRED TYPE 1 OTHERWISE 0')
(0034) READ(1,*)IJB
(0035) IF(IJB.EQ.1)CALL INFO
(0036) C
(0037) C
(0038) C
(0039) C INPUT ELECTRODE PARAMETERS
(0040) C
(0041) C A4=RADIUS OF COPPER ELECTRODE IN METRES
(0042) C A5=SEPERATION OF ELECTRODE AND GUARD RING IN METRES
(0043) C
(0044) C
(0045) C
(0046) READ(5,*)A4,A5
(0047) C
(0048) C
(0049) C
(0050) C READ TERMINAL TYPE FOR GRAPHICS OUTPUT
(0051) C
(0052) C
(0053) C
(0054) WRITE(1,1)
(0055) 1 FORMAT('INPUT TERMINAL TYPE BEING USED'//
(0056) *, ' TYPE 1 FOR TREND' /
(0057) *, ' TYPE 2 FOR T4010' /
(0058) *, ' TYPE 3 FOR S5600' /
(0059) *, ' TYPE 4 FOR S5660' )
(0060) READ(1,*)NDEV
(0061) C
(0062) C
(0063) C

```

```

(0063) C
(0064) C   READ SPECIMEN PARAMETERS
(0065) C
(0066) C   SPL1 =SPECIMEN LENGTH
(0067) C   SPL2 =LENGTH OF COPPER WHOSE EXPANSION IS TO BE COMPENSAT
(0068) C
(0069) C
(0070) C   READ(5,*)SPL1,SPL2
(0071) C   SPL1=SPL1*1.0D10
(0072) C   SPL2=SPL2*1.0D10
(0073) C
(0074) C
(0075) C
(0076) C   INPUT CAPACITANCE , TEMPERATURE DATA IN FREE FORMAT
(0077) C
(0078) C
(0079) C
(0080) C   R=0
(0081) 3   R=R+1
(0082) C   READ(5,*)Y(R),X(R)
(0083) C   W(R)=1.0D0
(0084) C   IF(Y(R).LT.1.0D-6)GO TO 2
(0085) C   GO TO 3
(0086) 2   M=R-1
(0087) C
(0088) C
(0089) C
(0090) C   WRITE TO OUTPUT LISTING NO. OF POINTS AND SPECIMEN LENGTH
(0091) C
(0092) C
(0093) C
(0094) C   WRITE(NOUT,99993)M
(0095) C   WRITE(NOUT,99980)SPL1
(0096) C   WRITE(NOUT,99990)
(0097) C
(0098) C
(0099) C   CALCULATE GAP FROM CAPACITANCE DATA
(0100) C
(0101) C
(0102) 180  AINIT=GAP(Y(1),X(1))*1.0D10
(0103) C   WRITE(1,1354)AINIT
(0104) C   WRITE(6,1354)AINIT
(0105) 1354 FORMAT(//'INITIAL GAP IN ANGSTROMS=',D13.6//)
(0106) C   DO 220 R=1,M
(0107) C   ALIMBO=GAP(Y(R),X(R))*1.0D10
(0108) C   D(R)=Y(R)
(0109) C   Y(R)=ALIMBO-AINIT
(0110) C   SPEXP(R)=Y(R)-AINIT
(0111) C   IF(IWGHT.NE.1)GO TO 200
(0112) C   GO TO 220
(0113) 200  CONTINUE
(0114) 220  CONTINUE
(0115) C
(0116) C
(0117) C   CALL BETA CUBED SPLINE FUNCTION ROUTINE
(0118) C   WITH INTERACTIVE GRAFICS.
(0119) C
(0120) C
(0121) C   CALL CSF(M)
(0122) C
(0123) C
(0124) C   WRITE TO OUTPUT FILE SPLINE PARAMETERS.

```

```

(0125) C
(0126) C
(0127) WRITE(NOUT,99994)NCAP
(0128) NCAP2=NCAP+2
(0129) NCAP3=NCAP+3
(0130) NCAP7=NCAP+7
(0131) IF(NCAP.EQ.1)GO TO 140
(0132) 120 IF(NCAP.EQ.1)GO TO 140
(0133) WRITE(NOUT,99989)
(0134) WRITE(NOUT,99988)(J,K(J),J=5,NCAP3)
(0135) 140 IF(IWOHT.NE.1)GO TO 160
(0136) GO TO 114
(0137) 160 WRITE(NOUT,99986)
(0138) 114 WRITE(NOUT,11112)
(0139) 11112 FORMAT(/,' KNOT(J+2) B-SPLINE COEFF C(J)')
(0140) DO 4 R=1,NCAP7
(0141) 4 WRITE(NOUT,99979)K(R),C(R)
(0142) 99979 FORMAT(2D20.5)
(0143) SS2=SS*SS
(0144) WS=0.0
(0145) DO 304 IKN=1,M
(0146) 304 WS=WS+W(IKN)
(0147) SS2=DSQRT(SS2/WS)
(0148) WRITE(NOUT,88885)SS2
(0149) 99993 FORMAT('CUBIC SPLINE FIT TO ARBITRARY DATA POINTS',/,
(0150) *'INPUT DATA',/, 'NUMBER OF DATA POINTS =',I4)
(0151) 99994 FORMAT(/22H NUMBER OF INTERVALS= ,I4)
(0152) 99991 FORMAT(/23H UNIT WEIGHTING FACTORS)
(0153) 99990 FORMAT(/32H USER SUPPLIED WEIGHTING FACTORS)
(0154) 99989 FORMAT(/20H J KNOT K(J)/)
(0155) 99988 FORMAT(13,D20.5)
(0156) 99986 FORMAT(/,' R ABSCISSA X(R) ORDINATE Y(R)
(0157) *' WEIGHT W(R)')
(0158) 99985 FORMAT(13,5D18.5)
(0159) 99980 FORMAT(/,'SPECIMEN LENGTH=',D20.5)
(0160) WRITE(NOUT,88888)
(0161) WRITE(NOUT,88887)(IBN,X(IBN),Y(IBN),YCALC(IBN),ARES(13),
(0162) *W(IBN),IBN=1,M)
(0163) C
(0164) C
(0165) C POWEL TEST FOR RANDOM DATA
(0166) C
(0167) C
(0168) JJL1=NCAP3+1
(0169) DO 104 L1=1,JJL1
(0170) 104 N(L1)=0
(0171) DO 101 L1=5,NCAP3
(0172) DO 102 I=1,M
(0173) IF(X(I).GT.K(L1))GO TO 101
(0174) N(L1)=N(L1)+1
(0175) 102 CONTINUE
(0176) 101 CONTINUE
(0177) N(4)=0
(0178) N(NCAP3+1)=M
(0179) WRITE(NOUT,88884)
(0180) DO 106 L1=5,JJL1
(0181) TR1(L1)=0.0D0
(0182) TR2(L1)=0.0D0
(0183) TR3(L1)=0.0D0
(0184) TR4(L1)=0.0D0
(0185) NJ(L1)=N(L1)-N(L1-1)
(0186) IF(NJ(L1).LT.2)GO TO 108

```

```

(0187)      GO TO 109
(0188) 108  WRITE(NOUT,88882)NJ(L1)
(0189)      GO TO 106
(0190) 109  CONTINUE
(0191)      JJAN1=N(L1-1)+1
(0192)      JJAN2=N(L1)
(0193)      DO 107 I=JJAN1,JJAN2
(0194)      TR1(L1)=TR1(L1)+ARES(I)*ARES(I+1)
(0195) 107  TR2(L1)=TR2(L1)+ARES(I)*ARES(I)
(0196)      TR3(L1)=TR2(L1)/(DSQRT(DBLE(FLOAT(NJ(L1)-1.))))
(0197)      TR4(L1)=TR2(L1)/(DSQRT(DBLE(FLOAT(NJ(L1)-1.)/2.)))
(0198)      L2=L1-4
(0199)      WRITE(NOUT,88883)L2,NJ(L1),K(L1),TR1(L1),TR3(L1),TR4(L1)
(0200) 106  CONTINUE
(0201)      C
(0202)      C
(0203)      C
(0204)      C
(0205)      C  WRITE TO OUTPUT FILE RESULTS.
(0206)      C
(0207)      C
(0208)      C
(0209)      WRITE(NOUT,88881)
(0210)      DO 1001 R=1,M
(0211)      GCUBIC=SPEXP(R)/(X(R)**3)
(0212) 1001  WRITE(NOUT,88880)R,X(R),SPEXP(R),GRAD(R),EX(R),GCUBIC
(0213) 88888 FORMAT(/,'                               LIST OF RESIDUES',/,
(0214)      *,' POINT          TEMP.          DELTA GAP          GAP FI
(0215)      *,' RESIDUES          WIEGHT.')
```

|        |       |  |  |  |  |
|--------|-------|--|--|--|--|
| (0216) | 88887 | FORMAT(I3,5D15.5)  |  |  |  |
| (0217) | 88886 | FORMAT(' IFAIL VALUES=',I3)  |  |  |  |
| (0218) | 88885 | FORMAT(' (RESIDUAL SUM OF SQUARES)/(NUMBER OF POINTS) =                |  |  |  |
| (0219) | 88884 | FORMAT('////',' INTERVAL          NO. OF PTS.          KNOT          R |  |  |  |
| (0220) |       | *, ' POWELL1          POWELL2'   |  |  |  |
| (0221) | 88883 | FORMAT(I3,'          ',I4,4D15.5)                                      |  |  |  |
| (0222) | 88882 | FORMAT('NO POWELL TEST SINCE NO. OF POINTS IN INTERVAL=',              |  |  |  |
| (0223) |       | *I3)   |  |  |  |
| (0224) | 88881 | FORMAT(' POINT          TEMP          THERMAL EXP.          2ND'       |  |  |  |
| (0225) |       | *, ' TERM          CU EXP.')   |  |  |  |
| (0226) | 88880 | FORMAT(I3,5D15.5)  |  |  |  |
| (0227) | 88879 | FORMAT('NO.          TEMP          ALPHA          DIFF. IN ALPHA')     |  |  |  |
| (0228) |       | C  |  |  |  |
| (0229) |       | C  |  |  |  |
| (0230) |       | C  |  |  |  |
| (0231) | C     | CALL INTERACTIVE GRAFICS ROUTINE TO INTEROGATE FINAL RESUL             |  |  |  |
| (0232) | C     | AND CLOSE FILE FOR DATA TO BE HARD COPIED ON CALCOMP.                  |  |  |  |
| (0233) |       | C  |  |  |  |
| (0234) |       | C  |  |  |  |
| (0235) |       | C  |  |  |  |
| (0236) |       | CALL GRAFIT(M,0)   |  |  |  |
| (0237) |       | WRITE(7,100)   |  |  |  |
| (0238) | 100   | FORMAT('0')  |  |  |  |
| (0239) |       | REWIND 7   |  |  |  |
| (0240) |       | CALL DCOPY   |  |  |  |
| (0241) |       | C  |  |  |  |
| (0242) |       | C  |  |  |  |
| (0243) | C     | ALGORITHM COMPLETE TERMINATE PROGRAM.                                  |  |  |  |
| (0244) |       | C  |  |  |  |
| (0245) |       | C  |  |  |  |
| (0246) |       | CALL EXIT  |  |  |  |
| (0247) |       | END  |  |  |  |

```

(0248)      DOUBLE PRECISION FUNCTION CUEX(B,A)
(0249)      C
(0250)      C
(0251)      C  THIS SUBROUTINE INTEGRATES THE HCOF COPPER EXPANSION DATA OV
(0252)      C  THE REQUIRED TEMPERATURE RANGE.
(0253)      C
(0254)      C  THE SUBROUTINE USES THE NAGF LIBRARY ROUTINE D01ACF
(0255)      C
(0256)      C
(0257)      IMPLICIT DOUBLE PRECISION(A-H,O-W)
(0258)      EXTERNAL FUN
(0259)      RELACC=1.0D-10
(0260)      ABSACC=0.0
(0261)      IFAIL=1
(0262)      CALL D01ACF(A,B,FUN,RELACC,ABSACC,ACC,CUEX,N,IFAIL)
(0263)      RETURN
(0264)      END
PROGRAM SIZE:  PROCEDURE - 000052  LINKAGE - 000046  STACK - 00003
NO ERRORS [CUEX :FTNLUT4-REV17.2]

```

```
(0265)      DOUBLE PRECISION FUNCTION FUN(X)
(0266)      C
(0267)      C
(0268)      C  FUNCTION FUN IS A DUMMY ROUTINE REQUIRED BY LIBRARY ROUTINE
(0269)      C  D01ACF.
(0270)      C
(0271)      C
(0272)      IMPLICIT DOUBLE PRECISION(A-H,O-Z)
(0273)      EXTERNAL ACU
(0274)      FUN=ACU(X)
(0275)      RETURN
(0276)      END
PROGRAM SIZE:  PROCEDURE - 000010    LINKAGE - 000026    STACK - 000030
NO  ERRORS [(FUN  )FTNLUT4-REV17.2]
```

```

(0277)      DOUBLE PRECISION FUNCTION GAP(A,AT)
(0278) C
(0279) C
(0280) C
(0281) C      FUNCTION TO CALCULATE GAP FROM CAPACITANCE FOR GUARD RING
(0282) C      PARRALLEL PLATE CAPACITOR.
(0283) C      ROUTINE USES NEWTON-RAPHSON TECHNIQUE
(0284) C      FOR FINDING THE ROOT OF A TRANS. FUNC.
(0285) C
(0286) C      F(X)=FUNCTION RELATING CAPACITANCE TO GAP.
(0287) C
(0288) C      MAX. NUMBER OF ITERATIONS IS 50
(0289) C      REQUIRED ACCURACY=1.0E-12
(0290) C      DF(X)=1ST DIFF. OF F(X)
(0291) C
(0292) C
(0293) C      IMPLICIT DOUBLE PRECISION (A-H,K-Z), INTEGER (I,J)
(0294) C      COMMON /B/ A1,A2,A3,IOUT,IIN,A4,A5
(0295) C      EXTERNAL F,DF
(0296) C      I=0
(0297) C      AT2=300.
(0298) C
(0299) C
(0300) C      SUBROUTINE CUCALL CALCULATE THE TEMPERATURE DEPENDANT
(0301) C      CONSTANTS REQUIRED FOR FUNCTION F(X).
(0302) C
(0303) C
(0304) C      CALL CUCALL(AT2,AT)
(0305) C      X=A1/A
(0306) 10    Y=F(X,A)
(0307) C      Z=DF(X,A)
(0308) C      XNEW=X-(Y/Z)
(0309) C      EPS=DABS(XNEW-X)/XNEW
(0310) C      X=XNEW
(0311) C      I=I+1
(0312) C
(0313) C
(0314) C      IF FUNCTION DOES NOT CONVERGE IN SUFFICIENT ITERATIONS
(0315) C      THEN TERMINATE ALGORITHM.
(0316) C
(0317) C
(0318) C      IF(I.GT.50)CALL EXIT
(0319) C      IF(EPS.GT.1.0D-12)GO TO 10
(0320) C      GAP=X
(0321) C      RETURN
(0322) C      END

```

PROGRAM SIZE:    PROCEDURE - 000130    LINKAGE - 000072    STACK - 000036  
 NO ERRORS [GAP    ]FTNLUT4-REV17.2]



```

(0323)          SUBROUTINE CUCALL(B,A)
(0324)  C
(0325)  C
(0326)  C
(0327)  C          ROUTINE TO COMPENSATE FOR EXPANSION OF
(0328)  C          COPPER ELECTRODES.
(0329)  C
(0330)  C          USES NAGF LIBRARY ROUTINE D01C
(0331)  C
(0332)  C
(0333)  C  THIS ROUTINE CALCULATES THE CONSTANTS REQUIRED BY FUNCTION F(
(0334)  C
(0335)  C
(0336)  C
(0337)          IMPLICIT DOUBLE PRECISION(A-H,O-Z)
(0338)          COMMON /B/A1,A2,A3,I1,I2,A4,A5
(0339)          EXTERNAL CUEX
(0340)          C=CUEX(B,A)
(0341)          A1=3.14159*A4*A4*(1.0-C)*8.85419
(0342)          A2=3.14159*A5/(A4*(1.0-C))
(0343)          A2=A2*((A5/(2.0*A4*(1.0-C)))+1.0)
(0344)          A3=0.22*A5/6.3
(0345)          RETURN
(0346)          END
PROGRAM SIZE:  PROCEDURE - 000114  LINKAGE - 000040  STACK - 000036
NO ERRORS [CUCALL]FTNLUT4-REV17.2]

```

```

(0347)      DOUBLE PRECISION FUNCTION ACU(T)
(0348)  C
(0349)  C
(0350)  C
(0351)  C      THIS FUNCTION EVALUATES THE EXPANSION COEFFICIENT OF H.C.O.F
(0352)  C      COPPER FOR ANY TEMPERATURE 2<T<300 K      USING DATA
(0353)  C      FROM KROEGER AND SWENSON(1977).
(0354)  C
(0355)  C
(0356)  C
(0357)      IMPLICIT DOUBLE PRECISION(A-M,D-Z)
(0358)      COMMON /B/ A1,A2,A3,NOUT,NIN,A4,A5
(0359)      A=0.0D0
(0360)      IF(T.GT.2.0D0)GO TO 17
(0361)      WRITE(NOUT,77777)
(0362)  17      IF(T.GT.2.50D1)GO TO 18
(0363)      ACU=2.53507D-10*T+2.66846D-11*(T*T*T)
(0364)      ACU=ACU+3.56435D-15*(T**5)+5.33091D-17*(T**7)
(0365)      ACU=ACU-8.23846D-20*(T**9)+3.62967D-23*(T**11)
(0366)      GO TO 24
(0367)  18      IF(T.GT.5.0D1)GO TO 19
(0368)      ACU=-5.40693D-7+1.17048D-7*T-9.73141D-9*T*T+3.9847D-10*T*T*T
(0369)      ACU=ACU-5.79623D-12*(T**4)+2.97174D-14*(T**5)
(0370)      GO TO 24
(0371)  19      IF(T.GT.1.0D2)GO TO 21
(0372)      ACU=-6.95076D-6-6.38706D-7*T+2.18457D-8*T*T-2.82703D-10*T*T*T
(0373)      ACU=ACU+1.74267D-12*T*T*T*T-4.25784D-15*(T**5)
(0374)      GO TO 24
(0375)  21      IF(T.GT.3.25D2)GO TO 22
(0376)      ACU=-1.12857D-5+4.13254D-7*T-2.60267D-9*T*T+1.03271D-11*T*T*T
(0377)      ACU=ACU-1.97422D-14*T*T*T*T+1.53667D-17*(T**5)
(0378)      GO TO 24
(0379)  22      WRITE(NOUT,77776)
(0380)      GO TO 21
(0381)  C
(0382)  C
(0383)  C      IF TEMPERATURE OUT OF RANGE      SAY SO.
(0384)  C
(0385)  C
(0386)      77776 FORMAT('OUT OF RANGE-TABOVE 325K')
(0387)      77777 FORMAT('OUT OF RANGE-BELLOW 2K')
(0388)      24      RETURN
(0389)      END

```

```

PROGRAM SIZE:  PROCEDURE - 000662      LINKAGE - 000046      STACK - 000044
NO ERRORS [(ACU )FTNLUT4-REV17.2]

```

```
(0390)      DOUBLE PRECISION FUNCTION F(X,B)
(0391)  C
(0392)  C
(0393)  C      THIS FUNCTION EVALUATES THE DIFFERENCE BETWEEN
(0394)  C      THE CAPACITANCE CORRESPONDING TO GAP X AND THE ACTUAL
(0395)  C      CAPACITANCE B
(0396)  C
(0397)  C
(0398)      IMPLICIT DOUBLE PRECISION(B-Z),INTEGER(A)
(0399)      COMMON /B/B1,B2,B3,A1,A2,B4,B5
(0400)      F=B1*((1.0/X)+(B2/(X+B3)))-B
(0401)      RETURN
(0402)      END
PROGRAM SIZE:  PROCEDURE - 000036  LINKAGE - 000032  STACK - 000036
NO ERRORS [(F      )FTNLUT4-REV17.2]
```

(0403) DOUBLE PRECISION FUNCTION DF(X,B)

(0404) C

(0405) C

(0406) C

(0407) C THIS FUNCTION EVALUATES THE FIRST DERIVATIVE  
(0408) C OF THE FUNCTION F(X,B).

(0409) C

(0410) C

(0411) IMPLICIT DOUBLE PRECISION(B-Z),INTEGER(A)

(0412) COMMON /B/B1,B2,B3,A1,A2,B4,B5

(0413) DF=-1.0\*B1\*((1.0/(X\*X))+(B2/((X+B3)\*\*2)))

(0414) RETURN

(0415) END

PROGRAM SIZE: PROCEDURE - 000050 LINKAGE - 000032 STACK - 000042  
NO ERRORS [ (DF )FTNLUT4-REV17.2]

```

(0416)      SUBROUTINE CSF(M)
(0417)  C
(0418)  C
(0419)  C
(0420)  C   THIS IS AN INTERACTIVE FITTING ROUTINE USING
(0421)  C   BETA CUBED SPLINE FUNCTIONS WITH INTERACTIVE GRAFICS.
(0422)  C
(0423)  C
(0424)  C
(0425)      IMPLICIT DOUBLE PRECISION (A-F,H,K,O-Q,S-Y),
(0426)      *INTEGER(I,J,L,M,N,R)
(0427)      *,REAL(G)
(0428)      COMMON /R/ IYT
(0429)      COMMON /A/ NCAP7,K(100),C(100),IFAIL,NCAP,SS,SDASH(4)
(0430)      COMMON /G/X(250),Y(250),W(250),
(0431)      *AGRAD(250),D(250),SPEXP(250),ARES(250),YCALC(250),
(0432)      *WORK1(200),WORK2(4,100),TR(4,50),XEX(250),SPL1,LSET
(0433)      *,SPL2
(0434)      COMMON /Z/ GX1(500),GY1(500),NV1,NS1,
(0435)      *GXS1(250),GYS1(250),ICUR,GMA,GMI,IW,IYY,IDEV
(0436)      EXTERNAL ACU
(0437)  C
(0438)  C
(0439)  C   INITIALISE FITTING PARAMETERS AND CALCULATE COPPER EXPANSION
(0440)  C   COEFFICIENTS.
(0441)  C
(0442)  C
(0443)      NCAP=1
(0444)      WRITE(1,10)
(0445)  10   FORMAT('FITTING ROUTINE'//
(0446)      *'PLOT RAW GAP DATA FIRST')
(0447)      DO 19 I=1,M
(0448)  19   XEX(I)=ACU(X(I))
(0449)  C
(0450)  C
(0451)  C   CALL NAGF LIBRARY ROUTINE E02BAF TO EVALUATE SPLINE.
(0452)  C
(0453)  C
(0454)  20   NCAP2=NCAP+2
(0455)      NCAP3=NCAP+3
(0456)      NCAP7=NCAP+7
(0457)      IFAIL=0
(0458)      CALL E02BAF(M,NCAP7,X,Y,W,K,WORK1,
(0459)      *WORK2,C,SS,IFAIL)
(0460)      IF(IFAIL.EQ.0)GO TO 30
(0461)      WRITE (1,150)IFAIL
(0462)  150  FORMAT('ERROR IN E02BAF,IFAIL= ',I3)
(0463)  C
(0464)  C
(0465)  C   EVALUATE THE FIT USING NAGF ROUTINE E02BCF,
(0466)  C   CALCULATE THE FIT,RESIDUALS, DERIVATIVE OF FIT
(0467)  C   AND EXPANSION COEFFICIENT.
(0468)  C
(0469)  C
(0470)  30   DO 88 I=1,M
(0471)      IFAIL=0
(0472)      NCAP4=NCAP+4
(0473)      IF(X(I).GT.K(NCAP4))GO TO 31
(0474)      IL=0
(0475)      CALL E02BCF(NCAP7,K,C,X(I),IL,SDASH,IFAIL)
(0476)      YCALC(I)=SDASH(1)
(0477)      ARES(I)=YCALC(I)-Y(I)

```

```

(0478)      AGRAD(I)=SDASH(2)/SPL1
(0479)      SPEXP(I)=(SPL2/1.0D10)*XEX(I)-AGRAD(I)
(0480)      GO TO 88
(0481)      C
(0482)      C
(0483)      C   IF ERROR IS FOUND SAY SO.
(0484)      C
(0485)      C
(0486)      31      WRITE(1,33)I,X(I),NCAP7,K(NCAP4)
(0487)      33      FORMAT('ERROR   I=',I3/
(0488)      *5X,'X(I)=' ,D20.8/
(0489)      *5X,'NCAP7=' ,I3/
(0490)      *'K(NCAP4)=' ,D20.8)
(0491)      YCALC(I)=Y(I)
(0492)      ARES(I)=0.0
(0493)      88      CONTINUE
(0494)      C
(0495)      C
(0496)      C   INPUT REQUIRED Y-AXIS FOR PLOTTING ROUTINE.
(0497)      C
(0498)      C
(0499)      WRITE(1,91)
(0500)      91      FORMAT('WHAT DO YOU WANT TO PLOT'//
(0501)      *'TYPE 1 FOR RESIDUALS' /
(0502)      *'TYPE 2 FOR GAP' /
(0503)      *'TYPE 3 FOR EXPANSION COEFFICIENT')
(0504)      READ(1,*)IJB
(0505)      C
(0506)      C
(0507)      C   CALL INTERACTIVE PLOTTING ROUTINE.
(0508)      C
(0509)      C
(0510)      GO TO (92,93,95),IJB
(0511)      93      IYT=1
(0512)      CALL GRAFIT(M,3)
(0513)      GO TO 94
(0514)      95      IYT=5
(0515)      CALL GRAFIT(M,5)
(0516)      GO TO 94
(0517)      92      IYT=4
(0518)      CALL GRAFIT(M,4)
(0519)      C
(0520)      C
(0521)      C   INTEROGATE IF FURTHER ATTEMPT AT FIT IS REQUIRED.
(0522)      C
(0523)      C
(0524)      94      WRITE (1,81)
(0525)      81      FORMAT('IF FIT IS SUFFICIENT AND YOU WISH TO ',
(0526)      *'RETURN TYPE 1' /
(0527)      *'IF FIT IS INSUFFICIENT AND YOU WISH TO CHANGE FIT TYPE 0' /
(0528)      *'IF YOU WISH TO FINISH TYPE 2')
(0529)      READ(1,*)I
(0530)      IF(I.EQ.1)RETURN
(0531)      IF(I.EQ.2)CALL EXIT
(0532)      GO TO 20
(0533)      END

```

PROGRAM SIZE:    PROCEDURE - 001016    LINKAGE - 000140    STACK - 000032  
 NO ERRORS [ (CSF    )FTNLUT4-REV17.2]

```

(0534)      SUBROUTINE GRAFIT(M,NY)
(0535)      C
(0536)      C
(0537)      C      THIS ROUTINE AND THE ROUTINE GRAFIC PROVIDE THE
(0538)      C      INTERACTIVE GRAPHICS PACKAGE.
(0539)      C
(0540)      C      ROUTINE GRAFIT PROVIDES DATA REQUIRED FOR
(0541)      C      DEVICE TO PLOT GRAPH AND GRAFIC DRAWS THIS GRAPH
(0542)      C      ON THE NOMINATED TERMINAL.
(0543)      C
(0544)      C
(0545)      IMPLICIT DOUBLE PRECISION(A,E)
(0546)      COMMON /A/ NCAP7,AK(100),AC(100),IFAIL,NCAP,ASS,ASDASH(4)
(0547)      COMMON /C/ APLOT(250,8),AWORK1(200),AWORK2(4,100)
(0548)      *,ATR(4,50),AEX(250),ASPL1,LSET,ASPL2
(0549)      COMMON /R/IYT
(0550)      COMMON /Z/ XRES(500),YRES(500),NVAL,NSYM,
(0551)      *XSYM(250),YSYM(250),ICUR,XMAX,XMIN,IW,IY,NDEV
(0552)      3      FORMAT('DO YOU WISH TO PLOT THE SAME ORDINATE AGAIN' /
(0553)      *'TYPE 1 FOR YES')
(0554)      NYIN=0
(0555)      ICUR=1
(0556)      IW=1
(0557)      IF(NY.EQ.0)NYIN=1
(0558)      XMAX=APLOT(M,1)
(0559)      XMIN=APLOT(1,1)
(0560)      2      IF(NYIN.EQ.1)NY=0
(0561)      C
(0562)      C
(0563)      C      IF Y-AXIS HAS NOT ALREADY BEEN NOMINATED ASK
(0564)      C      WHICH Y-AXIS REQUIRED.
(0565)      C
(0566)      C
(0567)      IF(NY.NE.0)GO TO 15
(0568)      ICUR=0
(0569)      IW=0
(0570)      WRITE(1,10)
(0571)      10      FORMAT('PLOTING ROUTINE' ///
(0572)      *' INPUT REQUIRED YAXIS' /
(0573)      *' 1=CAPACITANCE' /
(0574)      *' 2=GAP' /
(0575)      *' 3=FITTED GAP WITH DATA INCLUDED' /
(0576)      *' 4=RESIDUALS' /
(0577)      *' 5=EXP. COEF.')
(0578)      READ(1,*)NY
(0579)      IYT=NY
(0580)      NSYM=0
(0581)      15      IMIN=0
(0582)      IMAX=0
(0583)      IY=NY+1
(0584)      C
(0585)      C
(0586)      C      FIND MAXIMUM AND MINIMUM LIMITS OF X-AXIS
(0587)      C
(0588)      C
(0589)      30      DO 40 I=1,M
(0590)      IF(IMIN.NE.0)GO TO 35
(0591)      IF(APLOT(I,1).GE.XMIN)IMIN=I
(0592)      35      IF(IMAX.NE.0)GO TO 40
(0593)      IF(APLOT(I,1).GE.XMAX)IMAX=I
(0594)      40      CONTINUE
(0595)      NVAL=IMAX-IMIN

```

```

(0596) C
(0597) C
(0598) C      LOAD REQUIRED X AND Y AXES INTO PLOTTING ARRAYS.
(0599) C
(0600) C
(0601)      DO 50 I=1,NVAL
(0602)          I1=1+IMIN
(0603)          XSYM(I)=APLOT(I1,1)
(0604) 50      CONTINUE
(0605)          IF(NV.EQ.3)GO TO 60
(0606)          IF(NV.EQ.1)NP=5
(0607)          IF(NV.EQ.2)NP=2
(0608)          IF(NV.EQ.4)NP=7
(0609)          IF(NV.EQ.5)NP=6
(0610)      DO 70 I=1,NVAL
(0611)          I1=1+IMIN
(0612)          YSYM(I)=APLOT(I1,NP)
(0613) 70      CONTINUE
(0614)      NSYM=NVAL
(0615)      NVAL=0
(0616)      GO TO 90
(0617) 60      DO 75 I=1,NVAL
(0618)          I1=IMIN+I
(0619)          YSYM(I)=APLOT(I1,2)
(0620) 75      CONTINUE
(0621)      EX=(XMAX-XMIN)/500.
(0622) C
(0623) C
(0624) C      CALCULATE DATA FOR FITED GAP PLOT IF REQUIRED.
(0625) C
(0626) C
(0627)      DO 85 I=1,500
(0628)          XRES(I)=XMIN+EX*FLOAT(I)
(0629)          AXR=DBLE(XRES(I))
(0630)          IF(AXR.GE.AK(NCAP7))WRITE(1,356)AXR,AK(NCAP7)
(0631) 356      FORMAT('ERROR GRAFIT X=',D20.6/
(0632)          *,      AK(NCAP7)=' ,D20.6)
(0633)          IF(AXR.GE.AK(NCAP7))GO TO 357
(0634)          IF(AXR.LT.AK(1) )AXR=AK(1)
(0635)          IL=0
(0636)          CALL E02BBF(NCAP7,AK,AC,AXR,AFIT,IFAIL)
(0637) 357      YRES(I)=AFIT
(0638) 85      CONTINUE
(0639)      NSYM=NVAL
(0640)      NVAL=500
(0641) C
(0642) C
(0643) C      PLOT GRAF
(0644) C
(0645) C
(0646) 90      CALL GRAFIC
(0647) C
(0648) C
(0649) C      DECIDE IF MODIFIED PLOT REQUIRED.CALCULATE FIT PARAMETERS
(0650) C      IF IT IS SO.
(0651) C
(0652) C
(0653)      WRITE(1,3)
(0654)      READ(1,*)NCON
(0655)      IF(NCON.EQ.0)RETURN
(0656)      CALL CSF2(M)
(0657)      GO TO 2

```



```

(0659)          SUBROUTINE GRAFIC
(0660)  C
(0661)  C
(0662)  C      THIS ROUTINE PLOTS THE GRAF SET UP IN ROUTINE GRAFIT
(0663)  C
(0664)  C
(0665)          IMPLICIT DOUBLE PRECISION (Z)
(0666)          COMMON /A/ NCAP7,ZK(100),ZC(100),IFAIL,NCAP,ZSS,ZSDASH(4)
(0667)          COMMON /Z/ XR(500),YR(500),NVAL,NSYM,XS(250),YS(250)
(0668)          *,ICUR,XMAX,XMIN,IW,IY,NDEV
(0669)          COMMON /R/IYT
(0670)          EXTERNAL PEAR3
(0671)  C
(0672)  C
(0673)  C      CALL GINO LIBRARY ROUTINE FOR REQUIRED DEVICE
(0674)  C
(0675)  C
(0676)          GO TO(301,302,303,305),NDEV
(0677)  301      CALL TREND
(0678)          GO TO 304
(0679)  302      CALL F4010
(0680)          GO TO 304
(0681)  303      CALL S5600
(0682)          GO TO 304
(0683)  305      CALL S5660
(0684)  304      CONTINUE
(0685)  C
(0686)  C
(0687)  C      INITIALISE WINDOW AND CURSOR PARAMETERS.
(0688)  C
(0689)  C
(0690)          CALL WINDOW(2)
(0691)          CALL CURDEF(6HXYZO*.)
(0692)  C
(0693)  C
(0694)  C      CALCULATE POSITION AND SCALES FOR AXES.
(0695)  C
(0696)  C
(0697)          VXBEG=0.0
(0698)          VYBEG=0.0
(0699)          VXEND=0.0
(0700)          VYEND=0.0
(0701)          IF(NSYM.EQ.0)GO TO 10
(0702)          VXBEG=XS(1)
(0703)          VYBEG=YS(1)
(0704)          DO 5 I=1,NSYM
(0705)              IF(XS(I).LT.VXBEG)VXBEG=XS(I)
(0706)              IF(YS(I).LT.VYBEG)VYBEG=YS(I)
(0707)              IF(XS(I).GT.VXEND)VXEND=XS(I)
(0708)              IF(YS(I).GT.VYEND)VYEND=YS(I)
(0709)          5      CONTINUE
(0710)          10      IF(NVAL.EQ.0)GO TO 20
(0711)          DO 15 I=1,NVAL
(0712)              IF(XR(I).LT.VXBEG)VXBEG=XR(I)
(0713)              IF(XR(I).GT.VXEND)VXEND=XR(I)
(0714)              IF(YR(I).LT.VYBEG)VYBEG=YR(I)
(0715)              IF(YR(I).GT.VYEND)VYEND=YR(I)
(0716)          15      CONTINUE
(0717)          20      IF(IXSCAL.NE.1)IXSCAL=4
(0718)                  IYSCAL=1
(0719)  C      CALCULATE NO. OF INTERVALS
(0720)          AXINTS=AINTE(((VXEND-VXBEG)/5.))+1.)

```

```

(0721)      NXINTS=IFIX(AXINTS)
(0722)      AXIS=VYEND-VYBEG
(0723)  201  IF(AXIS.GT.1.0)GO TO 202
(0724)      AXIS =AXIS*100.
(0725)      GO TO 201
(0726)  202  IF(AXIS.LT.20.)GO TO 203
(0727)      AXIS=AXIS*0.2
(0728)      GO TO 202
(0729)  203  NYINTS=IFIX(AXIS)
(0730)      IF(NYINTS.GT.0)GO TO 212
(0731)      WRITE(1,213)NYINTS
(0732)  213  FORMAT('ERROR NYINTS= ',I3)
(0733)      NYINTS=10
(0734)  212  CONTINUE
(0735)      IF(VYBEG.LE.0.0)GO TO 214
(0736)      IF(NSYN.EQ.0)GO TO 215
(0737)      IF(IYT.EQ.5)GO TO 215
(0738)      DO 216 IBN=1,NSYM
(0739)  216  YS(IBN)=YS(IBN)-VYBEG
(0740)  215  IF(NVAL.EQ.0)GO TO 217
(0741)      DO 218 IBN=1,NVAL
(0742)  218  YR(IBN)=YR(IBN)-VYBEG
(0743)  217  VYEND=VYEND-VYBEG
(0744)      VYBEG=0.0
(0745)  214  ICROSS=0
(0746)      IF(VXBEG.LT.0.OR.VYBEG.LT.0)ICROSS=1
(0747)  C
(0748)  C
(0749)  C  CLEAR PICTURE AREA,
(0750)  C  CHANGE PEN COLOUR IF POSSIBLE AND
(0751)  C  DRAW AXES.
(0752)  C
(0753)  C
(0754)      IF(NDEV.EQ.1)GO TO 3412
(0755)      CALL PICCLE
(0756)  3412  IF(NDEV.EQ.4)CALL PENSEL(15,0.0,0)
(0757)      GO TO (1101,1102,1102,1103,1104),IYT
(0758)  1101  CALL AXIPLO(ICROSS,0.,0.,IXSCAL,IYSCAL,
(0759)      *NXINTS,NYINTS,VXBEG,VXEND,VYBEG,VYEND,
(0760)      *'TEMPERATURE',11,'CAPACITANCE',11)
(0761)      GO TO 1105
(0762)  1102  CALL AXIPLO(ICROSS,0.,0.,IXSCAL,IYSCAL,
(0763)      *NXINTS,NYINTS,VXBEG,VXEND,VYBEG,VYEND,
(0764)      *'TEMPERATURE',11,'DELTA GAP',9)
(0765)      GO TO 1105
(0766)  1103  CALL AXIPLO(ICROSS,0.,0.,IXSCAL,IYSCAL,
(0767)      *NXINTS,NYINTS,VXBEG,VXEND,VYBEG,VYEND,
(0768)      *'TEMPERATURE',11,'RESIDUALS',9)
(0769)      GO TO 1105
(0770)  1104  CALL AXIPLO(ICROSS,0.,0.,IXSCAL,IYSCAL,
(0771)      *NXINTS,NYINTS,VXBEG,VXEND,VYBEG,VYEND,
(0772)      *'TEMPERATURE',11,'EXP. COEF.',10)
(0773)  1105  CONTINUE
(0774)      CALL AXIDRA(-2,0,2)
(0775)  C
(0776)  C
(0777)  C  IF THERE ARE ANY INTERIOR KNOTS
(0778)  C  CHANGE PEN COLOUR IF POSSIBLE AND
(0779)  C  DRAW DOTTED LINE IN REQUIRED POSITION.
(0780)  C
(0781)  C
(0782)      CALL AXIDRA(2,0,1)

```

```

(0783)      NCAP3=NCAP+3
(0784)      IF(NCAP.EQ.0.OR.NCAP.EQ.1)GO TO 117
(0785)      CALL BROKEN(1)
(0786)      IF(NDEV.EQ.4)CALL PENSEL(1,0.0,0)
(0787)      DO 136 IBN=5,NCAP3
(0788)      XB=ZK(IBN)
(0789)      IF(XB.GT.VXEND)GO TO 136
(0790)      CALL GRAMOV(XB,VYBEG)
(0791)      CALL GRALIN(XB,VYEND)
(0792) 136   CONTINUE
(0793)      CALL BROKEN(0)
(0794)      C
(0795)      C
(0796)      C      PLOT X AT (X,Y) COORDINATES OF POINTS
(0797)      C
(0798)      C
(0799) 117   IF(NSYM.EQ.0)GO TO 30
(0800)      IF(NDEV.EQ.4)CALL PENSEL(3,0.0,0)
(0801)      C
(0802)      C
(0803)      C      IF CURVE THROUGH FITTED POINTS REQUIRED
(0804)      C      CHANGE PEN COLOUR AND DRAW IT.
(0805)      C
(0806)      C
(0807)      - CALL DRASYM(XS,YS,NSYM,4,0)
(0808) 30    IF(NVAL.EQ.0)GO TO 40
(0809)      IF(NDEV.EQ.4)CALL PENSEL(2,0.0,0)
(0810)      CALL DRAPOL(XR,YR,NVAL)
(0811) 40    CALL CHAPDS(1,1.)
(0812)      C
(0813)      C
(0814)      C      IF IT IS REQUIRED TO PLOT A HARD COPY OF THE GRAPH JUST COMPI
(0815)      C      OUTPUT PLOTTING PARAMETERS TO A FILE.
(0816)      C
(0817)      C
(0818)      WRITE(1,65)
(0819) 65    FORMAT('DO YOU WANT A HARD COPY',2X,'TYPE 1 FOR YES')
(0820)      READ(1,*)IJB
(0821)      IF(IJB.NE.1)GO TO 66
(0822)      WRITE(7,401)
(0823) 401   FORMAT('1')
(0824)      WRITE(7,402)ICROSS,IXSCAL,IYSCAL,NXINTS,NYINTS,
(0825)      *VXBEG,VXEND,VYBEG,VYEND
(0826)      WRITE(7,403)IYT
(0827) 402   FORMAT(5I3,4E12.5)
(0828)      WRITE(7,403)NCAP
(0829) 403   FORMAT(12)
(0830)      IF(NCAP.LT.2)GO TO 406
(0831)      DO 404 IJB=5,NCAP3
(0832)      XK=ZK(IJB)
(0833)      WRITE(7,405)XK
(0834) 404   CONTINUE
(0835) 405   FORMAT(E12.5)
(0836) 406   WRITE(7,407)NSYM
(0837) 407   FORMAT(I3)
(0838)      IF(NSYM.EQ.0)GO TO 410
(0839)      DO 408 IJB=1,NSYM
(0840) 408   WRITE(7,409)XS(IJB),YS(IJB)
(0841) 409   FORMAT(2E12.5)
(0842) 410   WRITE(7,411)NVAL
(0843) 411   FORMAT(I3)
(0844)      IF(NVAL.EQ.0)GO TO 414

```

```

(0845)      DO 412 IJB=1,NVAL
(0846) 412  WRITE(7,413)XR(IJB),YR(IJB)
(0847) 413  FORMAT(2E12.5)
(0848) 414  CONTINUE
(0849) 66   IF(ICUR.EQ.0)GO TO 41
(0850)      CALL CHAPDS(1.,1.)
(0851) C
(0852) C
(0853) C      CHANGE FITTING PARAMETERS AND SCALE FACTORS.
(0854) C
(0855) C
(0856)      WRITE(1,61)
(0857) 61   FORMAT('TYPE 1 IF YOU WISH TO CHANGE KNOTS')
(0858)      READ(1,*)IJB
(0859)      IF(IJB.NE.1)GO TO 41
(0860) C
(0861) C
(0862) C      CALCULATE PEARSON CORRELATION COEFFICIENT
(0863) C      TO OBTAIN A MEASURE OF THE VALUE OF FIT
(0864) C      ALREADY OBTAINED.
(0865) C
(0866) C
(0867)      PC1=PEARS(XS,YS,NSYM)
(0868)      WRITE(1,62)PC1
(0869) 62   FORMAT('PEARSON CORRELATION COEFF. =' ,E12.6)
(0870)      WRITE(1,63)
(0871) C
(0872) C
(0873) C      USE CURSOR (IF AVAILABLE ON PLOTTING DEVICE)
(0874) C      TO INPUT,DELETE OR OPTIMISE KNOT POSITIONS.
(0875) C
(0876) C
(0877) 63   FORMAT('TYPE X TO READ POSITION Y TO CONTINUE' /
(0878)      *'OR I TO DELETE' /
(0879)      *'OR C TO INPUT KNOT THEN OPTIMISE')
(0880) 68   IF(NDEV.NE.1)CALL CURSOR(ICOM,XGR,YGR)
(0881)      CALL SPAGRA(XGR,YGR,XSS,YSS)
(0882)      XGR=XSS
(0883)      IF(ICOM.EQ.2)GO TO 41
(0884)      IF(ICOM.EQ.3)CALL KDEL(VYBEG,VYEND,XGR,NDEV)
(0885)      IF(ICOM.EQ.3)GO TO 68
(0886)      CALL KCH(VYBEG,VYEND,XGR,NDEV)
(0887)      WRITE(1,64)XGR
(0888) 64   FORMAT('POSITION OF CURSOR IS  X=' ,E12.5)
(0889) C
(0890) C
(0891) C      IF REQUIRED (ICOM = 4) USE NAGF ROUTINE E04JAF TO
(0892) C      OPTIMISE POSITION OF KNOTS TO FIND A LOCAL MINIMUM
(0893) C      IN THE TOTAL MEAN SQUARE ERROR IN FIT.
(0894) C
(0895) C
(0896) C
(0897)      IF(ICOM.EQ.4)CALL OPTMIZ(VXBEG,VXEND,VYBEG,VYEND,NDEV)
(0898)      GO TO 68
(0899) 41   WRITE (1,51)
(0900) C
(0901) C
(0902) C      IF SCALE CHANGE REQUIRED THEN DO SO
(0903) C
(0904) C
(0905) 51   FORMAT('DO YOU WISH TO CHANGE SCALE' ,
(0906)      *' ,TYPE 0 FOR NO')

```

```

(0907)      READ (1,*) IJB
(0908)      IF(IJB.EQ.0)GO TO 52
(0909)      WRITE(1,59)
(0910) 59    FORMAT('TYPE X TO INPUT CURSOR POSITION ',
(0911)      *,'INPUT MIN THEN MAX POSITIONS')
(0912)      IF(NDEV.NE.1)CALL CURSOR(ICOM,XMIN,YGR)
(0913)      CALL SPAGRA(XMIN,YGR,XSS,YSS)
(0914)      XMIN=XSS
(0915)      IF(NDEV.NE.1)CALL CURSOR(ICOM,XMAX,YGR)
(0916)      CALL SPAGRA(XMAX,YGR,XSS,YSS)
(0917)      XMAX=XSS
(0918)      IF(XMIN.LT.ZK(1))XMIN=ZK(1)
(0919)      IF(XMAX.GT.ZK(NCAP7))XMAX=ZK(NCAP7)
(0920) 52    WRITE(1,53)
(0921) 53    FORMAT('DO YOU WISH TO CHANGE X-AXIS SCALE TYPE'
(0922)      *,'TYPE 1 FOR YES')
(0923)      READ(1,*) IJB
(0924)      IXSCAL=4
(0925)      IF(IJB.EQ.1)IXSCAL=1
(0926)      IF(IN.EQ.1)CALL WEIGHT(VXEND)
(0927)      CALL PICCLE
(0928)  C
(0929)  C
(0930)  C  GRAPH COMPLETED  TERMINATE DEVICE
(0931)  C
(0932)  C
(0933)      CALL DEVEND
(0934)      RETURN
(0935)      END

```

PROGRAM SIZE:    PROCEDURE - 003000    LINKAGE - 000244    STACK - 000071  
 NO ERRORS [(GRAPHIC)FTNLUT4-REV17.2]

## SUBROUTINE C1IN(I)

(0936)  
(0937) C  
(0938) C  
(0939) C SUBROUTINE T1IN IS A DUMMY ROUTINE TO COMPENSATE  
(0940) C FOR AN ERROR FOUND IN THE GRAPHICS LIBRARY ROUTINES.  
(0941) C  
(0942) C  
(0943) CALL T1IN(I)  
(0944) RETURN  
(0945) END

PROGRAM SIZE: PROCEDURE - 000006 LINKAGE - 000022 STACK - 000030  
NO ERRORS [C1IN 7FTNLUT4-REV17.2]

```

(0946)      FUNCTION PEARS(X,Y,N)
(0947)      C
(0948)      C
(0949)      C  THIS FUNCTION CALCULATES THE PEARSON CORRELATION
(0950)      C COEFFICIENT TO GIVE A MEASURE OF THE QUALITY
(0951)      C OF THE FIT
(0952)      C
(0953)      C
(0954)      DIMENSION X(250),Y(250)
(0955)      SX=0.
(0956)      SY=0.
(0957)      SXY=0.
(0958)      SX2=0.
(0959)      SY2=0.
(0960)      DO 1 I=1,N
(0961)      SX=SX+X(I)
(0962)      SY=SY+Y(I)
(0963)      SXY=SXY+X(I)*Y(I)
(0964)      SX2=SX2+X(I)*X(I)
(0965)      SY2=SY2+Y(I)*Y(I)
(0966)  1    CONTINUE
(0967)      PEARS =FLOAT(N)*SXY-SX*SY
(0968)      PEARS=PEARS/(SQRT((FLOAT(N)*SX2-SX*SX)*(
(0969)      *FLOAT(N) *SY2-SY * SY)))
(0970)      RETURN
(0971)      END

```

```

PROGRAM SIZE:  PROCEDURE - 000174  LINKAGE - 000040  STACK - 00044
NO ERRORS [(PEARS )FTNLUT4-REV17.2]

```

```

(0972)      SUBROUTINE KCH(YB,YE,X,NDEV)
(0973)      C
(0974)      C
(0975)      C      SUBROUTINE TO INSERT KNOT READ BY CURSOR INTO
(0976)      C      KNOT LIST IN STRICTLY ACCENDING ORDER IN
(0977)      C      TEMPERATURE.
(0978)      C
(0979)      C
(0980)      IMPLICIT DOUBLE PRECISION(K,C,S)
(0981)      COMMON /A/ NCAP7,K(100),C(100),IFAIL,NCAP,SS,SDASH(4)
(0982)      SX=DBLE(X)
(0983)      CALL BROKEN(1)
(0984)      IF(NDEV.EQ.4)CALL PENSEL(4,0.0,0)
(0985)      CALL GRAMOV(X,YB)
(0986)      CALL GRALIN(X,YE)
(0987)      CALL BROKEN(0)
(0988)      NCAP4=NCAP+4
(0989)      IHIGH=0
(0990)      DO 10 I=4,NCAP4
(0991)      IF(K(I).LT.SX)ILOW=I
(0992)      IF(IHIGH.NE.0)GO TO 10
(0993)      IF(K(I).GE.SX)IHIGH=I
(0994) 10      CONTINUE
(0995)      J=IHIGH-ILOW
(0996)      IF(J.NE.1)WRITE(1,20)J
(0997) 20      FORMAT('ERROR IN KNOTS,IHIGH-ILOW=',I3)
(0998)      NCAP=NCAP+1
(0999)      DO 30 I=IHIGH,NCAP7
(1000)      J=NCAP7+IHIGH-I
(1001)      J2=J+1
(1002)      K(J2)=K(J)
(1003) 30      CONTINUE
(1004)      K(IHIGH)=SX
(1005)      NCAP7=NCAP+7
(1006)      RETURN
(1007)      END
PROGRAM SIZE:  PROCEDURE - 000232  LINKAGE - 000064  STACK - 000040
NO ERRORS [(KCH )FTNLUT4-REV17.2]

```



```

(1008)      SUBROUTINE KDEL(YB,YE,X,NDEV)
(1009)      C
(1010)      C
(1011)      C      SUBROUTINE TO REMOVE NEAREST KNOT ABOVE CURSOR POSITION
(1012)      C      FROM KNOT LIST AND MAINTAIN STRICTLY ACCENDING ORDER.
(1013)      C
(1014)      C
(1015)      IMPLICIT DOUBLE PRECISION(K,C,S)
(1016)      COMMON /A/ NCAP7,K(100),C(100),IFAIL,NCAP,SS,SDASH(4)
(1017)      SX=DBLE(X)
(1018)      IF(NCAP.NE.1)GO TO 10
(1019)      WRITE (1,5)NCAP
(1020)      5  FORMAT('ERROR IN DELETE,NUMBER OF INTERVALS=',I3)
(1021)      RETURN
(1022)      10  NCAP4=NCAP+4
(1023)      DO 20 I=4,NCAP4
(1024)      20  IF(K(I).LT.SX)ILOW=I
(1025)      I=ILOW+1
(1026)      XB=K(I)
(1027)      CALL BROKEN(0)
(1028)      IF(NDEV.EQ.3.OR.NDEV.EQ.4)CALL PENSEL(1,0,0,6)
(1029)      CALL GRAMOV(XB,YB)
(1030)      CALL GRALIN(XB,YE)
(1031)      IF(NDEV.EQ.3.OR.NDEV.EQ.4)CALL PENSEL(1,0,0,0)
(1032)      NCAP=NCAP-1
(1033)      NCAP7=NCAP+7
(1034)      DO 30 J=1,NCAP7
(1035)      M=J+1
(1036)      K(J)=K(M)
(1037)      30  CONTINUE
(1038)      M=NCAP7+1
(1039)      DO 40 I=M,100
(1040)      40  K(I)=0.0D0
(1041)      RETURN
(1042)      END
PROGRAM SIZE:  PROCEDURE - 000264  LINKAGE - 000070  STACK - 000041
NO ERRORS [(KDEL )FTNLUT4-REV17.2]

```

```

(1043)      SUBROUTINE WEIGHT(X)
(1044)      C
(1045)      C
(1046)      C      SUBROUTINE TO CHANGE WEIGHT FACTOR OF ANY POINTS
(1047)      C      BETWEEN LIMITS IMPOSED BY CURSOR INPUT.
(1048)      C
(1049)      C
(1050)      IMPLICIT DOUBLE PRECISION(A)
(1051)      COMMON /C/AX(250),AY(250),AW(250),
(1052)      *AGR(250),AD(250),ASP(250),ARES(250),AYC(250),
(1053)      *AW1(200),AW2(4,100),AT(4,50),AE(250),ASPL1,LSET
(1054)      *,ASPL2
(1055)      COMMON /D/M
(1056)      60      WRITE(1,10)
(1057)      10      FORMAT('DO YOU WISH TO MODIFY WEIGHT FACTORS' /
(1058)      *'TYPE 1 FOR YES')
(1059)      READ(1,*)I
(1060)      IF(I.NE.1)RETURN
(1061)      WRITE(1,20)
(1062)      20      FORMAT('INPUT RANGE TO BE MODIFIED USING CURSOR' /
(1063)      *'AND TYPING X TO READ, LOWER VALUE FIRST')
(1064)      IF(NDEV.NE.1)CALL CURSOR(ICOM,XS1,YS1)
(1065)      CALL SPAGRA(XS1,YS1,XG1,YG1)
(1066)      IF(NDEV.NE.1)CALL CURSOR(ICOM,XS2,YS2)
(1067)      CALL SPAGRA(XS2,YS2,XG2,YG2)
(1068)      WRITE(1,30)
(1069)      30      FORMAT('NOW READ NEW WEIGHT FACTOR')
(1070)      READ(1,*)ADIN
(1071)      AXG1=XG1
(1072)      AXG2=XG2
(1073)      DO 40 I=1,M
(1074)      IF(AX(I).GT.AXG1.AND.AX(I).LT.AXG2)AW(I)=ADIN
(1075)      40      CONTINUE
(1076)      GO TO 60
(1077)      END

```

PROGRAM SIZE:    PROCEDURE - 000345    LINKAGE - 000106    STACK - 000032  
 NO ERRORS [ (WEIGHT)FTNLUT4-REV17.2]

```

(1079)      SUBROUTINE CSF2(M)
(1079)      C
(1080)      C
(1081)      C      SECOND FITTING ROUTINE TO CALCULATE FIT WHEN
(1082)      C      NECESARY DURING INTERACTIVE FITTING ROUTINE.
(1083)      C
(1084)      C
(1085)      IMPLICIT DOUBLE PRECISION(A-F,H,K,O-Q,S-Y),
(1086)      *INTEGER(I,J,L,M,N,R)
(1087)      COMMON /A/NCAP7,K(100),C(100),IFAIL,NCAP,SS,SDASH(4)
(1088)      COMMON /C/X(250),Y(250),W(250),AG(250),D(250),SP(250),
(1089)      *AR(250),YC(250),W1(200),W2(4,100),TR(4,50),EX(250),SPL1
(1090)      *,SPL2
(1091)      *,LSET
(1092)      NCAP7=NCAP+7
(1093)      IFAIL=0
(1094)      CALL E02BAF(M,NCAP7,X,Y,W,K,W1,W2,C,SS,IFAIL)
(1095)      DO 88 I=1,M
(1096)      IL=0
(1097)      CALL E02BCF(NCAP7,K,C,X(I),IL,SDASH,IFAIL)
(1098)      YC(I)=SDASH(1)
(1099)      AR(I)=YC(I)-Y(I)
(1100)      AG(I)=SDASH(2)/SPL1
(1101)      SP(I)=(SPL2/1.0D10)*EX(I)-AG(I)
(1102) 88      CONTINUE
(1103)      RETURN
(1104)      END
PROGRAM SIZE:  PROCEDURE - 000144  LINKAGE - 000104  STACK - 000032
NO ERRORS [(CSF2 )FTNLUT4-REV17.2]

```

```

(1105) SUBROUTINE OPTMIZ(ZXB,ZXE,ZB,ZE,NDEV)
(1106) C
(1107) C
(1108) C SUBROUTINE OPTMIZ.
(1109) C
(1110) C THIS SUBROUTINE TAKES THE PRESENT KNOT POSITIONS
(1111) C AND USES THESE AS THE START POINT FOR AN
(1112) C OPTIMISATION ROUTINE WHICH ADJUSTS POSITION OF KNOTS
(1113) C TO GIVE A LOCAL MINIMA IN TOTAL RMS ERROR.
(1114) C
(1115) C
(1116) C IMPLICIT DOUBLE PRECISION(A-H,K,O-Y),REAL(Z)
(1117) C COMMON /A/NCAP7,K(100),C(100),IFAIL,NCAP,SS,SDASH(4)
(1118) C COMMON /C/ X(250),Y(250),W(250),A1(3,250),A4(2,250),
(1119) C *A6(200),A7(4,100),A8(4,50),A9(250),A10,I1,A12
(1120) C COMMON /D/NPTS
(1121) C DIMENSION BL(20),BU(20),X1(20),IW(22),W1(500)
(1122) C
(1123) C RUBOUT KNOTS ALREADY PLOTTED TO AVOID CONFUSION.
(1124) C
(1125) C CALL BROKEN(0)
(1126) C IF(NDEV.EQ.3.OR.NDEV.EQ.4)CALL PENSEL(1,0.0,6)
(1127) C NCAP3=NCAP+3
(1128) C DO 10 I=5,NCAP3
(1129) C Z=K(I)
(1130) C IF(Z.LT.ZXB.OR.Z.GT.ZXE)GO TO 10
(1131) C CALL GRAMOV(Z,ZB)
(1132) C CALL GRALIN(Z,ZE)
(1133) 10 CONTINUE
(1134) C IF(NDEV.EQ.3.OR.NDEV.EQ.4)CALL PENSEL(1,0.0,0)
(1135) C
(1136) C SET UP PARAMETERS FOR LIBRARY ROUTINE.
(1137) C
(1138) C N=NCAP-1
(1139) C IBOUND=3
(1140) C BL(1)=X(1)
(1141) C BU(1)=X(NPTS)
(1142) C LIW=22
(1143) C LW=500
(1144) C IFAIL=1
(1145) C NCAP2=NCAP+2
(1146) C DO 20 I=5,NCAP3
(1147) C M1=I-4
(1148) C X1(M1)=K(I)
(1149) 20 CONTINUE
(1150) C
(1151) C
(1152) C CALL LIBRARY ROUTINE E04JAF.
(1153) C
(1154) C
(1155) C CALL ALUJAF(N,IBOUND,BL,BU,X1,F,IW,LIW,W1,LW,IFAIL)
(1156) C
(1157) C IF ERRORS FOUND SAY SO AND RETURN.
(1158) C
(1159) C IF(IFAIL.NE.0)WRITE(1,30)IFAIL
(1160) 30 FORMAT('ERROR IN E04JAF IFAIL=',I2)
(1161) C WRITE(1,40)F
(1162) 40 FORMAT('RESULTS OF OPTIMIZATION' /
(1163) C *'-----' /
(1164) C *// 'OPTIMUM ERROR / POINT =' ,D10.4)
(1165) C DO 70 I=5,NCAP3
(1166) C WRITE(1,80)I,K(I)

```

```
(1167) 80  FORMAT('KNOT ',I2,' IS AT ',D10.4)
(1168)      Z=K(I)
(1169)      IF(Z.LT.ZXB.OR.Z.GT.ZXE)GO TO 70
(1170)      CALL GRAMOV(Z,ZB)
(1171)      CALL GRAMOV(Z,ZE)
(1172) 70  CONTINUE
(1173)      RETURN
(1174)      END

PROGRAM SIZE:  PROCEDURE - 000522  LINKAGE - 004432  STACK - 000050
NO  ERRORS [(OPTMIZ)FTNLUT4-REV17.2]
```

```

(1175)      SUBROUTINE FUNCT1(N,XC,FC)
(1176)      C
(1177)      C
(1178)      C      THIS SUBROUTINE CALCULATES THE RMS ERROR
(1179)      C      OF A CUBIC SPLINE CALCULATED FROM THE GIVEN
(1180)      C      SUBSPACE VECTOR.
(1181)      C
(1182)      C
(1183)      IMPLICIT DOUBLE PRECISION(A-H,K,O-Z)
(1184)      COMMON /A/ NCAP7,K(100),C(100),IFAIL,NCAP,SS,SDASH(4)
(1185)      COMMON /C/X(250),Y(250),W(250),A(5,250),A6(200),
(1186)      *A2(4,100),A3(4,50),A9(250),A10,I1,A12
(1187)      COMMON /D/NPTS
(1188)      DIMENSION XG(20),XC(20)
(1189)      NCAP3=NCAP+3
(1190)      C
(1191)      C
(1192)      C      ARRANGE KNOTS IN STRICTLY INCREASING ORDER
(1193)      C
(1194)      C
(1195)      DO 20 I=1,N
(1196)      20  XG(I)=XC(I)
(1197)      DO 30 J=5,NCAP3
(1198)      XM=1000.
(1199)      DO 25 J=1,N
(1200)      IF(XG(J).EQ.0.0)GO TO 25
(1201)      IF(XG(J).LT.XM)XM=XG(J)
(1202)      IF(XG(J).EQ.XM)IK=J
(1203)      25  CONTINUE
(1204)      K(J)=XM
(1205)      XG(IK)=0.0
(1206)      30  CONTINUE
(1207)      IFAIL=1
(1208)      CALL E02BAF(NPTS,NCAP7,X,Y,W,K,A6,A2,C,FC,IFAIL)
(1209)      IF(IFAIL.NE.0)WRITE(1,50)IFAIL
(1210)      50  FORMAT('ERROR IN E02BAF (OPTIMIZATION)      IFAIL=',I2)
(1211)      C
(1212)      C
(1213)      C      CALCULATE RMS ERROR
(1214)      C
(1215)      C
(1216)      FC=0
(1217)      WT=0
(1218)      DO 88 I1=1,NPTS
(1219)      IL=0
(1220)      CALL E02BBF(NCAP7,K,C,X(I1),AFIT,IFAIL)
(1221)      FC=FC+(((AFIT-Y(I1))*W(I1))**2)
(1222)      WT=WT+W(I1)*W(I1)
(1223)      88  CONTINUE
(1224)      FC=FC/WT
(1225)      RETURN
(1226)      END

```

PROGRAM SIZE:    PROCEDURE - 000346    LINKAGE - 000240    STACK - 000044  
 NO ERRORS I<FUNCT1>FTNLUT4-REV17.21

```

(1227) SUBROUTINE DCOPY
(1228) C
(1229) C
(1230) C SUBROUTINE TO PLOT GRAPHS PREVIOUSLY STORED IN
(1231) C FUNIT 4 ON CALCOMP.
(1232) C
(1233) C
(1234) C DIMENSION XS(250),YS(250),XR(500),YR(500),XK(15)
(1235) C
(1236) C INITIALISE DEVICE AND SET WINDOW.
(1237) C
(1238) C CALL C1051N
(1239) C CALL WINDOW(2)
(1240) 1 READ(7,*)I
(1241) C
(1242) C IF END OF FILE RETURN
(1243) C
(1244) C IF(I.EQ.0)GO TO 1000
(1245) C
(1246) C READ AXIS TYPE POSITION ETC. CHOOSE PEN AND PLOT AXIS
(1247) C
(1248) C READ(7,2)IC,IX,IY,NX,NY,XB,XE,YB,YE
(1249) 2 FORMAT(8I3,4E12.5)
(1250) C READ(7,*)IYT
(1251) C CALL PENSEL(1,0.0,0)
(1252) C GO TO (1001,1002,1002,1003,1004),IYT
(1253) 1001 CALL AXIPLO(IC,0.,0.,IX,IY,NX,NY,XB,XE,YB,YE
(1254) C *'TEMPERATURE',11,'CAPACITANCE',11)
(1255) C GO TO 1005
(1256) 1002 CALL AXIPLO(IC,0.,0.,IX,IY,NX,NY,XB,XE,YB,YE
(1257) C *'TEMPERATURE',11,'DELTA GAP',9)
(1258) C GO TO 1005
(1259) 1003 CALL AXIPLO(IC,0.,0.,IX,IY,NX,NY,XB,XE,YB,YE
(1260) C *'TEMPERATURE',11,'RESIDUALS',9)
(1261) C GO TO 1005
(1262) 1004 CALL AXIPLO(IC,0.,0.,IX,IY,NX,NY,XB,XE,YB,YE
(1263) C *'TEMPERATURE',11,'EXP. COEF.',10)
(1264) 1005 CALL AXIDRA(2,0,-1)
(1265) C CALL AXIDRA(2,0,2)
(1266) C
(1267) C READ NUMBER OF KNOTS TO BE DRAWN AS VERTICAL DOTTED
(1268) C LINES , CHANGE PEN COLOUR AND DRAW THEM.
(1269) C
(1270) C READ(7,*)I
(1271) C IF(I.LT.2)GO TO 5
(1272) C I=I-1
(1273) C DO 3 J=1,I
(1274) 3 READ(7,*)XK(J)
(1275) C CALL BROKEN(1)
(1276) C CALL PENSEL(3,0.0,0)
(1277) C DO 4 J=1,I
(1278) C CALL GRAMOV(XK(J),YB)
(1279) C CALL GRALIN(XK(J),YE)
(1280) 4 CONTINUE
(1281) C CALL BROKEN(0)
(1282) C
(1283) C READ NUMER OF X'S TO BE PLOTTED , CHANGE PEN COLOUR
(1284) C AND DRAW THEM.
(1285) C
(1286) 5 READ(7,*)I
(1287) C IF(I.EQ.0)GO TO 8
(1288) C DO 6 J=1,I

```

```

(1289) 6 READ(7,7)XS(J),YS(J)
(1290) 7 FORMAT(2E12.5)
(1291) CALL PENSEL(4,0.0,0)
(1292) 11 CALL GRASYM(XS,YS,I,4,0)
(1293) C
(1294) C READ NUMBER OF POINTS THROUGH WHICH A CURVE IS
(1295) C TO BE DRAWN , CHANGE COLOUR AND DRAW THEM.
(1296) C
(1297) 8 READ(7,*)IV
(1298) IF(IV.EQ.0)GO TO 10
(1299) DO 9 J=1,IV
(1300) 9 READ(7,7)XR(J),YR(J)
(1301) CALL PENSEL(4,0.0,0)
(1302) CALL GRAPOL(XR,YR,IV)
(1303) C
(1304) C PICTURE FINISHED SO MOVE ON PAPER
(1305) C
(1306) 10 CALL PICCLE
(1307) GO TO 1
(1308) C
(1309) C IF GRAPHS FINISHED TERMINATE DEVISE.
(1310) C
(1311) 1000 CALL DEVEND
(1312) RETURN
(1313) END

```

PROGRAM SIZE: PROCEDURE - 001102 LINKAGE - 006042 STACK - 000026  
 NO ERRORS [DCOPY]FTNLUT4-REV17.2]



```

(1314) C      UPTODATE E04JAFTEXT
(1315) C      SUBROUTINE ALUJAF(N, IBOUND, BL, BU, X, F, IW, LIW, W, LW, IF
(1316) C*****
(1317) C
(1318) C      THIS ROUTINE IS A VERSION OF NAGF LIBRARY
(1319) C      ROUTINE E04JAF THAT HAS BEEN MODIFIED TO
(1320) C      CORRECT AN ERROR THAT WAS DETECTED IN THE
(1321) C      ORIGINAL LIBRARY PACKAGE.
(1322) C*
(1323) C*****
(1324) C
(1325) C      MARK 6 RELEASE NAG COPYRIGHT 1977
(1326) C
(1327) C*****
(1328) C
(1329) C      E04JAF IS AN EASY-TO-USE QUASI-NEWTON ALGORITHM FOR FINDING
(1330) C      MINIMUM OF A FUNCTION F(X1, X2, . . . XN), SUBJECT TO FIXED
(1331) C      UPPER AND LOWER BOUNDS ON THE INDEPENDENT VARIABLES X1, X2,
(1332) C      . . . , XN, USING FUNCTION VEO4ES ONLY.
(1333) C
(1334) C      GIVEN AN INITIAL ESTIMATE OF THE POSITION OF A CONSTRAINED
(1335) C      MINIMUM, THE ROUTINE ATTEMPTS TO COMPUTE THE POSITION OF THE
(1336) C      MINIMUM AND THE CORRESPONDING FUNCTION VEO4E. IT IS ASSUMED
(1337) C      THAT F IS TWICE CONTINUOUSLY-DIFFERENTIABLE.
(1338) C
(1339) C      THE ROUTINE IS ESSENTIALLY IDENTICAL TO THE SUBROUTINE BONDG
(1340) C      IN THE NPL ALGORITHMS LIBRARY (REF. NO. E4/49/F) AND CALLS
(1341) C      E04JSF WITH SUITABLE DEFAULT SETTINGS FOR PARAMETERS.
(1342) C
(1343) C      N.B. FUNCT1 IS A DESIGNATED NAME.
(1344) C      -----
(1345) C
(1346) C      THE REAL ARRAY W, USED AS WORKSPACE BY E04JAF, MUST BE
(1347) C      DIMENSIONED AT LEAST 12*N + N*(N - 1)/2, OR 13 IF N = 1. THE
(1348) C      INTEGER ARRAY IW, ALSO USED AS WORKSPACE BY E04JAF, MUST BE
(1349) C      DIMENSIONED AT LEAST (N + 2).
(1350) C
(1351) C      PHILIP E. GILL, WALTER MURRAY, SUSAN M. PICKEN, MARGARET H.
(1352) C      WRIGHT AND ENID M. R. LONG, D.N.A.C., NATIONAL PHYSICAL
(1353) C      LABORATORY, ENGLAND
(1354) C
(1355) C*****
(1356) C
(1357) C      .. SCALAR ARGUMENTS ..
(1358) C      DOUBLE PRECISION F
(1359) C      INTEGER IBOUND, IFAIL, LIW, LW, N
(1360) C      .. ARRAY ARGUMENTS ..
(1361) C      DOUBLE PRECISION BL(N), BU(N), W(LW), X(N)
(1362) C      INTEGER IW(LIW)
(1363) C      ..
(1364) C      .. LOCAL SCALARS ..
(1365) C#P 1
(1366) C      DOUBLE PRECISION SRNAME
(1367) C      DOUBLE PRECISION BNDMAX, BOUNDK, EPSMCH, ETA, FEST, GTG, PEI
(1368) C      * RSTEPS, STEPMX, U, XI, XTOL
(1369) C      INTEGER I, IFLAG, INTYPE, IPRINT, J, K, KIW, KW1, KW2, KW3, I
(1370) C      * LH, MAXFUN, NFTOTL, NWHY
(1371) C      LOGICAL LOCSCN
(1372) C      .. FUNCTION REFERENCES ..
(1373) C      DOUBLE PRECISION F05ABF, DSQRT, X02AAF
(1374) C      INTEGER P01AAF
(1375) C      .. SUBROUTINE REFERENCES ..

```

```

(1376) C      E04HBF, E04JBF, E04JBX, E04LBW
(1377) C      ..
(1378) C      EXTERNAL E04CGY, E04CGZ, E04JBQ
(1379) C      DATA SRNAME /8H E04JAF /
(1380) C
(1381) C      A MACHINE-DEPENDENT CONSTANT IS SET HERE. EPSMCH IS THE
(1382) C      SMALLEST POSITIVE REAL NUMBER SUCH THAT 1 + EPSMCH .GT. 1.
(1383) C
(1384) C      EPSMCH = X02AAF(1.0D0)
(1385) C
(1386) C      IF USER HAS NOT SPECIFIED HARD OR SOFT FAILURE, GIVE HARD
(1387) C      FAILURE
(1388) C
(1389) C      IF (IFAIL.NE.0 .AND. IFAIL.NE.1) IFAIL = 0
(1390) C
(1391) C      RTEPS = DSQRT(EPSMCH)
(1392) C      PEPS = EPSMCH**0.66666D+0
(1393) C      NWHY = 1
(1394) C      IF (N.LE.0 .OR. IBOUND.LT.0 .OR. IBOUND.GT.3) GO TO 80
(1395) C
(1396) C      COMPUTE THE LENGTH OF THE ARRAY WHICH HOLDS THE APPROXIMATE
(1397) C      HESSIAN MATRIX.
(1398) C
(1399) C      LH = N*(N-1)/2
(1400) C      IF (LH.EQ.0) LH = 1
(1401) C
(1402) C      CHECK THAT THERE IS SUFFICIENT WORKSPACE.
(1403) C
(1404) C      IF (LW.LT.12*N+LH) GO TO 80
(1405) C      IF (LIW.LT.N+2) GO TO 80
(1406) C
(1407) C      IF APPROPRIATE, E04JBF WILL CHECK THAT BL(I) .LE. BU(I)
(1408) C
(1409) C      NWHY = 0
(1410) C
(1411) C      SUPPRESS THE PRINT FREQUENCY.
(1412) C
(1413) C      IPRINT = 0
(1414) C
(1415) C      REQUEST CONFIRMATION OF THE MINIMUM.
(1416) C
(1417) C      LOCSCH = .TRUE.
(1418) C
(1419) C      THE FUNCTION, GRADIENT AND APPROXIMATE HESSIAN WILL BE
(1420) C      SUPPLIED BY E04HBF.
(1421) C
(1422) C      INTYPE = 1
(1423) C
(1424) C      ONLY 400*N FUNCTION EVALUATIONS ARE ALLOWED.
(1425) C
(1426) C      MAXFUN = 400*N
(1427) C
(1428) C      SET THE LINEAR SEARCH PARAMETER.
(1429) C
(1430) C      ETA = 5.0D-1
(1431) C      IF (N.EQ.1) ETA = 0.0D+0
(1432) C
(1433) C      SPECIFY THE OVERALL CONVERGENCE CRITERION.
(1434) C
(1435) C      XTOL = 1.0D+2*RTEPS
(1436) C
(1437) C      SPECIFY THE BOUND ON THE STEP-LENGTH

```

```

(1438) C
(1439) STEPMX = F05ABF(X,N)
(1440) IF (STPEMX.LT.1.0D+1) STEPMX = 1.0D+1
(1441) C
(1442) C COMPUTE THE ADDRESSES FOR THE ARRAYS USED IN E04HBF, E04LBW
(1443) C E04JBX AND E04JBF.
(1444) C
(1445) KW1 = 9*N + 1
(1446) KW2 = KW1 + N
(1447) KW3 = KW2 + LH
(1448) KW4 = KW3 + N
(1449) KIW = 3
(1450) C
(1451) C COMPUTE THE FINITE-DIFFERENCE INTERVALS AND THE INITIAL
(1452) C FUNCTION VE04E, GRADIENT VECTOR AND APPROXIMATE HESSIAN MAT
(1453) C BY CALLING E04HBF WITH SOFT FAILURE OPTION.
(1454) C
(1455) NWHY = 1
(1456) CALL E04HBF(N, E04CGY, X, NFTOTL, W(KW1), W(KW2), LH, W(KW3)
(1457) * W(KW4), IW, LIW, W, LW, NWHY)
(1458) NWHY = 0
(1459) C
(1460) C CHECK THAT E04HBF HAS COMPUTED AN ACCEPTABLE INITIAL
(1461) C APPROXIMATION TO THE HESSIAN. IF NOT, REPLACE IT BY THE UNI
(1462) C MATRIX,
(1463) C
(1464) BOUNDK = N
(1465) BOUNDK = 1.0D-2/(DSQRT(BOUNDK)*EPSMCH)
(1466) CALL E04LBW(W(KW3), N, BOUNDK, IFLAG, U)
(1467) IF (IFLAG.GT.0) CALL E04JBX(N, W(KW3), N, W(KW2), LH, U)
(1468) C
(1469) C COMPUTE AN ESTIMATE OF THE FUNCTION VE04E AT THE MINIMUM.
(1470) C
(1471) FEST = 0.0D+0
(1472) IF (DABS(F).LE.RTEPS) FEST = -1.0D+0
(1473) IF (F.LT.-RTEPS) FEST = 1.0D+1*F
(1474) C
(1475) C CALL S-ROUTINE E04JBF (WITH SOFT FAILURE OPTION) TO MINIMIZ
(1476) C THE FUNCTION.
(1477) C
(1478) NWHY = 1
(1479) CALL E04JBF(N, E04CGY, E04CGZ, IPRINT, LOCSCH, INTYPE, E04JB
(1480) * MAXFUN, ETA, XTOL, STEPMX, FEST, W(KW1), IBOUND, BL, BU, X,
(1481) *, LH, W(KW3), IW(KIW), F, W(KW4), IW, LIW, W, LW, NWHY)
(1482) IF (NWHY.LE.2 .OR. NWHY.EQ.4) GO TO 40
(1483) C
(1484) C IF THE LINEAR SEARCH HAS FAILED, ATTEMPT TO DETERMINE WHETH
(1485) C THE FAILURE IS DUE TO TOO SMALL A SETTING FOR XTOL.
(1486) C
(1487) U = 1.0D+0 + DABS(F)
(1488) U = PEPS*U*U
(1489) GTG = 0.0D+0
(1490) J = KIW
(1491) K = KW4
(1492) DO 20 I=1,N
(1493) IF (IW(J).GT.0) GTG = GTG + W(K)**2
(1494) J = J + 1
(1495) K = K + 1
(1496) 20 CONTINUE
(1497) C
(1498) C THE VE04ES 3, 5, 6, 7, 8 FOR NWHY HAVE THE FOLLOWING
(1499) C SIGNIFICANCE

```

```

(1500) C
(1501) C      NWHY = 5 - THE MINIMIZATION HAS PROBABLY WORKED.
(1502) C      NWHY = 6 - THE MINIMIZATION HAS POSSIBLY WORKED.
(1503) C      NWHY = 7 - THE MINIMIZATION IS UNLIKELY TO HAVE WORKED.
(1504) C      NWHY = 8 - THE MINIMIZATION IS VERY UNLIKELY TO HAVE WORK
(1505) C      NWHY = 3 - THE MINIMIZATION HAS FAILED.
(1506) C
(1507) C      IF (NWHY.EQ.5) NWHY = 3
(1508) C      IF (GTG.LE.1.0D+3*U) NWHY = 8
(1509) C      IF (GTG.LE.1.0D+2*U) NWHY = 7
(1510) C      IF (GTG.LE.1.0D+1*U) NWHY = 6
(1511) C      IF (GTG.LE.U) NWHY = 5
(1512) C      GO CONTINUE
(1513) C
(1514) C      TELL THE USER IF ANY VARIABLE IS LARGE AND NEGATIVE OR LARGE
(1515) C      AND POSITIVE. (THIS WOULD OCCUR, IN PARTICULAR, IF ANY X(I)
(1516) C      REACHED AN ARTIFICIAL BOUND SET BY E04JBF.)
(1517) C
(1518) C      BNDMAX = 0.99999D+6
(1519) C      DO 60 I=1,N
(1520) C          XI = X(I)
(1521) C          IF (XI.LT.BNDMAX .AND. XI.GT.-BNDMAX) GO TO 60
(1522) C          NWHY = 9
(1523) C          GO TO 80
(1524) C      GO CONTINUE
(1525) C
(1526) C      TERMINATION OF ALGORITHM
(1527) C
(1528) C      GO IF (NWHY.NE.0) GO TO 100
(1529) C      IFAIL = 0
(1530) C      RETURN
(1531) C      WRITE(1,1023)NWHY
(1532) C      FORMAT('IFAIL=',I2)
(1533) C      IF(NWHY.EQ.3)WRITE(1,1024)
(1534) C      IF(NWHY.EQ.5)WRITE(1,1025)
(1535) C      FORMAT('THE MINIMIZATION HAS PROBABLY WORKED')
(1536) C      IF(NWHY.EQ.6)WRITE(1,1026)
(1537) C      FORMAT('THE MINIMIZATION HAS POSSIBLY WORKED')
(1538) C      IF(NWHY.EQ.7)WRITE(1,1027)
(1539) C      FORMAT('THE MINIMISATION IS UNLIKELY TO HAVE WORKED')
(1540) C      IF(NWHY.EQ.8)WRITE(1,1028)
(1541) C      FORMAT('THE MINIMISATION IS VERY UNLIKELY TO ',
(1542) C      *'HAVE WORKED')
(1543) C      FORMAT('OPTIMIZATION ROUTINE HAS FAILED')
(1544) C      RETURN
(1545) C
(1546) C      END OF E04JAF (BCNDQ1)
(1547) C
(1548) C      END

```

PROGRAM SIZE:    PROCEDURE - 001354    LINKAGE - 000176    STACK - 000110  
 NO ERRORS [ALUJAF]FTNLUT4-REV17.2]

```

(1549) 2+ END OF E04JAFTEXT
(1550)      SUBROUTINE INFO
(1551)  :
(1552)  :
(1553)  :   THIS ROUTINE IS AN INFORMATION ROUTINE DESIGNED
(1554)  :   TO GIVE INFORMATION ON DATA FORMAT REQUIRED BY THE
(1555)  :   PACKAGE TO THE NOVICE USER.
(1556)  :
(1557)  :
(1558)      WRITE(1,10)
(1559) 10  FORMAT('DURING EXECUTION THIS PROGRAM REQUIRES' /
(1560)      *'THREE DATA FILES TO BE MADE AVAILABLE , THESE ARE' ///
(1561)      *'FORTRAN CHANEL 5-GENRAL DATA INPUT FILE CONTAINING' /
(1562)      *'      ELECTRODE INFORMATION' /
(1563)      *'      SPECIMEN AND COPPER LENGTHS' /
(1564)      *'      CAPACITANCE TEMPERATURE DATA' ///
(1565)      *'FORTRAN CHANEL 6-FILE TO WHICH ALL OUTPUT LISTS ARE' /
(1566)      *'      TO BE SENT' ///
(1567)      *'FORTRAN CHANEL 7-FILE FOR TEMPORARY STORAGE OF PLOTTING' /
(1568)      *'      DATA.' ///)
(1569)      WRITE(1,20)
(1570) 20  FORMAT('THESE FILES ARE CONVIENIENTLY OPPENED BY' /
(1571)      *'TYPING THE FOLLOWING SEQUENCE' ///
(1572)      *'  INPUT (FILE NAME 1)' //
(1573)      *'  LISTING (FILE NAME 2)' //
(1574)      *'  BINARY (FILE NAME 3)' ///)
(1575)      RETURN
(1576)      END

```

PROGRAM SIZE: PROCEDURE - 000514 LINKAGE - 000026 STACK - 000024  
 NO ERRORS [INFO >FTNLUT4-REV17.2]

|     |     |         |                |
|-----|-----|---------|----------------|
| EEE | IJB | IJB4859 | EEEEEEEEEEEEEE |
| EEE | IJB | IJB4859 | EEEEEEEEEEEEEE |
| EEE | IJB | IJB4859 | EEEEEEEEEEEEEE |

THE OBSERVATION OF  $\text{Cr}^{2+}$  IN  $\text{Al}_2\text{O}_3$  BY LOW TEMPERATURE  
RELATIVE THERMAL EXPANSION MEASUREMENTS

by

I.J. Brown and M.A. Brown

Department of Physics

Loughborough University of Technology

Loughborough, Leicestershire LE11 3TU

A B S T R A C T

A three-terminal, capacitance dilatometer has been constructed and used to measure the linear thermal expansion over the temperature range 3 to 9K of  $\gamma$ -irradiated  $\text{Al}_2\text{O}_3:\text{Cr}$  relative to "pure"  $\text{Al}_2\text{O}_3$ . A positive Schottky-like peak has been observed in the expansivity curve at  $\sim 3.9\text{K}$  and its presence is attributed to the concentration of  $\text{Cr}^{2+}$  (produced by  $\gamma$ -irradiation) in the specimen. The peak is shown to be removed by U-V bleaching of the sample at 365nm.

## 1. INTRODUCTION

### (i) Background

The properties of strongly-coupled magnetic ions in dielectrics have been the subject of a great deal of experimental and theoretical work. (See Bates (1978) for recent review). The theoretical approach to these systems has evolved from a simple static crystalline field model to a dynamic Jahn-Teller model in which the electronic states of the ion are coupled to the vibrations of the neighbouring atoms (Fletcher and Stevens (1969), Bates and Dixon (1969)). The potential energy of the ion and its neighbours may be reduced by a distortion in either of the three equivalent directions for a cubic material; distortions in other directions lower the energy less so that the equivalent distortions are separated by energy barriers. Tunnelling between the three different modes of distortion occurs and the resulting lattice disturbance is dynamic. The lowest eigenstates are separated by a tunnelling splitting which will change rapidly with crystal volume.

The quantitative measurement or even the detection of small quantities of strongly-coupled impurity ions is difficult. Typically the energy level splittings are in the range  $1\text{-}10\text{cm}^{-1}$  and are often impossible to measure using conventional electromagnetic or acoustic radiation. However, with ions strongly coupled to the lattice, thermal expansion at low temperatures can provide useful information (Sheard (1972)), especially when coupled with specific heat data, about the pressure dependence of the energy level splittings. In particular, the determination of the magnetic Grüneisen coefficients for the Schottky anomaly would provide a good test for the multimode Jahn-Teller model.

Apart from this work, the only attempt, that we are aware of, to observe

magnetic ions in host lattices using thermal expansion techniques was made by Sheard et al (1977) who looked at the thermal expansion of ZnS doped with various concentrations of Fe. The experimental results were shown to be consistent with a static crystal field model although the presence of a weak Jahn-Teller effect was not precluded. With their success in using the three-terminal capacitance dilatometer to resolve the magnetic contribution to the thermal expansion, it was an obvious step to apply the technique to a known strongly-coupled magnetic ion which was thought to produce a dynamic Jahn-Teller system.

The system chosen for immediate study was  $\text{Cr}^{2+}$  in  $\text{Al}_2\text{O}_3$  which has the advantage that the Debye temperature of  $\text{Al}_2\text{O}_3$  is 1034K (Fugate and Swenson (1969)) so that the lattice thermal expansion at low temperatures should be small and should not dominate any magnetic contributions. Other practical advantages are that large single crystals of ruby are available and that the concentration of  $\text{Cr}^{2+}$  in  $\text{Al}_2\text{O}_3$  can be increased (to about 5% of total Cr concentration) by  $\gamma$ -irradiation and removed by U-V treatment (Brown and Robach (1978)).

#### (ii) Initial experiments

The initial experiments measured the linear thermal expansion of two  $\gamma$ -irradiated ruby samples (one containing  $8100 \pm 200$  ppm Cr and the other  $\sim 800$  ppm Cr) and a "pure"  $\text{Al}_2\text{O}_3$  sample in a three-terminal, capacitance, H.C.O.F. (High Conductivity Oxygen Free), copper cell of classical design (Brown and Brown (1981)). The specimen length changes relative to the copper cell as a function of temperature were found by measuring the capacitance between an electrode on the sample and a "fixed" electrode within a guard-ring in the cell, using the commercial General Radio 1615A Capacitance Bridge. With this system length changes  $\sim 1\text{\AA}$  could be detected



and from the results the linear thermal expansion coefficient of the samples could be found over the temperature range 2.5K to 10K. Corrections for the thermal expansion of the H.C.O.F. copper cell had to be made, using the data of Kroeger and Swenson (1977). The results showed positive, peaked structures at  $\sim 3.9\text{K}$  in the linear thermal expansion data of the  $\gamma$ -irradiated ruby samples, with the more heavily Cr-doped sample having the largest peaked structure, whereas no such structure was seen in the linear thermal expansion data of "pure"  $\text{Al}_2\text{O}_3$ .

These peaked structures were tentatively ascribed to the presence of  $\text{Cr}^{2+}$ , but it was not possible to resolve them properly with the equipment then available. The work presented in this paper, using much improved equipment and a modified measurement technique, set out (a) to confirm the earlier data, and (b) to confirm the assignment of  $\text{Cr}^{2+}$  as the cause of the peaked structure by using U-V to remove the  $\text{Cr}^{2+}$  from a  $\gamma$ -irradiated Cr-doped  $\text{Al}_2\text{O}_3$  sample.

## 2. EXPERIMENTAL TECHNIQUE

One of the major difficulties in using the classical H.C.O.F. thermal expansion cell is that to obtain the absolute linear thermal expansion of the specimen corrections have to be applied to account for the thermal expansion of the copper. These corrections arise in two ways: firstly, in the obvious changes in length of the copper cell against which the specimen length is measured and secondly, in changes in the electrode diameter with consequent changes in measured capacitance. Although corrections were made using the detailed data for copper reported by Kroeger and Swenson (1977) below  $\sim 10\text{K}$  the thermal expansion of copper cannot be considered a reproducible standard for it is slightly sample dependent presumably

because of some impurity mechanism.

In order to eliminate the major uncertainty, namely the calculation of the changes in length of the copper cell as a function of temperature, the expansion cell design was changed. Four identical, monocrystalline, "pure"  $\text{Al}_2\text{O}_3$  specimens were obtained from the same crystal supplier in the form of cylinders, 5mm in diameter and 50.4mm long. The c-axes were  $60^\circ$  to the cylinder axes. Three of these specimens were used to form the reference length of the cell so that the changes in length of a doped specimen relative to "pure"  $\text{Al}_2\text{O}_3$  were measured. The practical arrangement is shown in Figure 1, and shows the upper electrode plate pulled towards the base plate by springs but separated by the "pure"  $\text{Al}_2\text{O}_3$  legs. A copper former was used to locate the  $\text{Al}_2\text{O}_3$  legs and to act as an isothermal chamber, the machining tolerances being set to ensure good, mechanical stability. A copper screw was used to set the sample in a suitable position so that whilst the electrode separation produced a capacitance that was easily measureable, and was sensitive to small changes in length, it was not so small that the capacitance transducer was highly sensitive to slight non-parallelism of the electrodes or was non-linear (Khan et al (1980)). A suitable initial electrode separation was  $\sim 250\mu\text{m}$  giving a capacitance  $\sim 7\text{pF}$ .

The capacitance measurement system was also greatly improved. Firstly, a 1616 GenRad Precision Capacitance Bridge was purchased, which is in principle two orders of magnitude more sensitive than the original bridge. To exploit this potential a tuned null detector was replaced by a full phase sensitive detection system operating on in-phase and quadrature phases, both phases being additionally filtered by coherent filters. The system has an independent earth, sits in a series of Faraday cages, and uses

long time constants.

The other major improvement that had to be tackled was one of vibration. Clearly if the cryostat suffers vibration, the capacitance between the expansion cell electrodes will be noisy and the same problem can arise on the other side of the bridge with the capacitance standards. This problem was solved crudely, but most effectively, by setting the cryostat into 1½ tons of reinforced concrete and siting this assembly on another 50 ton concrete plinth set into bed rock and vibrationally isolated from the building. The electronics were also placed on this plinth and carefully temperature stabilised to  $\pm 0.1\text{K}$ .

This apparatus can now detect changes of capacitance of  $0.05\text{aF}$  ( $5 \times 10^{-20}\text{F}$ ), equivalent to a specimen length change of  $\sim 10^{-20}\text{\AA}$ , but more significantly it can reproduce a capacitance (giving change of specimen length) versus temperature measurement taken over several hours to within  $\pm 0.2\text{aF}$ . The reliability of the mounting system has been tested in that measurements of thermal expansion taken after a sample has been removed from the cell and then simply replaced, are also reproduced within the experimental errors indicated in figure 2.

### 3. RESULTS

Three thermal expansion measurements relative to "pure"  $\text{Al}_2\text{O}_3$  were made: (a) the 4th "pure"  $\text{Al}_2\text{O}_3$  specimen not being used to form the cell supports, (b) the 8100 ppm Cr doped  $\text{Al}_2\text{O}_3$  specimen after  $\gamma$ -irradiation treatment followed by rapid cooling to  $\sim 77\text{K}$  and (c) the same Cr doped  $\text{Al}_2\text{O}_3$  specimen after bleaching with U-V radiation at 365nm for 60 hours. The results are shown in figure 2.

As in the initial work with the H.C.O.F. copper cell, the relative

thermal expansion curves (solid lines) of figure 2 were obtained by fitting cubic  $\beta$ -spline functions to the relative length change versus temperature data and numerically differentiating. The data points only indicate the temperatures at which specimen length measurements were taken and the error limits in figure 2 are produced from the limits of "plausible" fits to the raw data and are probably somewhat pessimistically large.

The thermal expansion of "pure"  $\text{Al}_2\text{O}_3$  relative to the identical "pure"  $\text{Al}_2\text{O}_3$  supporting legs, shown in figure 2(a), is essentially a calibration curve. Clearly if the "pure"  $\text{Al}_2\text{O}_3$  sample is identical to the expansion cell's  $\text{Al}_2\text{O}_3$  supporting legs and if all corrections for the expansion of any H.C.O.F. copper parts are made correctly, then zero relative thermal expansion should be obtained at all temperatures. This is not quite obtained but it is clear that any small errors resulting from these effects are small and are not rapidly varying with temperature.

This expansion cell calibration curve has been used to correct the expansion data of the doped sample, the corrected curves being shown in Figures 2(b) and 2(c). The results clearly show a sharp peak at  $\sim 4\text{K}$  in the relative thermal expansion of  $\gamma$ -irradiated  $\text{Al}_2\text{O}_3:\text{Cr}$  which is removed by U-V bleaching. The two sets of results for the  $\text{Al}_2\text{O}_3:\text{Cr}$  sample, immediately after  $\gamma$ -irradiation and then after dismantling and U-V bleaching treatment, are virtually identical above  $\sim 6\text{K}$ , which gives some indication of the reproducibility of the measurements. We estimate that the anomalous peak height in the  $\gamma$ -irradiated  $\text{Al}_2\text{O}_3:\text{Cr}$  data to be  $\sim (2.5 \pm 0.5) \times 10^{-8} \text{ K}^{-1}$  and the half width to be  $\sim 1 - 1.5\text{K}$ . We also observe a negative thermal expansion above and below the large anomalous peak indicating some negative Grüneisen coefficients corresponding to the energy levels of the contributing system.

#### 4. DISCUSSION

The fact that the thermal expansion peaks scale with total chromium concentration and that it is present in  $\gamma$ -irradiated  $\text{Al}_2\text{O}_3:\text{Cr}$  but removed by U-V bleaching strongly suggests that the peaks are caused by the  $\text{Cr}^{2+}$  ion which is known to be strongly-coupled (Brown et al (1973)). Further work using samples with different chromium concentrations, and doing the U-V bleaching by stages and in-situ, should be done to study this system.

If one takes this assignment of responsible centre, the recently published theoretical energy levels of  $\text{Cr}^{2+}$  in  $\text{Al}_2\text{O}_3$  (Bates and Wardlaw (1980)) can be used to compute the Schottky specific heat anomaly. The result peaks at a temperature of 2.6K at a value of  $20 \times 10^{-24} \text{ J K}^{-1}$  per ion. If one then crudely compares the value of the thermal expansion at the anomaly with the computed specific heat and uses the published values for the isothermal compressibility of  $\text{Al}_2\text{O}_3$  (Schauer (1965)) with an estimate of 5% for the number of  $\text{Cr}^{3+}$  ions converted to  $\text{Cr}^{2+}$  by  $\gamma$ -irradiation (Brown et al (1972)), a rough estimate of an average Grüneisen coefficient  $\gamma_s = 50 \pm 15$  is obtained. Unfortunately, estimates of the average Grüneisen coefficient,  $\gamma_s$ , have not been made for  $\text{Al}_2\text{O}_3:\text{Cr}^{2+}$ , although some work has been done on  $\text{MgO}:\text{Cr}^{2+}$  (Sheard (1971)). However, it is anticipated that the two systems will be qualitatively similar and in particular that a small negative value of  $\gamma_s$  will be predicted by a static field model, whereas a large positive value ( $\sim 30$  for MgO) will be predicted by the dynamic Jahn-Teller model.

However, one only expects the specific heat and thermal expansion Schottky anomalies to be of the same form if the magnetic Grüneisen coefficients are approximately the same for each level. The fact that the computed specific heat for  $\text{Cr}^{2+}$  peaks at a slightly lower temperature, is far

broader than the observed anomaly in the thermal expansion data (if we attribute the effect to  $\text{Cr}^{2+}$ ) and has a low temperature negative "tail", may be explained by different energy levels having quite different Grüneisen coefficients (meaning that different levels respond in different ways to changes in volume). Theoretical work is now being done (Bates, private communication) to estimate the Grüneisen coefficients for each of the 15 lowest lying energy levels of  $\text{Cr}^{2+}$  in  $\text{Al}_2\text{O}_3$ .

## 5. CONCLUSION

A large, positive Schottky-type peak has been observed in the low temperature thermal expansion of  $\gamma$ -irradiated  $\text{Al}_2\text{O}_3:\text{Cr}$  at  $\sim 3.9\text{K}$ , which is removed by U-V bleaching. Earlier work shows that the size of the peak varies with total chromium concentration and the peak is attributed to the presence of  $\text{Cr}^{2+}$ .

A detailed analysis of the results awaits a detailed extension of the existing theoretical treatment of the  $\text{Cr}^{2+}$  ion in  $\text{Al}_2\text{O}_3$ . However, the results are not inconsistent with the dynamic Jahn-Teller model, which would predict a large positive average magnetic Grüneisen coefficient.

## 6. ACKNOWLEDGEMENTS

We would like to thank the Science and Engineering Research Council and the Scientific Affairs Division of NATO for financial support of the research programme which is being carried out in collaboration with Service Basses Temperatures, Centre d'Etude Nucleaires, Grenoble, France. We would also like to thank Dr. F.W. Sheard and Dr. C.A. Bates for helpful discussions and Mr. A.R. Khan for his helpful assistance with some of the experiments.

## 7. REFERENCES

- Bates, C.A. (1978), Phys. Rep., 35, 187-304.
- Bates, C.A. (1982) (private communication), Nottingham University.
- Bates, C.A. and Dixon, D. (1969), J. Phys. C., 2, 2209-25.
- Bates, C.A. and Wardlaw, R.S., (1980), J. Phys. C., 13, 3609-23.
- Brown, M.A., de Goer, A.M., Devismes, N., and Villedieu, M., (1972)  
Conference Internationale sur la Diffusion des Phonons dans les Solides,  
Paris, p.272-5. (Ed. H.J. Albany, C.E.N. Saclay, France).
- Brown, M.A., Challis, L.J., Moore, W.S., Yalcin, T. and Waldorf, D.C. (1973),  
J. Phys. C., 6, 1063-73.
- Brown, M.A. and Robach, Y., (1978), J. Phys. C., 10, 4939-43.
- Brown, I.J. and Brown M.A., (1981), Phys. Rev. Letters, 46, 835-8.
- Fletcher, J.R. and Stevens, K.W.H., (1969), J. Phys. C., 2, 444-56.
- Fugate, R.Q. and Swenson, C.A., (1969), J. Appl. Phys., 40, 3034-36.
- Khan, A.R., Brown, I.J. and Brown, M.A., (1980), J. Phys. E., 13, 1280-1.
- Kroeger, F.R. and Swenson, C.A. (1977), J. Appl. Phys., 48, 853-64.
- Schauer, A., (1965), Can. J. Phys., 43, 523-31.
- Sheard, F.W., (1971), J. de Physique, C1, 32, 939-40.
- Sheard, F.W., (1972), Thermal Expansion - 1971 Ed. M.G. Graham and H.E. Hapy  
(AIP Conference Proceedings 3, American Institute of Physics, New York, p.155-68.
- Sheard, F.W., Smith, T.F., White, G.K. and Birch, J.A. (1977), J. Phys. C.,  
10, 645-55.

## FIGURE CAPTIONS

Figure 1 Diagram of expansion cell using "pure"  $\text{Al}_2\text{O}_3$  as a reference standard. 1 = electrode on sample, 2 = fixed electrode on cell surrounded by a guard ring, 3.

Figure 2(a) Calibration data of differential linear thermal expansion coefficient of "pure"  $\text{Al}_2\text{O}_3$  compared with "pure"  $\text{Al}_2\text{O}_3$  as a function of temperature used to correct subsequent experimental data.

----- = estimate of limit of uncertainty in curve fitting procedure.

Figure 2(b) Differential linear thermal expansion coefficient of  $\sim 8100\text{ppm}$  Cr doped  $\text{Al}_2\text{O}_3$ , after  $\gamma$ -irradiation and rapid cooling, compared with "pure"  $\text{Al}_2\text{O}_3$  as a function of temperature (solid line) corrected using data in figure 2(a).

----- = estimate of limit of uncertainty in curve fitting procedure.

Figure 2(c) Differential linear thermal expansion coefficient of  $\sim 8100\text{ppm}$  Cr doped  $\text{Al}_2\text{O}_3$ , after subsequent U-V bleaching (see text) compared with "pure"  $\text{Al}_2\text{O}_3$  as a function of temperature (solid line) corrected using data in figure 2(a).

----- = estimate of limit of uncertainty in curve fitting procedure.



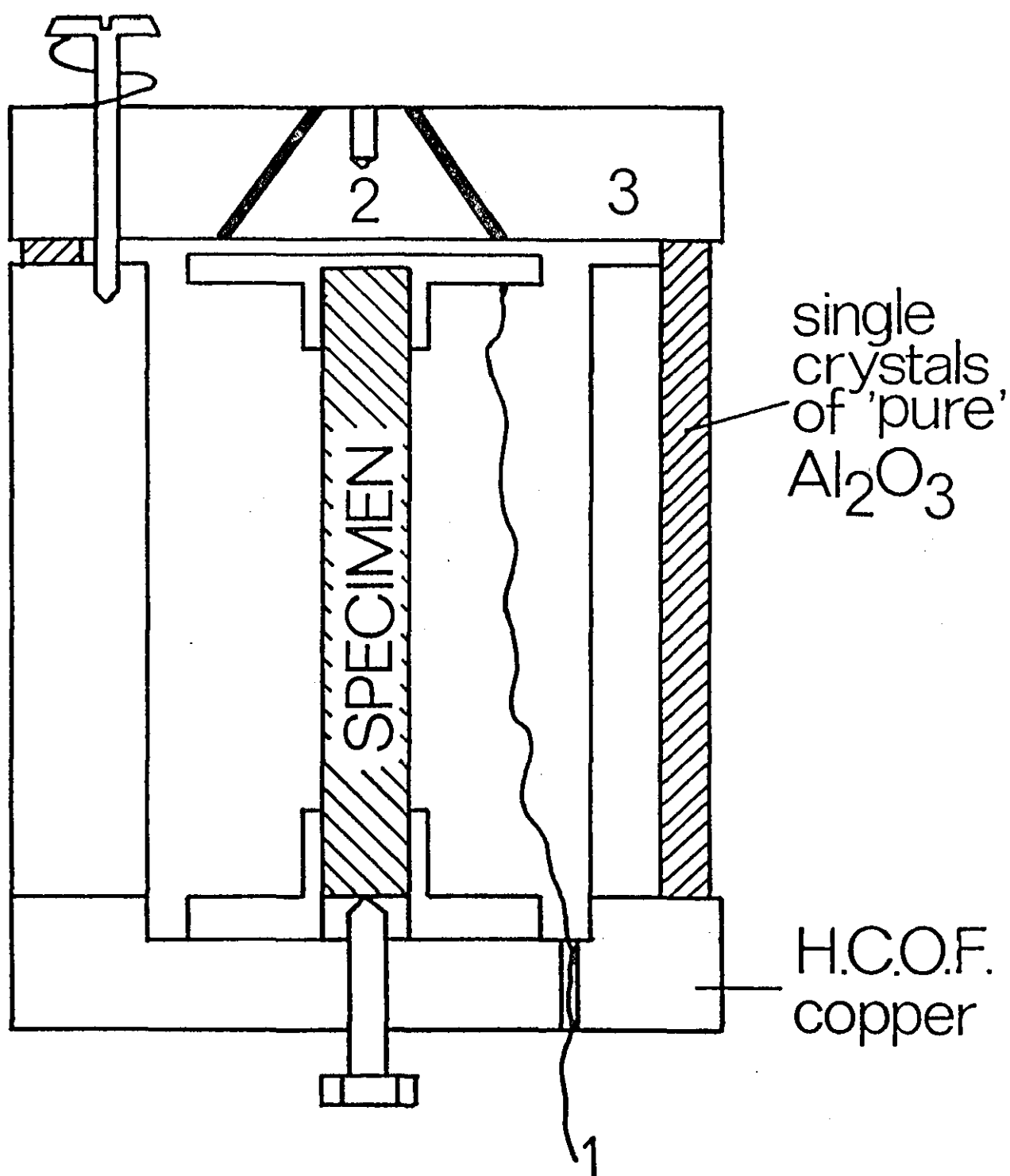
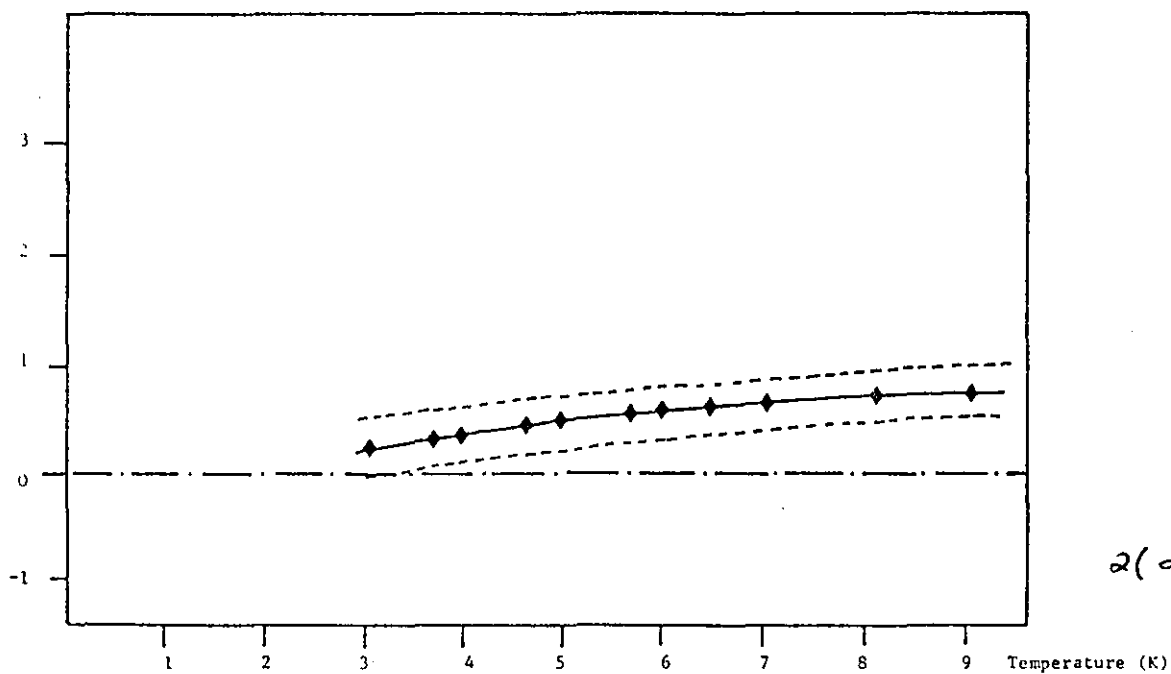


FIGURE 1 Diagram of expansion cell using "pure"  $\text{Al}_2\text{O}_3$  as a reference standard.

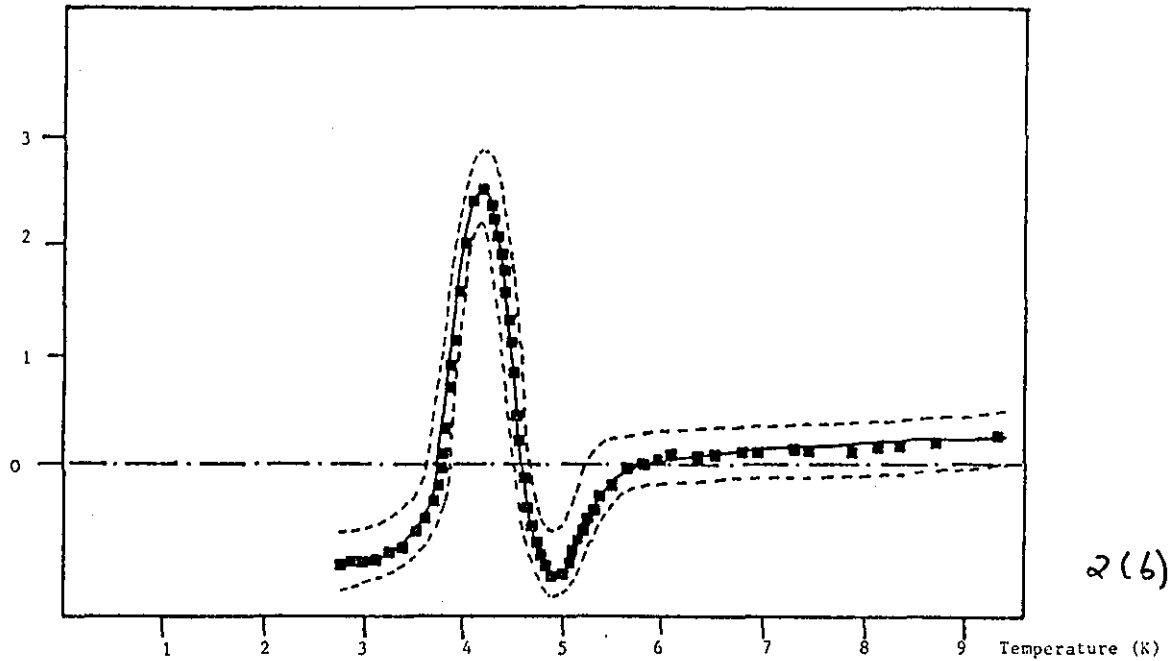
1 = electrode on sample, 2 = fixed electrode on cell surrounded by a guard ring, 3.

Differential Linear Expansion Coefficient  $\times 10^4$  (K<sup>-1</sup>)



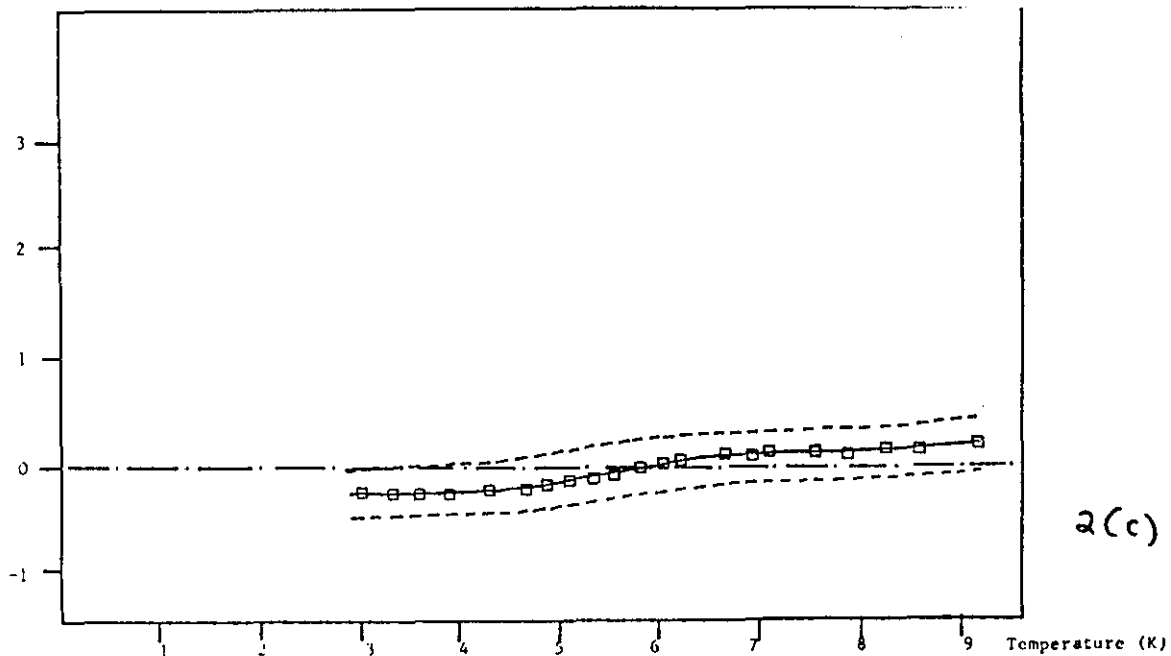
2(a)

Differential Linear Expansion Coefficient  $\times 10^{-3}$  (K<sup>-1</sup>)



2(b)

Differential Linear Expansion Coefficient  $\times 10^4$  (K<sup>-1</sup>)



2(c)

# The behaviour of capacitance displacement transducers using epoxy resin as an electrode-guard ring spacer

A R Khan, I J Brown and M A Brown

Department of Physics, Loughborough University of Technology, Loughborough, Leicestershire, LE11 3TU, UK

Received 28 February 1980, in final form 12 June 1980

**Abstract** Measurements of the linearity of a guard-ring, three-terminal capacitance transducer have been made with precision and the effects of slight non-parallelism of the electrodes of the order of minutes of arc have been observed for small electrode separations.

Although the results can be explained by the classical theory for large electrode separations ( $g > r/75$ , where  $g$  is the electrode separation and  $r$  is the radius of the central electrode) no such agreement is obtained for the small electrode separation data.

## 1 Background

Investigations of the performance of a parallel-plate capacitance displacement transducer using a guard-ring attached to the central electrode by means of an epoxy-resin dielectric (Brown and Bulleid (1978), hereafter referred to as paper I) showed that at electrode separations less than  $r/75$  (where  $r$  is the radius of the central electrode) the system was non-linear.

The non-linearity could not be satisfactorily explained by the classical Maxwellian expression (Maxwell 1873) which assumes a vacuum between the central electrode and the guard-ring,

$$C = \frac{A\epsilon_0}{g} \left[ 1 + \frac{w}{r} \left( 1 + \frac{w}{2r} \right) \left( 1 + \frac{0.22w}{g} \right)^{-1} \right]$$

(where  $A$  is the area of the central electrode,  $g$  is the electrode separation and  $w$  is the width of the gap between the central electrode and its guard-ring) or by a modified version

$$C = \frac{A\epsilon_0}{g} \left[ 1 + \frac{w}{r} \left( 1 + \frac{w}{2r} \right) \left( 1 + \frac{0.22w}{\epsilon g} \right) \right]$$

where  $\epsilon$  is the relative permittivity of the epoxy-resin dielectric.

It was also apparent that the capacitance obtained was strongly dependent on the angle between the electrodes at low electrode separations.

This note describes further work carried out at a higher order of precision.

## 2 Experimental details

The basic technique reported in paper I, has been retained, in that an adjustable assembly with a capacitor and guard-ring plate, is moved towards the other plain plate, the change in position of the assembly being detected by a Michelson interferometer arrangement (using a He-Ne laser as the displacement standard).

The capacitor electrode and guard-ring geometry were retained but, after hand lapping, the stainless-steel plates were optically polished by Rank, Hoffman and Taylor to a curvature less than a quarter of a wavelength of sodium light over the entire width ( $\sim 60$  mm).

The mechanism controlling the orientation of the plain plate was modified so that the plate could be rotated about two mutually perpendicular axes by small but controlled amounts, using long heavy levers and precision bearings throughout. Such an arrangement allowed us to approach a 'perfectly parallel' plate situation.

The linear movement of one plate relative to the other was controlled by an electric clock motor, so that transmitted vibration and backlash was minimised, and was slow enough that optical fringes could be counted manually. In addition, the measurements were done in conditions where the temperature was constant to  $\pm \frac{1}{2}^\circ\text{C}$  and during the days over Christmas when the Physics building was vibrationally and electrically 'quiet'. Finally, the operating frequency of the capacitance bridge was increased to 7.2 kHz, at which frequency the best signal-to-noise ratio was obtained.

## 3 Results

By the technique outlined above, measurements of plate separation,  $g$ , and the corresponding capacitance,  $C$ , were obtained with various relative orientations of the plates. Firstly, the plates were aligned as near as parallel as possible by fine adjustment to maximise the value of the capacitance obtainable. The separation of the plates was then systematically increased whilst monitoring the capacitance and the results are shown in figure 1, plotted as  $1/C$  against  $g$ . The

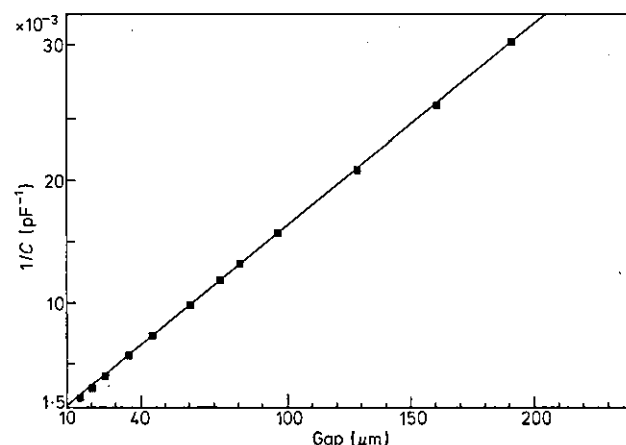


**Figure 1** Reciprocal capacitance ( $1/C$ ) against electrode separation  $g$  for 'parallel' electrodes.

data obtained for  $g$  give relative changes in plate separations but, as was described in detail in paper I, the data can be corrected to produce the 'absolute' plate separation  $g$  and these values are the ones used throughout this paper.

As can be seen from figure 1, an approximately linear relationship is obtained between  $1/C$  and  $g$ , but small departures from linearity can be observed at small values of  $g$ . As in paper I, this becomes clearer when the results are displayed in a different form: the point-to-point gradients are calculated and plotted as a function of plate separation,  $g$ . Measurements were also taken after one of the plates had been rotated (i) clockwise by  $1^\circ$ , (ii) clockwise by  $2^\circ$ , (iii) clockwise by  $5^\circ$ , (iv) reset to 'perfect' parallelism, and (v) anticlockwise by  $4^\circ$ . The results are displayed in figure 2.

All the different orientations produced results that tend to the same gradient ( $1/Cg$ ) of  $161.8 \times 10^{-6} (\text{pF } \mu\text{m})^{-1}$  at large plate separations. From equation (1) the gradient  $G = 1/Cg = 1/\epsilon_0 A$  and thus one can calculate the effective area of the inner

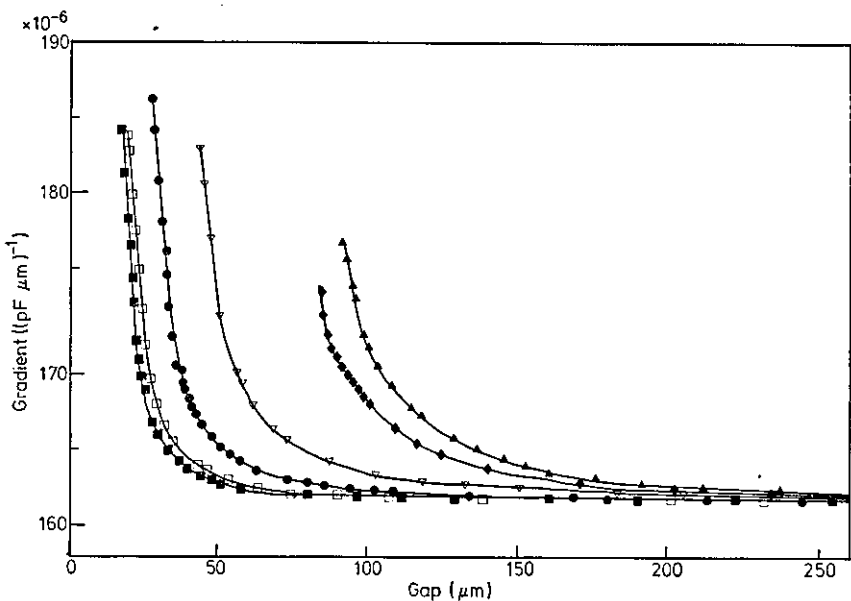


Figure 2 Point-to-point gradients against electrode separation with electrodes: (i) ■, 'parallel', (ii) ●, rotated clockwise 1' from parallel; (iii) △, 2' clockwise from parallel; (iv) ▲, 5' clockwise from parallel; (v) □, reset 'parallel'; (vi) ◆, rotated 4' anticlockwise.

electrode of the guard ring plate. The value obtained is  $698.3 \pm 0.2 \text{ mm}^2$ . The physical area of the electrode, measured using a travelling microscope, was  $674.3 \pm 0.3 \text{ mm}^2$ , giving a ratio between the effective and physical areas of  $1.036 \pm 0.003$ .

4 Discussion

Both models agree at the limit  $g \rightarrow \infty$  and can be interpreted to mean that the effective area of the inner electrode of the guard-ring system is

$$A^* = A(1 + \eta)$$

where  $A = \pi r^2$  is the physical area of the electrode and  $\eta$  is a correction factor. Of course, the values of  $\eta$  are different in the two different models although they agree at large plate separations when  $\eta \rightarrow (w/r)[1 + (w/2r)]$ , giving a value of  $\eta = 0.038 \pm 0.002$  if one substitutes the measured values of  $w$  and  $r$ . Thus a ratio of  $1.038 \pm 0.002$  between the effective and physical areas of large values of  $g$  is predicted, compared with the experimental value of  $1.036 \pm 0.003$ . It would seem that for electrode separations above  $\sim 200 \mu\text{m}$  (corresponding to  $r/75$ ), the experimental values can be explained by the classical Maxwellian expression (or the modified version) provided that the electrodes are parallel to  $\sim 5'$ . However, the data show that deviations from linearity occur below this separation, the point of onset depending on the non-parallelism of the plates.

At small values of  $g$  ( $g \rightarrow 0$ ), both models predict that the gradient should tend to a value of  $(\pi \epsilon_0 r^2)^{-1} = 167.9 \times 10^{-6} (\text{pF } \mu\text{m})^{-1}$ . Such an intercept was not obtained experimentally even though non-parallelism was certainly less than  $\frac{1}{2}'$  and the 'parallel' data were quite reproducible. The reasons for this lack of agreement are not clear and certainly it cannot be explained by applying classical theory of plate rotation to the problem. It is possible, that in this unusual, small electrode separation situation (a situation often approached in precision dilatometer measurements) surface effects, other than roughness, may become important.

It is also noted that, for small values of  $g$ , the unusual condition of  $w > g$  is obtained and that also the central electrode geometry (being cone-shaped for mechanical convenience and stability) does not correspond to the classical theoretical model. However, it is clear that for this capacitance transducer, in the small  $g$  situation, deviations from linear

behaviour are observed even when the electrodes are parallel to  $\lesssim \frac{1}{2}'$  of arc.

5 Conclusions

When the separation between the 'parallel electrodes' of a capacitance transducer,  $g$ , is greater than  $\sim 200 \mu\text{m}$  ( $g > r/75$ ) any effects of non-parallelism are small and any differences between the classical theoretical model are unlikely to be important. With smaller plate separations, the effects of non-parallelism ( $\sim$  few minutes) can be appreciable.

For smaller electrode separations, the behaviour of the device cannot be explained by simple classical theory and further experimental and theoretical work is to be carried out.

Acknowledgments

We would like to thank the Science Research Council and the Scientific Affairs Division of NATO for financial support of a research project, of which this study forms a part, and one of us (ARK) would like to thank the Government of Pakistan for personal financial support.

We would also like to acknowledge the help and advice of Rank Taylor Hobson in preparing optically flat and polished electrode systems.

References

Brown M A and Bulleid C E 1978 The effect of tilt and surface damage on practical capacitance displacement transducers  
*J. Phys. E: Sci. Instrum.* **11** 429-32  
Maxwell J C 1873 Theory of Thomson's guard-ring  
*A Treatise on Electricity and Magnetism, Article No. 201* (Oxford: Clarendon)

## Low-Temperature Thermal Expansion of $\gamma$ -Irradiated Ruby

I. J. Brown and M. A. Brown

*Department of Physics, Loughborough University of Technology, Loughborough,  
Leicestershire LE11 3TU, United Kingdom*

(Received 7 November 1980)

Measurements of the low-temperature thermal expansion of  $\gamma$ -irradiated rubies have been made with use of a three-terminal capacitance dilatometer. The data exhibit a positive Schottky-type anomaly at  $\sim 3.9$  K, not present in the data obtained for a pure  $\text{Al}_2\text{O}_3$  sample, and this contribution to the thermal expansion has been tentatively attributed to the presence of  $\text{Cr}^{2+}$  (produced by  $\gamma$  irradiation) exhibiting a large positive magnetic Grüneisen coefficient as predicted by a dynamic Jahn-Teller model.

PACS numbers: 65.70.+y, 61.80.Ed

A great deal of experimental and theoretical work, over several years, has been done on the properties of various paramagnetic ions in several host lattices (see Bates<sup>1</sup> for an extensive bibliography). Of particular interest are ions which, with use of static field theory, have  $E$  orbitals in an octahedral environment, such as  $\text{Cr}^{2+}(3d^4, 5D)$  in  $\text{MgO}$ , when it is thought that the orbit-lattice interaction is so strong that a simple description using static crystal theory is inadequate. In this situation, the electronic states couple to the vibrations of the neighboring atoms producing a dynamic Jahn-Teller system<sup>2</sup> which has been calculated in some detail for this particular case.<sup>3</sup>

Experimentally, the quantitative measurement, or even the detection, of small quantities of impurity ion is extremely difficult. The energy-level splittings of such ions are typically in the range  $\sim 1$ – $10$   $\text{cm}^{-1}$  and are difficult to measure by resonance techniques which use electromagnetic or acoustic radiation. Sheard<sup>4</sup> suggested, however, that thermodynamic quantities may provide useful information. Specific-heat measurements give useful information on energy-level splittings and ionic concentrations but are experimentally difficult measurements to perform and lack the absolute precision of spectroscopic techniques. Thermal expansion provides additional information (since it also depends on the pressure dependence of the splittings), such as the magnetic Grüneisen coefficient  $\gamma_s$  which, when determined, would point in a more direct way to the existence of a tunnelling splitting and provide a clear test for a dynamic Jahn-Teller model.

The standard Grüneisen theory<sup>5</sup> may be generalized to include the effect of two-level impurity ions, with level splitting  $E_s$ . The volume expansion coefficient  $\beta$  is then given by

$$\beta/\chi_T = (\gamma_L C_L + \gamma_s C_s)/V,$$

where  $C_L$  and  $C_s$  are the heat capacities at constant volume  $V$  of the lattice and ions, respectively,  $\chi_T$  is the isothermal compressibility, and  $\gamma_L$  and  $\gamma_s$  are the magnetic Grüneisen coefficients, respectively. This theory can be readily generalized to a many-level system. There will be an observable effect in the thermal expansion when  $\gamma_L C_L \sim \gamma_s C_s$ , and the theoretical work of Sheard<sup>6</sup> indicated that this condition should be readily satisfied for strongly coupled magnetic ions at low temperatures. Recently, experimental observations of the thermal expansion of natural crystals of  $\text{ZnS}$  containing  $\text{Fe}$  impurities<sup>7</sup> have been made and the experimental results were shown to be consistent with the predictions of a static crystal-field model (suggesting a magnetic Grüneisen parameter of  $-\frac{5}{3}$ ), although the presence of a weak Jahn-Teller effect was not precluded.

With the success of the three-terminal capacitance dilatometers in resolving the magnetic contribution to the thermal expansion,<sup>8</sup> it seemed appropriate to apply the technique to a known strongly coupled ion which was thought to produce a dynamic Jahn-Teller system. The system of  $\text{Cr}^{2+}$  in  $\text{Al}_2\text{O}_3$  was chosen for several reasons: (a) The Debye temperature of  $\text{Al}_2\text{O}_3$  is 1034 K (Ref. 9) so that at low temperatures the lattice thermal expansion is small and should not dominate any magnetic contributions; (b) the amount of  $\text{Cr}^{2+}$  present in  $\text{Al}_2\text{O}_3$  can be changed by  $\gamma$  irradiation and uv treatment<sup>10</sup>; (c) large single crystals of ruby were available; (d) although  $\text{Cr}$  substitutes for  $\text{Al}$ , which experiences essentially a trigonally distorted cubic field, there is evidence<sup>11,12</sup> that  $\text{Cr}^{2+}$  produces an almost pure cubic field environment for itself; and (e) the static cubic-field model does not explain the behavior of  $\text{Cr}^{2+}$  in  $\text{Al}_2\text{O}_3$ ,<sup>13</sup> and consequently the dynamic Jahn-Teller model has been recently developed<sup>12</sup> for this system.

The experimental details will be published later

but essentially a "standard" three-terminal capacitance method<sup>8</sup> was used, the sample being compared with a H.C.O.F. copper cell, corrected with use of the thermal-expansion data of Kroeger and Swenson.<sup>14</sup> The three monocrystalline samples were cylindrical in form (the  $c$  axis being  $\sim 60^\circ$  to the specimen axis), one being a "pure"  $\text{Al}_2\text{O}_3$  sample, another being doped with  $\sim 800$  ppm Cr (manufacturer's quoted value), and the third sample containing  $8100 \pm 200$  ppm Cr (value obtained by optical measurements<sup>15</sup>—the manufacturer's estimate having been  $\sim 1.04\%$ ). The dimensions of the cylindrical samples were diameters 12, 10, and 5 mm and lengths 100, 100, and 50 mm for the pure, 800-ppm Cr-doped and 8100-ppm Cr-doped samples, respectively. The change in specimen length as a function of temperature was monitored with use of a General Radio precision capacitance bridge from 3.2 to 300 K, although only the temperature range of immediate interest is presented in this Letter.

The results obtained for the pure  $\text{Al}_2\text{O}_3$  sample and the ruby samples after  $\gamma$  irradiation are shown in Fig. 1 and the Cr-doped samples show clear step anomalies not present in the data for the pure sample. Indeed, recent measurements on V-doped  $\text{Al}_2\text{O}_3$  samples also show no such structure. The lines drawn through the data in Fig. 1 were obtained by fitting  $\beta$ -cubic spline functions to the data with use of Loughborough University of Technology's Prime system so that, by numerical differentiation, the thermal expansion of the specimens could be obtained. The re-

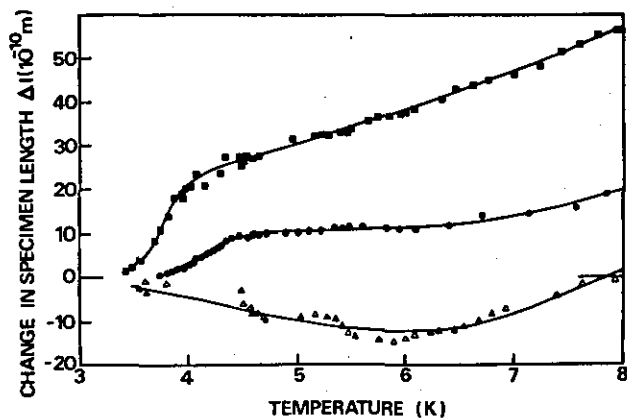


FIG. 1. Change in specimen length as a function of temperature after  $\gamma$  irradiation for: open triangles, "pure"  $\text{Al}_2\text{O}_3$ ; closed circles,  $\text{Al}_2\text{O}_3$  doped with  $\sim 800$  ppm Cr; and closed squares,  $\text{Al}_2\text{O}_3$  doped with 8100 ppm Cr. The solid lines are computer fits with use of  $\beta$ -cubic spline functions.

sults of this exercise are shown in Fig. 2. Clearly, peaked anomalies are produced with a peak at  $\sim 3.9$  K and this is tentatively ascribed to the presence of  $\text{Cr}^{2+}$  (produced from  $\text{Cr}^{3+}$  by  $\gamma$  irradiation). Obviously, the height and position of the peaks in Fig. 2, depending on the point of inflection in the fitted curve, will be sensitive to the exact computer fit, but we estimate that the peaks in the thermal-expansion curves are correct to  $\sim 20\%$  and that the temperature at which the peaks occur is  $\sim 3.9 \pm 0.2$  K. The fact that the anomalous peaks apparently occur at slightly different temperatures is not thought to be physically significant; the smaller peak, in particular, is near the present limit of the sensitivity of the measurement technique and unfortunately measurements could not be made below 3.5 K, making the identification of the point of inflection in this curve very difficult.

We also note that Fig. 2 shows the "pure"  $\text{Al}_2\text{O}_3$  sample to have a small negative linear thermal-expansion coefficient up to  $\sim 6$  K. This may be an "apparatus effect," perhaps partially caused by the H.C.O.F. copper of the expansion cell expanding in a slightly different way than that of Kroeger and Swenson,<sup>14</sup> or it could be a "real effect," perhaps due to the presence of other impurities in this sample (and possibly all three samples) and with negative magnetic Grüneisen coefficients. However, this small effect in the "pure"  $\text{Al}_2\text{O}_3$  thermal-expansion "baseline" should not affect the interpretation of the impurity results significantly.

If one takes the recently published energy levels of  $\text{Cr}^{2+}$  in  $\text{Al}_2\text{O}_3$ ,<sup>12</sup> the Schottky specific-heat anomaly can be computed, the result peaking at

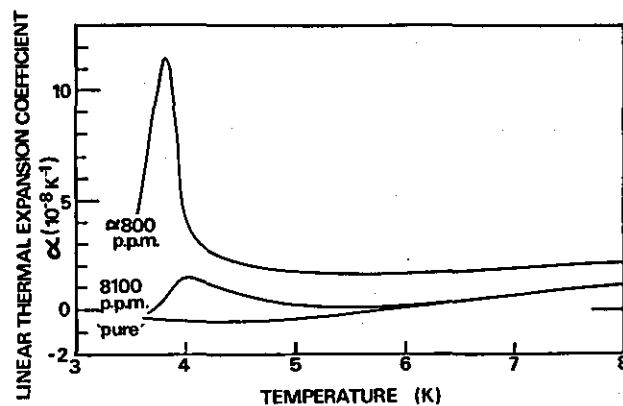


FIG. 2. Thermal expansion of the three samples as a function of temperature, derived from the computer fits shown in Fig. 1.

a temperature of 2.6 K to a value of  $20 \times 10^{-24}$  J  $\text{K}^{-1}$  per ion. One only expects the specific-heat anomaly and the thermal-expansion anomaly to peak at exactly the same temperature if the Grüneisen coefficients for each level are the same. Unfortunately, although estimates of the magnetic Grüneisen coefficients  $\gamma_s$  have been made for  $\text{MgO}:\text{Cr}^{2+}$ , no such detailed work has yet been done for  $\text{Al}_2\text{O}_3:\text{Cr}^{2+}$ . However, it is anticipated that the system will be qualitatively similar and in particular that a small negative value of  $\gamma_s$  will be predicted by the static field model whereas a large positive value ( $\sim 30$  for  $\text{MgO}:\text{Cr}^{2+}$ ) will be predicted by the dynamic Jahn-Teller model.<sup>6</sup> Clearly, from Fig. 2, a positive contribution to the thermal expansion is obtained; and by using the theoretical Schottky specific-heat values, a value for the isothermal compressibility<sup>16</sup> of  $\text{Al}_2\text{O}_3$  of  $3.78 \times 10^{-12}$   $\text{Pa}^{-1}$ , the estimated total chromium concentration, and an estimate of 5% for the number of  $\text{Cr}^{3+}$  ions converted to  $\text{Cr}^{2+}$  ions by  $\gamma$  irradiation (based on low-temperature thermal-conductivity measurements and earlier work<sup>17</sup>), we obtained an admittedly crude estimate for  $\gamma_s$  of  $\sim 80$  ( $\pm 40$ ).

In conclusion, although we clearly have to do a great deal of further work, we have observed an anomaly in the thermal expansion of  $\gamma$ -irradiated  $\text{Al}_2\text{O}_3:\text{Cr}$  which has been interpreted in terms of a Schottky anomaly due to  $\text{Cr}^{2+}$ . The anomaly is positive and large and is consistent with a dynamic Jahn-Teller model.

We would like to thank the Science Research Council and the Scientific Affairs Division of NATO for financial support of the research program, carried out in collaboration with Service Basses Températures, Centre d'Etude Nucléaires,

Grenoble, France.

<sup>1</sup>C. A. Bates, Phys. Rep. **35C**, 187 (1978).

<sup>2</sup>M. D. Sturge, in *Solid State Physics*, edited by H. Ehrenreich, F. Seitz, and D. Turnbull (Academic, New York, 1967), Vol. 20, p. 91.

<sup>3</sup>J. R. Fletcher and K. W. H. Stevens, J. Phys. C **2**, 444 (1969).

<sup>4</sup>F. W. Sheard, Phys. Lett. **30A**, 156 (1969).

<sup>5</sup>J. G. Collins and G. K. White, Prog. Low Temp. Phys. **4**, 450 (1964).

<sup>6</sup>F. W. Sheard, in *Thermal Expansion—1971*, edited by M. C. Graham and H. E. Nagy, AIP Conference Proceedings No. 3 (American Institute of Physics, New York, 1972), p. 155.

<sup>7</sup>F. W. Sheard, T. F. Smith, G. K. White, and J. A. Birch, J. Phys. C **10**, 645 (1977).

<sup>8</sup>G. K. White, Cryogenics **1**, 151 (1961).

<sup>9</sup>R. Q. Fugate and C. A. Swenson, J. Appl. Phys. **40**, 3034 (1969).

<sup>10</sup>M. A. Brown and Y. Robach, J. Phys. C **10**, 4939 (1978).

<sup>11</sup>M. A. Brown, Ph.D. thesis, Nottingham University, United Kingdom, 1971 (unpublished).

<sup>12</sup>C. A. Bates and R. S. Wardlaw, J. Phys. C **13**, 3609 (1980).

<sup>13</sup>L. J. Challis and A. M. de Goer, Phys. Lett. **31A**, 463 (1970).

<sup>14</sup>F. R. Kroeger and C. A. Swenson, J. Appl. Phys. **48**, 853 (1977).

<sup>15</sup>M. Villedieu, private communication.

<sup>16</sup>A. Schauer, Can. J. Phys. **43**, 523 (1965).

<sup>17</sup>M. A. Brown, A. M. de Goer, N. Devismes, and M. Villedieu, in *Proceedings of the International Conference on Phonon Scattering in Solids, Paris, France, June 1972*, edited by H. J. Albany (Service de Documentation, Centre d'Etudes Nucléaires de Saclay, Gif-sur-Yvette, France, 1973), p. 272.

